N° d'Ordre : D.U. 1633

UNIVERSITE BLAISE PASCAL
(U. F. R. de Recherche Scientifique et Technique)

ECOLE DOCTORALE DES SCIENCES FONDAMENTALES
N° 475

THESE

Présentée pour obtenir le grade de

DOCTEUR D'UNIVERSITE
Spécialité : Volcanologie

Par

FUKUSHIMA Yo

Diplômé de Master

Transferts de magma au volcan du Piton de la Fournaise déterminés par la modélisation 3D de données d'interférométrie radar entre 1998 et 2000

Soutenue publiquement le 16 décembre 2005, devant la commission d'examen composée de :

President :	MERLE Olivier	Université Blaise Pascal Clermont II
Rapporteur :	CORNET François-Henri	Institut de Physique du Globe de Paris
Rapporteur :	MASSONNET Didier	Centre National d'Etudes Spatiales
Examinateur :	JAUPART Claude	Université de Paris VII
Invité :	DURAND Philippe	Centre National d'Etudes Spatiales
Directeur de thèse :	LÉNAT Jean-François	Université Blaise Pascal Clermont II
Directrice de thèse :	CAYOL Valérie	Université Blaise Pascal Clermont II

Abstract

After five and a half years of quiescence, Piton de la Fournaise volcano (Réunion Island, Indian Ocean) entered into a new active period in March 1998. Synthetic aperture radar interferometry (InSAR) data show complex displacements associated with the first five eruptions that occurred between 1998 and 2000. A method was developed to find realistic geometries and overpressures of dike intrusions from the InSAR data. This method is based on a combination of a fully 3D boundary element method and a Monte Carlo inversion. The noise characteristics of the data are taken into account in the inversions. Synthetic tests show that a model is successfully retrieved within predicted narrow confidence intervals. Neglecting topography was shown to result in poor modelling at depth and in overestimation of overpressure or opening. Application of the method to each eruption requires specific parameterizations of the model(s); in some cases, a curved dike surface must be introduced, and in other cases, simultaneous inversions for two dikes are required. Most of the estimated dikes dip seaward with a typical angle of 65 degrees. The dike associated with the first eruption of the cycle (March 1998) is found to originate from sea level (2600 m below the summit), whereas those dikes associated with subsequent eruptions are estimated to be shallower than about 1000 m below the ground. Laterally elongated dikes, preeruption deformations and seismic swarms can be explained by a level of neutral buoyancy less than 1000 m beneath the ground. This is consistent with the presence of magma reservoirs at this level. For the studied period, the intruded volume amounts to 8% of the lava flow volume. The spatial periodicity of dike intrusions from the northern to the southern flank is consistent with stress transfer models. Finally, Coulomb stress analysis shows that the five eruptions modelled mostly encourage slip on potential subhorizontal planes located 1000–1500 m above sea level.

Résumé

Après cinq ans et demi de sommeil, le volcan du Piton de la Fournaise (île de la Réunion, Océan Indien) est entré dans un nouveau cycle d'activité en mars 1998. Des données d'interférométrie radar (InSAR) montrent que des déplacements complexes sont associés aux cinq premières éruptions du cycle survenues entre 1998 et 2000. Une méthode a été développée pour déterminer des géométries réalistes et les surpressions des intrusions de dykes à partir de données InSAR. Cette méthode est basée sur la combinaison d'une méthode d'éléments frontières 3D et d'une inversion de type Monte Carlo. Les caractéristiques du bruit des données sont prises en compte dans les inversions. Des tests synthétiques montrent qu'un modèle est retrouvé avec succès dans la limite d'intervalles de confiance étroits. Il a été montré que négliger la topographie induit une erreur de modélisation en profondeur et une surestimation des surpressions ou des ouvertures. L'application de la méthode à chaque éruption requiert des paramétrisations spécifiques des modèles. Dans certains cas, un dyke incurvé en surface doit être introduit, dans d'autres, l'inversion simultanée de deux dykes est nécessaire. La plupart des dykes déterminés ont un pendage vers la mer de 65 degrés. Le dyke associé à la première éruption du cycle (mars 1998) s'enracine au niveau de la mer (2600 m sous le sommet), tandis que les dykes suivants sont situés à moins de 1000 m sous la surface du sol. La forme latéralement allongée des dykes, les déformations pré-éruptives et les essaims sismiques peuvent être expliqués par un niveau de flottabilité neutre situé à moins de 1000 m sous la surface. Ceci est cohérent avec la présence de réservoirs magmatiques à ce niveau. Pour la période étudiée, le volume injecté dans le volcans représente 8% du volume des coulées de lave. La périodicité spatiale des intrusions de dykes, du flanc nord au flanc sud, est cohérente avec les modèles de transfert de contraintes. Finalement, des analyses en terme de contraintes de Coulomb montrent que les cinq éruptions modélisées ont principalement favorisé le glissement sur des plans potentiels subhorizontaux situés entre 1000 et 1500 m au dessus du niveau de la mer.

Acknowledgements

First of all, I wish to thank Valérie Cayol. Without her advice, support, patience and encouragement, it would not have been possible for me to continue working on this challenging subject for three years. Inspite of extra works she had to do for me, she has showed no sign of complaint and has been always helpful; her such attitude has been my spiritual support. (I only hope she has not worn out!)

I am deeply grateful to François-Henri Cornet and Didier Massonnet for having accepted to be the *rapporteurs*, and to Philippe Durand, Claude Jaupart and Olivier Merle for being the members of jury.

Special thanks go to Jean-François Lénat who has always cared about my work. He has kindly given me an opportunity to visit Réunion Island and Piton de la Fournaise volcano. This saved me from misunderstanding that volcanoes are something I see on the computer screen. I benefited also from his expertise on the Piton de la Fournaise volcano.

This study benefited from a collaborative project between the French Centre National d'Etudes Spatiales (CNES) and the Canadian Space Agency (CSA) through the Applications Development and Research Opportunity program sponsored by CSA. I highly appreciate those who have devoted time and effort to the project, especially Didier Massonnet for launching the project, and Philippe Durand for computing the interferometric data which this thesis is based on.

I thank the staffs of the Observatoire Volcanologique du Piton de la Fournaise for having warmly greeted me during my visit to Réunion Island, and for providing me seismicity data. Especially, Thomas Staudacher further gave me useful information on what he and his colleagues observed in the field during the eruptions that I worked on. I have enjoyed fruitful discussions with Valérie Ferrazzini and Keiiti Aki. Regretfully, Keiiti Aki has passed away in May 2005, but the memory of the dinner and talks we had is unforgettable.

I have benefited a lot from the members of the laboratory. I first acknowledge the countless helps of Jean-Luc Froger (his ground meshing program was especially useful), as well as many constructive discussions with him. Fabien Ranvier has kindly helped me get used to the techniques of the boundary element method when I knew nothing about it. Philippe Labazuy has supported me and let me use his Linux machine, which was very important. I also thank Thierry Souriot, who helped me in phase unwrapping at an early stage of the study. Benjamin van Wyk de Vries has supported and encouraged me throughout the period as the head of the volcanology group. I have also learnt many things from discussions with petrologists and geochemists in the laboratory: Pierre Boivin, Didier Laporte and Olgeir Sigmarsson. I have enjoyed talking to two Japanese Ken Koga and Tatsuhiko Kawamoto, not only because I could speak in my mother tongue but also because of their insights. Philippe Cacault and Thierry Souriot gave me helps on the computer enviroment.

I am grateful to Jean Battaglia for relocated seismicity data. There were lots of things to learn from discussion with Patrick Bachèlery. Nicolas Villeneuve and Aline Peltier have been answering my questions and I acknowledge their help. Freysteinn Sigmundsson has kindly given me his note on estimation of the radius of magma conduits. Malcolm Sambridge has provided me his inversion code which I used at an early stage of the study. I should not forget the continuous supports of Takeshi Nishimura (it was him who suggested me of working with Valérie), Motoo Ukawa, Hideki Ueda and Haruo Sato.

For the paper presented in Chapter 2, I am grateful to the contributions of the co-authors Valérie Cayol and Philippe Durand. François-Henri Cornet, Ariel Provost, Jean-François Lénat reviewed the manuscript before submission, and Benjamin van Wyk de Vries reviewed and corrected English before and after submission. Long and thoughtful comments of the three reviewers, two anonymous and Sigurjón Jónsson and the Associate Editor L. Mastin contributed to improve the quality of the paper.

I have enjoyed the company of my officemates: Fabien Ranvier, Jean-François Oehler, Pierre Tinard and Silke Lohmar. I have also enjoyed being with other Ph.D. students and postdocs, especially Sévérine Jannot, Sévérine Moune, Perrine Lebti-Paquereau and Vinciane Debaille, with whom I share the memory of these three years.

The thesis work was financially supported by a grant from the French government. I thank Madame Compte-Rome, the responsible of the grant at CROUS, for taking care of small things around me and my family.

My mother and mother-in-law have come all the way to France for taking care of house chores, when I was at a loss how to juggle both work and household, so that I could concentrate on writing the thesis. I thank my father for his discreet but thoughtful care on my life and professional career. Last but not least, I deeply thank my dear wife Aiko for her comprehension, support and encouragement (yes, she also helped me typing in the reference list), and my dear son Shotaro for giving me the energy to work on the thesis.

Contents

List of Tables

List of Figures

Chapter 1

Introduction

Volcanic eruptions mark the final stage of magma transfer from the mantle. In a shallow part of the crust, magma movements cause detectable changes of various physical parameters that are detectable on the ground. Geodetic measurements provide data that can be quantitatively interpreted in order to understand magma transfer mechanisms; this quantitative interpretation is carried out through *modelling*.

The recently developed interferometric synthetic aperture radar (InSAR) technique allows to map ground displacement field in unprecedented precision and resolution. Complex displacements revealed by InSAR call for numerical modelling analyses that can take into account more realistic situations than simple analytical models.

The field of work of this thesis is Piton de la Fournaise volcano, a very active basaltic shield volcano that occupies the southeastern part of Réunion Island, Indian Ocean. From detailed analyses of the InSAR data associated with five consecutive eruptions that occurred between 1998 and 2000, this study attempts to develop a model of the magma transfer system of the volcano as well as to give inference on its volcano-tectonic structures.

In this chapter, introductions are given to Piton de la Fournaise, displacement measurements using InSAR, geodetic data modelling on volcanoes, and modelling of dike emplacements. Chapter 2 describes the development of the modelling method based on a combination of a boundary element and a Monte Carlo inversion methods. Application to the five consecutive eruptions at Piton de la Fournaise is presented in Chapter 3. Overpressure and geometry of the coeruptive magma intrusions are estimated by inverting InSAR data. Chapter 4 investigates the magma storage, transfer and emplacement mechanisms, as well as the volcano-tectonics of the volcano, based on the results obtained in Chapter 3 and complementary analyses. Finally, conclusions are given on the new findings revealed in this study.

1.1 Piton de la Fournaise Volcano

1.1.1 Geological settings

Réunion Island is a French oversea *département* located about 700 km east of Madagaskar in the Indian Ocean (Figure 1.1). This island has a dimension of 70×50 km elongated in NW-SE (Figure 1.2), with a height of 7 km from the sea floor [*Lénat et al.*, 1989b] and a volume of 75,000 km^3 [*de Voogd et al.*, 1999]. The northwestern part of the island is occupied by an extinct volcano, Piton des Neiges (3069 m). As a consequence of deep erosions, Piton des Neiges has

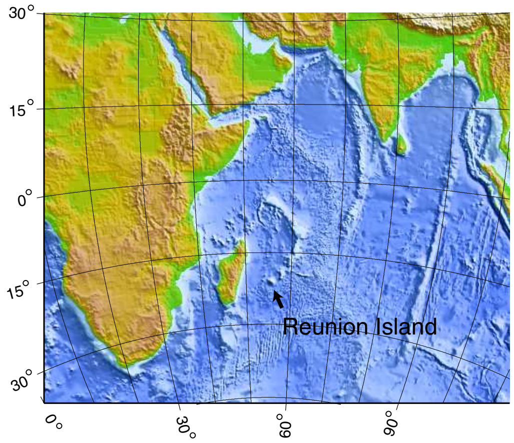

Figure 1.1: Shaded relief map showing the location of Réunion Island. Colors correspond to altitudes.

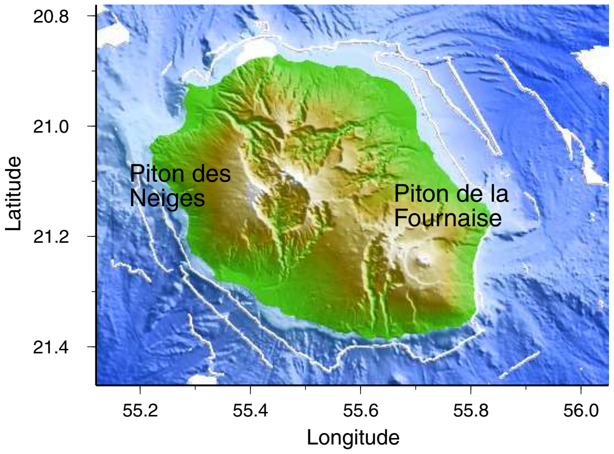

Figure 1.2: Shaded relief map of Réunion Island and surrounding bathymetry. Colors correspond to altitudes, except for white area in submarine part where data are missing. [Courtesy of Jean-François Oehler for the DEM data.]

three cirques that open toward the ocean. On the southeastern part of the island lies our field of work, Piton de la Fournaise (2631 m; Figure 1.2).

The origin of Réunion Island volcanism is a hot spot. This hot spot may be the one that created Deccan Trapp (India) 65 Ma ago [*Courtillot et al.*, 1986], or a recent one (less than 10 Ma) of which activity is only restricted to this island [*Burke*, 1996; *Sheth*, 2005].

Piton de la Fournaise started its activity more than 530,000 years ago [*Gillot and Nativel*, 1989]. It has a caldera-like depression that opens to the ocean called Enclos-Fouqué caldera (Figure 1.3). This depression, at least its western part, formed 5000 years ago [*Bachèlery*, 1981]. On the caldera floor, a central cone has two summit craters called Bory and Dolomieu. The volcano also has arcuate rift zones, oriented N10° and N170° with respect to the summit, where surface fractures and eruptive vents are preferentially located.

Bory crater already existed and was close to its present state in 1766 [*Lénat and Bachèlery*, 1990], whereas the Dolomieu crater, on the contrary, has been experiencing numerous collapses and refillings [*Bachèlery*, 1981]; the most recent pit crater formation in Dolomieu took place in December 2002 and partial refillings of Dolomieu occurred in May to June and December 2003. The summit craters have concentric fissures that are normally noneruptive, and whose origin is probably related to crater collapses [*Bachèlery*, 1981].

Piton de la Fournaise is often compared with Hawaiian volcanoes, which are also basaltic shield volcanoes of hot-spot origin. The characteristics of the rift zones, however, are significantly different. Hawaiian rift zones are associated with numerous vertical dike intrusions, resulting in distinct ridges that extend for tens of kilometers. In contrast, those of Piton de la Fournaise open seaward and there is no ridge structure. Since 1644, about five percent of the eruptions occurred outside Enclos-Fouqué caldera [*Stieltjes and Moutou*, 1989], with the most recent ones in 1977 and 1998 to the north and in 1986 to the south (Figure 1.4).

The submarine part of Réunion Island provides important information on the volcano-tectonic evolution of Piton de la Fournaise. The age and volume of landslide materials on the

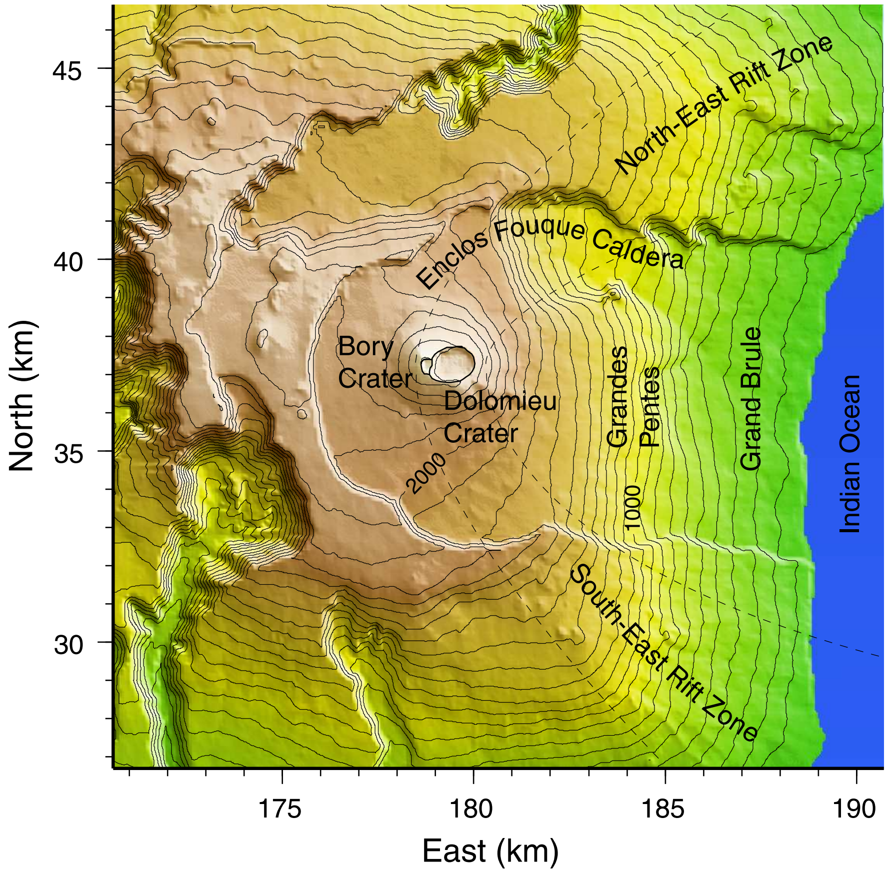

Figure 1.3: Map showing the geological setting of Piton de la Fournaise volcano. Colors correspond to altitudes. Contours are drawn every 100 m. The summit craters, Bory and Dolomieu, are outlined. The coordinates are given in Gauss-Laborde kilometric coordinates.

submarine eastern flank of the volcano clearly indicate recurrent seaward landslides [*Labazuy*, 1996]. It is still under debate whether the most recent one, associated with the formation of Enclos-Fouqué caldera, was caused by a single landslide [*Labazuy*, 1996; *Lénat and Bachèlery*, 1990; *Lénat et al.*, 2001], or by a coupled mechanism involving a landslide close to the ocean (the Grand-Brûlé area, Figure 1.3) and a collapse in the central area [*Bachèlery*, 1995; *Bachèlery and Mairine*, 1990; *Chevallier and Bachèlery*, 1981; *Duffield et al.*, 1982]. *Merle and Lénat* [2003] showed by analogue experiments that the latter scenario is possible when the core of the volcano is hydrothermally altered.

A drilling in the Grand-Brûlé area evidenced a large intrusive and cumulate complex [*Rançon et al.*, 1989] 1000 m beneath the ground. Gravitational and geomagnetic data [*Lénat et al.*, 2000, 2001] strongly support the presence of such a complex. According to *Lénat et al.* [2001], this complex is related to an ancient volcano (named the Alizés), and it may have provided the basal plane for the eastward landslides of Piton de la Fournaise.

1.1.2 Eruption monitoring

Quantitative eruption monitoring started when a volcano observatory *l'Observatoire Volcanologique du Piton de la Fournaise* was installed in 1980. As of October 2005, it maintains dense seismic (short period and broad band), deformation (tiltmetry, extensometry, distansometry and continuous and campaign GPS), radon probe and magnetometric networks (information from the website of the observatory: http://volcano.ipgp.jussieu.fr:8080/reunion/stationreu2.html). Data of these networks have largely contributed to the understanding of the eruption dynamics.

InSAR provides an excellent complement to the geodetic monitoring networks. Although this technology is not useful for short-term eruption forecasts, which require continuous monitoring, it instead measures precise displacements in the area uncovered by vegetation with resolution of 20 m. This advantage has enabled us to model the dike emplacements at Piton de la Fournaise in detail [*Froger et al.*, 2004; *Fukushima et al.*, 2005; *Sigmundsson et al.*, 1999]. Since 1995, SAR images on Piton de la Fournaise have been captured by the satellite RADARSAT-1 lauched by the Canadian Space Agency. It is these data that the present study benefits from. In March 2002, the European Space Agency launched a satellite ENVISAT. At the Laboratoire Magmas et Volcans, interferograms are systematically computed and archived for all the eruptions after August 2003.

1.1.3 Magmatic system

In the last two centuries, Piton de la Fournaise experienced more than 200 eruptions; this corresponds to one eruption in every ten months on average [*Stieltjes and Moutou*, 1989]. The mean lava output rate is about 0.32 m^3/s, which is one order less than that at Kilauea and comparable to that at Etna [*Bachèlery*, 1999].

Since the installation of the observatory, geodetic data showed no clear preeruptive inflation and posteruptive deflation that show evidence of a common magma reservoir responsable for all or majority of the eruptions. (However, in the last several years, systematic preeruptive inflation of typically several weeks is observed, A. Peltier, personal communication, 2005.) The hypocenters of the preeruption volcano-tectonic microearthquakes are, in many cases, restricted above sea level, and do not always occur in the same region. These observations led *Lénat and Bachèlery* [1990] to propose the presence of a shallow magma reservoir that consists of many small interconnected dikes and sills, between sea level and several hundred meters beneath the

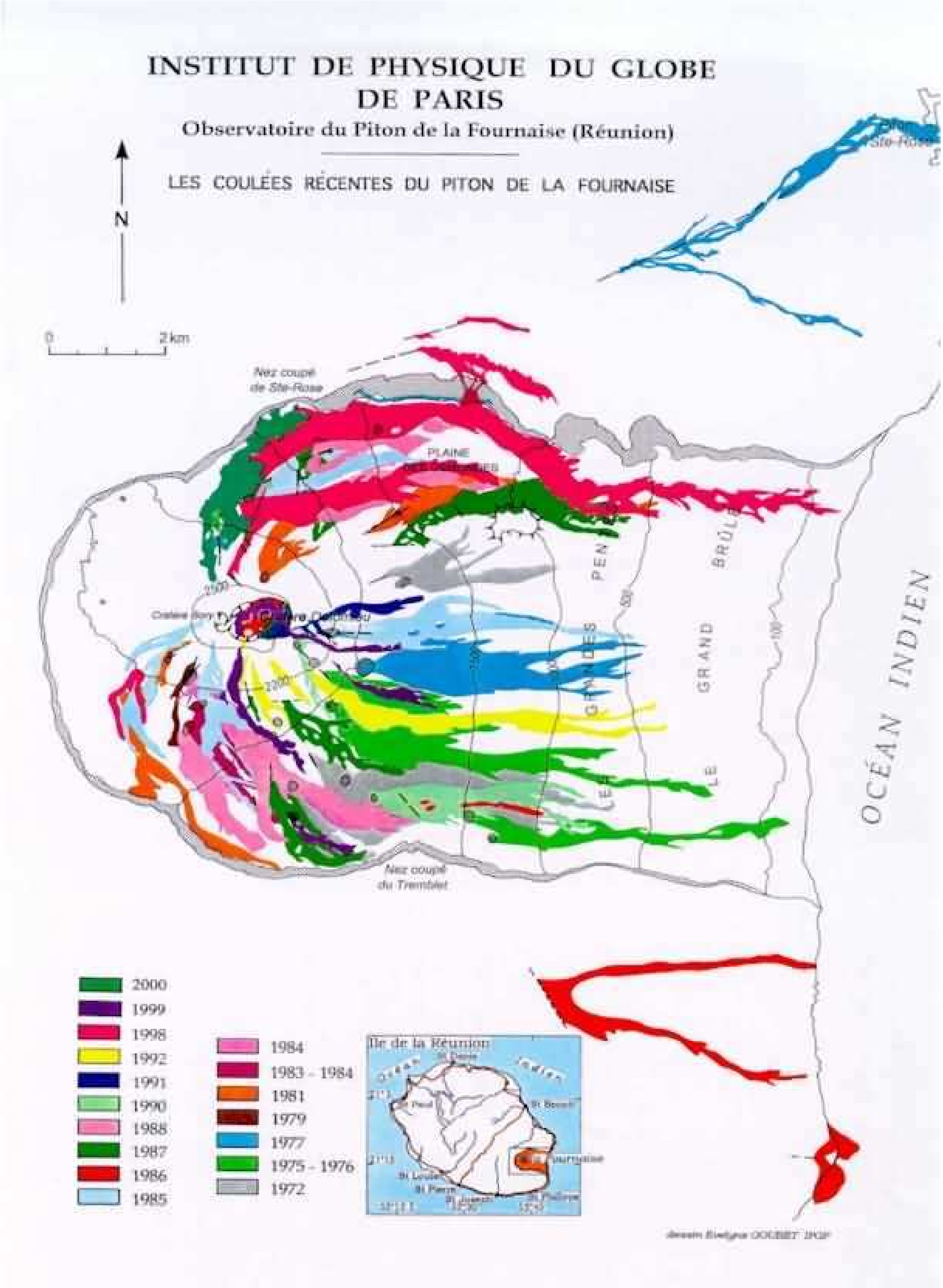

Figure 1.4: Lava flows between 1972 and 2000. [From the website of Observatoire Volcanologique du Piton de la Fournaise.]

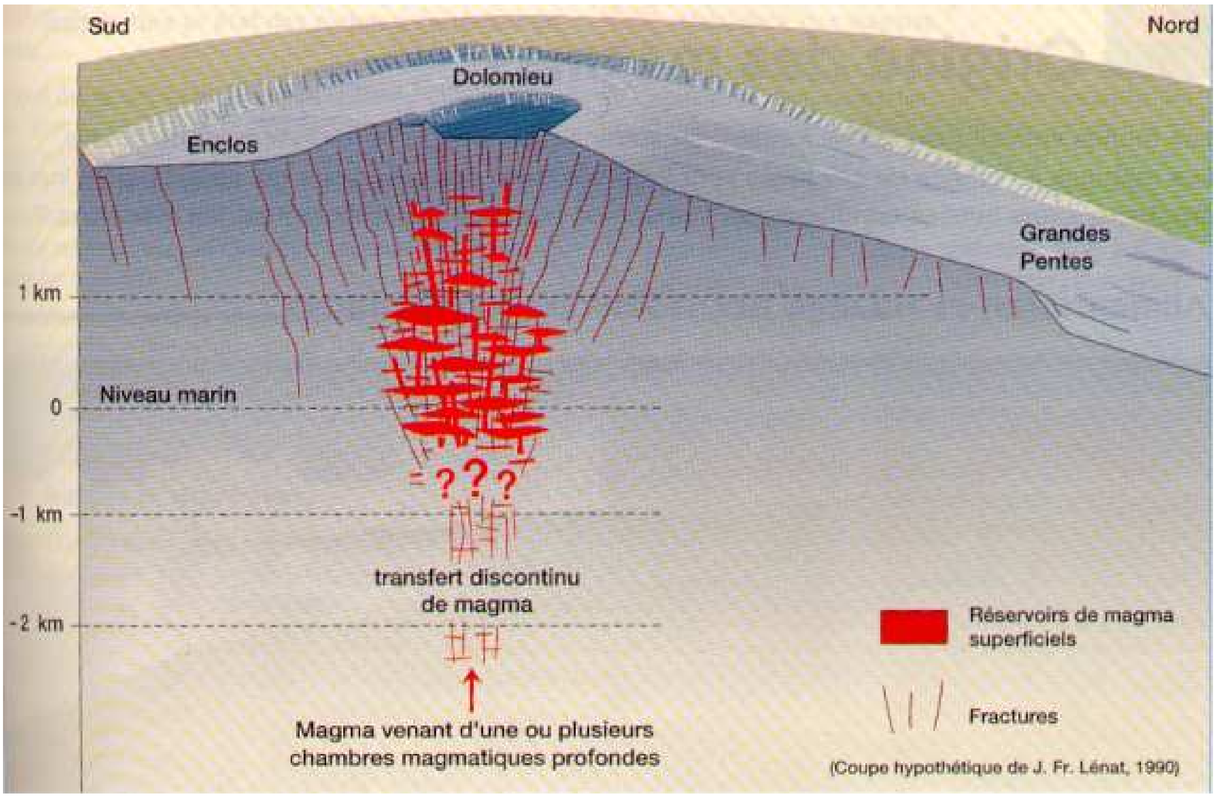

Figure 1.5: Magma reservoir model proposed by Lénat and Bachèlery [1990]. It consists of many storage units of dikes and sills, connected to each other (After Lénat and Bachèlery [1990]).

summit (Figure 1.5). *Carter* [2004] proposed an existence of a magma reservoir 1 km below the Dolomieu floor from applying field fracture observation to the result of analogue experiments on crater formation of *Roche et al.* [2001]. Recent pit-crater formations [*Longpré et al.*, 2004] show evidence of magma storage at a very shallow level.

In contrast, seismic and geodetic (InSAR and photogrammetry) data suggest a deeper magma reservoir. A seismic tomography found a low velocity zone of 1.5 km in diameter at a depth of 1.5 km below sea level, which was proposed as a magma chamber [*Nercessian et al.*, 1996]. *Aki and Ferrazzini* [2000] proposed a model that consists of relatively deep reservoirs and channels (between 0 and 5 km below sea level), from their analyses on coda localization and preeruption long-period events. *Cayol and Cornet* [1998a] estimated the shallower limit of the depth of the magma reservoir that fed the 1983–1984 eruption at 19 km, from the fact that no deflation source was indicated by photogrammetric data. *Sigmundsson et al.* [1999] calculated interferograms from RADARSAT-1 images for pre-, co- and post-eruption displacements associated with the March 1998 eruption at Piton de la Fournaise, and modelled them. These interferograms did not also show any deflation, which led them to conclude that magma should have been transported from more than 7 km depth below sea level.

Geochemical and petrological studies indicate at leat two levels of magma storage beneath the volcano. *Vlastélic et al.* [2005] studied the Pb isotopes and trace elements of the lava emitted during 1998 and 2002, and found two levels of magma storage: one at the level of oceanic crust and the other at a shallower level in the edifice. *Bureau et al.* [1998] proposed, from a study of melt inclusions in olivine phenocrysts, that magmas were stored at different depths, from shallow levels to 15 km or more, beneath the summit. Similarly, *Boivin and Bachèlery* [2003] found two populations of clinopyroxene in the lavas emitted between 1977 and 1998, indicating that the magma evolution took place at two different, intermediate and shallow, depths. The shallow storage system is probably located within the edifice, as evidenced by the interactions of magma with hydrothermally-altered materials. Data dispersion of Al/Ti ratio further suggested the evolution in different isolated storage units (at the same depth level), which supports the Lénat and Bachèlery model (Figure 1.5). *Sigmarsson et al.* [2005] identified two different magma storage depths from analyses of residence times using U-series disequilibria. They concluded that the deeper reservoir system is poorly replenished and magma resides on timescales of the order of 1000 years, whereas the shallower one is consistent with a residence time of 25 years and a volume of 0.35 km^3. The latter, according to them, might correspond to the reservoir at the volcanic edifice–oceanic crust interface (7 km beneath the summit).

1.2 Displacement Measurements by SAR Interferometry

1.2.1 Background

Radars, as the origin of the word *radio detecting and ranging* indicates, detect distant objects and determine their position and velocity [see e.g. *Zebker et al.*, 2000]. The processed radar image, called Single Look Complex, contains the amplitude and phase of radar career signals (electromagnetic waves). The principle of interferometry is to compare the phase in two radar images in order to map range changes, where range means the distance between the radar antenna and the object. Its first applications in the 1970s and 1980s concerned topography mapping [see *Massonnet and Feigl*, 1998, for a review]. After technical developments in the late 1980s [*Gabriel et al.*, 1989; *Massonnet*, 1985], geophysical applications of radar interferometry to measure small (of the order of 1 cm) ground displacements have exploded in the early 1990s and thereafter, with the launches of ERS-1 satellite and successors.

InSAR is revolutionary with respect to conventional geodetic methods in that it can map surface motions with fine resolution (20–100 m) over large swaths (tens of kilometers), and that no instrument is needed on the field. The former characteristic obviously contributes to better constraining geophysical models of the deformation source, while the latter enables studying volcanoes that lack on-site deformation monitoring networks (due to remoteness of the volcano, financial limitations, etc.), as in Aleutian and Alaska [*Lu et al.*, 2000a,b,c, 2002, 2003; *Mann et al.*, 2002; *Masterlark and Lu*, 2004], Galápagos [*Amelung et al.*, 2000a; *Jónsson et al.*, 1999, 2005; *Yun et al.*, 2005], and the Andes [*Pritchard and Simons*, 2002, 2004a,b].

Since its birth, InSAR has experienced persistent and rapid methodological developments. Permanent Scatterers [*Feretti et al.*, 2001; *Salvi et al.*, 2004] or Persistent Scatterers [*Hooper et al.*, 2004] (PS) technique can detect displacements on terrestrial spots where backscattering characteristics change little with time, even in regions where incoherency of signals dominates. PS can also be used to enhance the signal-to-noise ratio of interferograms [*Lyons and Sandwell*, 2003]. Efforts have also been made to obtain a fine time series of InSAR data [*Bechor and Zebker*, 2004; *Lundgren et al.*, 2001; *Schmidt and Bürgmann*, 2003]. It is, in principle, possible to develop a time series of InSAR data with temporal resolution equivalent to the repeat period of the satellite. Apart from interferometry which treats the phase information, amplitudes of backscattered radar signals can also be useful. By detecting the offsets of corresponding points in two images, ground displacements in azimuth (direction parallel to the satellite's traveling direction) can be extracted [*Michel et al.*, 1999a]. Despite relatively large uncertainty in data of typically several tens of centimeters, this technique often provides complementary data in a horizontal direction for studying large earthquakes [*Feigl et al.*, 2002; *Fialko et al.*, 2001b; *Jónsson et al.*, 2002; *Michel et al.*, 1999a,b].

1.2.2 Production of interferograms

Resolution of a radar depends on its aperture. Synthetic aperture radars are designed for particular signal processings to synthesize a large aperture, that is, to have a fine resolution. Taking the difference of career signal phase in two processed images (Single Look Complex) acquired at different times generates fringes that are associated with topography, ground displacements that accumulated between data acquisitions, and difference in atmospheric properties (principally water vapor distribution; *Hanssen* [2001]). Here, one fringe corresponds to half the wavelength of the radar career signal. The phase differences caused by topography (topographic fringes) are removed by forming synthetic fringes from a digital elevation model (DEM). Those created by the difference in atmospheric properties, on the contrary, are in many cases difficult to remove, and they normally put limitation on the precision of an interferogram (order of one to several centimeters; e.g., *Hanssen* [2001]; *Massonnet and Feigl* [1998]).

Theoretically, two images taken from the same viewpoint should generate fringes that are uncorrelated with topography. In reality, this condition is never met and the satellite is positioned at slightly different locations for the two acquisitions. The larger the difference in view angles of the two images, the more sensitive the interferogram is to topography. This sensitivity is often expressed through the altitude of ambiguity h_a, the elevation difference that corresponds to a fringe (2π phase change) [*Massonnet and Rabaute*, 1993]

$$h_a \sim \frac{R\lambda \tan\theta}{2B_h} \tag{1.1}$$

where B_h is the horizontal separation between the image acquisition points (the horizontal baseline), R is the observation range, θ is the incidence angle, and λ is the wavelength.

1.2.3 Unwrapping of interferograms

For data inversions, it is normally desirable to convert the phase values (known only modulo 2π) to physically-meaningful displacements along the line-of-sight direction of the satellite, by counting the phase cycles (fringes). This conversion is called phase unwrapping (or simply unwrapping). For a phase value of a pixel at i-th row and j-th column ϕ_{ij} of a two-dimensional array, the unwrapped displacement at the corresponding pixel u_{ij} can be written as

$$u_{ij} = \frac{\lambda}{2}\frac{n_{ij}\phi_{ij}}{2\pi} + l, \tag{1.2}$$

where λ is the wavelength of the radar signal, n_{ij} is an integer, and l is a constant. Unwrapping consists of determining n_{ij} for all combinations of i and j. The constant l can be determined in such a way that the displacements far from deformation sources are zero, or as done in this study, that the discrepancy between observed and modelled displacements becomes minimum (Section 2.3.4).

Numbers of unwrapping algorithms exist, but they all assume that the true unwrapped displacement field varies slowly enough that in most places, neighboring phase values are within one-half cycle (π rad) [*Chen and Zebker*, 2000]. Unwrapping intrinsically includes a risk of errors because supplementary information (integers n_{ij} at all the pixels) is added to the original phase data. It is therefore important to check if unwrapping was properly done. Proper unwrapping provides smooth displacements consistent with the number of fringes in the original interferogram where no displacement discontinuity is expected, and discontinuity correlated with geological features (earthquake faults, for example).

1.2.4 Applications

Applications of InSAR covers various fields: tectonic deformation, volcanism, subsurface fluid movement, terrain classifications, glacial processes, landslides, and so on [*Bürgmann et al.*, 2000; *Massonnet and Feigl*, 1998]. *Bürgmann et al.* [2000] gives an exhaustive review on previous works (before 2000) that used InSAR data of coseismic, postseismic and interseismic deformation, volcano deformation including inflation and deflation of magma chambers and dike and sill intrusions, and land subsidence. Indeed, more than 90 papers have been published in these research areas from major journals at the time of writing (July 2005).

The fine spatial resolution of InSAR data allows estimating a detailed slip distribution of an earthquake fault [e.g. *Jónsson et al.*, 2002; *Pedersen et al.*, 2003, see also the next section]. Major studied regions are: California (Landers in 1992 [e.g. *Massonnet et al.*, 1993], Hector Mine in 1999 [e.g. *Jónsson et al.*, 2002]), Alaska (Nenana Mountain in 2002 [*Wright et al.*, 2003] and Denali in 2002 [*Wright et al.*, 2004]), Iceland [*Pagli et al.*, 2003; *Pedersen et al.*, 2001], Turkey (İzmit in 1999 [*Bos et al.*, 2004; *Feigl et al.*, 2002], Düzce in 1999 [*Bürgmann et al.*, 2002]), and Bam earthquake in 2003 [*Fialko et al.*, 2005; *Talebian et al.*, 2004]. Besides the studies of coseismic deformation, postseismic deformation is also actively studied using InSAR because it can reveal valuable information about the rheology of the Earth's crust. InSAR studies in this category include afterslips following major earthquakes [e.g. *Jacobs et al.*, 2002; *Peltzer et al.*, 1998], poroelastic rebound [e.g. *Peltzer et al.*, 1998],viscoelastic deformation [e.g. *Pollitz et al.*, 2000], and reactivated slip on nearby faults [*Fialko et al.*, 2002].

On volcanoes, InSAR elucidated complex displacement fields that originate from inflation and deflation of magma chambers, dike and sill intrusions, lava flow subsidences, and geothermal activities. In addition, InSAR also drew great attention as a means of eruption monitoring of remote and "non-equiped" volcanoes. Studied volcanic systems include Etna [e.g. *Briole et al.*, 1997; *Froger et al.*, 2001; *Lundgren and Rosen*, 2003; *Massonnet et al.*, 1995; *Ranvier*, 2004], Campi Flegrei [e.g. *Avallone et al.*, 1999; *Lanari et al.*, 2004; *Lundgren et al.*, 2001], Alaskan volcanoes [e.g. *Lu et al.*, 2000a,b,c], Icelandic volcanoes [e.g. *Pedersen et al.*, 2003; *Sigmundsson et al.*, 1997], volcanoes and geothermal field in Western United States [e.g. *Fialko and Simons*, 2001; *Fialko et al.*, 2001c; *Wicks et al.*, 1998], Kilauea volcano [*Cervelli et al.*, 2002], the Andes [*Pritchard and Simons*, 2002, 2004a,b], Galápagos volcanoes [*Amelung et al.*, 2000a; *Jónsson et al.*, 1999; *Yun et al.*, 2005], Piton de la Fournaise [*Froger et al.*, 2004; *Fukushima et al.*, 2005; *Sigmundsson et al.*, 1999], Fogo [*Amelung and Day*, 2002] and some others.

On Réunion Island, volcanic deformation at Piton de la Fournaise and local landslides at Piton des Neiges have been studied using InSAR. *Sigmundsson et al.* [1999] estimated a seaward-dipping dike from an interferogram that recorded the coeruptive displacements of the March 1998 eruption at Piton de la Fournaise. *Fukushima et al.* [2005], the paper presented in Chapter 2, developed a method based on a 3D mixed boundary element method [*Cayol and Cornet*, 1997] and a Monte Carlo inversion algorithm [*Sambridge*, 1999a,b]. They applied the method to interferograms of the Februrary 2000 eruption. *Froger et al.* [2004] studied the August 2003 eruption from the interferograms calculated from ENVISAT images with the method of *Fukushima et al.* [2005]. *Raucoules et al.* [2003] identified landslides in the Salazie Cirque (northeast cirque of Piton des Neiges). They worked on interferograms computed from both JERS-1 (L-band: wavelength 23.5 cm) and RADARSAT-1 (C-band: wavelength 5.7 cm) images, and concluded that data from L-band satellites would be useful to monitor landslides at Réunion Island.

1.3 Ground Deformation Data Modelling on Volcanoes

Dvorak and Dzurisin [1997] compiled the geodetic measurements and modelling studies that had been made on active magmatic systems until 1997 (i.e., before the extensive applications of InSAR), with the major findings obtained from the modelling studies. According to them, the dawn of ground deformation measurements of active volcanoes dates back to 1819 on Campi Flegrei. Since then, monitoring networks have been developed on about 50 volcanic areas and a considerable amount of knowledge has been achieved through modelling. Today, we are in the next stage of great advance in modelling of volcanic systems with the aid of the new technologies of GPS and InSAR.

1.3.1 What is modelling?

In scientific contexts, a *model*, when used as a noun, means a schematic and simplified description of a phenomenon or an object. *To model* means, depending on the context, either to (conceptually) construct a model, or to quantitatively explain data based on a model.

In the domain of geodesy, modelling (in both meanings) gives light on the characteristics of the source of signals, such as the position, spatial dimensions, amount of dislocation, as well as on the rheology of the medium. Namely, modelling helps explaining the physical processes that occur beneath the ground. Modelling first requires a mathematical, numerical or empirical expression (model) that predicts signals when characteristics of the source is known. Obtaining this relation is referred to as *forward problem*. Several assumptions are made at this step because we have to approximate or idealize the complex Earth as a simple body. Once such an expression is obtained, the next problem is to infer the characteristics of the buried source, which are normally unknown, from the observed (known) signals. This kind of problem is referred to as *inverse problem*; we *invert* data to know about their source. Solving an inverse problem is called *inversion* (Section 1.3.4).

See *Chevallier and Verwoerd* [1988] and *De Natale and Pingue* [1996] for a review of the methods and problems in modelling of ground deformations in volcanic areas.

1.3.2 Analytical models

Mogi [1958] developped an analytic formulation for the ground deformation due to the inflation of a deep magma body, by considering a point pressure source of radial expansion in an elastic half-space. Because of its simplicity, Mogi's model has been extensively applied to inflation or deflation of a magma chamber or a geothermal source [e.g. *Björnsson et al.*, 1977; *Dvorak et al.*, 1983; *Furuya*, 2004; *Lu et al.*, 2000a,b,c, 2002, 2003; *Mogi*, 1958; *Pritchard and Simons*, 2002, 2004a,b; *Sigmundsson et al.*, 1997; *Vadon and Sigmundsson*, 1997; *van Dalfsen et al.*, 2004; *Yokoyama*, 1986]. Other analytical expressions for a volumetric pressure source in elastic media have been developed for a finite sphere [*McTigue*, 1987], an oblate ellipsoid [*Yang et al.*, 1988] with applications by several workers [*Fialko and Simons*, 2000; *Lanari et al.*, 2004; *Lundgren et al.*, 2001; *Pritchard and Simons*, 2004a], and a penny-shaped fracture [*Fialko et al.*, 2001a] with applications by *Fialko et al.* [2001c] and *Fialko and Simons* [2001]. By distributing point sources in a 3D space, *Vasco et al.* [1988], *Vasco et al.* [2002], *Mossop and Segall* [1999], and *Masterlark and Lu* [2004] modelled an arbitrary shape of pressure source.

Okada [1985] formulated analytical expressions for the ground displacements due to a finite rectangular dislocation (having both slip and tensile components) in an elastic half-space. Okada's model has also been extensively applied to dike and sill intrusions [e.g. *Amelung et al.*, 2000b; *Jónsson et al.*, 1999, 2005; *Lundgren and Rosen*, 2003; *Okada and Yamamoto*, 1991; *Okamura et al.*, 1988; *Owen et al.*, 1995, 2000; *Sigmundsson et al.*, 1999; *Ueda et al.*, 2005; *Wicks et al.*, 1998, 2001] and fault slips [e.g. *Amelung and Bell*, 2003; *Cervelli et al.*, 2001; *Fujiwara et al.*, 1998; *Lohman et al.*, 2002; *Pagli et al.*, 2003]. When enough data points are located close to a deformation source, we can go further and estimate the opening distribution for intrusions [*Amelung et al.*, 2000a; *Aoki et al.*, 1999; *Pedersen and Sigmundsson*, 2004a,b; *Troise et al.*, 1999; *Yun et al.*, 2005] or the slip distribution for earthquakes [e.g. *Bürgmann et al.*, 2002; *Feigl et al.*, 2000; *Jónsson et al.*, 2002; *Nishimura et al.*, 2001; *Pedersen et al.*, 2003; *Segall and Harris*, 1986; *Ward and Barrientos*, 1986; *Wright et al.*, 2003] on an assumed source geometry. Most of these studies first invert for the geometry of the rectangular source by assuming a constant slip, and then invert for the slip distribution on the determined fault. Some studies chose more appropriate approach; they grid-searched for some of the optimum source geometry parameters, with a slip (opening) inversion for each set of model parameters defining the source geometry [*Fialko*, 2004; *Fialko et al.*, 2005; *Simons et al.*, 2002; *Yun et al.*, 2005].

Williams and Wadge [2000] and others developped an approximate analytical technique for including topographic effects. Relaxing the assumption of linear elasticity, analytical solutions are obtained also for a point source in viscoelastic [*Bonafede et al.*, 1986], thermoelastic [*Bonafede*, 1990; *Furuya*, 2005] and anisotropic media.

1.3.3 Numerical models

Numerical model computations are time consuming compared to analytical ones, but this disadvantage is becoming less crucial with recent advances in computer performance. Numerical models can, depending on their functionalities, incorporate several structures of arbitrary shape, topography, and take into account various rheological characteristics.

One of the main applications of numerical modelling methods is to investigate the effects of complex conditions, such as complex source geometries, often to assess the limitations of more simplistic analytical models. Using a finite element method, *Dieterich and Decker* [1975] examined the effects of different geometries of either axisymmetric or plane strain (two dimensional) sources. *Pollard et al.* [1983] made two-dimensional boundary element calculations to obtain useful empirical relationships between the parameters that define dike characteristics and the ground displacements. *Cayol and Cornet* [1998b], *Williams and Wadge* [2000] and *Lungarini et al.* [2005] investigated the effects of topography with an application to Mount Etna. *Masterlark* [2004] systematically examined the possible biases of model estimation that result from the assumptions of homogeneous, isotropic, Poisson-solid, and half-space. *Paul et al.*

[1987] applied a two-dimensional numerical method called “Bloc”, derived from a finite element method, to the landslide of Mount St. Helens in 1980. This method can take into account anisotropy, heterogeneity, linear and nonlinear elasticity, elastoplasticity of the media, as well as fractures.

Another main axis of applications of numerical models is the inversion of data for which the position and/or geometry of the source is relatively constrained a priori. By applying the mixed boundary element method, *Cayol and Cornet* [1998a] and *Beauducel et al.* [2000b] searched for the overpressure and a combination of the overpressure and shear stress on a fixed pressure source that best explain data, and *Cayol et al.* [2000] searched also for the source geometry. *Beauducel and Cornet* [1999] performed an inversion for the source location and volume change, though with limited iterations. *Rubin* [1992] studied the normal faulting induced by dike propagation and resulting graben subsidence in volcanic rift zones, with application on leveling data at Krafla, Iceland, by using a three-dimensional boundary element method. *Cervelli et al.* [2002] used a boundary element method to model a dike of uniform overpressure, after inverting for the best fitting uniform opening source, in pretty much the same way as the “two step inversions” made for estimating an opening distribution described in Section 1.3.2. *Yun et al.* [2005] tested a diapiric geometry for a magmatic source with a boundary element method and compared the result with their sill model determined from inversions of analytic sources.

The present study belongs to the latter axis of applications, but performs a thorough inversion on the dike geometry associated with fissure eruptions at Piton de la Fournaise. This has become possible by the combination of an optimized boundary element calculation procedure and an efficient inversion algorithm. This method was successfully applied to the August 2003 eruption at Piton de la Fournaise [*Froger et al.*, 2004].

1.3.4 Data inversion

Suppose that we have n data points and that a given model explains the data with m parameters. If we define the data vector $\mathbf{d} = (d_1, d_2, ..., d_n)$ and the model vector $\mathbf{m} = (m_1, m_2, ..., m_m)$, we can write that

$$\mathbf{F}(\mathbf{m}) = \mathbf{d}, \tag{1.3}$$

where $\mathbf{F}$ is an operator that relates the model vector to the data vector. To solve such problems, m should be equal to or less than n. When $\mathbf{F}$ consists of linear equations, then Equation 1.3 can be solved by a linear least-square method. If the operator $\mathbf{F}$ cannot be expressed by linear equations, then the problem is called nonlinear, and the word *inversion* normally refers to solving such nonlinear problems.

In inversions, a misfit function, or a cost function, is defined to quantify the discrepancy between observation and model expectation. An inversion algorithm then searches for model(s) that minimizes the misfit function in the model space which can be bounded by predefined model parameter limits.

Since measured data are given as an input, inversions are inherently concerned with uncertainty that stems from measurement uncertainties. In geophysical applications, we normally have, in addition to measurement uncertainties, modelling uncertainties that come from model assumptions. Moreover, ground observations in two dimensions obviously put a limitation for resolving three-dimensional processes. Due to these features, inverse problems generally have non-unique solutions. We must therefore bare in mind that inversions only give possible solutions in the assumed conditions. A model that well explains data is not necessarily realistic, and even worse, a model that looks realistic might not correspond to what is happening in the Earth. To deduce reliable results from inversions, it is important to know the applicability limit of the assumptions, and also to compare obtained results with other data including field observation and expectations from theoretical studies.

To solve an inverse problem, one must choose between derivative (gradient) based or Monte Carlo (direct) algorithms. The former are generally suitable when the problem is expected to have a simple data-model relationship (a concave misfit function) as they require fewer model calculations than Monte Carlo methods. When the relationship becomes complex, the misfit function will increase complexity with multiple local minima of the function. In this case, Monte Carlo methods are favoured because they are (1) more reliable in the optimization/parameter search stage (a derivative based search would normally converge to a local minimum), and (2) usually more reliable in the estimation of uncertainties [*Sambridge and Mosegaard*, 2002].

The neighbourhood algorithm [*Sambridge*, 1999a,b] used in this study is one of the Monte Carlo methods. It consists of two stages: search and appraisal. The search stage aims to preferentially search good data-fitting (low misfit) regions in the model space, rather than find a single optimal model [*Sambridge*, 1999a]. This algorithm has been used in crustal deformation inversions [*Froger et al.*, 2004; *Fukushima et al.*, 2005; *Lohman et al.*, 2002; *Pritchard and Simons*, 2002, 2004a,b]. The appraisal stage can estimate the statistical characteristics of the model parameters, such as uncertainties and trade-offs, without further forward model calculations (which are more time-consuming for numerical modelling methods than anlytical ones) that are required in other appraisal methods [*Sambridge*, 1999b].

1.4 Modelling of Dike Emplacement

1.4.1 Force of Dike Opening

A number of theoretical solutions have been derived on the shape of a stationary fluid-filled crack [e.g. *Pollard*, 1976; *Rubin and Pollard*, 1987; *Secor and Pollard*, 1975; *Weertman*, 1971]. Such solutions can be compared to the shape of an actual dike [e.g. *Delaney and Pollard*, 1981; *Pollard and Muller*, 1976; *Reches and Fink*, 1988] by assuming that the dike was in equilibrium at the end of its emplacement, more specifically, that the dike was emplaced while being molten and solidified while keeping its shape. The present study is also based on this assumption (see also Section 2.1). It should be noted that, for accurate modelling of dike propagation, i.e., its spatio-temporal evolution, one should consider a more complex system including the dynamics of magma flow [e.g. *Fialko and Rubin*, 1998; *Lister and Kerr*, 1991; *Mériaux and Jaupart*, 1995, 1998; *Turcotte et al.*, 1987], fracturing at the dike tip [e.g. *Ingraffea*, 1987; *Khazan and Fialko*, 1995; *Rubin*, 1993b], heat transfer including viscous dissipation (heat generated by viscous flow) [e.g. *Fialko and Rubin*, 1998, 1999; *Rubin*, 1993a], and so on; see also a review of *Rubin* [1995] on propagation of magma-filled cracks and the references therein.

For a dike connected to the magma reservoir to remain open, the overpressure of internal magma, defined by the magma pressure subtracted by the normal stress on the dike surface, should be positive on majority of the dike wall. The overpressure is first created at the magma reservoir, by oversaturation of volatile species in the reservoir [*Tait et al.*, 1989] or by replenishment of the reservoir from a deeper level. During ascent, magma can change its density by vesiculation and degassing [e.g. *Jaupart*, 2000]. The geometry of the dikes arrested in the edifice can be, therefore, determined by several different processes.

When the dike reaches the ground, i.e., when an eruption starts, the situation greatly changes. To explain the behaviour of dikes in such a case, a two-dimensional vertical dike is considered (Figure 1.6). For simplicity, host rock and magma are assumed to have constant densities of ρ_r and ρ_m. Magma is subject to buoyancy [*Rubin*, 1995]

$$\Delta\rho g + d(\Delta S_n)/dz, \tag{1.4}$$

where $\Delta\rho = (\rho_r - \rho_m)$, g is the gravitational acceleration, and ΔS_n is the deviation of the horizontal stress from the vertical lithospheric stress $S_n - \rho_r g z$. The term $d(\Delta S_n)/dz)$ can be several times $\Delta\rho g$ within the brittle crust [*Rubin*, 1995]. For this reason, buoyancy cannot be solely discussed in terms of the density contrast $\Delta\rho$ in this thesis which works on the shallowest several kilometers of the crust.

For positive buoyancy, magma can ascend with any value of reservoir overpressure. The buoyancy provides an overpressure for dike opening such that the overpressure is larger for shallower depth. The shape of the dike reflects such an overpressure profile (Figure 1.6a, b). If, on the other hand, magma is submitted to negative buoyancy, then the magma flow is driven solely by the overpressure at the reservoir. In this case, the dike is submitted to an overpressure such that the greater the depth, the larger the overpressure (Figure 1.6c, d).

Dikes submitted to negative buoyancy should not be able to propagate upward to the ground [*Rubin and Pollard*, 1987]. Observations indicate that Piton de la Fournaise start with lava fountaining, sometimes associated with a whistling noise [*Villeneuve*, 2000], which is consistent with very low density and large buyoyancy of magma. On the other hand, gravity measurement performed after a dike emplacement [*Lénat et al.*, 1989a] suggests that dikes are denser than the surrounding rock. These observations indicate that dikes open because of buoyancy forces associated with a gas rich magma and that this magma is progressively replaced by a denser magma.

1.4.2 Direction of Dikes

Theoretical studies predict that dikes intruding into intact rock should propagate perpendicular to the direction of the minimum principal stress [e.g. *Anderson*, 1938]. Several field studies found, on the other hand, dikes that intruded on faults or other preexisting fractures [e.g. *Delaney and Gartner*, 1997; *Gudmundsson*, 1983]. By calculating the stress at the dike tip, *Ziv et al.* [2000] investigated the ability of magma to propagate along preexisting fractures oblique to the least principal stress. They concluded that dikes can intrude into preexisting fractures if one or more of the following conditions are satisfied: (1) the fracture is nearly perpendicular to the least principal stress, (2) the resolved shear stress on the fracture is small compared to the excess magma pressure, (3) the effective ambient dike-normal stress is small compared to the rock tensile strength. These conditions make dikes difficult to intrude into faults at midcrustal to lower crustal depths [*Ziv et al.*, 2000].

At Piton de la Fournaise, numerous dry fractures are observed on the ground [*Carter*, 2004], with a slight preferential distribution along the rift zones. Anomalies in spontaneous polarization, which reflect fractured zones in which fluids are preferentially channeled, are consistent with this surface fracture distribution [*Michel and Zlotnicki*, 1998]. Considering the in situ compressive strength of rocks and the gravitational stress field, open fractures may exist down to about 1 km beneath the ground [*Rubin*, 1995]. Existence of these open fractures are not expected to modify the direction of dikes since the fractures themselves should have been created

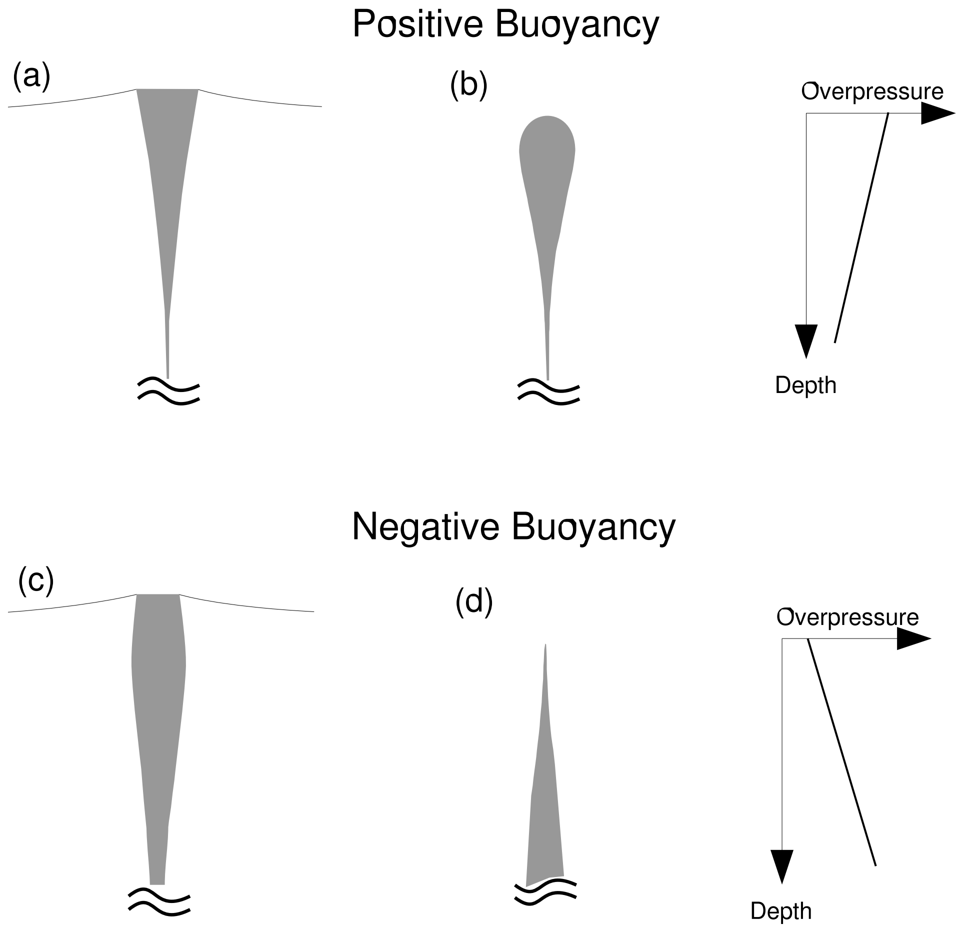

Figure 1.6: Cross-sectional sketches for a two-dimensional vertical dike. Dike thickness is greatly exaggerated. When the buoyancy is positive, the dike opening reflects the positive overpressure gradient toward the ground and vice versa. (a) Buoyancy is positive, dike reaching the ground. (b) Buoyancy is positive, dike far from the ground. (c) Buoyancy is negative, dike reaching the ground. (d) Buoyancy is negative, dike far from the ground.

by the similar stress field as the dikes are subjected to. Therefore, it can reasonably be considered that dikes are emplaced perpendicular to the direction of the minimum principal stress even at these superficial levels.

1.5 Aim of the Study

The first aim of this study is to develop a method to estimate the overpressure and detailed geometry of intrusions from InSAR data. The mixed boundary element method [*Cayol and Cornet*, 1997] is used to model the ground displacements caused by intrusions. This method can take into account arbitrary geometries of intrusions as well as topography, which allows complex and realistic modelling. The neighbourhood algorithm [*Sambridge*, 1999a,b] is chosen as an inversion method, because it efficiently samples the model space with a small number of forward calculations, and also because it offers a model appraisal without any supplementary forward calculations, which is important for a problem using a time-consuming numerical modelling method.

The second, and broader, aim is to get a better image of the magmatic and volcano-tectonic systems of Piton de la Fournaise from analyzing the displacements associated with the five eruptions that occurred between 1998 and 2000. Dike geometries estimated from InSAR data give direct evidence on the path in which magma had propagated, as well as the direction of the minimum principal stress. InSAR data can further detect the presence of any shallow magma reservoir that fed an eruption. Dike intrusions also lead to volcano growth and instability; it is important to consider the cumulative effect of such intrusions for predicting future development of the volcano.

Chapter 2

Method for Realistic Dike Model Estimation - SAR Interferometry, Mixed BEM and Monte Carlo Inversion

This chapter presents a method to find realistic and detailed dike models from InSAR data, using a combination of the mixed BEM and a Monte Carlo inversion algorithm. A dike model, in this thesis, constitue an ensemble of dike position, geometry and overpressure. First of all, assumptions on dike emplacements and mechanical state of the edifice are presented. Next, a paper published by Journal of Geophysical Research [*Fukushima et al.*, 2005] describes the method with application to the February 2000 eruption at Piton de la Fournaise. The paper also discusses the magma storage system and tectonics of the volcano, which will be resummarized in the following chapter. Figures and explanations that complement the description of the paper are added at the end.

2.1 Model Assumptions

This study models the coeruptive ground displacements by assuming pressurized fractures in an elastic medium. This assumption is validated by large aspect ratios of basaltic dikes and by short time scales (order of a few days) associated with their formation [*Lister and Kerr*, 1991; *Rubin*, 1993c]. Viscous effects (ductile flow) of host rock would become important for more viscous magma at greater depth and larger time scale of deformation, in which case magma ascends as a diapir instead of a dike [*Rubin*, 1993c]. Theoretical studies predict that some plastic deformation or microcracking should occur at the dike tip region (called process zone) [*Delaney et al.*, 1986; *Maaloe*, 1987; *Pollard*, 1987]. Indeed, inelastic deformation, associated with the formation of joints, breccias, fluidized clastic rocks, etc., is sometimes observed to extend from tens of centimeters to tens of meters from eroded dikes [*Rubin*, 1995]. This process zone, however, little affects the shape and dynamics of propagating dikes [*Maaloe*, 1987]. During a fissure eruption, the dike, being the magma path, is in a mechanical equilibrium; and it can solidify retaining its shape (Section 1.4). Moreover, no time-dependent displacement is observed after eruptions (dike formations) at Piton de la Fournaise, except for those associated with magma contraction due to cooling, suggesting that time-dependent viscoelastic and poroelastic deformations need not to be considered. With the above reasons, the formation of dikes can be suitably analyzed by elastostatic models.

This study assumes that dikes are only submitted to normal stress (overpressure) and to no shear stress. This is valid if the stress field is isotropic or if dikes intrude perpendicular to the direction of the minimum principal stress. Indeed, field observations show that the majority of dikes crosscut horizontal or nearly horizontal layers of lava flows and sediments without creating any vertical offset of the horizontal layers [*Gudmundsson*, 2002; *Pollard*, 1987; *Rubin*, 1995], validating the assumption.

The submitted overpressure is assumed constant. A vertical overpressure gradient may give a better approximation; however, a preliminary study showed that this overpressure gradient cannot be constrained by inversions, suggesting that such a model does not describe the reality any better than the constant overpressure model. Considering more complex overpressure distribution prevents an inversion from converging in acceptable duration of time.

This study assumes that the edifice is homogeneous. However, obviously, the edifice is heterogeneous. A tomographic study [*Nercessian et al.*, 1996] found a high velocity plug of 1.5 km in diameter below the summit crater, surrounded by a lower velocity ring. This is the most distinct heterogeneity that we expect around the depth we are concerned with. Observations of the InSAR data indicate no correlation with this potential plug and ring structure, suggesting that the heterogeneity has a negligible effect and that the homogeneity assumption can be made. The effects of local heterogeneities of rock properties due to indivisual dike intrusions etc. are averaged out by considering effective elastic moduli.

This study assumes that the edifice is isotropic. Anisotropy, however, can be caused by stratified lava flows on volcanic edifices. *Ryan et al.* [1983] estimated a 1.4 times greater Young's modulus in the horizontal direction than in the vertical direction at Kilauea volcano. Such anisotropy certainly biases the estimated models obtained with the isotropy assumption. Because the respective ratio of vertical versus horizontal displacements are not properly accounted for, this simplification probably affects the depth and dip of dikes, but little affects the parameters that define the lateral length of dikes. The degree of such biases should be examined by a further study. The remaining question, however, concerns what kind of anisotropy model should be considered, because our studied area has many intruded dikes that locally cause anisotropy in different directions.

This study takes realistic topography into account. With improvements in amount and quality of data, the effects of topography on inverting deformation data has caught attention [*Cayol and Cornet*, 1998b; *Lungarini et al.*, 2005; *Masterlark*, 2003, 2004; *McTigue and Segall*, 1988; *Williams and Wadge*, 1998, 2000]. As for Piton de la Fournaise, the average slope of the eastern flank of the central cone exceeds 20 degrees. This causes a significant effect even if the source is located below the edifice [*Cayol and Cornet*, 1998b]; the effect is enhanced in this study where the source (dike) reaches the ground surface. The effects of topography will be shown to be important in Section 2.3.5.

This study assumes that the system is in mechanical equilibrium when dikes are being emplaced, and that dikes solidify while keeping their shapes. Dikes can be practically solidified when lava stops being emitted from the eruptive fissures [*Delaney and Pollard*, 1982]. Indeed, dikes of a thickness of 1 m, which is thicker than typical dikes at Piton de la Fournaise [*Grasso and Bachèlery*, 1995], would solidify in about 2 days assuming typical values for temperatures of magma and rock and thermal diffusivity (Section 4.1.3). After emplacement, solidified dikes contract due to cooling. The amount of contraction is time-dependent, but it can be up to 10–15% [*Yoder*, 1976]. Since interferograms generally record ground displacements several days to several months after dike solidification, such contraction inherently leads to underestimation of overpressure of up to 10–15%.

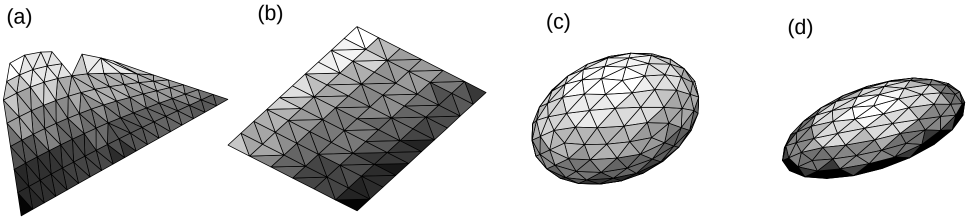

Figure 2.1: Geometries of the four pressure source models used in this study. (a) Quadrangle-like fracture with segmented superficial parts reaching the ground (for dikes), (b) rectangular fracture not reaching the ground (for dikes and sills), (c) oblate ellipsoid (for magma reservoirs), and (d) half oblate ellipsoid (for laccoliths).

In general, fissure eruptions are localized to one or several vents in an order of several hours to a day after the eruption onset. Such localizations do not affect the estimation of dike characteristics, since the magma paths connected to the localized vents are created by brecciation and removal of surrounding wall [e.g. *Delaney and Pollard*, 1981; *Walker*, 1993], a process that only causes local deformation around the vents.

2.2 Geometry of Pressure Sources

The present study assumes four models for the pressure source to explain the ground displacements. This section gives detailed descriptions for how the geometrical parameters of these models are defined. Explained models are (Figure 2.1): (a) quadrangle-like fracture with segmented superficial parts reaching the ground (for dikes), (b) rectangle not reaching the ground (for dikes and sills), (c) oblate ellipsoid (for magma reservoirs), and (d) half oblate ellipsoid (for laccoliths).

2.2.1 Quadrangle-like fracture with superficial segments

This model is applied to the dike intrusions that reach the ground, i.e., that are associated with an eruption from segmented eruptive fissures. The top of the dike can be fixed at the location of the eruptive fissures, which is known from field observation. It is assumed that the direction of en echelon eruptive fissures are due to rotation of the maximum principal stress close to the ground and that these fissures are linked to a single dike at depth. Under this assumption, a dike is modelled with two parts: a segmented superficial part and a deeper main part.

The geometry of the bottom side of the main part is defined by six parameters (Figure 2.2). These parameters are chosen to be able to restrict the geometry to physically plausible models. Three parameters determine the position of the bottom middle point: (1) angle of the maximum gradient measured from horizontal (Dip), (2) angle between the line connecting the middle points of the top and bottom sides and the vector of the maximum gradient (Shear), and (3) elevation of the bottom middle point (Botelv). The other three parameters determine the position of the two end points of the bottom side relative to the bottom middle point: (4) length of the bottom side scaled by that of the top side (Botlen), (5) horizontal angle between the top and bottom sides (Twist), and (6) vertical angle of the bottom side (Botang). The top side of the main dike that connects to the segments is a curve parallel to the topography; for this reason, the

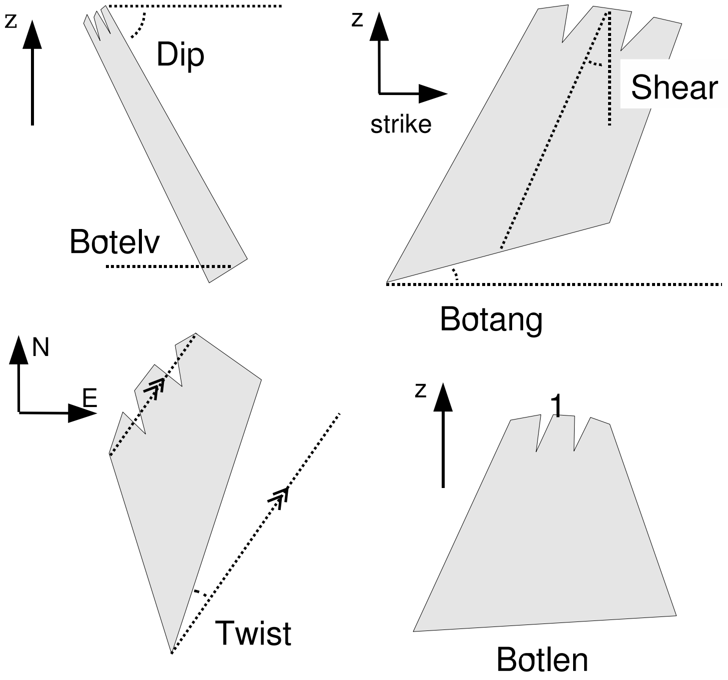

Figure 2.2: Six parameters used to determine the bottom side geometry of the mesh of type (A). These parameters were chosen to be able to restrict the geometry to physically plausible models. See text for explanations of the parameters. This figure is the same as Figure 4 in JGR paper.

main part is not exactly a quadrangle. Because the top of the dike is segmented, and because the segments' strike are generally not the same as that of the main part, a virtual top side is defined (Figure 2.3). This virtual top side is used as the reference axis for determining the bottom side geometry.

In the JGR paper presented later in this chapter, the geometry of the superficial segmented part was fixed for the February 2000 eruption because it was less sensitive than that of the main part. It is not always the case, however, and some additional parameters are introduced to allow different geometries of the superficial part. The along-dip length of the segmented part is defined by D_top (Figure 2.4). The relative lengths of the bottom side of the segments can also be specified. For a March 1998 dike model (Model A in Section 3.3.3), two segments are considered with the ratio of the lengths of the two segments as a model parameter (Segratio; Figure 2.4).

We can further introduce parabolic curvatures of dikes: Botcurv and Vertcurv, corresponding to curvatures along the strike and along the dip, respectively. The curvature along the strike Botcurv is called for shallow dikes, whose bottom sides have large influence on the dike geometry. This curvature is defined by the angle between the line connecting the bottom endpoints and the tangential line at the endpoints. The curvature along the strike is introduced in models of the July 1999 dike (Section 3.4.3) and the September 1999 dike (Section 3.5.3). The curvature along the dip Vertcurv is also possible and is introduced when data are not well explained. This curvature is defined by the angle between the line connecting the top and bottom points and the tangential line at the top and bottom points. The vertical curvature is introduced in a June 2000 dike model (Section 3.7.3).

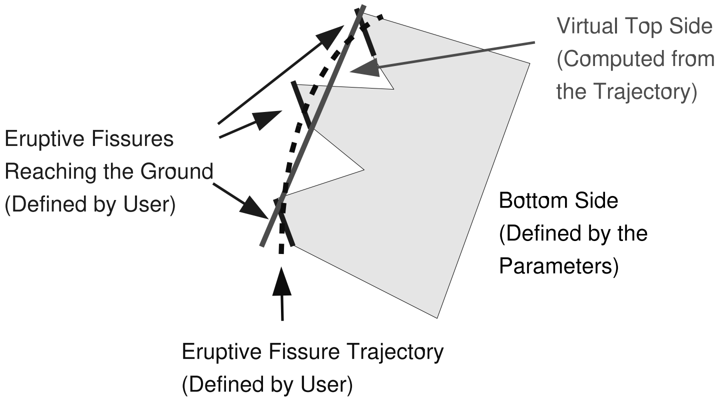

Figure 2.3: Virtual top side, which is used as a reference to determine the geometry of the bottom side, is defined from the eruptive fissure trajectory in such a way that it parallels the line connecting the endpoints of the trajectory and its midpoint coincides the mean of the trajectory.

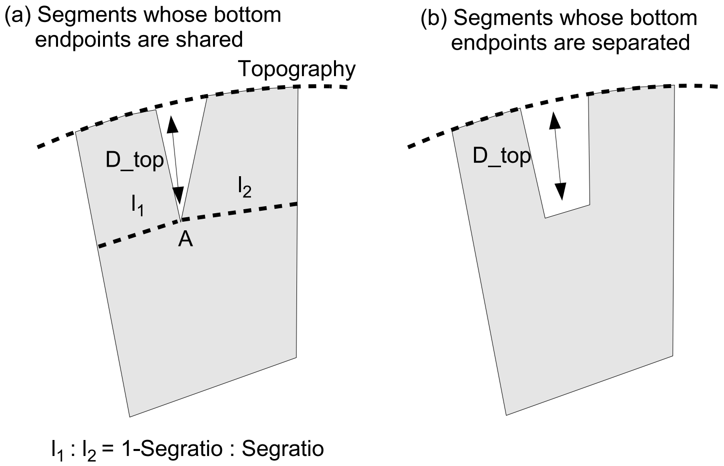

Figure 2.4: Schematic figure explaining the parameterization of the segmented part. D_top is the along-dip length of the segmented parts. (a) Two segments share an endpoint. Segratio defines the ratio of the bottom lengths of two segments. D_top and Segratio define the position of the joint point A on the curved dike surface. (b) Two segments can also be apart from each other.

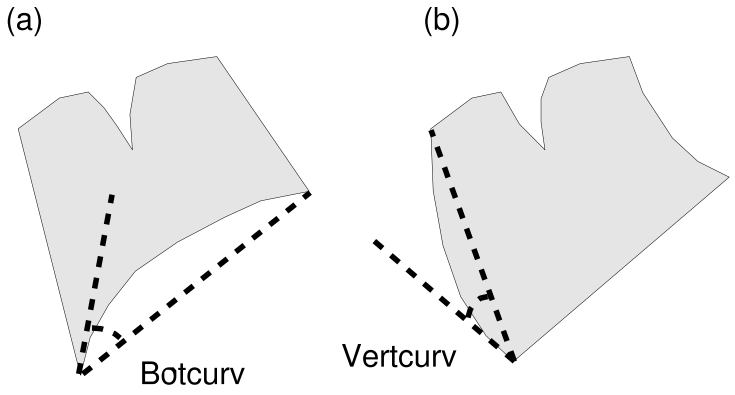

Figure 2.5: (a) Curvature along the strike, defined by the angle between the line connecting the bottom endpoints and the tangential line at the endpoints. (b) Curvature along the dip, defined by the angle between the line connecting the top and bottom points and the tangential line at the top and bottom points.

2.2.2 Rectangle not reaching the ground

A rectangle is assumed for a dike or sill not reaching the ground. Figure 2.6 explains the eight parameters that define the geometry: the position of the midpoint of the top line (X,Y,Z), horizontal length (Length), strike angle (Strike; clockwise from north), vertical angle (Vertang; from horizontal) of the top and bottom sides, dip angle (Dip; the direction of the maximum gradient measured from horizontal), distance between top and bottom sides (Height). This model is used in the March 1998 analysis (Model C, Figure 3.19).

2.2.3 Oblate ellipsoid

A magma reservoir can be modelled by an oblate ellipsoid. The geometry is defined by nine parameters (Figure 2.7). (X,Y,Z) define the position of the center, (S_1,S_2,S_3) define the lengths of the three axes ($S_1 > S_2 > S_3$), Az and Vertang define the horizontal (clockwise from north) and vertical (from horizontal) angles of the longest axis, and Rotang defines the rotation angle around the longest axis. This model is used in the March 1998 analysis (Model C, Figure 3.20).

2.2.4 Half oblate ellipsoid

Laccoliths have a domed shape with their bottom surface concordant to the country rock bedding, as is the case for sills. A half oblate ellipsoid is used to model a laccolithic intrusion associated with the September 1999 eruption (Figure 3.30). The geometrical parameters are: position of the center of the bottom ellipsoid (X,Y,Z), lengths of the long and short axes of the ellipsoid (S_1, S_2), and height (Height). The directional parameters introduced in the oblate ellipsoid model are not used for this model because they are well constrained from data (Section 3.5.3).

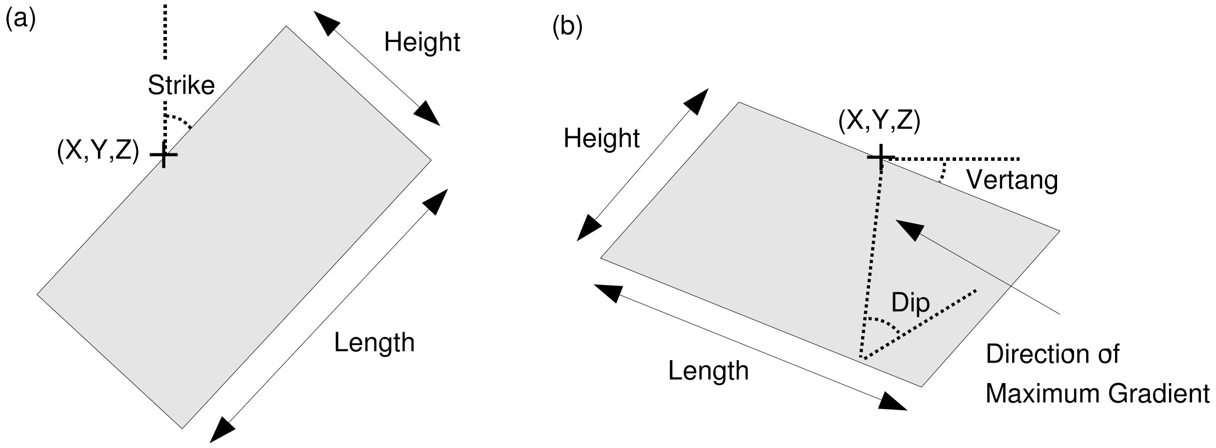

Figure 2.6: Parameters defining the geometry of the rectangle pressure source. See text for explanations. (a) Plane view. (b) Lateral view.

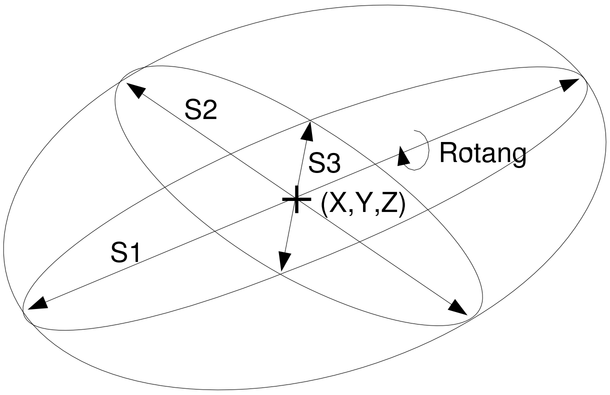

Figure 2.7: Parameters defining the geometry of the oblate ellipsoidal source. See text for explanations.

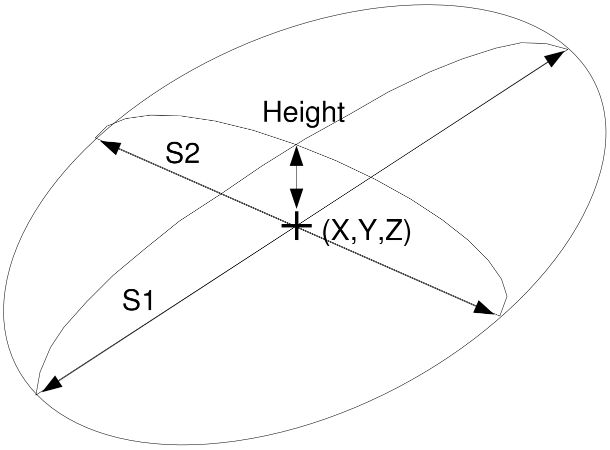

Figure 2.8: Parameters defining the geometry of the half oblate ellipsoidal source. See text for explanations.

2.3 JGR Paper

2.3.1 Introduction

2.3.2 Method

2.3.3 Synthetic Tests

2.3.4 Application to the February 2000 eruption at Piton de la Fournaise

2.3.5 Discussion

2.3.6 Conclusions

JOURNAL OF GEOPHYSICAL RESEARCH, VOL. 110, B03206, doi:10.1029/2004JB003268, 2005

Finding realistic dike models from interferometric synthetic aperture radar data: The February 2000 eruption at Piton de la Fournaise

Y. Fukushima and V. Cayol
Laboratoire Magmas et Volcans, Université Blaise Pascal, CNRS UMR 6524, Clermont-Ferrand, France

P. Durand
Centre National d'Etudes Spatiales, Toulouse, France

Received 28 June 2004; revised 2 December 2004; accepted 3 January 2005; published 23 March 2005.

[1] Dike intrusions often cause complex ground displacements that are not sufficiently explained by simple analytical models. We develop a method to find complex and realistic dike geometries and overpressures from interferometric synthetic aperture radar (InSAR) data. This method is based on a combination of a boundary element method with realistic topography and a neighborhood algorithm inversion. Dike model geometry is roughly a quadrangle with its top reaching the ground. The inversion has two stages: search and appraisal. The appraisal stage involves calculations of model marginal probability density functions using misfit values calculated during the search stage. The misfit function takes into account the variance and correlation of data noise. Synthetic tests show that a model is successfully retrieved within predicted narrow confidence intervals. We apply the method on InSAR data of the February 2000 flank eruption at Piton de la Fournaise and get a trapezoid dike dipping seaward (61.0°–67.3°) with its bottom passing 800–1000 m beneath the summit. A model with a basal slip plane does not better explain observed asymmetric displacements, and thus this asymmetry is solely attributed to the dipping dike. The dike lies above a narrow band of preeruption seismicity, suggesting that lateral magma propagation occurred. Neglecting topography results in poor modeling at depth and in overestimations of overpressure (or opening), height (both about 30%), and volume (about 20%).

Citation: Fukushima, Y., V. Cayol, and P. Durand (2005), Finding realistic dike models from interferometric synthetic aperture radar data: The February 2000 eruption at Piton de la Fournaise, *J. Geophys. Res.*, *110*, B03206, doi:10.1029/2004JB003268.

1. Introduction

[2] In the domain of ground deformation modeling, analytical solutions have frequently been used [e.g., *Mogi*, 1958; *Okada*, 1985]. There are mainly three reasons for this: (1) the calculations are simple and rapid, (2) observations were in some cases sufficiently explained by the models, and (3) the quality and quantity of deformation data were not enough to consider more complex models. The second and third reasons are linked; indeed, we can only evaluate models within the resolution and precision of data. Interferometric synthetic aperture radar (InSAR) data measure high-resolution and large-scale ground displacements [*Massonnet and Feigl*, 1998]. InSAR data often indicate complex displacements that cannot be sufficiently explained by simple analytical models.

[3] On the other hand, numerical modeling methods offer more complex and realistic analyses. For example, a three-dimensional mixed boundary element method (BEM) for linear elastic media [*Cayol and Cornet*, 1997, 1998] can incorporate realistic topography and any number of pressure sources and/or shear faults of arbitrary shape. The main disadvantage of numerical modeling in inversion problems is long calculation time. Previous studies only applied inversions with limited iterations [*Beauducel and Cornet*, 1999] or restricted its use to overpressure or slip estimation on a fixed source geometry [*Cervelli et al.*, 2002; *Masterlark*, 2003]. However, advances in computer performance and modeling techniques are making detailed inversions practicable.

[4] The method presented here aims to extract more complex and realistic dike models from InSAR data than simple rectangular dikes assumed by most previous studies. The mixed BEM is used to compute the ground displacements. The neighborhood algorithm [*Sambridge*, 1999a], one of the Monte Carlo inversion methods, is used to search for good data-fitting dike models. Each forward modeling involves a remeshing of the dike and a boundary element computation. Once the search converges, the models evaluated during the search process are used to estimate the model confidence intervals and trade-offs [*Sambridge*, 1999b]. This model appraisal is done by constructing the posterior probability density function (PPD), which is, by

0148-0227/05/2004JB003268$09.00

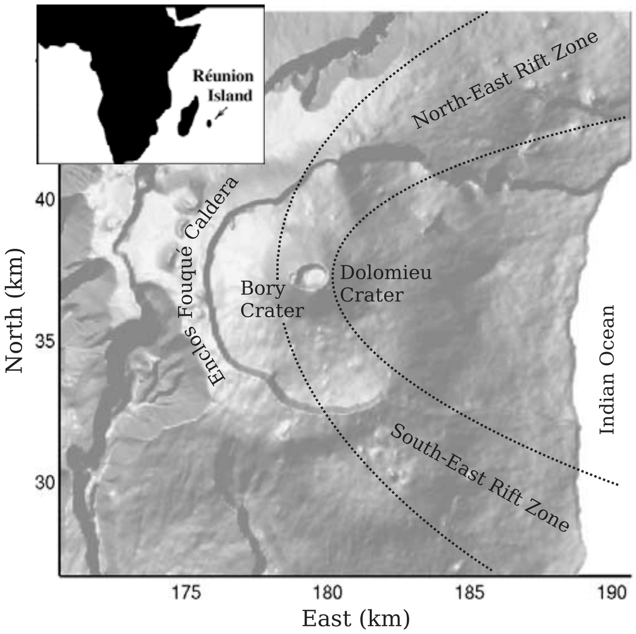

Figure 1. Geographical setting of Piton de la Fournaise. The volcano has two summit craters, Bory and Dolomieu, and a horseshoe-shaped depression called Enclos Fouqué caldera. The coordinates are given in Gauss-Laborde kilometric coordinates.

definition, the solution to an inverse problem from the Bayesian viewpoint. The appraisal stage involves no forward modeling, contrary to the procedures normally taken in Monte Carlo inversions [e.g., *Cervelli et al.*, 2001; *Wright et al.*, 2003].

[5] The developed method is tested with synthetic data, in order to find appropriate inversion settings and to check the method capabilities. It is then applied to the dike intrusion associated with the February 2000 eruption at Piton de la Fournaise volcano (Figure 1). The displacements caused by this dike intrusion were captured by the Canadian RADARSAT-1 satellite from two ascending and two descending orbits. This rich data set is suitable for testing and evaluating the developed method.

2. Method

2.1. Modeling: Mixed BEM

[6] The mixed BEM is based on a combination of two boundary element methods: the direct method and displacement discontinuity method. The direct method allows accurate and fast modeling of structures such as topography, cavities or reservoirs, whereas the displacement discontinuity method is suitable for fractures. The edifice is assumed to be linearly elastic, homogeneous and isotropic. The prescribed boundary conditions are tractions; they represent perturbations of an initial state of stress, and are null on the ground and equal to overpressure on deformation sources. Precision of the mixed BEM has been carefully tested [*Cayol and Cornet*, 1997] and the method has been applied to several studies [e.g., *Beauducel and Cornet*, 1999; *Cayol et al.*, 2000; *Dieterich et al.*, 2000].

2.1.1. Boundary Meshing

[7] Structures (in our case, the ground surface and a dike) are meshed by planar triangle elements. The ground mesh used in this study (Figure 2) is made from a digital elevation model (DEM). The mesh size is chosen in such a way that the edge effect can be neglected; we use a mesh covering a circular area of 6 km in radius. This area is about 5 times as large as the presumed deformation source dimension. The mesh is denser close to the eruptive fissures (bold lines in Figure 2) where displacement gradients are large, and coarser farther away. The caldera boundary is not explicitly considered because the data show no displacement continuity across the caldera wall. A dike mesh is generated automatically before each forward boundary element computation. Its geometry is determined by six model parameters that will be defined later.

[8] Model computation time is proportional to the square of the number of calculation points when disk swap is not required. We seek mesh densities that minimize computation time without significant loss of precision. Precision is evaluated by the following two error functions. The first one is

$$\mathrm{Err}(\%) = \frac{\sum |u_{\mathrm{ref}} - u|}{\sum |u_{\mathrm{ref}}|} \times 100, \tag{1}$$

which compares displacements on a coarse mesh u with the reference displacements on a fine mesh u_{ref}. The second one is

$$\mathrm{Err}_{\mathrm{rel}}(\%) = \frac{\sum |u_{\mathrm{ref}} - ku|}{\sum |u_{\mathrm{ref}}|} \times 100, \tag{2}$$

where a constant k is determined analytically to minimize the function. This second function evaluates the differences only in displacement patterns. As ground mesh nodes are

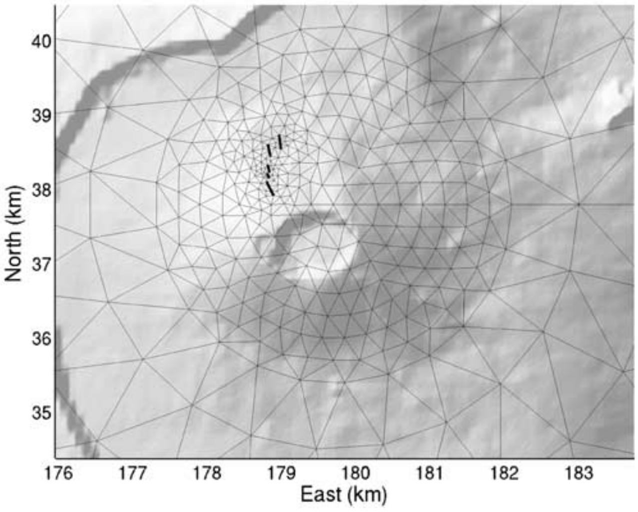

Figure 2. Part of the ground mesh used in this study superposed on a shaded relief map. The mesh includes eruptive fissure lines (bold line) which are shared by the dike mesh.

Table 1. Calculation Time and Precision for Different Mesh Intervals

Average Interval, m	Calculation Time, s	Err, %	$\mathrm{Err}_{\mathrm{rel}}$, %	k
30[a]	332			
90	30	9.8	0.98	0.91
150	20	15.3	1.80	0.87
300	15	29.1	3.60	0.78

[a] Reference mesh.

heterogeneously distributed, computed displacements are interpolated within a 100 m spacing uniform grid covering significantly displaced area to evaluate the errors.

[9] For a ground mesh with 376 elements, we obtain a negligible displacement error with Err 2.4%, where the reference displacements are computed using a very dense mesh (1286 elements). For dikes, we test three mesh densities with average node intervals of 90, 150, and 300 m, where the reference mesh assumes 30 m. Table 1 shows that relative displacement errors $\mathrm{Err}_{\mathrm{rel}}$ are 1 order less than displacement errors Err. It suggests that displacements with acceptable precision can be obtained by multiplying the displacements computed using a coarse dike mesh by the scaling factor k. We observe that k is smaller than unity for all the cases, which indicates that displacements are overestimated. This seems to be a general effect of discretization in the displacement discontinuity method [*Crouch and Starfield*, 1983]. In the framework of linear elasticity, displacements are proportional to the imposed overpressure. Thus, using a coarse mesh only results in overpressure underestimation by a factor of k. By taking into account the calculation time and $\mathrm{Err}_{\mathrm{rel}}$, we consider that dike mesh density with 150 m of node interval is most appropriate to our problem. Overpressure values are rescaled once a search run is finished (section 4.3.1).

2.1.2. Model Parameters

[10] We assume that the directions of the en echelon eruptive fissures are due to rotation of the maximum principal stress close to the ground and that these fissures are linked to a single dike at depth. Under this assumption, we model a dike with two parts: a superficial part and a deeper part (Figure 3).

[11] The superficial part is made of several segments; their top is connected to the ground at the locations of the eruptive fissures, and their bottom is connected to the deeper part. The deeper part is roughly a quadrangle. Its top is a smooth curve that runs 100 m below the surface fissures. We verified that varying this depth in the range 0–200 m has a negligible influence on our problem. The bottom of the quadrangle is a straight line whose position and geometry are determined by six parameters (Figure 4). These parameters are chosen in order to be able to restrict the search to mechanically plausible dike geometries. Three parameters, i.e., dip angle (Dip), angle between the line that connects the middle points of the top and bottom sides and the direction of the maximum gradient (Shear) and elevation of the bottom middle point (Botelv), determine the position of the bottom middle point. The other three parameters, i.e., length of the bottom side scaled by that of the top side (Botlen), horizontal angle between the top and bottom sides (Twist) and vertical angle of the bottom side (Botang), determine the position of the two end points of the bottom side. We use constant overpressure (P_0) as another model parameter, which makes a total of seven model parameters.

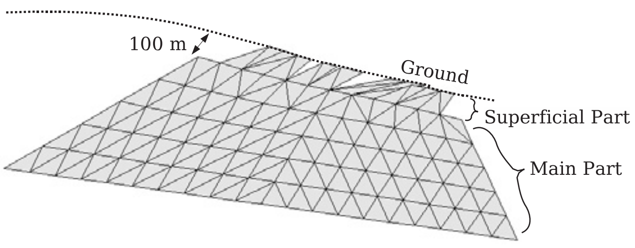

Figure 3. Example of a dike mesh. It consists of a superficial part and a deeper part. Each segment of the superficial part reaches an eruptive fissure on the ground surface and is connected to the deeper part. The deeper part is roughly a quadrangle whose geometry can change while its top side is fixed to the superficial part at 100 m from the ground.

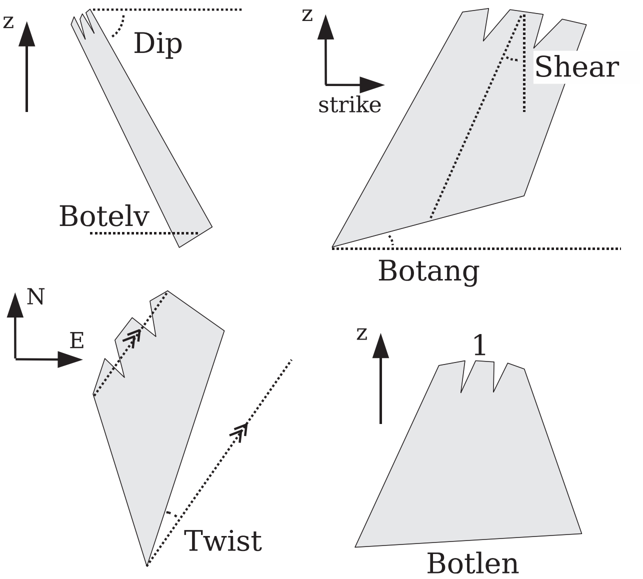

Figure 4. Six parameters used to determine the dike model geometry. These parameters were chosen to be able to restrict the geometry to physically plausible models. See text for explanations of the parameters.

2.1.3. Elastic Moduli

[12] Deformations in linearly elastic, homogeneous and isotropic media are controlled by two elastic moduli. We use Young's modulus E and Poisson's ratio ν. Displacement amplitudes are proportional to Young's modulus. We use $E = 5$ GPa, which was estimated by *Cayol and Cornet* [1998] for Piton de la Fournaise from in situ density [*Rançon et al.*, 1989] and seismic velocities [*Nercessian et al.*, 1996] with correction to a static value. As for Poisson's ratio, we evaluate its effect using the error function (equation (1)) in the range 0.1–0.4. The maximum error found is Err = 4.0%, with $\nu = 0.25$ assumed as the reference. This error is much smaller than what we obtain by changing the model parameter values in a realistic range, suggesting that fixing this modulus will

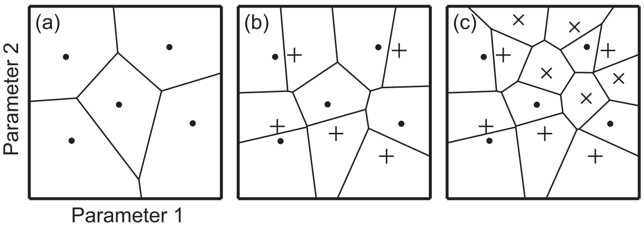

Figure 5. Example showing the search process, in the case $n = 5$ in two model dimensions. (a) Initial. Five initial models (dots) are randomly generated, and Voronoi cells are defined. (b) First iteration. Five new models (pluses) are generated in the Voronoi cells around the five best models (in this case, in every initial cell), and new Voronoi cells are defined. (c) Second iteration. Five new models (crosses) are generated around the five best models, and new Voronoi cells are defined. Note that the newly generated points modify the shapes of the surrounding cells.

little affect the estimation of the model parameters. We use $\nu = 0.25$ for our calculations.

2.2. Model Space Search

[13] In order to find the models that well explain observed data, a misfit function is defined to quantify the discrepancy between observed and modeled data. An inversion algorithm then searches for a model that minimizes the misfit within the predefined model parameter bounds.

2.2.1. Neighborhood Algorithm

[14] The neighborhood search algorithm [*Sambridge*, 1999a] aims to preferentially search good data-fitting (low misfit) regions in the model space, rather than find a single optimal model. It has already been used in some studies on ground deformation modeling. *Lohman et al.* [2002] applied this algorithm to estimate the location and slip of an earthquake fault from InSAR data and seismic waveforms. *Pritchard and Simons* [2002] used it to estimate the locations and volume changes of volcanic pressure sources from InSAR data.

[15] The algorithm we use works as follows (Figure 5). First, n initial models are randomly chosen. This is equivalent to generating n random points in the model space. Misfits at the n points are then calculated. Next, at each iteration, n points are newly generated in the neighborhood of the n lowest misfit points (one point in each), and misfits for the new points are calculated. Iterations continue until the misfit is not significantly lowered any more. The neighborhood around a point is defined by a Voronoi cell, which covers the region closer to that point than any other point (see Figure 5). Small n leads to a concentrated search in a limited model region and quick convergence, while large n leads to extensive search and slow convergence. The original method allows more complex algorithms (see *Sambridge* [1999a] for details).

[16] We use a misfit function expressed as

$$\chi^2(\mathbf{m}) = (\mathbf{u}_o - \mathbf{u}_m)^T C_d^{-1} (\mathbf{u}_o - \mathbf{u}_m), \tag{3}$$

where $\mathbf{u}_o$ and $\mathbf{u}_m$ represent observed and modeled displacements, respectively. The data covariance matrix C_d accounts for the uncertainties of observed displacements and their correlations. It is determined from InSAR noise analysis as explained later in this section.

[17] For convenience, we define a maximum misfit $\chi^2_{\max}$,

$$\chi^2_{\max} = \mathbf{u}_o^T C_d^{-1} \mathbf{u}_o. \tag{4}$$

A misfit is replaced by $\chi^2_{\max}$ in the following two cases: (1) it is greater than $\chi^2_{\max}$, (2) the dike intersects the ground. The search stops when the standard deviation of the n misfit values in one iteration becomes less than 0.3% of $\chi^2_{\max}$. This threshold was empirically determined and hence it is not applicable to other problems.

2.2.2. Data Covariance Matrix

[18] SAR interferograms have correlated noise caused by atmospheric disturbances. Correlated random noise is expressed by the autocorrelation function or covariance function [e.g., *Tarantola*, 1987]. Specifically, the exponential autocorrelation function is expressed as

$$C(r) = \sigma_d^2 \exp(-r/a), \tag{5}$$

where r is the spatial lag, σ_d^2 is the variance of the noise, and a is the correlation length. This equation indicates that noise of two data points between which the distance is over the correlation distance a is practically uncorrelated.

[19] We calculate the autocorrelation function of InSAR data noise by assuming its randomness. We follow the procedure described by *Fukushima et al.* [2003], who calculated the autocorrelations of velocity fluctuations in rocks samples. The autocorrelation function may depend on the size of the calculation area. We are not interested in the correlations of wavelengths longer than the maximum distance between points, thus the autocorrelation is calculated for spatial lags smaller than the size of the area used in the inversions. Figure 6a shows the autocorrelation

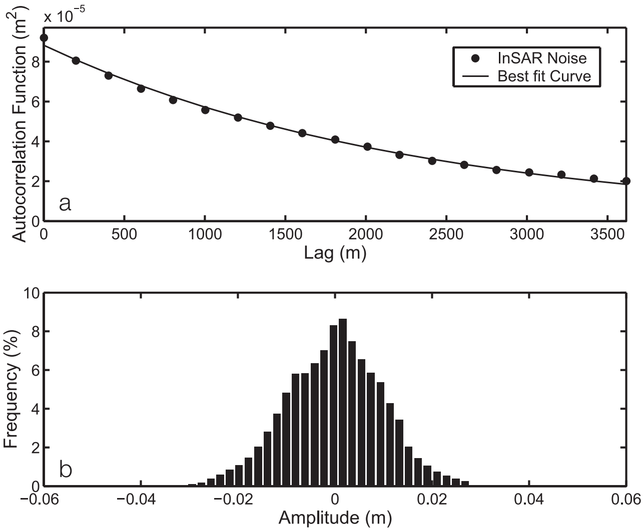

Figure 6. (a) Autocorrelation function estimated from the noise part of the four InSAR data sets (dots) and the best fit exponential curve (solid curve). The good fit indicates that the exponential autocorrelation function well represents the noise characteristics. (b) Histogram of the noise amplitudes. It is consistent with a Gaussian distribution.

function averaged over our four InSAR data sets plotted against spatial lag. The calculation was made in a roughly circular area of 7 km in diameter, with the area affected by the eruption masked. The InSAR noise is well approximated by the exponential-type random noise. The estimated variance σ_d^2 and correlation length a from the fitting are 8.8×10^{-5} m^2 and 2308 m, respectively. Figure 6b shows the histogram of the noise amplitudes. It is consistent with a Gaussian distribution, which validates the Gaussian probability density function of equation (6).

[20] Once the noise variance σ_d^2 and correlation distance a are estimated, the data covariance matrix C_d is determined from these values. The diagonal terms of the matrix correspond to σ_d^2 (single value for all the data points), and off-diagonal terms are calculated by considering the distance between points using equation (5) with the estimated values of σ_d^2 and a.

2.3. Model Appraisal

[21] The second stage of the neighborhood algorithm concerns the appraisal problem [*Sambridge*, 1999b], i.e., estimation of the model uncertainties. The method follows the framework of Bayesian inference (see *Tarantola* [1987] for a summary). It allows to calculate useful properties such as the mean model, posterior model covariance matrix, resolution matrix, or marginal posterior probability density functions.

[22] The Bayesian solution to an inverse problem is the posterior probability density function (PPD). When the Gaussian approximation is acceptable, the PPD can be written as

$$P(\mathbf{m}) = k \exp\left(-\frac{1}{2}\chi^2(\mathbf{m})\right), \tag{6}$$

where k is a normalizing constant and we assumed a uniform prior probability distribution. One of the key points of the method is that the PPD in a Voronoi cell around a point is represented by the PPD of that point. Namely, we accept a neighborhood approximation to the PPD as

$$P_{\mathrm{NA}}(\mathbf{m}) = P(\mathbf{p}_i), \tag{7}$$

where $\mathbf{p}_i$ is the closest point in those generated during the search stage to point $\mathbf{m}$ [*Sambridge*, 1999b]. Note that $P_{\mathrm{NA}}(\mathbf{m})$ is defined all over the model space. Bayesian integrals are then calculated from the approximated PPD by using a Monte Carlo integration technique. The technique used in the neighborhood algorithm numerically integrates functions by generating random points (Monte Carlo integration points) in the model space such that their distribution follows the approximated PPD [*Sambridge*, 1999b]. In our problem, 10,000 points are generated for Monte Carlo integrations with acceptable precision. At this stage, no further forward modeling is made.

[23] We calculate the mean model and marginal PPDs. The mean model of the ith parameter m_i is given by

$$\langle m_i \rangle = \int_{\mathcal{M}} m_i P_{\mathrm{NA}}(\mathbf{m}) d\mathbf{m}, \tag{8}$$

where the integral is taken in the model space $\mathcal{M}$. The marginal PPDs are, intuitively, projections of the posterior probability density to a model axis (one-dimensional) or to a model plane (two-dimensional). They are useful even when multiple maxima exist in the PPD. The one-dimensional marginal PPD of ith parameter is calculated by

$$M(m_i) = \int_{\mathcal{M}} P_{\mathrm{NA}}(\mathbf{m}) \prod_{\substack{k=1 \\ k \neq i}}^{d} dm_k, \tag{9}$$

and for the two-dimensional marginal PPD of ith and jth parameters,

$$M(m_i, m_j) = \int_{\mathcal{M}} P_{\mathrm{NA}}(\mathbf{m}) \prod_{\substack{k=1 \\ k \neq i,j}}^{d} dm_k. \tag{10}$$

The one-dimensional marginal PPDs provide the confidence intervals of the model parameters, while the two-dimensional counterparts provide additional information on trade-offs.

3. Synthetic Tests

[24] We perform some synthetic tests in order (1) to find a suitable value of the inversion parameter n and a suitable subsampling method and (2) to check the capabilities of the method. We test with four synthetic InSAR data sets that correspond to the two ascending and two descending data sets we have for the February 2000 eruption at Piton de la Fournaise. They are created by superposing exponential-type random noise to the line-of-sight displacements caused by a plausible model (which we call the "test model") for the eruption (Figure 7). Noise in each synthetic data is assumed to have the same variance and correlation length as those for the real data estimated in section 2.

3.1. Subsampling Method

[25] To make the misfit calculations manageable, we reduce the number of InSAR data points by subsampling. Here, we test how the subsampling method affects the inversion result. The first subsampling method interpolates the points on a regular 250 m side grid (Figure 8a). The second one distributes points circularly; points are concentrated in the vicinity of the eruptive fissures and become sparse in farther area (Figure 8b). The third one distributes points according to a quadtree algorithm [e.g., *Jónsson et al.*, 2002]; in our implementation, the points are created in such a way that the density roughly corresponds to the data amplitude (Figure 8c). The last one is such that the points correspond to the ground mesh nodes used to compute model displacements (Figure 8d). Except for the last one, model prediction is linearly interpolated to obtain the displacements on the subsampled points. For all the subsampled point sets, points on the recent lava flows are removed as we do not want to model them, making a total of 457, 369, 320, and 200 points for the regular, circular, quadtree and ground mesh node subsampling methods, respectively.

[26] The four synthetic InSAR data sets are subsampled and simultaneously inverted. It means that the length of the

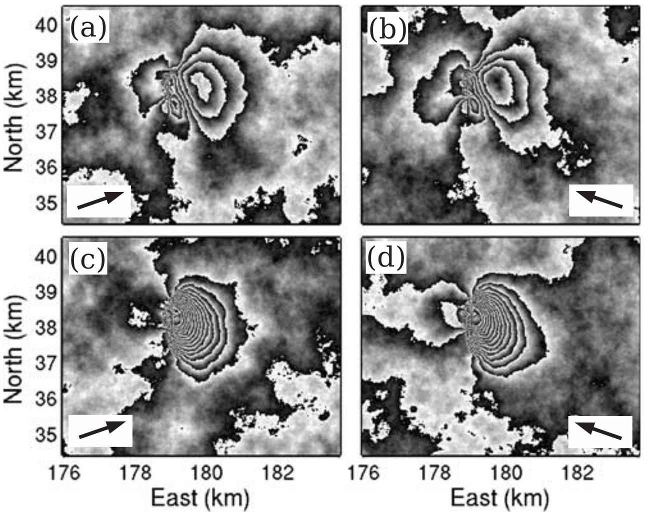

Figure 7. Synthetic data sets created by superposing exponential-type noise to modeled line-of-sight displacements caused by our test model. One shading cycle of black-gray-white corresponds to a displacement of 2.83 cm toward the satellite. Same line-of-sight directions as the actual InSAR data were assumed. Four data sets correspond to (a) F2N and (b) F4F (ascending) and (c) F3N and (d) F5F (descending) orbits. Arrows indicate the surface projection of the line-of-sight directions. See Table 3 for the line-of-sight vectors. See color version of this figure at back of this issue.

data and model vectors ($\mathbf{u}_o$ and $\mathbf{u}_m$ in equation (3)) is 4 times the number of subsampled data points. The inversion parameter n is set to 50; that is, 50 models are generated and evaluated in each iteration.

[27] Figure 9 shows the 95% confidence intervals determined from the one-dimensional marginal PPDs. The intervals estimated using the four subsampled data sets all include the test model as expected, indicating that all the subsampling methods are appropriate to our problem. We do not discuss here the differences in the length of the confidence intervals, because such small differences might come from the random nature of the Monte Carlo search method. However, for the overpressure (P_0), there is a systematic offset of the center of the confidence intervals from the test model; this is probably an effect of added noise. The maximum PPD (best fit) model is also plotted in Figure 9. It appears that the maximum PPD model does not necessarily coincide with the test model, mainly because of insufficient search within the maximum PPD region. This shows that determination of acceptable model ranges is more meaningful than obtaining a single optimum model.

3.2. Inversion Parameter

[28] As mentioned, the inversion parameter n controls the search behavior. We compare the results obtained using n = 10, 30, 50 and 70, in order to find a suitable value for our problem. The circular subsampled data set was used. Figure 9 shows that the test model is equally well retrieved by the maximum PPD model for the four cases. However, Figure 9 also shows that the confidence intervals of some parameters for n = 10 fail to include the test model. This is because the search was not extensive enough to find the global minimum. The results for n = 30, 50 and 70 do not show any significant difference.

[29] We decide to use n = 50 because (1) the risk of being caught in local minima is less than using smaller values, (2) large n leads to a better approximation of the PPD for the appraisal, and (3) the calculation time is manageable. Figure 10 shows how a search converges when n = 50 is taken. After about 20 iterations (1000 forward modelings), the search starts to focus toward the test model. The speed of convergence is different for each model parameter. The search characteristics for real applications are similar to this test result. One search run with n = 50 converges in about 20 hours on a Linux computer with a dual processor of 500 MHz. The appraisal normally takes several days on the same computer, but it can be shortened by running the program on several computers in parallel.

3.3. Marginal Probability Distributions

[30] In order to show the capability of the method, the marginal PPDs estimated using n = 50 and the circular data points are shown in Figure 11, together with the test, maximum PPD and mean models. The one-dimensional PPDs are quasi-symmetric and have a single peak. The similarity between the maximum PPD and mean models suggests symmetric and single-peaked distribution of the PPD also in the full seven-dimensional model space. The two-dimensional PPDs show insignificant trade-offs. The same type of confidence regions were obtained by *Cervelli et al.* [2002] using a bootstrap method for a dike intrusion problem at Kilauea volcano. Therefore quasi-symmetric and single-peaked characteristics of probability

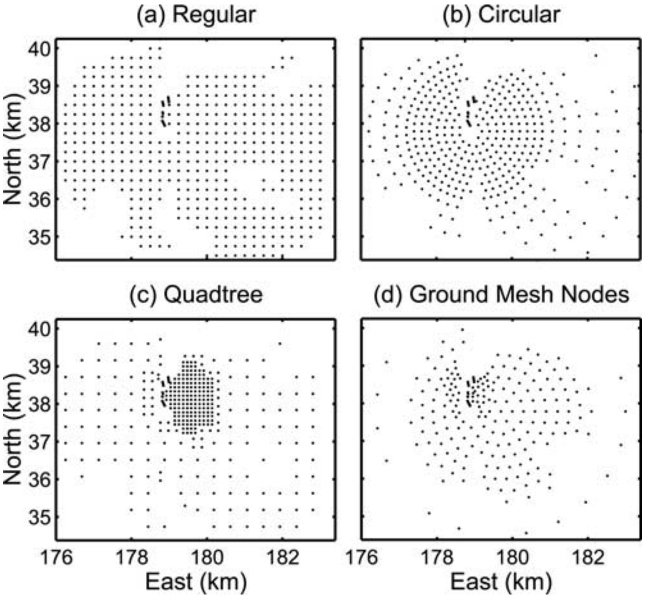

Figure 8. Points subsampled with different methods. (a) Regularly gridded points. (b) Circular points. (c) Points made with a quadtree algorithm. (d) Points coinciding with the ground mesh nodes (Figure 2). Locations of the eruptive fissures are indicated by solid lines. Areas without points correspond to recent lava flows where we do not have displacements associated with the dike intrusion.

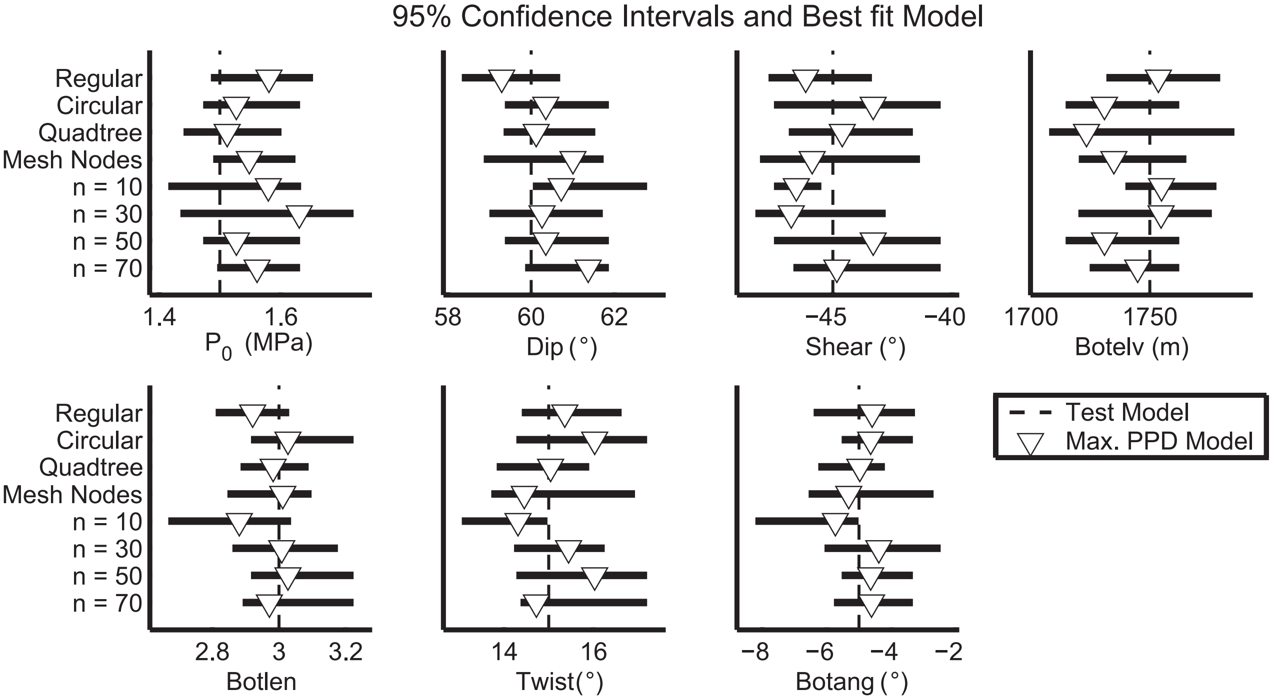

Figure 9. Maximum PPD (best fit) model and 95% confidence intervals (thick lines) determined from one-dimensional marginal PPDs, obtained using four subsampling methods (with $n = 50$) and different n values (with circular subsampling method). Dashed vertical lines indicate our test model. Estimation of confidence intervals is considered appropriate when the test model is within the confidence intervals.

distribution may be common characteristics in the inverse problems of ground deformation caused by dikes.

4. Application to the February 2000 Eruption at Piton de la Fournaise

4.1. Description of the Eruption

[31] Piton de la Fournaise is an active basaltic shield volcano of hot spot origin. It occupies the southeast of Réunion Island (France), situated 800 km east of Madagascar. The volcano has arcuated rift zones where eruptions and surface fractures are preferentially located (Figure 1). After 5 years of quiescence, the volcano entered a new cycle of activity in March 1998 with one of its largest eruptions of the last century. The February 2000 eruption was the fourth eruption in this cycle (Table 2). It occurred along the northern rift zone and caused a distinct seaward (eastward) displacements similar to that observed for the March 1998 eruption [*Sigmundsson et al.*, 1999]. At around 2315 LT on 13 February, changes in seismic activity and ground deformation were detected by the seismometer, tiltmeter and extensometer networks of the Observatoire Volcanologique

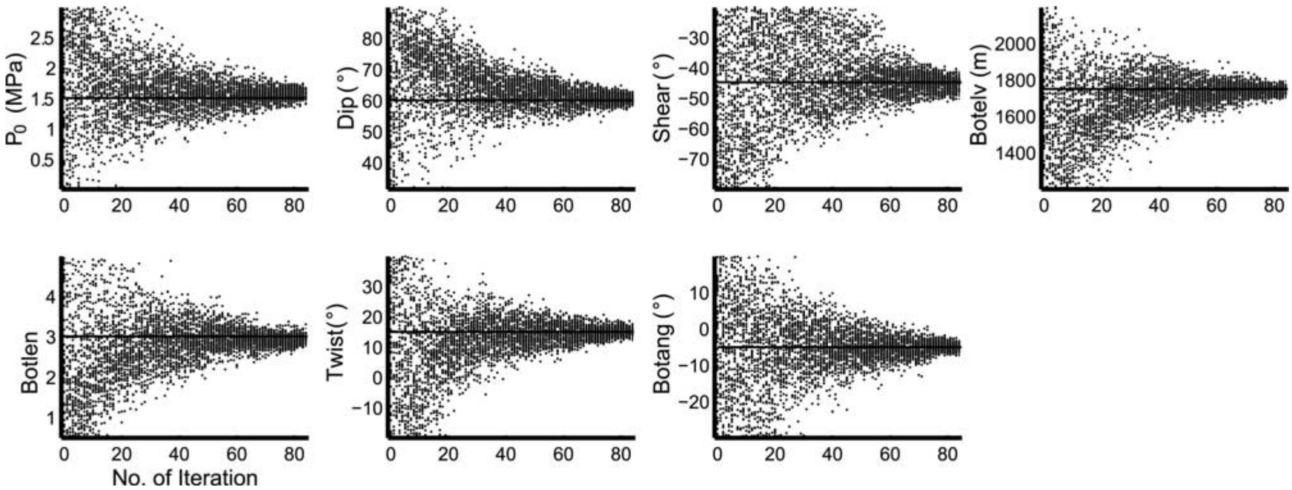

Figure 10. Parameter values plotted against number of iteration, in the case of a search with $n = 50$ using circularly subsampled synthetic data. Solid lines indicate the test model.

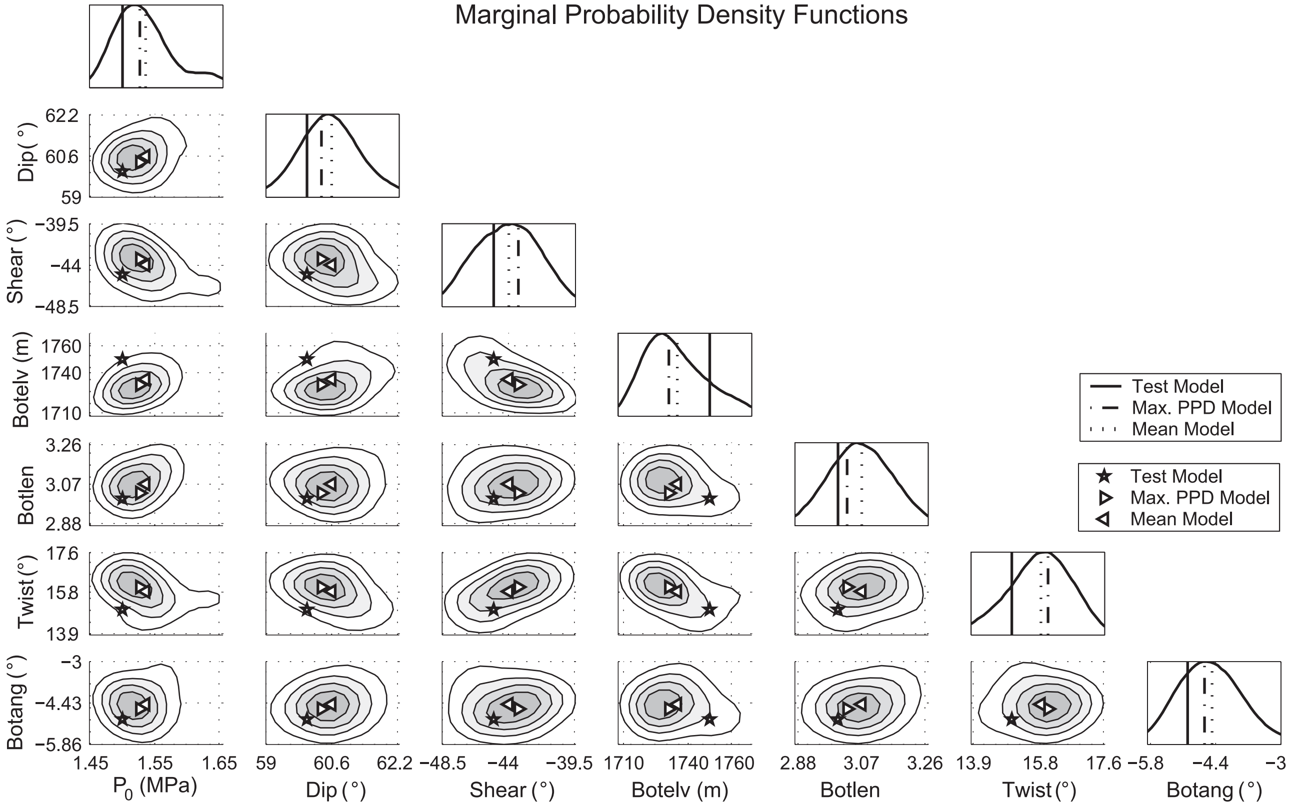

Figure 11. One-dimensional (diagonals) and two-dimensional (off-diagonals) marginal PPDs plotted with the test, maximum PPD and mean models, for the synthetic test with circular data points and $n = 50$. Contour interval is 0.2 times the maximum value.

du Piton de la Fournaise [*Staudacher et al.*, 2000]. The eruption started at 0018 LT on 14 February, about an hour after the detection of the precursors. The main eruptive activity quickly focused on the lowermost eruptive fissure and the eruption ceased at 1800 LT on 4 March.

4.2. Data

[32] RADARSAT-1 is a C-band satellite with 24 days of repeat time. Unlike the March 1998 eruption where a large number of images were available for one incidence angle before and after the eruption [*Sigmundsson et al.*, 1999], we only had a few images available because of the short interruption intervals before and after the eruption (Table 2). On the other hand, the archive offered different incidence angles both from ascending and descending orbits, which provides slightly different information on displacements. Four pairs of images with different incidence angles (Table 3) were found to be acceptable with respect to the time period and altitude of ambiguity [*Massonnet and Feigl*, 1998]. The interferograms were computed with DIAPASON software developed by French Centre National d'Etudes Spatiales. Topographic fringes were subtracted using a DEM provided by French Institut Géographique National. The altitudes of ambiguity indicate that the topographic effect on the interferograms is less than a tenth of a fringe. For one of the descending pairs (F3N), the azimuth spectrum was cut in Single Look Complex data to maximize the coherence and signal to noise ratio in the interferogram [*Durand et al.*, 2002].

[33] The four interferograms are shown in Figure 12a. The two ascending and two descending interferograms covering different time periods show similar displacements. Considering that the differences in the line-of-sight vectors are small, it suggests that there is negligible time-dependent deformation. The data clearly show asymmetric displacements: large displacements to the east and small displacements to the west of the eruptive fissures. The descending interferograms have about 14 fringes, indicating a maximum displacement toward the satellite of about 40 cm. The ascending data have 4 to 5 fringes, indicating

Table 2. Eruptions Since March 1998[a]

	Period	Eruptive Fissure Location	Lava Flow Volume, Mm^3
March 1998	9 March 1998 to 15 Sept. 1998	northern flank	40–50
July 1999	19 July 1999 to 31 July 1999	summit	1.8
Sept. 1999	28 Sept. 1999 to 23 Oct. 1999	summit/southern flank	1.5
Feb. 2000	14 Feb. 2000 to 4 March 2000	northern flank	6–8
June 2000	23 June 2000 to 30 July 2000	southeastern flank	10

[a] *Villeneuve* [2000].

Table 3. Interferograms Used in This Study

Orbit	Period	Line-of-Sight Vector [East, North, Up]	Incidence Angle, deg	h_a,[a] m
F2N (ascending)	7 Feb. 2000 to 13 May 2000	[−0.63, −0.17, 0.76]	40.7	−272.9
F4F (ascending)	14 Dec. 1999 to 19 March 2000	[−0.69, −0.19, 0.70]	45.7	−130.4
F3N (descending)	22 Oct. 1999 to 25 May 2000	[0.64, −0.17, 0.75]	41.8	−88.0
F5F (descending)	16 Dec. 1999 to 1 June 2000	[0.70, −0.19, 0.69]	46.8	494.1

[a] Altitude of Ambiguity.

a maximum displacement away from the satellite of about 14 cm. Subsidences associated with lava flow contractions are observed at the locations of the March 1998 and July and September 1999 lava flows.

[34] The interferograms were unwrapped with the SNAPHU unwrapping algorithm [*Chen and Zebker*, 2001]. The narrow fringes associated with a large displacement gradient in the descending interferograms did not allow a satisfactory unwrapping in a single calculation. Therefore the interferograms were unwrapped iteratively using the following algorithm: (1) unwrapping of the original interferogram, (2) low-pass filtering of the result with cutoff wavelength of about 500 m, (3) rewrapping of the filtered unwrapped data, (4) residual interferogram calculation by subtracting the phase of the rewrapped interferogram from that of the original interferogram, (5) unwrapping of the residual interferogram, (6) addition of the unwrapped data (product of (5)) to the product of (2), and (7) back to (2) or termination if the maximum amplitude is consistent with the number of fringes. Subsampled data sets were then created with the circular subsampling method after removing the speckles by low-pass filtering. Each of the four unwrapped data sets contains an unknown constant offset; this offset is adjusted automatically when evaluating the misfit so as to minimize the discrepancy between observed and modeled data.

4.3. Analysis

[35] We simultaneously invert the two ascending and two descending data sets, in order to search for the models that explain the four data sets equally well. This simultaneous inversion reduces the influence of atmospheric noise because each interferogram contains different noise. As decided from the synthetic tests, the number of models

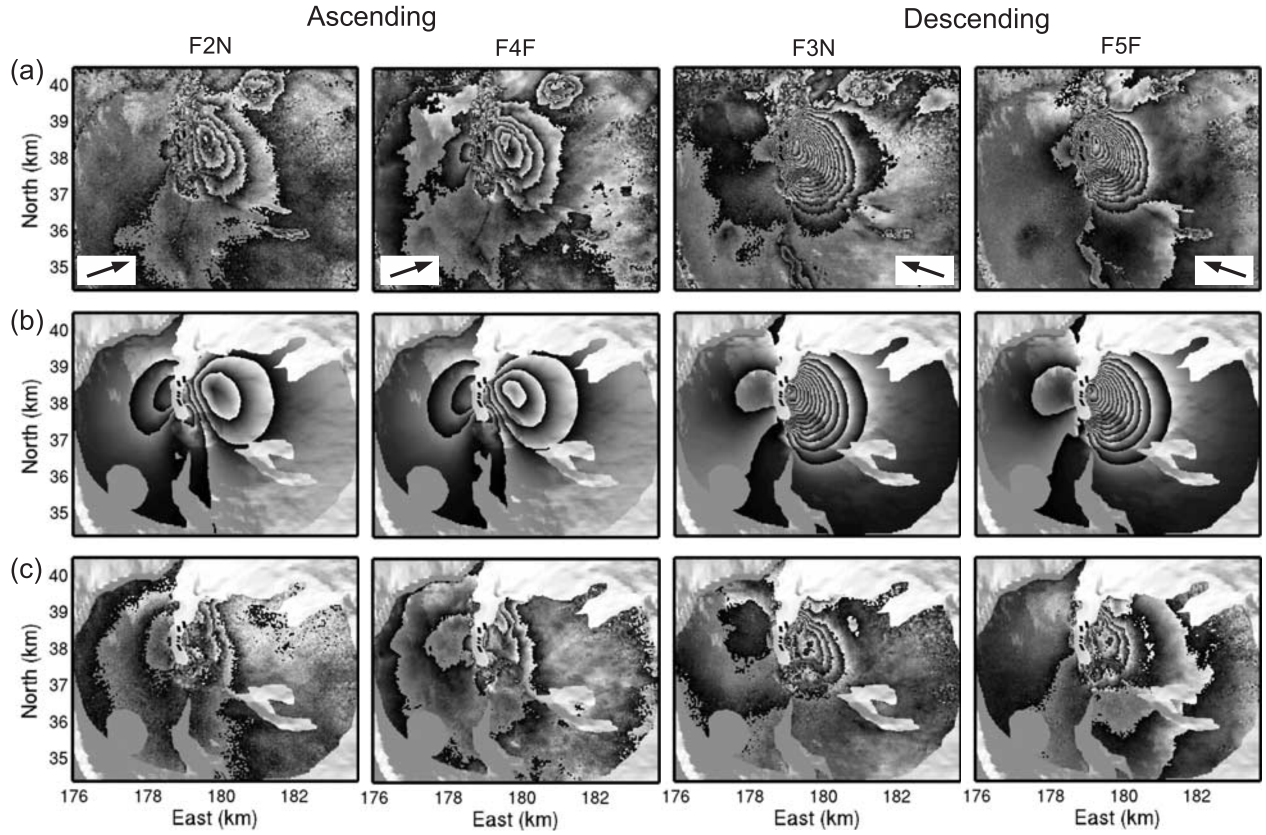

Figure 12. (a) Four interferograms indicating the ground displacements caused by the dike intrusion associated with the February 2000 eruption, superimposed on a DEM. Refer to the caption of Figure 7 for the meanings of gray scale shading and arrows and to Table 3 for data acquisition information. (b) Rewrapped modeled displacements for the four line-of-sight directions corresponding to the maximum PPD model. Recent lava flow areas not used in the misfit evaluation are masked out. (c) Residual displacements between observed and modeled data. See color version of this figure at back of this issue.

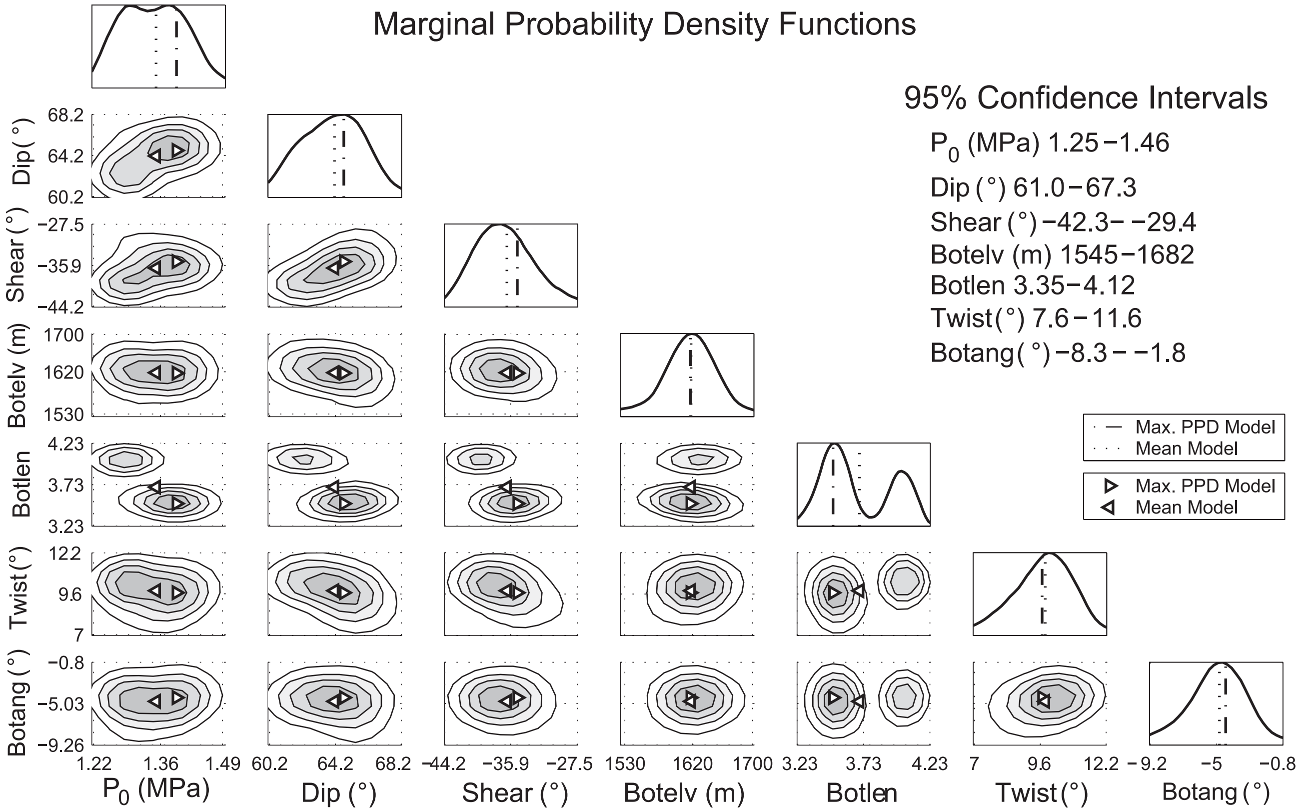

Figure 13. One- and two-dimensional marginal PPDs for the dike model. Contour interval is 0.2 times the maximum value. The 95% confidence intervals are also indicated. Parameters are well constrained with small uncertainties.

generated per iteration *n* is set to 50 in the search program.

4.3.1. Corrections to the Tested Models and the Misfit

[36] When a search finishes, we apply corrections to the overpressure and misfit values. As mentioned, overpressure correction is needed because a coarse dike mesh is used. The displacements for the maximum PPD model obtained with a coarse dike mesh are compared with those recalculated with a dense mesh to obtain the scaling factor. Then the overpressure of all the evaluated models is multiplied by the factor.

[37] A difference from the synthetic tests is that, in addition to the statistical uncertainties associated with data noise, we now have uncertainties which arise from the simplifications introduced by the model. These are taken into account by reestimating the data variance σ_d^2 used in the data covariance matrix. This correction is for the appraisal where the misfit is directly related to the probability density (equation (6)). In the search stage, the variance can be set to any value since the algorithm only uses the rank of the misfits. We first run a search with $\sigma_d^2 = 1$ and then rescale the resulting misfits by the variance calculated from the residual (observed minus best modeled) data. A typical reevaluated data variance is around 6×10^{-4} m^2, which is significantly larger than the variance of pure atmospheric noise (8.8×10^{-5} m^2).

4.3.2. Results

[38] Figures 12b and 12c show the modeled displacements for the maximum PPD model and residual displacements, respectively, corresponding to the four InSAR data sets. Comparisons are shown in the area where the circular subsampled points are placed. The model well explains the main characteristics of the observed data, such as limited displaced area east of the eruptive fissures (both ascending and descending data), a small lobe south of the fissures (ascending data), and little displacements west of the fissures (descending data). However, we observe some nonnegligible residuals. The model does not sufficiently explain the displacement asymmetry in the ascending directions. Also, three to four fringes of residuals are localized east of the eruptive fissures in the descending directions. Possible origins of the residuals are: atmospheric noise, oversimplification of the model, and other pressure sources such as a deflating deeper magma reservoir. Atmospheric noise can be ruled out as it is unlikely to have a strong atmospheric signal at the same place in the two independent interferograms of ascending or descending directions. The latter two possibilities are discussed later.

[39] The marginal PPDs (Figure 13) indicate that the model parameters are well constrained. For example, the 95% confidence intervals of the dip angle (Dip) and elevation of the middle point of the dike bottom side (Botelv) are as small as 6.3° and 137 m, respectively. We observe two peaks in the one- and two-dimensional marginal PPDs concerning Botlen, as well as minor trade-offs for some parameter pairs (e.g., Dip and P_0); however, these have little effect because of the small confidence intervals.

[40] The dike geometry of the maximum PPD model is shown in Figure 14. The geometries of all the acceptable models which have parameter values within the confidence

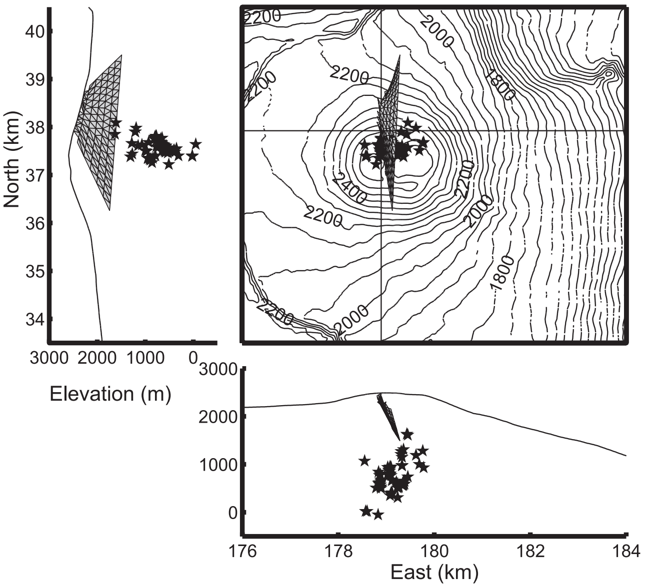

Figure 14. Map view and cross sections of the maximum PPD dike geometry, plotted with the hypocenters of the seismic swarm prior to the eruption [*Battaglia*, 2001]. The acceptable models have geometries similar to this because of the small model uncertainties.

intervals would be similar to Figure 14 because of the small model uncertainties. The acceptable models have common characteristics: a seaward dipping (61.0°–67.3°) trapezoid with its bottom passing 800–1000 m beneath the summit Dolomieu crater parallel to the rift zone. This result is in accordance with the seismicity and tilt data. Hypocenters of the seismic swarm showed an upward migration toward the summit (see Figure 14), while the tilt data indicated lateral propagation of magma from the summit area to the eruptive fissures [*Staudacher et al.*, 2000]. These data sets also suggest that magma reached the central to southern part of our estimated dike bottom and propagated laterally.

[41] Dikes open in response to the applied overpressure. The opening distribution for the maximum PPD model shows that the dike center opened by 59 cm (Figure 15). The average opening for the whole dike and that on the ground are 35 and 25 cm, respectively. The relatively small opening on the ground is attributed to the limited extent of the ground surface fissures. The average opening on the ground is consistent with the field observation of around 30 cm of openings (T. Staudacher, personal communication, 2003). Most of the old dike intrusions found at the bottom of deep eroded cliffs a few kilometers away from the summit have less than 1 m of thickness [*Grasso and Bachèlery*, 1995], which is consistent with our estimated value. The volume of the corresponding dike is estimated to be 6.5×10^5 m^3, which is about 6 times smaller than the estimated lava flow volume (4×10^6 m^3, *Staudacher et al.* [2000]).

5. Discussion

5.1. Influence of the Misfit Function Definition

[42] Our misfit function is controlled by the variance σ_d^2 and correlation length a of data noise. As estimation of these parameters inherently contains inaccuracy, it is important to know what we would obtain if different values were assumed.

[43] When a uniform variance and independency of data noise are assumed, the data covariance matrix becomes diagonal. In this case, the misfit function (equation (3)) becomes

$$\chi'^2(\mathbf{m}) = \frac{1}{\sigma_d^2}\sum^{N}(u_o - u_m)^2, \qquad (11)$$

where N denotes the length of the data and model vectors. We tested the influence of this misfit definition and obtained a significantly different maximum PPD model (Dip = 54.0°, Botelv = 1790 m, Twist = 16.3°) from that obtained assuming correlated data noise. On the other hand, assuming a correlation length a = 1500 m (a plausible value for different atmospheric conditions) instead of 2308 m did not lead to significantly different maximum PPD model. From these tests, we conclude that considering data noise correlation has a significant effect, but the result is not very sensitive to the assumed correlation length. Note also that it is indispensable to take data noise correlation into account in the appraisal stage where the misfit values are meaningful.

[44] The data variance σ_d^2 also affects the appraisal; the larger the value, the broader the confidence intervals. We investigated its influence by assuming half the data variance used in the analysis. We obtained confidence intervals that are only 71% shorter on average for the seven parameters, indicating that the data variance has a limited impact on the confidence intervals.

5.2. Comparisons With Simpler Models

[45] Many dike modeling studies using ground deformation data assume a rectangular dislocation in elastic half-space [*Okada*, 1985]. In order to compare this model with the three-dimensional mixed BEM, an inversion is performed using Okada's equations. Model parameters are the opening (uniform), location (three parameters), length, width, dip angle and strike angle. We use the same inversion method and same data set as before.

[46] Table 4 compares the maximum PPD Okada model with that obtained by our method. The length and strike of the Okada model are close to those at the top of the mixed

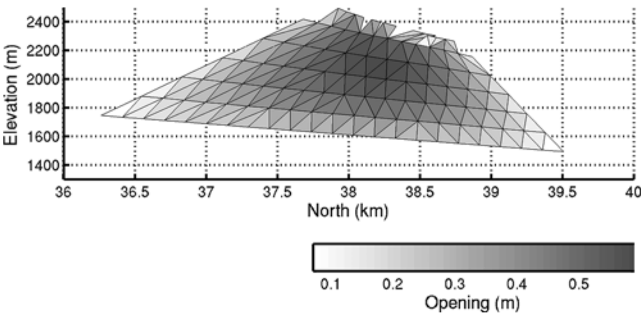

Figure 15. Opening of the dike in response to the constant overpressure for the maximum PPD model. The maximum opening is 59 cm, the average on the whole area and that on the ground surface are 35 and 25 cm, respectively.

Table 4. Maximum PPD Mixed BEM and Okada Models

	Opening, cm	Dip, deg	Length, m	Bottom Depth, m	Strike, °N	Area, Mm^2	Volume, Mm^3
Mixed BEM	35	64.7	930–3257	745	12.5–2.8	1.8	0.65
Okada	63	67.0	1182	1029	12.2	1.3	0.79

For the mixed BEM model, opening and bottom depth are given in average, length and strike are given in dike top, bottom values. Top of the Okada model is estimated at 51 m below the ground.

BEM model, suggesting that Okada-type models tend to predict the geometry close to the ground and poorly predict the geometry at depth. Indeed, the dike bottom depth is 38% greater than the average depth of the mixed BEM model. Moreover, it gives an opening 80% larger than the averaged opening of the BEM model. This is partly because Okada's model predicts the dike area where opening is large. If we calculate the average opening of the mixed BEM model on an area similar to the Okada model, we get 48 cm, in which case the discrepancy reduces to 30%. The resulting displacements (Figure 16a) are significantly different from the observed data (Figure 12a). There are too many fringes west of the eruptive fissures, and the displacement patterns are too elongated to east-west direction.

[47] Some more detailed studies assume a realistic opening distribution rather than a uniform opening by considering a number of Okada-type rectangular segments [*Aoki et al.*, 1999; *Amelung et al.*, 2000]. These studies do not generally estimate the dike geometry and opening distribution simultaneously, but if they did, they would obtain a similar model to that obtained by the mixed BEM with a flat ground surface assumption. An inversion is performed for a flat ground surface at the elevation of 2300 m. The maximum PPD model has significantly different values of P_0, Botelv, Botlen and Botang than the model with realistic topography (Table 5). The overpressure P_0 is overestimated by 24%. The last three parameters are related to the dike bottom; in this particular case, the bottom deepens toward south instead of north and reaches 934 m above sea level at its southern edge (compare with Figure 14). The difference in Botelv (the elevation of the middle point of the bottom line) is about 300 m, which corresponds to about 30% of difference in the dike height. The similar degree of discrepancies to those for the Okada model suggests that part of the differences found with the Okada model originate from neglecting the topography. The modeled displacements (Figure 16b) are still too elongated in the east-west direction.

5.3. Model Assumptions

[48] We assumed that the edifice is homogeneous, isotropic and linearly elastic. Since relaxing these assumptions lead to different prediction of ground displacements, such assumptions might bias the dike model estimation.

[49] A tomographic study [*Nercessian et al.*, 1996] indicates a high velocity plug of 1.5 km in diameter below the summit crater, surrounded by a lower-velocity ring. This is the most distinct heterogeneity that we expect around the depth we are concerned with. The InSAR fringes are uncorrelated to this potential plug and ring structure, suggesting that the homogeneity assumption is valid. The effects of local heterogeneities due to individual dike intrusions etc. are averaged out by considering effective elastic moduli.

[50] Anisotropy can be caused by stratified lava flows. *Ryan et al.* [1983] estimated a 1.4 times greater Young's modulus in the horizontal direction than in the vertical direction at Kilauea volcano. Such anisotropy could be responsible for the observed asymmetric displacements between the eastern and western sides of the eruptive fissures. However, our studied area has many intruded dikes that locally cause anisotropy in different directions. Thus it is not clear what kind of anisotropy model is appropriate to our problem.

[51] Inelastic deformation generally occurs close to the eruptive fissures. We do not observe any systematic residual displacements correlated to the fissure locations, probably because we masked the area close to the fissures. Thus inelastic effects do not affect our result.

[52] Volcanic edifices are expected to have complex stress fields due to surface topography, material heterogeneities associated with previous dike intrusions, etc. Therefore the constant dike overpressure assumed in this study is probably an oversimplification. A vertical overpressure gradient would give a better approximation; however, a preliminary study showed that this overpressure gradient cannot be constrained by the inversion, suggesting that such a model does not describe the reality any better than the constant overpressure model. We probably need to consider a

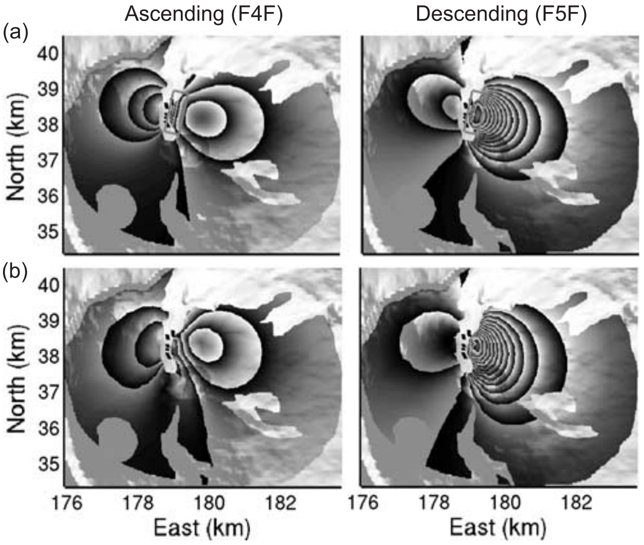

Figure 16. Rewrapped maximum PPD displacements modeled using (a) Okada's equations and (b) the mixed BEM with a flat ground surface, in an ascending (F4F) and a descending (F5F) directions. Gray rectangle line in Figure 16a indicates the projected model geometry. A set of small Okada-type segments with different opening values would create similar displacements as those shown in Figure 16b. See color version of this figure at back of this issue.

Table 5. Maximum PPD Mixed BEM Models With Realistic and Flat Topographies

	P_0, MPa	Dip, deg	Shear, deg	Botelv, m	Botlen	Twist, deg	Botang, deg	Area, Mm^2	Volume, Mm^3
Realistic	1.3	64.7	−35.1	1617	3.50	9.7	−4.4	1.8	0.65
Flat	1.7	68.4	−35.7	1333	3.97	10.5	13.2	2.1	0.81

more complex overpressure distribution as well as a shear stress distribution, for instance by taking into account the stress associated with topography [*Pinel and Jaupart*, 2004].

[53] The top of the dike was fixed at the locations of the eruptive fissures in our modeling, while the ascending data (Figure 12a) seem to indicate that the superficial fissures extend further to the north. However, simple extension of the dike top by 500 m did not lead to a better fit. Extension of the dike to the south was also tested by adding a vertex between the southern top and bottom vertexes of the quadrangle, which makes the dike model to be pentagonal (nine dike geometry parameters), but the optimum model was similar to that obtained by the quadrangle model. These tests suggest that the data residuals are not caused by an error in the location of the dike top.

5.4. Effect of a Basal Plane

[54] The horseshoe-shaped depression of Enclos-Fouqué caldera has been interpreted by several authors as the head wall of an eastward moving landslide [e.g., *Lénat et al.*, 2001]. This idea is supported by the age and volume of landslide materials found on the submarine eastern flank of the volcano [*Labazuy*, 1996], though the landslides may have been restricted to the area close to the ocean [e.g., *Merle and Lénat*, 2003].

[55] In order to test the hypothesis that reactivation of the basal plane of the caldera caused the observed asymmetric displacement pattern, such a plane is modeled with the mixed BEM (Figure 17a). We assume that the eastern part is freely slipping in response to the dike inflation so that it has a null stress boundary condition. The western part is assumed to be locked so that it is not modeled. The dike is assumed to be vertical only to see the effect of the plane. The basal plane is connected to the ground at sea level on the east end, and to the dike at 700 m above sea level so that the westward extension of the plane reaches the caldera wall.

[56] Modeled displacements with the basal plane (Figure 17c) have a larger wavelength pattern than those without it (Figure 17b). This is inconsistent with the InSAR data. In addition, preliminary inversions with a rectangular slip plane (seaward dip and elevation of the plane are additional model parameters) beneath the dike did not indicate any better fit to the data. We therefore conclude that the observed asymmetric displacement patterns were not caused by a basal plane slip but, as we found, by the dip of the dike.

5.5. Magma Transfer System

[57] We showed with a high confidence that the dike bottom side lies 800 to 1000 m below the ground. The preeruption seismic swarm (Figure 14) indicates that the dike intrusion started around sea level (2600 m below the summit), and that magma came from a greater depth. This leads to two questions: (1) Where was the source of magma that fed the eruption located? and (2) Why is the estimated dike model significantly shallower than what is expected from the seismic swarm?

[58] An answer to the first question can be deduced from the fact that the InSAR data do not indicate any deflation source that accounts for the lava flow and dike volumes. Geodetic measurements rarely find a deflation source that accounts for the erupted and intruded magma volume [*Owen et al.*, 2000; *Amelung and Day*, 2002], but this may be due to limited detectability of signals.

[59] In order to determine the minimum depth for the source of magma to cause undetectable surface displacements, we assume that the volume leaving the magma reservoir (Vr) and the erupted/intruded volume (Ve) balance. The major factors that affect the magma balance are: (1) magma degassing during ascent, (2) lava contraction associated with cooling, and (3) vesicles and cavities in the lava flow. The first factor leads to Vr > Ve by a few percent [*Tait et al.*, 1989], the second one to Vr > Ve by 10–15% [*Yoder*, 1976], and the last one to Vr < Ve by roughly 20–50% [*Cas and Wright*, 1987]; in all, the magma balance assumption is roughly valid.

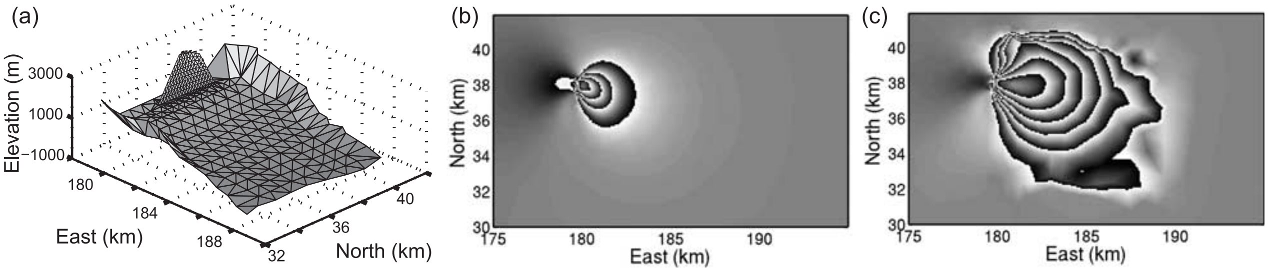

Figure 17. (a) Dike and basal plane meshes used to evaluate the effect of a basal plane. See text for explanations. (b) Line-of-sight displacements in a descending direction (F5F) modeled without the basal plane. A small overpressure 0.13 MPa was assumed for a better display of the results. (c) Displacements modeled with the basal plane. The same line-of-sight direction and overpressure as Figure 17b were assumed. Note that the basal plane creates a seaward slip of a larger wavelength.

[60] We modeled a spherical deflation source using the mixed BEM, with a diameter of 1000 m and a volume loss equal to the sum of the lava flow and dike volumes (4.7×10^6 m^3). It should be noted that the modeled displacements are mainly sensitive to the magma reservoir volume change, and insensitive to the reservoir dimension at the considered depth. We found that if the center of the source was located deeper than 3000 m below sea level, it would create less than one fringe along the line-of-sight directions. Such a small fringe could be hidden by those created by the dike intrusion and atmospheric noise. Consequently, the source of magma should be located deeper than 3000 m below sea level (5600 m beneath the summit).

[61] To answer the second question; that is, to explain the depth difference between the preeruption seismic swarm and the dike model, two scenarios are possible. The first one is that magma intruded through a path too narrow to cause detectable displacements on InSAR data. Such a narrow path is suggested by *Amelung and Day* [2002] on Fogo volcano, Cape Verde, where InSAR data for the 1995 eruption did not show any evidence of a shallow magma reservoir as in our case. The second one is that the deeper magma path closed once the eruption ceased. This scenario is possible if magma withdrew from the path back into the magma reservoir or if magma ascended by buoyancy after the overpressure in the magma reservoir was relaxed [*Dahm*, 2000].

[62] *Lénat and Bachèlery* [1990] proposed a shallow storage system that consists of discrete magma pockets on the basis of the diversity of preeruptive seismicity and tilt changes. Petrological characteristics of lavas emitted in recent 25 years are in accordance with their model [*Boivin and Bachèlery*, 2003]. Taking into account our consideration, such a system may exist provided that magma in shallow pockets is pushed toward the ground by the arrival of magma from depth. If the densities of the two magmas are the same, such a mechanism would create no deformation.

[63] To further investigate the magma transfer system, a comprehensive study of seismicity and continuous geodetic data is needed. An interesting feature worth noting in addition is that the upper limit of the hydrothermal system has been identified by a geoelectrical study at a few hundred meters beneath the summit area of the volcano [*Lénat et al.*, 2000], which is consistent with the depth of our model. It suggests that the hydrothermal system might play a role in the magma propagation behavior.

5.6. What Controls the dip of the Dike?

[64] The inversion results and the discussion on the basal plane strongly suggests a 61.0°–67.3° seaward dipping dike. Interferograms for other dike intrusions along the northern rift zone of Piton de la Fournaise show similar asymmetric pattern [*Sigmundsson et al.*, 1999; *Froger et al.*, 2004], suggesting similar dip angles. This indicates that the minimum principal stress along the rift zone on the northern flank of the volcano is in east-west direction and inclined about 25° vertically (the normal direction of the dike surface). Such a stress condition may be associated with a weakness area created by gravitational instability, though further studies are needed to unravel the mechanism. This is fundamental to the formation of the rift zones of Piton de la Fournaise and hence is a key point to predict the future development of the volcano.

6. Conclusions

[65] We showed that a combination of InSAR data, a three-dimensional mixed boundary element method and a neighborhood algorithm inversion gives detailed and reliable information on a dike intrusion. Inversions with synthetic data showed that a test model can be well retrieved by the inversion method within predicted uncertainties, and that all the tested subsampling methods are acceptable for our dike intrusion problem. For the InSAR data, the marginal probability density functions of model parameters indicate small uncertainties and trade-offs. Incorporating data noise correlation is found to be important; a misfit function that takes this into account leads to a significantly different maximum PPD (best fit) model.

[66] The acceptable models of the dike intrusion at Piton de la Fournaise well explain the main characteristics of the InSAR data. The maximum PPD dike model predicts an average ground opening of 25 cm, consistent with field observation. Acceptable models share common characteristics: a seaward dipping (61.0°–67.3°) trapezoid with its bottom passing 800–1000 m beneath the summit Dolomieu crater parallel to the rift zone.

[67] Models that neglect the topography, including a single rectangular dislocation model, poorly estimate overpressure (or opening) and geometry at depth. Overestimations in overpressure (or opening) and dike height amount to about 30%, and in volume to about 20%. This indicates the importance of taking realistic topography into account. A model with a basal slip plane, which may exist under Enclos-Fouqué caldera, shows that the dike inflation did not reactivate the plane, and that the observed asymmetric displacements are solely attributed to the dipping dike. The magma which supplied the eruption should be sourced deeper than 3000 m below sea level (5600 m beneath the summit), considering the fact that the observed data do not indicate any deflation source. Taking into account the lack of inflation related to a magma path from the source and the estimated dike, we propose one of the following feeding systems: (1) a narrow path or (2) a path that closes once an eruption ceases.

[68] This detailed and careful analysis gives constraints on the mechanisms of the magma transfer system and formation of the rift zones. Further analyses of InSAR data for other eruptions and incorporation of other kinds of data could provide a better understanding on the eruption behavior and structure of the volcano.

[69] **Acknowledgments.** We are grateful to the Canadian Space Agency for the RADARSAT-1 data provided through ADRO2 253 and to D. Massonnet for launching the project. We thank M. Sambridge for his NA inversion codes, J.-L. Froger for suggestions in interferogram unwrapping and the ground meshing program, T. Souriot for his help on unwrapping, P. Boivin for discussions on the volcano magma system, and J. Battaglia for the seismicity data. We also thank F. Cornet, J.-F. Lénat, and A. Provost for reviewing the manuscript before submission and B. van Wyk de Vries for reviewing and English improvement before and after submission. Long and thoughtful comments of the three reviewers (two anonymous and Sigurjón Jónsson) and the Associate Editor L. Mastin contributed to improve the quality of the paper.

References

Amelung, F., and S. Day (2002), InSAR observations of the 1995 Fogo, Cape Verde, eruption: Implications for the effects of collapse events upon island volcanoes, *Geophys. Res. Lett.*, *29*(12), 1606, doi:10.1029/2001GL013760.

Amelung, F., S. Jónsson, H. Zebker, and P. Segall (2000), Widespread uplift and 'trapdoor' faulting on Galàpagos volcanoes observed with radar interferometry, *Nature*, *407*, 993–996.

Aoki, Y., P. Segall, T. Kato, P. Cervelli, and S. Shimada (1999), Imaging magma transport during the 1997 seismic swarm off the Izu Peninsula, Japan, *Science*, *286*, 927–930.

Battaglia, J. (2001), Quantification sismique des phénomènes magmatiques sur le Piton de la Fournaise entre 1991 et 2000, thèse de doctrat, Univ. Paris 7 Denis Diderot, Paris, France.

Beauducel, F., and F. H. Cornet (1999), Collection and three-dimensional modeling of GPS and tilt data at Merapi volcano, Java, *J. Geophys. Res.*, *104*, 725–736.

Boivin, P., and P. Bachèlery (2003), The behaviour of the shallow plumbing system at La Fournaise volcano (Réunion Island). A petrological approach, paper presented at EGS-AGU-EUG Joint Assembly, Nice, France.

Cas, R. A. F., and J. V. Wright (1987), *Volcanic Successions*, CRC Press, Boca Raton, Fla.

Cayol, V., and F. H. Cornet (1997), 3D mixed boundary elements for elastostatic deformation fields analysis, *Int. J. Rock Mech. Min. Sci. Geomech. Abstr.*, *34*, 275–287.

Cayol, V., and F. H. Cornet (1998), Three-dimensional modeling of the 1983–1984 eruption at Piton de la Fournaise Volcano, Reunion Island, *J. Geophys. Res.*, *103*, 18,025–18,037.

Cayol, V., J. H. Dieterich, A. Okamura, and A. Miklius (2000), High magma storage rates before the 1983 eruption of Kilauea, Hawaii, *Science*, *288*, 2343–2346.

Chen, C. W., and H. A. Zebker (2001), Two-dimensional phase unwrapping with use of statistical models for cost functions in nonlinear optimization, *J. Opt. Soc. Am.*, *18*, 338–351.

Cervelli, P., M. H. Murray, P. Segall, Y. Aoki, and T. Kato (2001), Estimating source parameters from deformation data, with an application to the March 1997 earthquake swarm off the Izu Peninsula, Japan, *J. Geophys. Res.*, *106*, 11,217–11,237.

Cervelli, P., P. Segall, F. Amelung, H. Garbeil, C. Meertens, S. Owen, A. Miklius, and M. Lisowski (2002), The 12 September 1999 Upper East Rift Zone dike intrusion at Kilauea Volcano, Hawaii, *J. Geophys. Res.*, *107*(B7), 2150, doi:10.1029/2001JB000602.

Crouch, S. L., and A. M. Starfield (1983), *Boundary Element Methods in Solid Mechanics*, Allen and Unwin, London.

Dahm, T. (2000), On the shape and velocity of fluid-filled fractures in the Earth, *Geophys. J. Int.*, *142*, 181–192.

Dieterich, J., V. Cayol, and P. Okubo (2000), The use of earthquake rate changes as a stress meter at Kilauea volcano, *Nature*, *408*, 457–460.

Durand, P., M. van der Kooij, and F. Adragna (2002), An update in the evolution of Radarsat1 Azimuth Doppler for differential interferometry purposes, paper presented at Colloques International Geoscience and Remote Sensing Symposium, Geosci. and Remote Sens. Soc., Toronto, Canada.

Froger, J. L., Y. Fukushima, P. Briole, T. Staudacher, T. Souriot, and N. Villeneuve (2004), The deformation field of the August 2003 eruption at Piton de la Fournaise, Reunion Island, mapped by ASAR interferometry, *Geophys. Res. Lett.*, *31*, L14601, doi:10.1029/2004GL020479.

Fukushima, Y., O. Nishizawa, H. Sato, and M. Ohtake (2003), Laboratory study on scattering characteristics in rock samples, *Bull. Seismol. Soc. Am.*, *93*, 253–263.

Grasso, J. R., and P. Bachèlery (1995), Hierarchical organization as a diagnostic approach to volcano mechanics: Validation on Piton de la Fournaise, *Geophys. Res. Lett.*, *22*, 2897–2900.

Jónsson, S., H. Zebker, P. Segall, and F. Amelung (2002), Fault slip distribution of the 1999 M_w 7.1 Hector Mine, California, earthquake, estimated from satellite radar and GPS measurements, *Bull. Seismol. Soc. Am.*, *92*, 1377–1389.

Labazuy, P. (1996), Recurrent landslides events on the submarine flank of Piton de la Fournaise volcano (Reunion Island), in *Volcano Instability on the Earth and Other Planets*, edited by W. J. McGuire, A. P. Jones, and J. Neuberg, *Geol. Soc. Spec. Publ.*, *110*, 295–306.

Lénat, J.-F., and P. Bachèlery (1990), Structure et fonctionnement de la zone centrale du Piton de la Fournaise, in *Le voicanisme de la Réunion*, edited by J.-F. Lénat, pp. 257–296, Cent. de Rech. Volcanol., Clermont-Ferrand, France.

Lénat, J.-F., D. Fitterman, and D. B. Jackson (2000), Geoelectrical structure of the central zone of Piton de la Fournaise volcano (Réunion), *Bull. Volcanol.*, *62*, 75–89.

Lénat, J.-F., B. Gilbert-Malengreau, and A. Galdéano (2001), A new model for the evolution of the volcanic island of Réunion (Indian Ocean), *J. Geophys. Res.*, *106*, 8645–8663.

Lohman, R. B., M. Simons, and B. Savage (2002), Location and mechanism of the Little Skull Mountain earthquake as constrained by satellite radar interferometry and seismic waveform modeling, *J. Geophys. Res.*, *107*(B6), 2118, doi:10.1029/2001JB000627.

Massonnet, D., and K. L. Feigl (1998), Radar interferometry and its application to changes in the Earth's surface, *Rev. Geophys.*, *36*, 441–500.

Masterlark, T. (2003), Finite element model predictions of static deformation from dislocation sources in a subduction zone: Sensitivities to homogeneous, isotropic, Poisson-solid, and half-space assumptions, *J. Geophys. Res.*, *108*(B11), 2540, doi:10.1029/2002JB002296.

Merle, O., and J.-F. Lénat (2003), Hybrid collapse mechanism at Piton de la Fournaise volcano, Reunion Island, Indian Ocean, *J. Geophys. Res.*, *108*(B3), 2166, doi:10.1029/2002JB002014.

Mogi, K. (1958), Relations between the eruptions of various volcanoes and the deformation of the ground surfaces around them, *Bull. Earthquake Res. Inst. Univ. Tokyo*, *36*, 99–134.

Nercessian, A., A. Hirn, J.-C. Lepine, and M. Sapin (1996), Internal structure of Piton de la Fournaise volcano from seismic wave propagation and earthquake distribution, *J. Volcanol. Geotherm. Res.*, *70*, 123–143.

Okada, Y. (1985), Surface deformation due to shear and tensile faults in a half-space, *Bull. Seismol. Soc. Am.*, *75*, 1135–1154.

Owen, S., P. Segall, M. Lisowski, A. Miklius, M. Murray, M. Bevis, and J. Foster (2000), January 30, 1997 eruptive event on Kilauea Volcano, Hawaii, as monitored by continuous GPS, *Geophys. Res. Lett.*, *27*, 2757–2760.

Pinel, V., and C. Jaupart (2004), Magma storage and horizontal dyke injection beneath a volcanic edifice, *Earth Planet. Sci. Lett.*, *221*, 245–262.

Pritchard, M. E., and M. Simons (2002), A satellite geodetic survey of large-scale deformation of volcanic centres in the central Andes, *Nature*, *418*, 167–171.

Rançon, J.-P., P. Lerebour, and T. Auge (1989), The Grand-Brulé exploration drilling: New data on the deep framework of the Piton de la Fournaise volcano. Part 1: Lithostratigraphic units and volcanostructural implications, *J. Volcanol. Geotherm. Res.*, *36*, 113–127.

Ryan, M. P., J. Y. K. Blevins, A. T. Okamura, and R. Y. Koyanagi (1983), Magma reservoir subsidence mechanics: Theoretical summary and application to Kilauea Volcano, Hawaii, *J. Geophys. Res.*, *88*, 4147–4181.

Sambridge, M. (1999a), Geophysical inversion with a neighbourhood algorithm: I. Searching a parameter space, *Geophys. J. Int.*, *138*, 479–494.

Sambridge, M. (1999b), Geophysical inversion with a neighbourhood algorithm: II. Appraising the ensemble, *Geophys. J. Int.*, *138*, 727–746.

Sigmundsson, F., P. Durand, and D. Massonnet (1999), Opening of an eruptive fissure and seaward displacement at Piton de la Fournaise Volcano measured by RADARSAT satellite radar interferometry, *Geophys. Res. Lett.*, *26*, 533–536.

Staudacher, T., N. Villeneuve, J.-L. Cheminée, K. Aki, J. Battaglia, P. Catherine, V. Ferrazzini, and P. Kowalski (2000), Piton de la Fournaise, *Bull. Global Volcanism Network*, *25*, 14–16.

Tait, S., C. Jaupart, and S. Vergniolle (1989), Pressure, gas content and eruption periodicity of a shallow crystallising magma chamber, *Earth Planet. Sci. Lett.*, *92*, 107–123.

Tarantola, A. (1987), *Inverse Problem Theory*, Elsevier, New York.

Villeneuve, N. (2000), Apports multi-sources à une meilleure compréhension de la mise en place des coulées de lave et des risques associés au Piton de la Fournaise, thèse de doctorat, Inst. de Phys. du Globe de Paris, Paris, France.

Wright, T. J., Z. Lu, and C. Wicks (2003), Source model for the M_w 6.7, 23 October 2002, Nenana Mountain Earthquake (Alaska) from InSAR, *Geophys. Res. Lett.*, *30*(18), 1974, doi:10.1029/2003GL018014.

Yoder, H. S. (1976), *Generation of Basaltic Magma*, Natl. Acad. Sci., Washington, D. C.

V. Cayol and Y. Fukushima, Laboratoire Magmas et Volcans, Université Blaise Pascal, CNRS UMR 6524, 5 rue Kessler, F-63038 Clermont-Ferrand, France. (valerie.cayol@opgc.univ-bpclermont.fr; yofukushima@opgc.univ-bpclermont.fr)

P. Durand, Centre National d'Etudes Spatiales, 18 Avenue E. Belin, F-31055 Toulouse, France. (philippe.durand@cnes.fr)

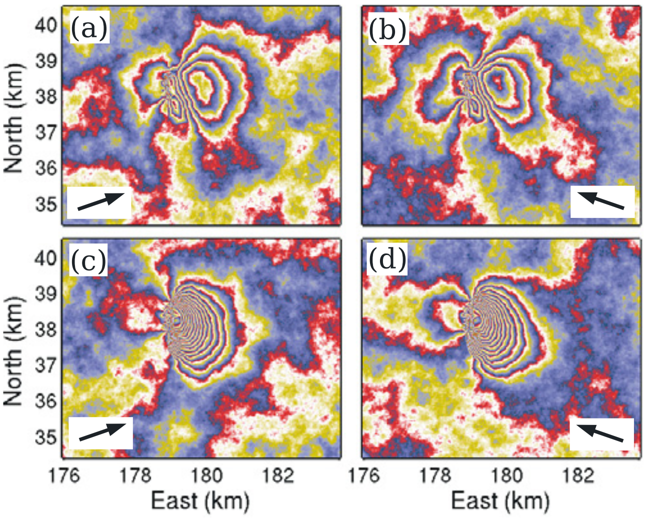

Figure 7. Synthetic data sets created by superposing exponential-type noise to modeled line-of-sight displacements caused by our test model. One shading cycle of black-gray-white corresponds to a displacement of 2.83 cm toward the satellite. Same line-of-sight directions as the actual InSAR data were assumed. Four data sets correspond to (a) F2N and (b) F4F (ascending) and (c) F3N and (d) F5F (descending) orbits. Arrows indicate the surface projection of the line-of-sight directions. See Table 3 for the line-of-sight vectors.

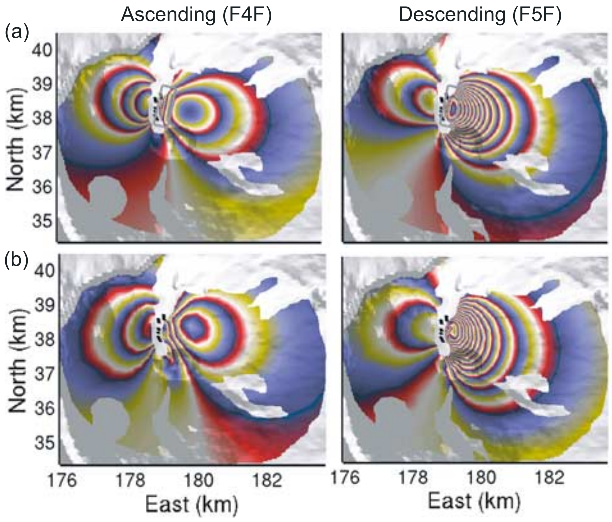

Figure 16. Rewrapped maximum PPD displacements modeled using (a) Okada's equations and (b) the mixed BEM with a flat ground surface, in an ascending (F4F) and a descending (F5F) directions. Gray rectangle line in Figure 16a indicates the projected model geometry. A set of small Okada-type segments with different opening values would create similar displacements as those shown in Figure 16b.

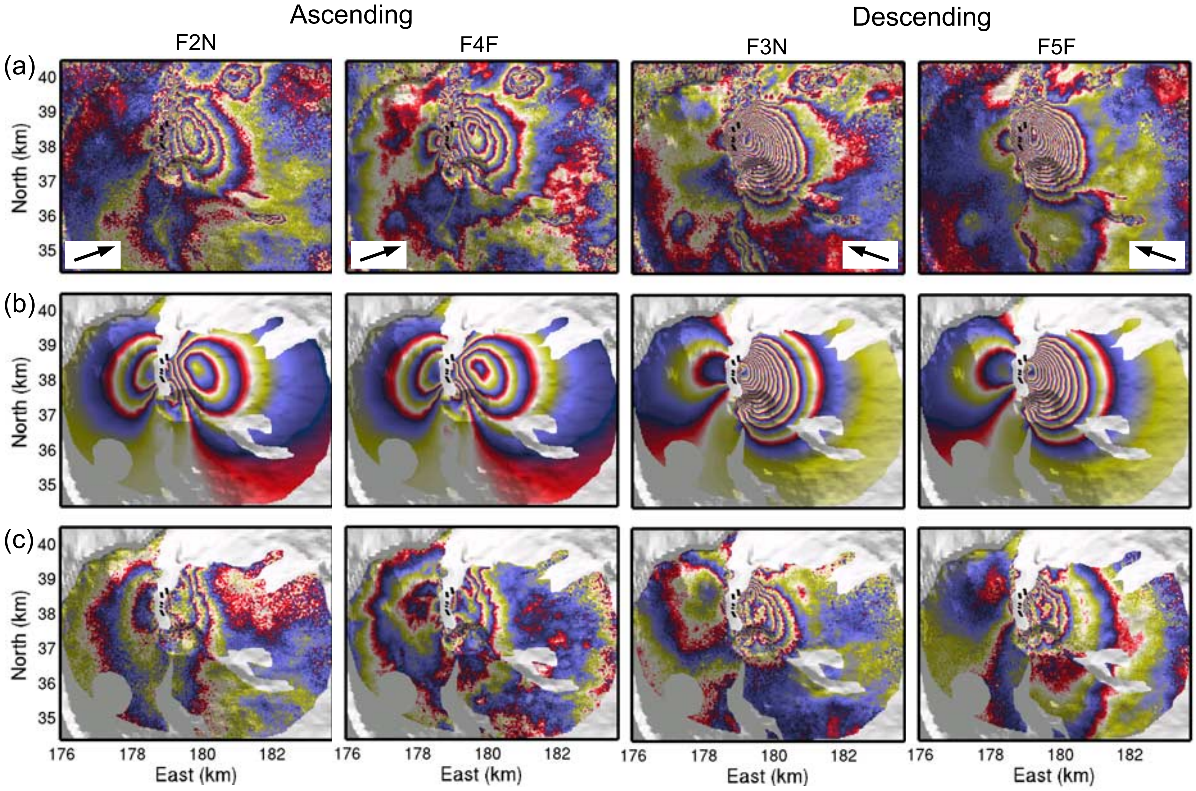

Figure 12. (a) Four interferograms indicating the ground displacements caused by the dike intrusion associated with the February 2000 eruption, superimposed on a DEM. Refer to the caption of Figure 7 for the meanings of gray scale shading and arrows and to Table 3 for data acquisition information. (b) Rewrapped modeled displacements for the four line-of-sight directions corresponding to the maximum PPD model. Recent lava flow areas not used in the misfit evaluation are masked out. (c) Residual displacements between observed and modeled data.

2.4 Supplements

2.4.1 Estimation of noise characteristics

The misfit function used in the method assumes that the noise in InSAR data is random and correlated (Section 2.3.2). Correlated random sequences are characterized by the autocorrelation function (ACF), which is defined as [e.g. *Sato and Fehler*, 1998]

$$C(r) = \langle u(\mathbf{x})u(\mathbf{x}+\mathbf{r})\rangle, \tag{2.1}$$

where $\langle ... \rangle$ denotes an ensemble average, $u(\mathbf{x})$ is the noise displacement at position $\mathbf{x}$, $\mathbf{r}$ is a vector having an amplitude r. For a one-dimensional profile with a regular grid interval $\{u(0), u(1), ..., u(N)\}$, the ACF can be calculated as

$$C_1(l) = \frac{1}{N-l}\sum_{k=0}^{N-1-l} u(k)u(k+l), \qquad \{l = 0, 1, 2, ..., N\} \tag{2.2}$$

and for a grid interval of dl,

$$C(r) = C(ldl) = C_1(l). \tag{2.3}$$

In Section 2.3.2, Equations 2.2 and 2.3 were applied, with a slight modification so that masked area is not taken into account in the calculation, on several profiles of rows and colums of the four InSAR noise data sets of the February 2000 eruption (Figure 2.9). The ACFs were averaged and approximated by an exponential curve to characterize the noise by its variance and correlation distance (Equation 5 and Figure 6 in Section 2.3.2).

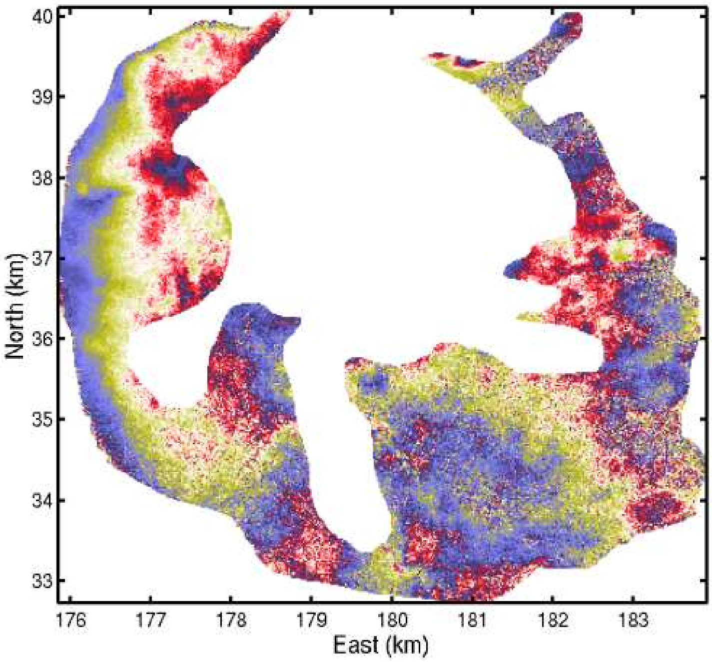

Figure 2.9: Example of an InSAR noise data set showing the range change caused mainly by the atmospheric perturbation in a period including the February 2000 eruption. The area affected by the eruption is masked and not used in the calculation of the ACF.

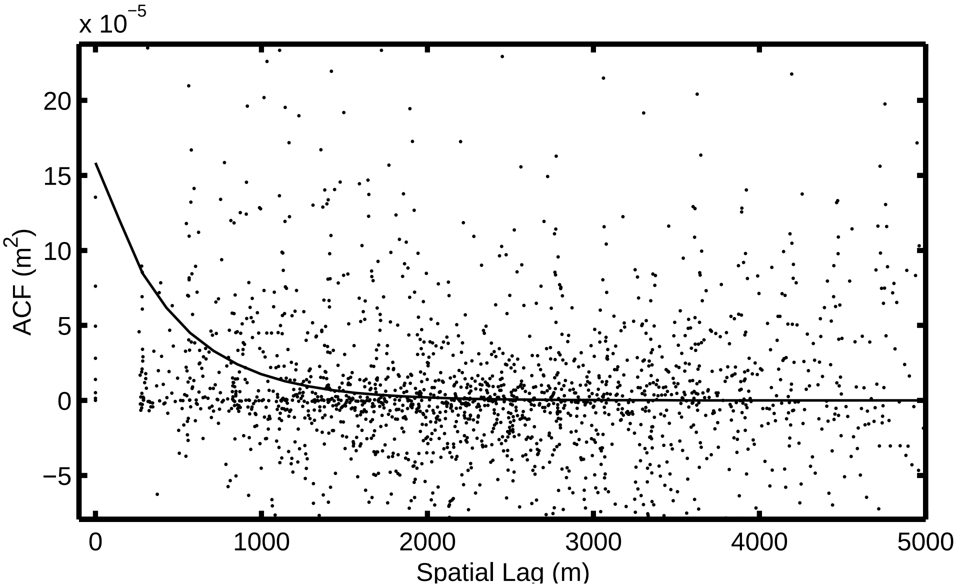

Figure 2.10: Example showing the calculation of the autocorrelation function for a heterogeneous data point set. The product of the noise amplitudes of two points is plotted against the distance for every combination of subsampled data points, and fitted by an exponential curve (Equation 5 in Section 2.3.2) in a least-square manner.

The interferometric data for the other eruptions analyzed in Chapter 3 do not contain enough data points corresponding to undeformed areas, because of fewer interferograms available (only one for the March 1998, July and September 1999 eruptions) or of a large deformed area (the June 2000 eruption). Therefore, a different strategy is taken. First, a search (first stage of the inversion) is made by assuming a plausible value of the noise correlation distance. Then, by assuming that the residual data are randomly correlated and follow the exponential-type ACF, the variance and correlation distance of the residual data are calculated. This calculation can be made in such a way that the product of the residual amplitudes of two points is plotted against the distance for every combination of subsampled data points, and fitted by an exponential curve in a least-square manner (Figure 2.10). If the estimated correlation distance of the residual data is not different from the value assumed in the misfit function more than 30%, then the search result is considered appropriate, and an appraisal (second stage of the inversion) is performed. Indeed, Section 2.3.5 showed that a difference in the correlation distance of 35% did not lead to a significantly different result. If the deviation is larger, another search is made using the estimated correlation distance.

The noise variance assumed does not affect the search of the maximum probability model (Section 2.3.4), but it affects the appraisal. Thus, for the appraisal stage, the misfit values obtained in the search stage is scaled by the variance estimated from the residual data.

2.4.2 Topography effect

Figure 2.11 complements the discussion in Section 2.3.5 on the importance of taking realistic topography into account. The figure compares the geometry of the maximum probability model obtained assuming realistic topography (transparent) with those obtained assuming half-space

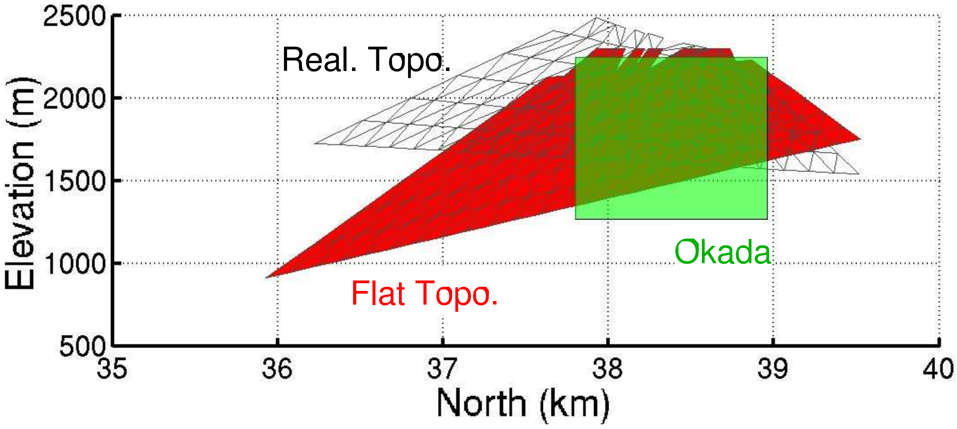

Figure 2.11: North-south cross-sectional view of the geometries of the maximum probability models obtained assuming realistic topography (transparent) and half space (red: mixed BEM, green: Okada's model).

(red: mixed BEM, green: Okada's model [*Okada*, 1985]; see Section 2.3.5 for details). As discussed, Okada-type models tend to predict a realistic geometry close to the ground but poorly predict the geometry at depth. The flat topography model obtained using the mixed BEM has a similar trapezoidal geometry as that obtained assuming realistic topography, however, the southern end of the bottom side is located at twice the depth of that of the realistic topography model. These differences as well as the opening or overpressure differences mentioned in Section 2.3.5 show that, at Piton de la Fournaise, the half-space assumption may lead to an imprecise estimation of dike geometries and overpressures and hence to an erroneous interpretation.

2.4.3 Recursive unwrapping algorithm

Unwrapping of interferograms having narrow fringes associated with large displacement gradients does not often produce the expected amount of displacements in a single calculation (Figure 2.12). To overcome this problem, this study makes a recursive unwrapping (Section 2.3.4). This recursive unwrapping algorithm is reexplained in Figure 2.13, by showing the products created in an iteration.

The key point of the algorithm is that the low-pass filtered unwrapped data (which include unsuccessfully unwrapped phase) somewhat mimic the “true” displacements. By taking the residual of the input phase and the rewrapped phase of the low-pass filtered unwrapped data, we obtain broader fringes compared to the input interferogram, which enables a proper unwrapping. The cutoff wavenumber starts from a large value (corresponding to wavelength of typically 500 m), then successively lowered as the iteration proceeds. The iteration finishes when the mean of the unwrapped residual phase (Figure 2.13e) does not become smaller than that of the preceding iteration.

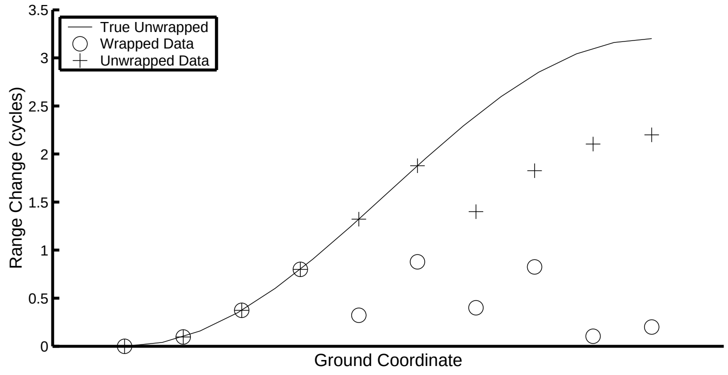

Figure 2.12: Schematic figure showing an example of unsuccessful unwrapping. Wrapped input data corresponding to a large displacement gradient may not be properly unwrapped. As a consequence, the unwrapped data corresponding to the area having larger displacements than that of the improper unwrapping point have an offset compared with the true unwrapped data.

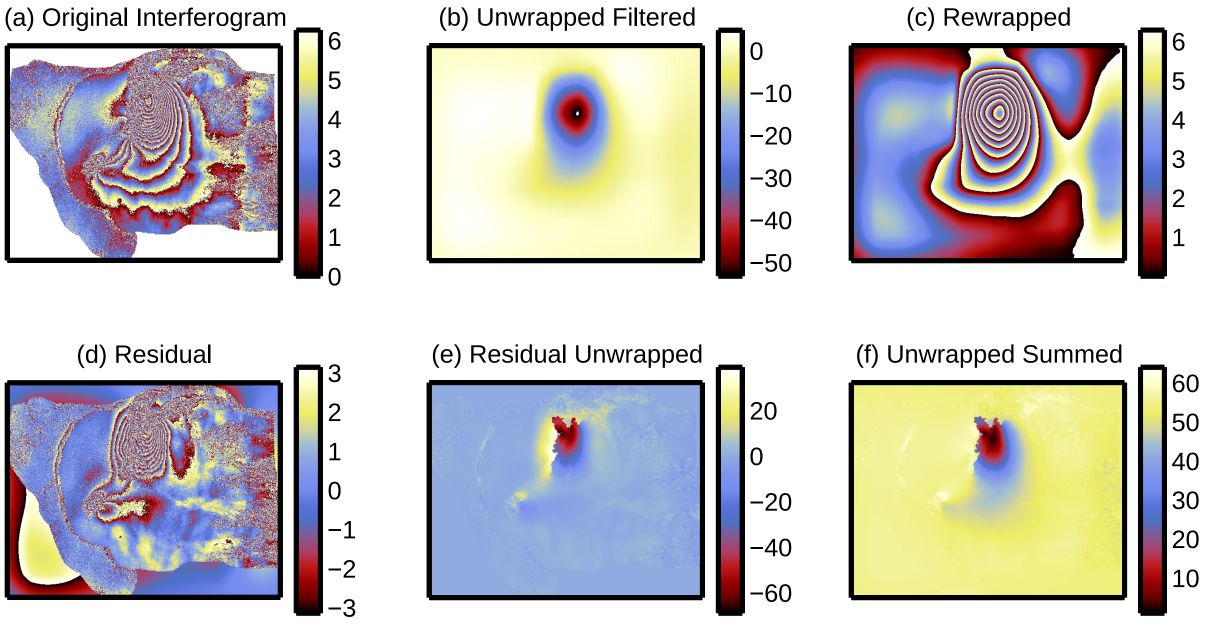

Figure 2.13: Products in an iteration of the recursive unwrapping algorithm, with an example of the March 1998 interferogram. Scales are given in radian. (a) The original interferogram (phase) to be unwrapped. (b) The unwrapped phase of the preceding iteration (corresponding to (f)) is low-pass filtered with a smaller cutoff wavenumber than that of the preceding iteration. (c) The filtered unwrapped phase (b) is rewrapped. (d) The residual phase of the original phase (a) and the rewrapped phase (c) is calculated. (e) The residual phase (d) is unwrapped. (f) The filtered unwrapped phase of the preceding iteration (b) is summed to the unwrapped residual phase (e).

Chapter 3

Dike Models for the Eruptions 1998–2000

The method developed in the previous section is applied to the five consecutive eruptions that occurred between March 1998 and June 2000 (refer to Table 2 in Section 2.3.4 for the eruption periods, locations and volumes of the eruptions). The first section introduces the interferograms used in this study. In the second section, the basic analysis strategy is given. The following sections present an eruption overview, explanation of different sources of signals, and analysis settings and results for each eruption. The eruption overviews are based on the reports to Bulletin of Global Volcanism Network from the Observatoire Volcanologique du Piton de la Fournaise [*Staudacher and Cheminée*, 1999; *Staudacher et al.*, 1998, 1999, 2000] and *Villeneuve* [2000]. Procedures specific to application of each eruption are explained in the text. The final section summarizes the results obtained for the five eruptions.

3.1 Data

3.1.1 Processing and selection of data

The displacements associated with the five eruptions that occured between March 1998 and June 2000 have been recorded by RADARSAT-1, a Canadian C-band (wavelength 5.7 cm) satellite. This satellite has several view angles with 24 days of repeat time. From the images recorded in fine mode, a total of 18 ascending and descending interferograms were computed by Philippe Durand (CNES; Centre National d'Etudes Spatiales). The DIAPASON software developed by CNES was used for the computation. Topographic fringes were subtracted using a $20\,\mathrm{m} \times 20\,\mathrm{m}$ digital elevation map (DEM) provided by French Institut Géographique National. This DEM was originally created from a $100\,\mathrm{m} \times 100\,\mathrm{m}$ DEM of about two meters of precision.

Figures 3.1–3.5 show the ten interferograms that will be modelled in this chapter (Table 3.1). The interferograms have a good coherence in areas covered by old lava flows within Enclos Fouqué caldera. The eastern part in the caldera (Grandes Pentes and Grand Brulé; see Figure 1.3) is largely covered by vegetation, which prevents us from obtaining meaningful signals in this area. One descending interferogram is used for the March 1998 (Figure 3.1), July 1999 (Figure 3.2) and September 1999 (Figure 3.3) eruptions; four interferograms, two from ascending and two from descending orbits, are used for the February 2000 eruption (Figure 3.4); two ascending and one descending interferograms are used for the June 2000 eruption (Figure 3.5). The interferograms are unwrapped and converted to line-of-sight displacements (Section 2.3.4) to compare with the model expectations. Inspite of the risk of unwrapping explained in Section 1.2.3, unwrapping allows to define a misfit function with a physically-

Table 3.1: Interferograms used in this study

Eruption	Orbit*	Period (DD.MM.YY)	Line-of-Sight Vector [East, North, Up]	Incidence Angle (°)	Altitude of Ambiguity (m)
March 1998	F5F (D)	30.04.97 – 30.07.98	[0.70, -0.19, 0.69]	47.1	348.0
July 1999	F5F (D)	01.04.98 – 11.09.99	[0.70, -0.19, 0.69]	46.8	40.1
Sept. 1999	F5F (D)	11.09.99 – 16.12.99	[0.70, -0.19, 0.69]	46.7	-162.6
Feb. 2000	F2N (A)	07.02.00 – 13.05.00	[-0.63, -0.17, 0.76]	40.7	-272.9
	F4F (A)	14.12.99 – 19.03.00	[-0.69, -0.19, 0.70]	45.7	-130.4
	F3N (D)	22.10.99 – 25.05.00	[0.64, -0.17, 0.75]	41.8	-88.0
	F5F (D)	16.12.99 – 01.06.00	[0.70, -0.19, 0.69]	46.8	494.1
June 2000	F2N (A)	13.05.00 – 30.06.00	[-0.63, -0.17, 0.76]	40.7	-190.4
	F4F (A)	19.03.00 – 03.09.00	[-0.69, -0.19, 0.70]	45.8	-55.2
	F5F (D)	08.05.00 – 25.06.00	[0.70, -0.19, 0.69]	46.6	53.8

*A: Ascending orbit, D: Descending orbit.

meaningful quantity, i.e., displacements (Equation 3 in Section 2.3.2), which enables relating the misfit function to probability (Equation 6 in Section 2.3.2). Explanations of different sources of signals in the interferograms are given in the following sections.

Besides the interferograms used in the inversions, Figure 3.6 shows an interferogram covering the periods of the March 1998, July and September 1999 eruptions. These eruptions originated from three different eruptive fissure locations, i.e., north and southwest (March 1998), summit (July 1999) and south (September 1999), and created a broad eastward (seaward) displaced area as if it were caused by a single long dike. As discussed by *Sigmundsson et al.* [1999], accumulation of such eastward displacements would facilitate seaward landslides such as those recurrently occurred on this volcano [e.g. *Bachèlery*, 1995; *Duffield et al.*, 1982; *Labazuy*, 1996; *Lénat et al.*, 2001; *Merle and Lénat*, 2003; *Oehler et al.*, 2004]. The effect of displacements accumulated between March 1998 and June 2000 will be discussed in Section 4.3.1.

The eruptions occurred in a spatially-periodic manner, with eruptive fissures opening successively on the northern flank (March 1998), at the summit (July 1999), on the southern flank (Sept. 1999), again on the northern flank (Feb. 2000), and then on the southeastern flank (June 2000). The reason for the spatial periodicity will be examined by stress change analyses (Section 4.3.2).

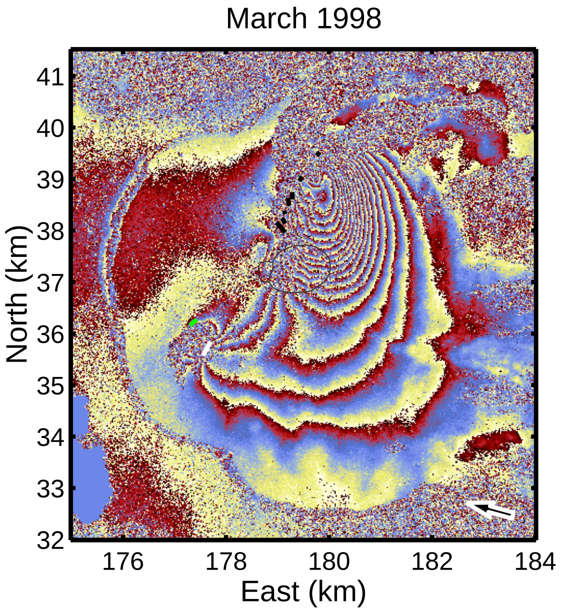

Figure 3.1: Interferogram showing the ground displacements associated with the March 1998 eruption. One color cycle of blue-red-yellow corresponds to a displacement of 2.83 cm toward the satellite. The arrow indicates the surface projection of the line-of-sight direction of the satellite. Refer to Table 3.1 for information on the interferogram. Dolomieu and Bory craters are outlined. Black thick lines on the northern flank indicate the position of the eruptive fissures drawn after Villeneuve [2000]. The white line is the position of the southwestern eruptive fissure assumed for inversions, whereas green line indicates the position of the eruptive fissure measured by the observatory. Interpretation of the signals visible in this interferogram are given in Figure 3.14.

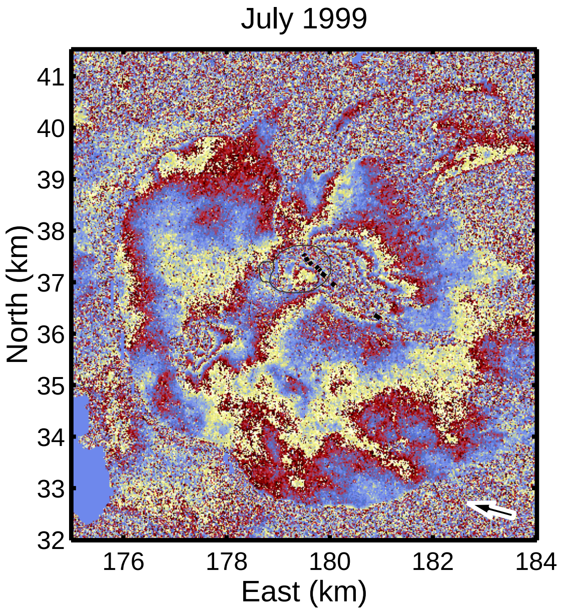

Figure 3.2: Interferogram showing the ground displacements associated with the July 1999 eruption. See caption of Figure 3.1 for meanings of the color, curves and lines. Interpretation of signals are given in Figure 3.24.

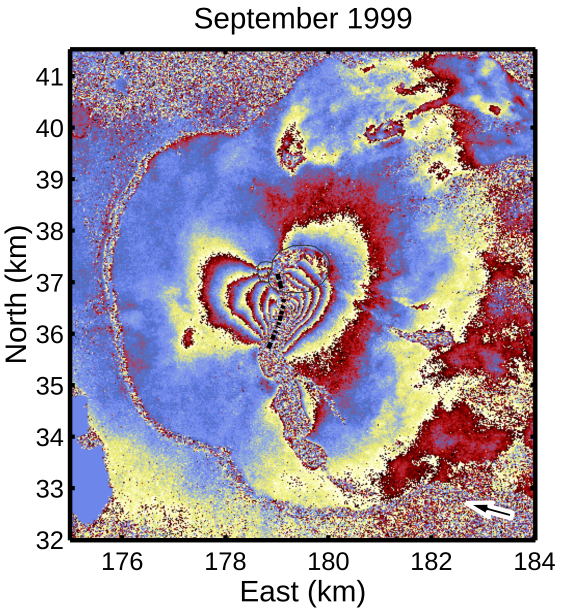

Figure 3.3: Interferogram showing the ground displacements associated with the September 1999 eruption. See caption of Figure 3.1 for meanings of the color, curves and lines. Interpretation of signals are given in Figure 3.27.

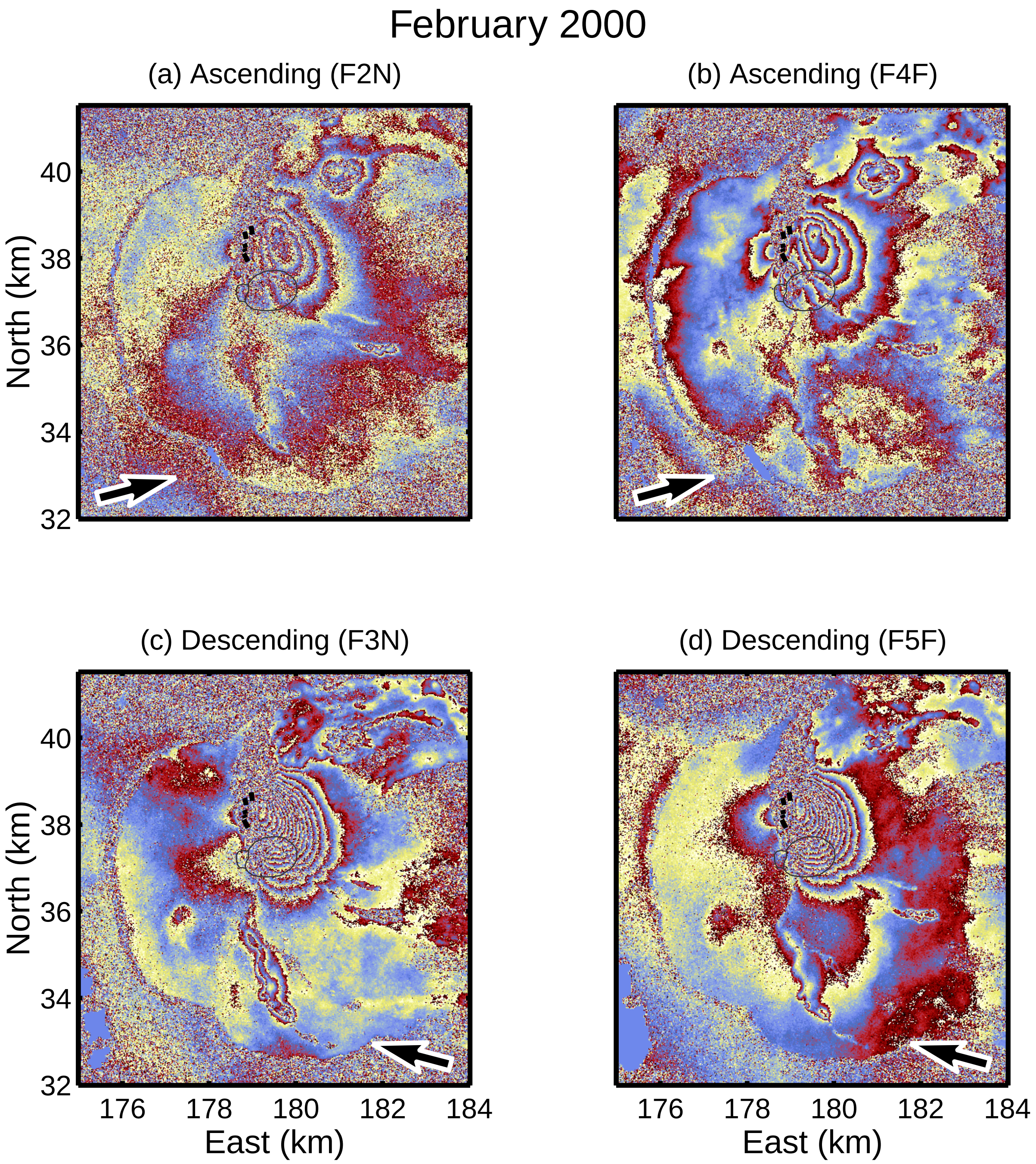

Figure 3.4: Interferograms showing the ground displacements associated with the February 2000 eruption. (a) Ascending direction (F2N orbit). (b) Ascending direction (F4F orbit). (c) Descending direction (F3N orbit). (d) Descending direction (F5F orbit). See caption of Figure 3.1 for meanings of the color, curves and lines.

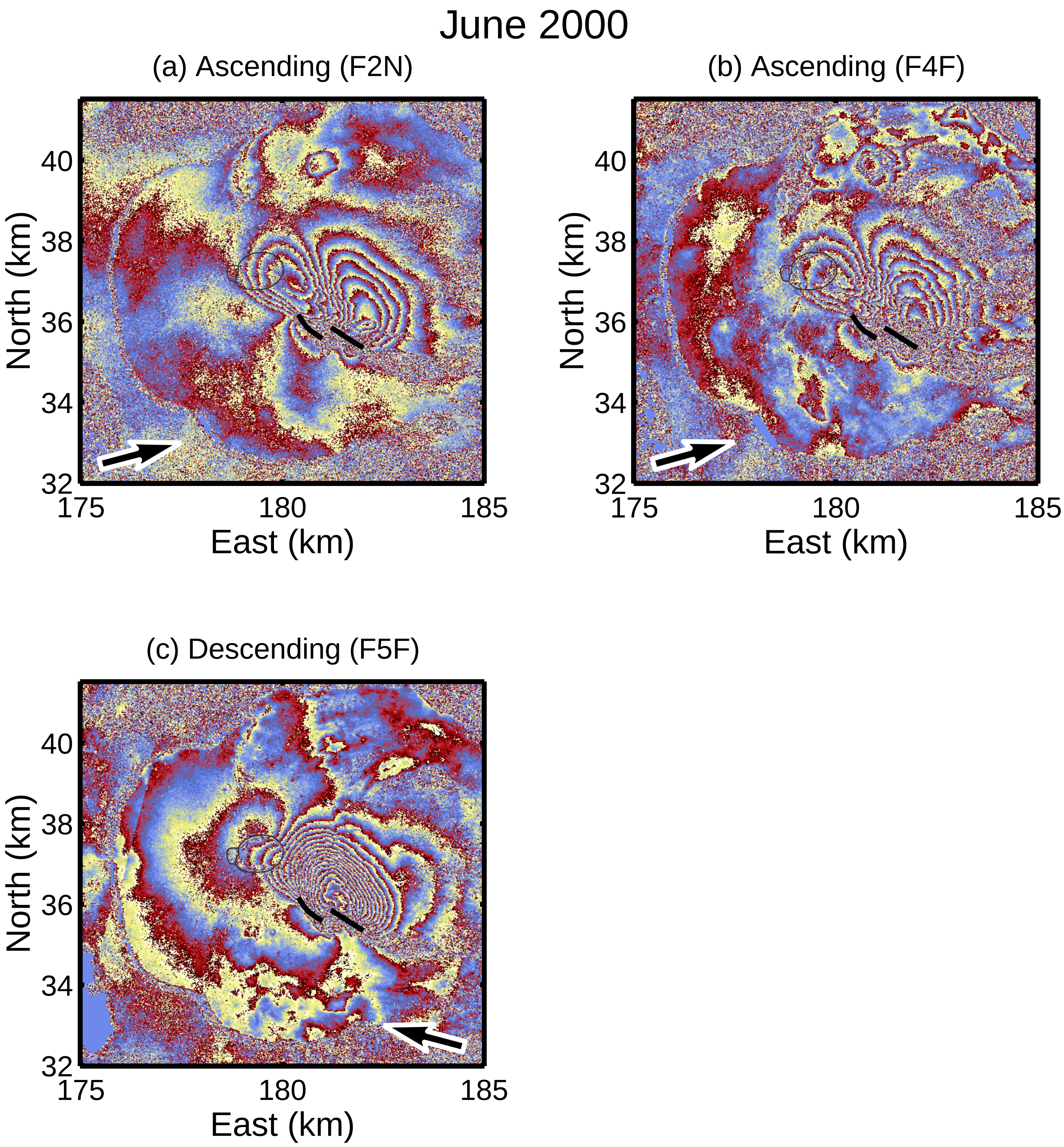

Figure 3.5: Interferograms showing the ground displacements associated with the June 2000 eruption. (a) Ascending direction (F2N orbit). (b) Ascending direction (F4F orbit). (c) Descending direction (F5F orbit). Interpretation of signals are given in Figure 3.32. See caption of Figure 3.1 for meanings of the color, curves and lines.

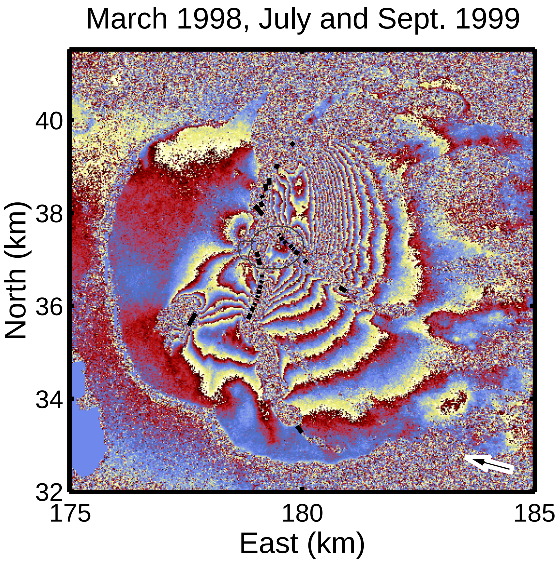

Figure 3.6: Interferogram for a time period covering the March 1998, July and September 1999 eruptions.

3.1.2 Removing altitude-correlated fringes

The descending interferogram of the June 2000 eruption (Figure 3.5c) includes some altitude-correlated fringes. Since a pressure source beneath the summit would create displacements uncorrelated with the altitude (because of the oblique line-of-sight direction; *Beauducel et al.* [2000a], see also Figure 4.1), these altitude-correlated fringes are probably created by different atmospheric stratification for the two days of image acquisition [*Beauducel et al.*, 2000a; *Hanssen*, 2001]. These fringes are removed in such a way that the number of altitude-correlated fringes becomes minimum. This correction is done on the interferogram, i.e., before unwrapping the phase.

To explain the algorithm, let us first concentrate on pixels that correspond to a certain altitude range, say, between 2000 and 2200 m (Figure 3.7a). The pixels contain phase values $\phi = (\phi(1), \phi(2), ...)$ correlated with the altitude $\phi_{alt} = (\phi_{alt}(1), \phi_{alt}(2), ...)$ and uncorrelated with the altitude $\phi_{other} = (\phi_{other}(1), \phi_{other}(2), ...)$; that is, for the k-th pixel,

$$\phi(k) = \phi_{alt}(k) + \phi_{other}(k). \tag{3.1}$$

Note that $\phi(k)$, $\phi_{alt}(k)$, and $\phi_{other}(k)$ take values between 0 and 2π. The histogram of ϕ shows no preferred phase value (Figure 3.7b).

Next, we assume a model such that, in the considered altitude range, the unwrapped phase of the altitude-correlated component is linearly correlated with the altitude:

$$p^m_{alt}(k) = a(z(k) - z_1), \tag{3.2}$$

where a is a constant, $z(k)$ is the altitude corresponding to the k-th pixel, z_1 is the minimum bound of the considered altitude range (2000 m in our example). The wrapped phase value corresponding to $p^m_{alt}(k)$ is,

$$\begin{aligned} \phi^m_{alt}(k) &= mod\,[p^m_{alt}(k),\, 2\pi] \\ &= mod\,[a(z(k) - z_1), 2\pi], \end{aligned} \tag{3.3}$$

where $mod\,[..., 2\pi]$ denotes modulo 2π.

The residual phase between the observed value and that asssuming a linear dependency of the unwrapped phase to the altitude is

$$\begin{aligned} \Delta\phi(k) &= \phi(k) - \phi^m_{alt}(k) \\ &= \phi(k) - mod\,[a(z(k) - z_1),\, 2\pi] \\ &= mod\,[\phi_{alt}(k) - a(z(k) - z_1),\, 2\pi] + \phi_{other}(k). \end{aligned} \tag{3.4}$$

To remove the altitude-correlated component, we determine the coefficient a that makes the first term of Equation 3.4 close to constant over considered pixels (Figure 3.7c). Under the assumption that ϕ_{other} has a uniform distribution of phase values between 0 and 2π, the optimum value for a gives a phase distribution of $\Delta\phi$ peaked at a certain phase value (Figure 3.7d). Inversely, the optimum value for a can be estimated in such a way that the maximum frequency of the histogram of $\Delta\phi$ becomes the largest. As the algorithm of this optimisation problem, the downhill simplex method [e.g. *Nelder and Mead*, 1965; *Press et al.*, 1992] is used, with multiple initial values to avoid being caught in a local minimum.

To remove the altitude-correlated fringes in the whole area of interest, we simply perform the optimisation at different ranges of altitudes. For the application to the June 2000 interferogram, only the area having clear altitude-correlated phases was used in the calculation (Figure

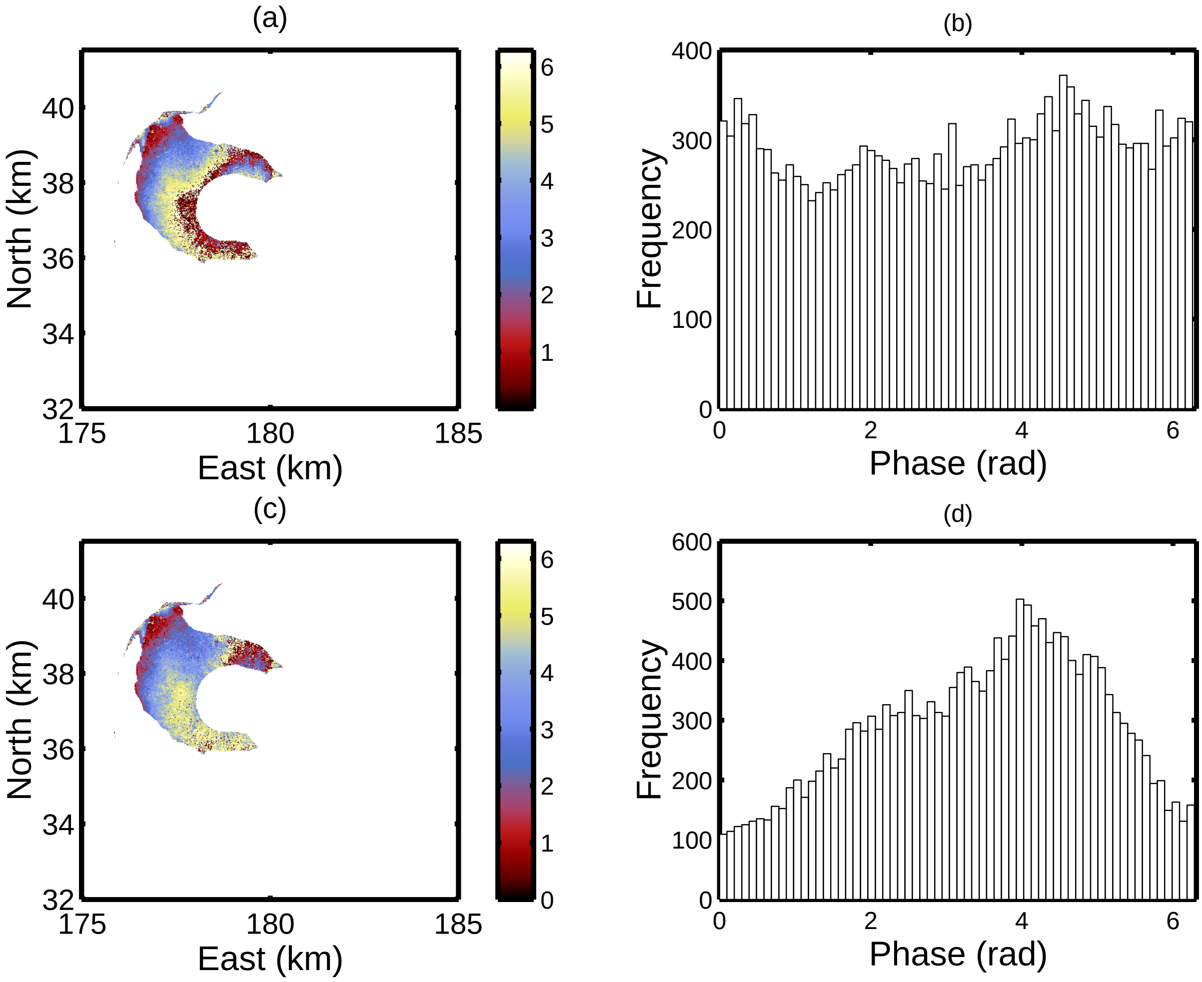

Figure 3.7: Example showing the algorithm of removing altitude-correlated fringes. (a) Original interferogram (phase values). Only the pixels corresponding to altitudes between 2000 and 2200 m are shown. (b) Histogram of the phase values shown in (a). In this example, the phase range 0 to 2π is divided into 64 boxes. The distribution is close to uniform. (c) Residual phase values where altitude-correlated phase values are subtracted from (a) (Equation 3.4 for an optimised a; see text for explanation). (d) Histogram of the phase values shown in (c). Since the altitude-correlated component is removed, the histogram shows a single peak.

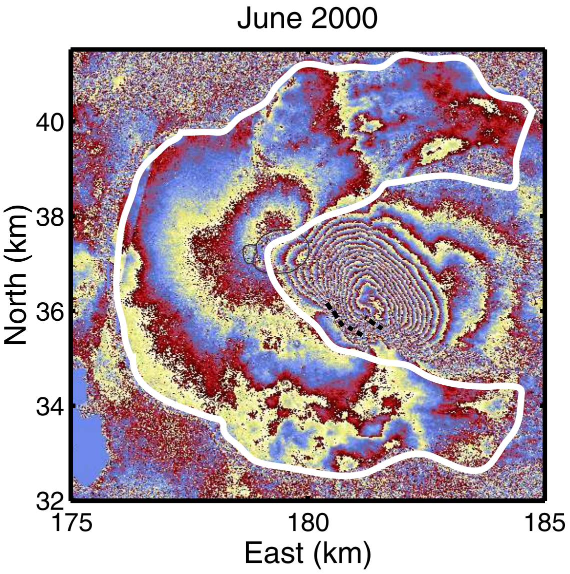

Figure 3.8: Enclosed area is used in the calculation of altitude–unwrapped phase relationship.

3.8), though the algorithm could be applied to areas containing phases uncorrelated with the altitude (we may want to do this when the area having enhanced altitude-correlated phases is not sufficiently large to give reliable estimates). After trials and errors, the phase width of the histogram boxes is set to $2\pi/256$, and the optimisation is performed at several ranges of altitude having an interval of 200 m. Once the altitude–unwrapped phase profile is obtained for the whole altitude range of interest, the curve is smoothed by taking a moving average (Figure 3.9). Then the altitude-correlated phases in the original interferogram can be removed by creating a synthetic altitude-correlated interferogram based on the smoothed altitude–unwrapped phase relationship (Figure 3.10), and subtracting it from the original interferogram.

By comparing with the original interferogram (Figure 3.8), we notice that the corrected interferogram (Figure 3.11) no longer contains the wide fringes around the central cone. In addition, the displacements south of the eruptive fissures in the corrected interferogram, which are associated with the dike intrusion, seem to be mechanically more plausible. This further confirms that the altitude-correlated fringes were atmospheric artifacts.

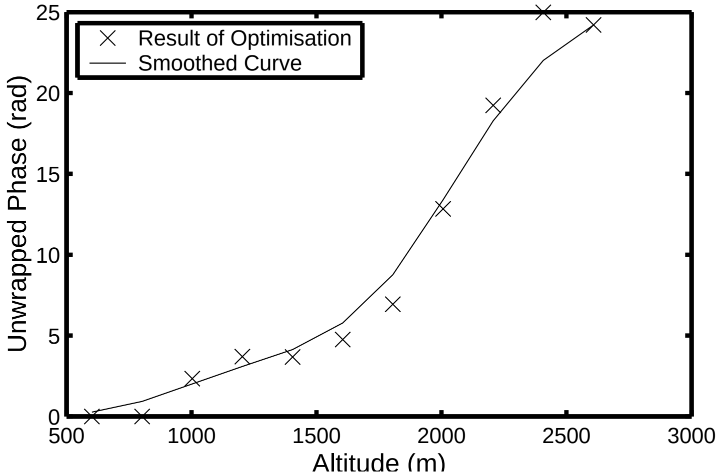

Figure 3.9: Estimated altitude–unwrapped phase relationship that best represents the altitude-correlated phases in the descending interferogram of the June 2000 eruption (Figure 3.8).

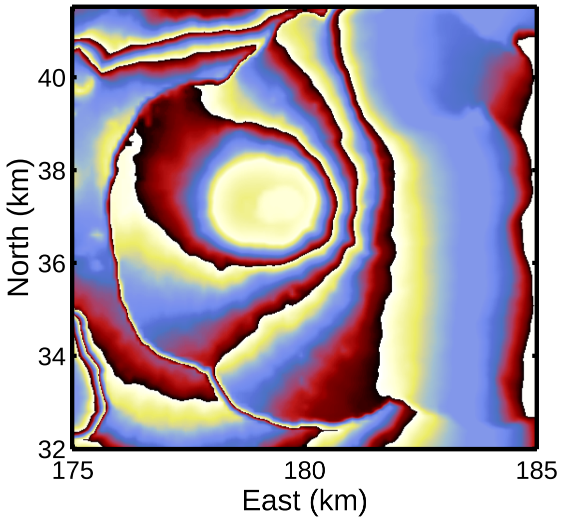

Figure 3.10: Synthetic interferogram created assuming the altitude–unwrapped phase relationship of Figure 3.9. This interferogram is subtracted from the original interferogram (Figure 3.8) to remove the altitude-correlated phases.

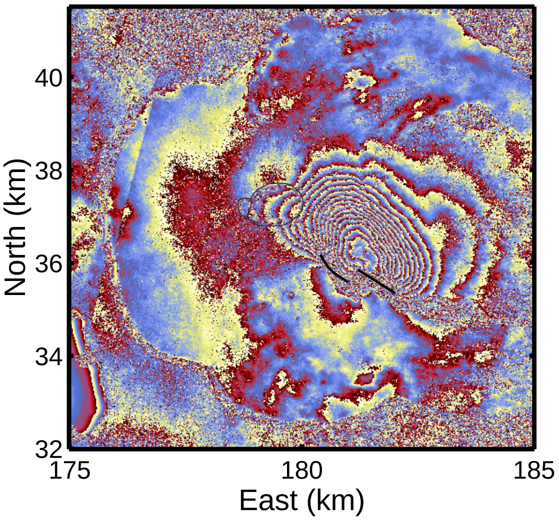

Figure 3.11: Interferogram corrected for the altitude-correlated noise fringes in the original interferogram (Figure 3.8).

3.2 Analysis Strategy

3.2.1 Treating several pressure sources

The complex coeruptive displacements of the March 1998, July 1999 and June 2000 eruptions may be due to presence of several pressure sources. Inverting for two or more pressure sources from a data set calls for special care.

When the pressure sources are far from each other (a rule of thumb is more than three times the characteristic size of the source), then the interaction between the sources is negligible and the displacements around a source are not much affected by the other sources. In such a case, an appropriate strategy is first to invert for one source using data surrounding it and then to invert for other ones using the residual data (Figure 3.12a).

When two dikes are spatially close to each other, but when their emplacements are temporarily separated so that the first dike is solidified before the emplacement of the second one, then the interaction between the sources is again negligible. However, interferograms covering the whole period of dike emplacements contain signals created by the two sources. An appropriate strategy for this case is to invert for the sources by superposing the displacements associated with boundary element models corresponding to each source (Figure 3.12b).

When the pressure sources are close to each other and when the second source is emplaced before the first one solidifies, then the mechanical interaction between the sources has a significant effect. In this case, inversion should be performed by taking into account the several sources in a single boundary element model (Figure 3.12c).

The first case allows a relatively large number of source model parameters. The latter two require, in the problems of this study, either reducing the number of parameters or decreasing the number of models n evaluated in each iteration (Section 2.3.2) so that the search is more exploitative rather than explorative; otherwise the solution would take too much time to converge. Decreasing n increases the risk for the solution to be caught in a local minimum.

Because the computation time largely depends on the misfit function structure, there is no systematic relation between the time required for an inversion and the number of parameters or the number of models evaluated in each iteration n. Typically, for the problems considered in the present study, an eight-parameter inversion with a sufficient number of models evaluated in each iteration ($n = 50$, see Section 2.3.3) converges in an acceptable time of several days on Linux computers with a processor of 1 GHz.

3.2.2 Percentage of explained data

The misfit function used in inversions (Equation (3) in Section 2.3.2) do not give a direct indication of data fit because it is a function of data noise variance, correlation distance and the residual between observed and modelled data. The percentage of explained data defined as follows gives an intuitive indication of data fit instead:

$$S = \left\{ 1 - \frac{\sum (u_o + l - u_c)^2}{\sum (u_o + l)^2} \right\} \times 100, \tag{3.5}$$

where u_o and u_c are the observed and modelled line-of-sight displacements, l is an offset analytically calculated in such a way that S is minimized, and the sums are taken for the subsampled data points used in inversions. Consideration of the offset is necessary because unwrapped

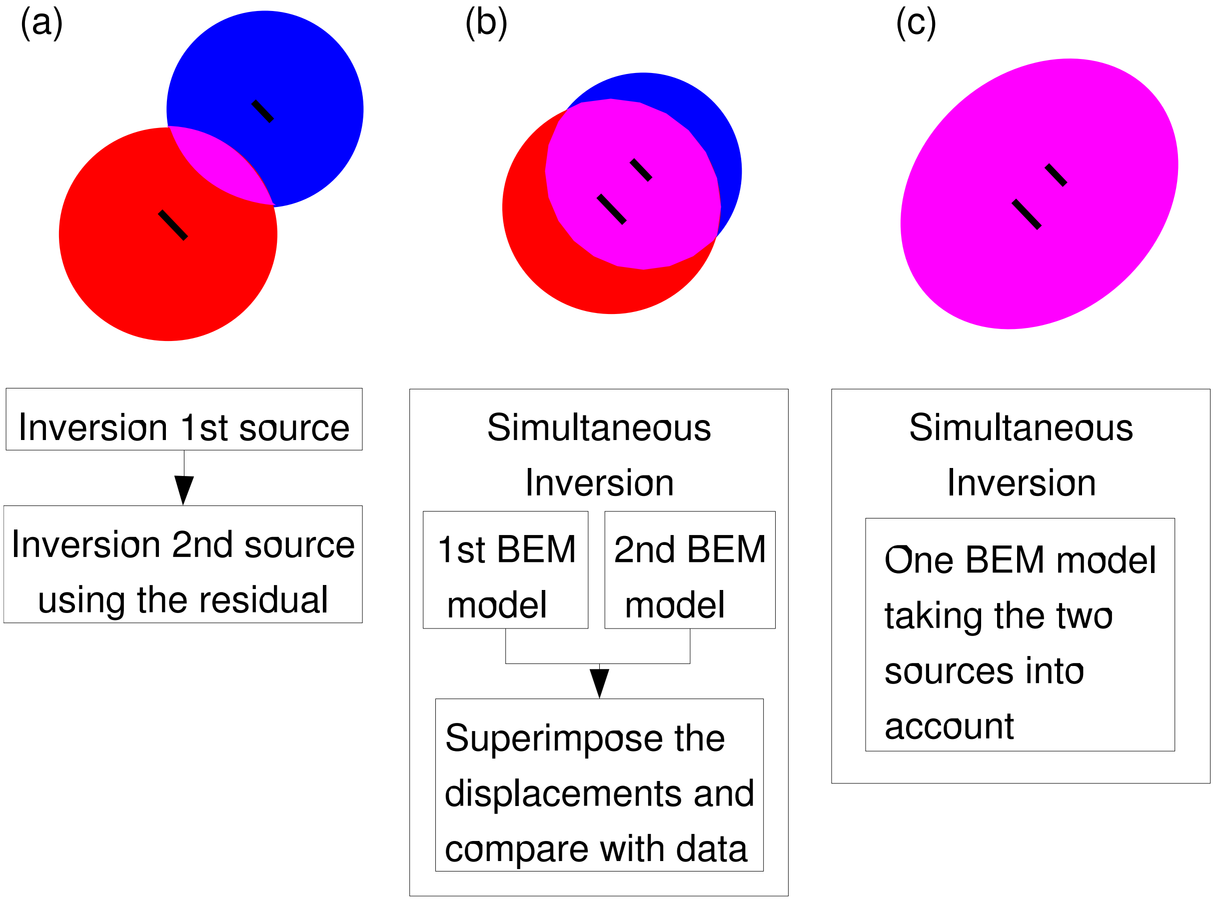

Figure 3.12: (a) When the pressure sources are far from each other, then inversions can be performed one after another. Subsequent inversions use the residual data. (b) When the sources are close to each other but when their formations are temporarily separated, a simultaneous inversion can be performed in such a way that one forward modelling consists of two boundary element computations and superposing the displacements. (c) When the sources are close to each other and when they are simultaneously formed, a simultaneous inversion can be performed in such a way that one forward modelling consists of a single boundary element computation that takes into account all the sources.

displacements contain a constant offset of less than half the radar wavelength. When the percentage of explained data S is small, it means that the model does not appropriately represent the reality and/or that the signal-to-noise ratio is large. It should be noted that two values can be compared only if the same data set is used in inversions.

3.3 March 1998 Eruption

3.3.1 Overview

The March 1998 eruption occurred after an unusually quiet period of five years and a half. Preeruptive microearthquakes, which started 36 hours before the onset of the eruption, clearly migrated from 5 km below sea level toward the summit [*Battaglia et al.*, 2005]. Summit deformation began about an hour before the eruption onset, when the hypocenter of the microearthquakes were located around sea level. The eruption first started from a fissure at 2450 m on the northern flank, then the activity quickly migrated northward to lower altitudes (Figure 3.13). The activity then focused on two fissures near the bottom of the central cone. Two scoria cones formed at the place where lava fountains were most active. One of them, Piton Kapor, continued to erupt until 21 September.

Three days after the northern vent opening, a fissure of about 200 m long opened at the southwestern flank of the volcano (Figure 3.13). The activity quickly localized to a single vent, forming a scoria cone later named Hudson crater; this crater was active for less than 20 days. Geochemical and petrological studies [*Boivin and Bachèlery*, 2003; *Semet et al.*, 2003; *Vlastélic et al.*, 2005] found more primitive lava for this southern eruption site than that for the northern one, indicating different origins of the magmas. The magma from the north had a similar composition to the majority of historical and pre-historical eruptions which involve storage in the edifice, whereas the magma emitted from the south suggests a rapid transfer of magma from depths of more than 15 km [*Semet et al.*, 2003].

In middle August, two fissures opened outside the Enclos Fouqué caldera, emitting degassed lava. The activity at these fissures continued until a few days before the end of Piton Kapor eruption.

3.3.2 Sources of interferometric signals in data

The dike intrusion associated with this eruption caused an asymmetric fringe pattern (Figure 3.14) similar to that of February 2000 (Figure 3.4), except for a few wide fringes that link the northern and southern eruption sites. The maximum displacement toward the satellite amounts to 60 cm east of the northern eruptive fissures, while little displacements of one fringe ($\sim$ 3 cm) are observed on the west side. The wide fringes indicate a deeper intrusion than that associated with the February 2000 eruption. The origin of these fringes will be investigated later in this section. As for the southern eruptive fissure associated with Hudson crater, the location corresponds to the green line on Figure 3.1 according to the observatory (T. Staudacher, personal communication, 2005); however, the data seems to indicate an eruptive fissure about 250 m farther south as indicated by the white line. Thus, the white line is assumed to be the position where the southern dike reaches the ground. One or two fringes between the green and white lines probably result from a superficial intrusion of a small volume of material and are not modelled. Several interferograms spanning later periods show continuous but exponentially

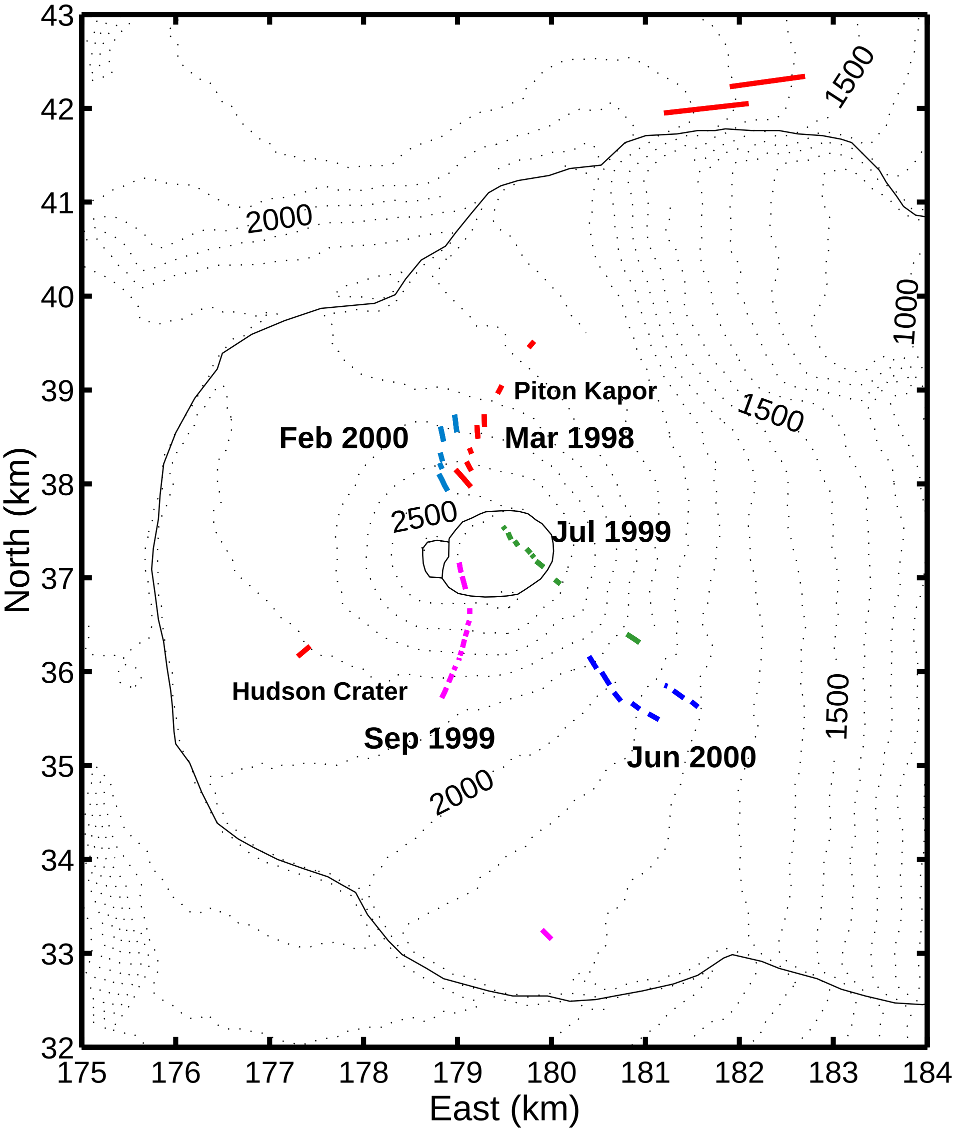

Figure 3.13: Locations of the eruptive fissures for the five eruptions [Villeneuve, 2000]. Contour lines are drawn every 100 meters. Bory, Dolomieu and Enclos Fouqué borders are outlined.

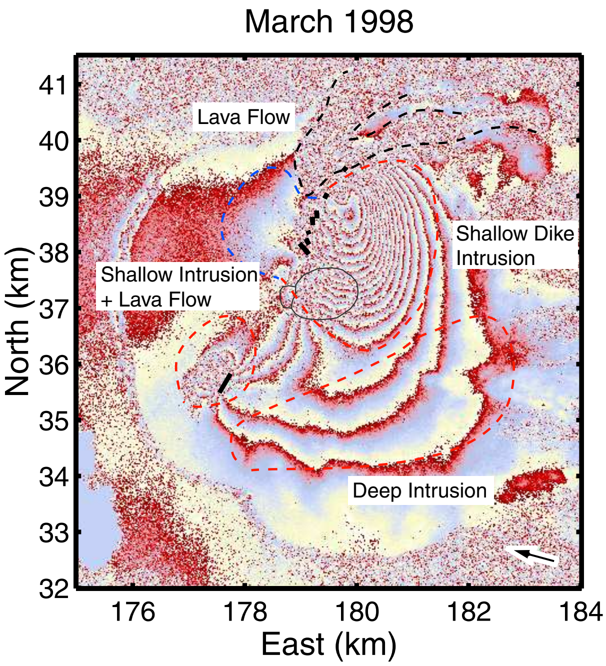

Figure 3.14: Interpretation of signals of the March 1998 interferogram (Figure 3.1). Red dashed curve: displacements toward the satellite. Blue dashed curve: displacements away from the satellite. Black dashed curve: decorrelated area due to lava flows.

decaying deflation in this area (Figures 3.2 – 3.4), which suggests thermal contraction of the injected magma.

3.3.3 Analysis and results

At the time of the second image acquisition (30 July, 1998), the eruption still continued at Piton Kapor. For the reason previously given in Section 2.1, this continuation of eruption at Piton Kapor should not affect the dike and our interpretation of the displacements. The validity of this assumption is supported by the interferogram of the July 1999 event (Figure 3.2), whose first image was taken on 1 April 1998, showing no global signal corresponding to the vent of the ongoing March 1998 eruption. The eruption outside the caldera occurred in a vegetation area where coherent interferometric signals cannot be computed, thus it will not be investigated in this study.

The coherent areas of the interferogram were successfully unwrapped using the procedure explained in Section 2.4.3. The unwrapped data were subsampled on circular points as was done in Section 2.3.4 for each inversion.

The short-wavelength displacements (dense fringes) east of the northern eruptive fissures are undoubtedly caused by a dike intrusion. It is not obvious, however, whether the large-wavelength displacements (wide fringes) are attributed to a deep root of the dike or to another pressure source. Thus, the displacements are inverted assuming the following four models:

(Model A) Y-shaped single dike, with two segmented parts reaching the northern and southern eruption sites,

(Model B) Dikes to the north and the south,

(Model C)	A deep inflation source and dikes to the north and the south,
(Model D)	A deep dike at the location of the preeruption earthquake locations (only to explain large-wavelength displacements).

Model A: single dike

First, a Y-shaped dike with two segmented parts reaching the northern and southern eruption sites is assumed to explain both the short and long wavelength displacements. For simplicity, the seven eruptive fissures on the northern flank (Figure 3.13) are approximated by a smooth single fissure, so that the northern and southern eruption sites are approximated by two fissures. This approximation leads to inaccurate prediction of displacements close to the northern eruptive fissures, but has little effect on the estimation of the whole geometry and overpressure, as there are only few subsampled points close to the northern eruption site. In addition to the seven model parameters (P0, Dip, Shear, Botelv, Botlen, Twist, Botang) assumed in the JGR paper (Figure 2.2), two additional parameters are introduced to determine the geometry of the segmented part: D_top and Segratio (Figure 2.4a). D_top defines the along-dip length of the segmented part, whereas Segratio defines the ratio of the bottom lengths of the two segments. The solution of an inversion converged to a geologically unrealistic model; the horizontal angle between the top and bottom sides (Twist) converged to its minimum bound of -60 degrees (Figure 3.15; inversion #980301 on Table 3.2). Supplementary inversions confirmed that separating the two superficial segments (Figure 2.4b) or introducing the dike bottom side curvature (Figure 2.5) do not lead to a more realistic model and to a significantly better data fit.

To force a more realistic solution, an inversion was performed with the parameter Twist fixed to zero (inversion #980302 on Table 3.2). However, similarly to the previous inversion of #980301, the maximum probability model little explained the displacements east of the southern eruptive fissure.

*Table 3.2: Inversion settings and results. Superscripts and subscripts indicate smaller and larger limits of the confidence interval. Inversion parameter (number of models evaluated in each iteration) $n = 50$ is used unless otherwise stated (see Section 2.3.2 for the definition of parameter n). At the end of each application for the five eruptions, preferred models are proposed. They are marked with the symbol * in the column "Preferred Models".*

Quadrangle-type dike connected to the ground (seven to ten parameters)

#ID	ϵ^2 (10^{-4} m^2)	a (m)	P$_0$ (MPa)	Dip (deg)	Shear (deg)	Botelv (m)	Botlen	Twist (deg)	Botang (deg)	D_top (m)	Other Parameters	Volume (Mm^3)	Explained[a] Data (%)	Preferred Model
Mar. 1998														
980301		750	4.8	53	5	1418	0.4	– 56	– 16	312	0.52[b]	5.5	95	
980302		750	4.2	44	30	1172	0.1	0 (fixed)	– 12	673	0.17[b]	4.2	93	
980303	4.8	750	$0.7^{1.0}_{0.5}$	70^{79}_{63}	-47^{-37}_{-58}	357^{560}_{-121}	$1.3^{2.2}_{0.8}$	-39^{-29}_{-54}	16^{33}_{2}	78^{108}_{44}		2.1	98	*
980304	1.5	250	$0.36^{0.94}_{0.10}$	69^{90}_{47}	5^{24}_{-18}	430^{926}_{51}	$9.1^{13.0}_{5.1}$	0 (fixed)	0 (fixed)	0 (fixed)		0.3	59[c]	*
980307		750	5.4	36	– 56	1642	0.8	-24	-10	20		3.2	98	
980308		250	0.28	53	– 45	1647	4.5	0 (fixed)	0 (fixed)	0 (fixed)		0.3	87	
Jul. 1999														
990701[d]	1.73	500	$9.1^{12.4}_{6.6}$	106^{119}_{96}	-15^{8}_{-42}	1771^{1865}_{1597}	$1.0^{1.2}_{0.7}$	-20^{-12}_{-35}	23^{31}_{14}	357^{489}_{257}		0.2	93	
Sep. 1999														
990901	1.33	395	$3.5^{4.3}_{3.2}$	108^{119}_{102}	15^{23}_{0}	2203^{2216}_{2173}	$1.2^{1.5}_{1.1}$	10^{14}_{7}	10^{14}_{7}	0 (fixed)		0.2	93	*
Feb. 2000														
000201	6.0	2308	$1.4^{1.5}_{1.3}$	65^{67}_{61}	-35^{-29}_{-42}	1617^{1682}_{1545}	$3.5^{4.1}_{3.4}$	10^{12}_{8}	-4^{-2}_{-8}	100 (fixed)		0.7	89	*
Jun. 2000														
000601		1000	0.6	60	19	635	2.5	-17	5	201		1.8	74	
000602		750	0.6	56	30	699	2.5	-13	9	300 (fixed)	0.0[e]	1.6	75	
000603	17.8[g]	544	$0.7^{1.1}_{0.5}$	43^{61}_{26}	33^{54}_{2}	931^{1252}_{657}	$2.1^{3.3}_{1.3}$	-23^{-9}_{-43}	18^{35}_{-12}	350 (fixed)	-2^{33}_{-29} [e], 39^{56}_{22} [f]	1.7	81	*
000604		750	0.6	52	6	815	2.0	-40	37	447		1.9	78	

[a] Equation 3.5. Note that the percentages for inversions using different data points cannot be directly compared. [b] Segratio. [c] This small value is attributed to small signal to noise ratio. [d] Bottom side is assumed to have the same curvature as the top one. [e] Botcurv (deg). [f] Vertcurv (deg). [g] This large value is attributed to large modelling error (residual).

Table: *Continued.*

Simultaneous inversions

#ID		ϵ^2 (10^{-4} m^2)	a (m)	P$_0$ (MPa)	Dip (deg)	Shear (deg)	Botelv (m)	Botlen	Twist (deg)	Botang (deg)	D_top (m)	Volume (Mm^3)	Explained Data (%)	Preferred Model
Jul. 1999														
990702[a]	northern dike	1.4	500	$6.0^{12.2}_{2.3}$	108^{119}_{93}	-38^{-17}_{-49}	2151^{2230}_{2029}	$0.9^{1.3}_{0.5}$	-37^{-22}_{-49}	-33^{1}_{-38}	200 (fixed)	0.1	96	*
	southern dike			$1.4^{7.5}_{0.5}$	62^{88}_{49}	0 (fixed)	1646^{1949}_{1414}	1 (fixed)	0 (fixed)	0 (fixed)	254	0.05		
Jun. 2000														
000605[b]	western dike		544	0.4	63	54	901	4.5	67	32	0 (fixed)	1.2	80	
	eastern dike			1.2	74	37	589	0.8	15	22	0 (fixed)	0.6		

[a] n = 10 used. [b] n = 5 used.

Table: *Continued.*

Nine parameter rectangular model

#ID	ϵ^2 (10^{-4}m^2)	a (m)	P$_0$ (MPa)	X (km)	Y (km)	Z (m)	Length (m)	Strike (deg)	Vertang (deg)	Dip (deg)	Height (m)	Volume (Mm^3)	Explained Data (%)	Preferred Model
Mar. 1998														
980305[a]	0.6	1000	$4.3^{10.7}_{1.7}$	$178.99^{179.47}_{178.65}$	$37.36^{37.89}_{36.71}$	988^{1425}_{395}	4253^{5394}_{3121}	37^{57}_{18}	3.4^{21}_{-11}	32^{49}_{13}	1144^{1488}_{555}	4.9	93	

[a] $n = 30$ used. (X, Y, Z): midpoint of the top side, Length: horizontal length, Strike: strike angle (clockwise from north), Vertang: vertical angle (from horizontal) of the top and bottom sides, Dip: Dip angle, Height: height (distance between top and bottom sides).

Ten parameter oblate ellipsoidal model

#ID	ϵ^2 (10^{-4}m^2)	a (m)	P$_0$ (MPa)	X (km)	Y (km)	Z (m)	S$_1$ (m)	S$_2$ (m)	S$_3$ (m)	Az (deg)	Vertang (deg)	Rotang (deg)	Volume Change (Mm^3)	Explained Data (%)	Preferred Model
Mar. 1998															
980306[a]		1000	1.8	179.44	36.99	893	5532	2118	256	41	-3	-34	5.0	93	

[a] $n = 20$ used. (X, Y, Z): coordinate of the center, (S$_1$, S$_2$, S$_3$): axis lengths (S1 >S2 >S3), (Az, Vertang): horizontal (clockwise from north) and vertical (from horizontal) angles of the longest axis, Rotang: rotation angle around the longest axis.

Seven parameter half oblate ellipsoidal (laccolith) model

#ID	ϵ^2 (10^{-4}m^2)	a (m)	P$_0$ (MPa)	X (km)	Y (km)	Z (m)	S$_1$ (m)	S$_2$ (m)	Height (m)	Volume Change (Mm^3)	Explained Data (%)	Preferred Model
Sep. 1999												
990902	0.5	100	$7.3^{11.1}_{2.8}$	$179.34^{179.40}_{179.26}$	$34.70^{34.92}_{34.57}$	1887^{1924}_{1844}	1822^{1161}_{652}	40^{46}_{21}	74^{88}_{55}	0.01	84	

(X, Y, Z): coordinate of the center of the basal ellipsoidal plane, (S$_1$, S$_2$): long and short axis lengths of the ellipsoid.

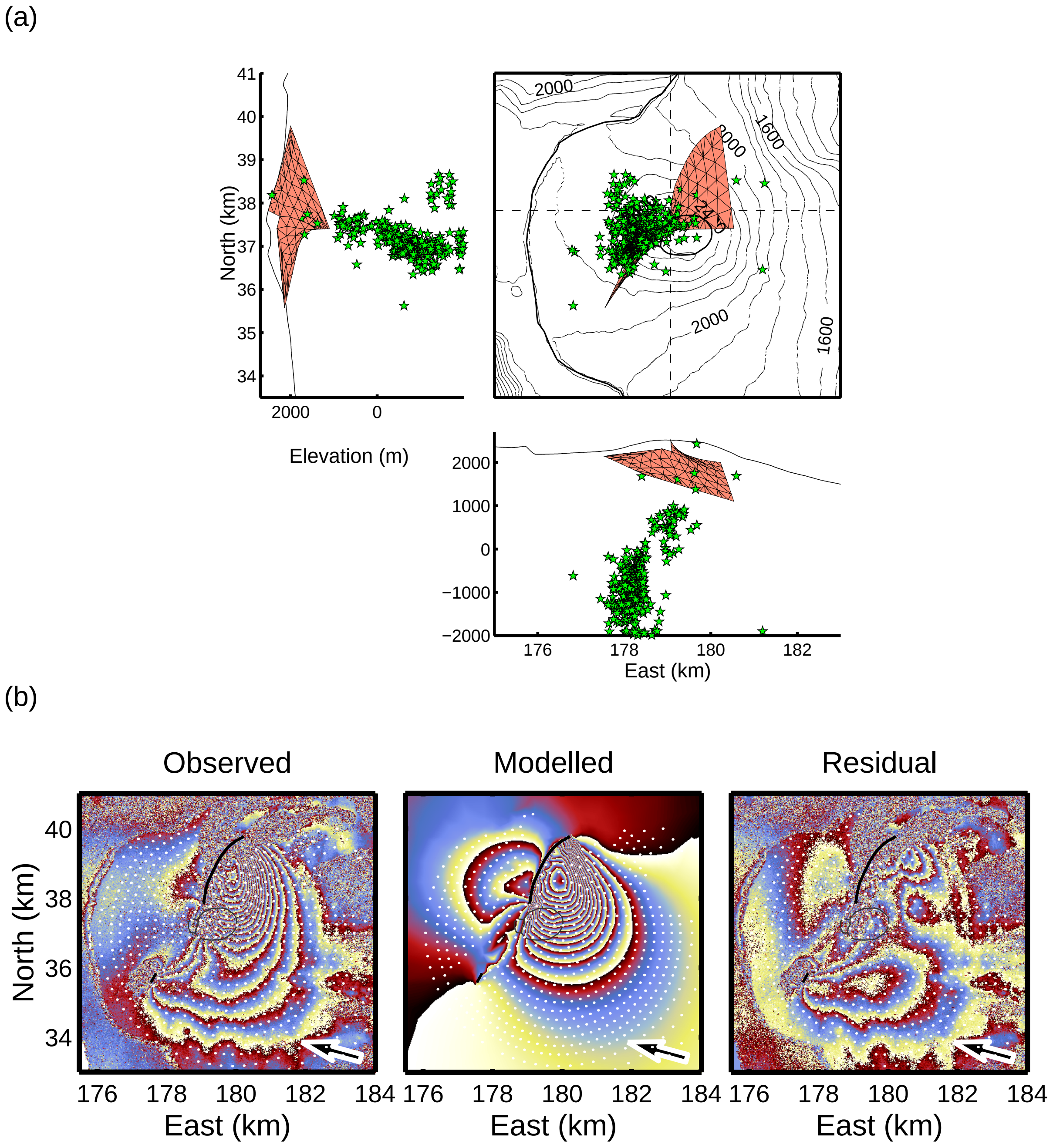

Figure 3.15: ***[March 1998, Model A]*** *(a) Geometry of the maximum-probability Y-shaped dike model that reaches the northern and southern eruption sites (#980301 on Table 3.2), plotted with the preeruption seismicity (green stars) relocated based on similarity of waveforms [Battaglia, 2001]. (b) Observed, modelled and residual interferograms corresponding to the model shown in (a). The dike was assumed to reach the ground at the location indicated by black lines. White dots denote subsampled data points.*

Model B: northern dike + southern dike

Next, two distinct dikes are considered to be associated with the northern and southern eruptions. As these two fissures are far from each other (Section 3.2.1, Figure 3.12), a two-step inversion is made. The data close to the northern eruptive fissure are first inverted to model the northern dike, and then the residual data around the southern eruptive fissure are inverted to model the southern dike.

The first inversion is for the northern dike (inversion #980303 on Table 3.2). The dike is assumed to consist of seven superficial segments reaching the eruptive fissures and a deeper part. In addition to the six geometry parameters taken in the JGR paper (Figure 2.2), the along-dip height of the segmented parts (D_top) is additionally taken as a parameter. The data fit is fairly good (Figure 3.16b), with about two fringes ($\sim 6\,\mathrm{cm}$) of residuals east of the eruptive fissures and less than a fringe to the west. The residual interferogram (Figure 3.16b, right) shows wide fringes east of the southern eruptive fissure. Interestingly, the deepest point of the dike model is located 2200 m beneath the Hudson crater at sea level. Appraisal indicates a good constraint on the model (Table 3.2).

The residual displacements (Figure 3.16b, right) are then inverted to estimate the geometry and overpressure of the southern dike. Note that the superficial part of the dike is not segmented because there is only one eruptive fissure for the southern eruption. Taking the same six parameters as were taken in the JGR paper (Figure 2.2) leads to a model whose bottom side extends 5 km to the east (Figure 3.17), because of the large-wavelength displacements. Presence of such a dike is, however, neither indicated by seismicity [*Battaglia et al.*, 2005] nor by tilt change [*Battaglia and Bachèlery*, 2003]. Thus, these large wavelength displacements probably result from either an oversimplified parameterization of the northern dike or the presence of a third pressure source that accounts for large-wavelength displacements (this latter one is considered in Model C). Assuming the first possibility, the parameters Twist (horizontal angle between the top and bottom sides) and Botang (vertical angle of the bottom side) of the southern dike are fixed to zero in order to obtain a more realistic dike geometry. The superimposed displacements of the northern and southern dike models of maximum probability (Figure 3.18a) well explain the observed data (Figure 3.18b). Both dikes were estimated to have practically the same dip angle of about 70 degrees. The estimated overpressure for the southern dike (0.36 MPa) is half that for the northern dike (0.7 MPa), suggesting that the single Y-shaped dike model with a constant overpressure (Model A) was less appropriate.

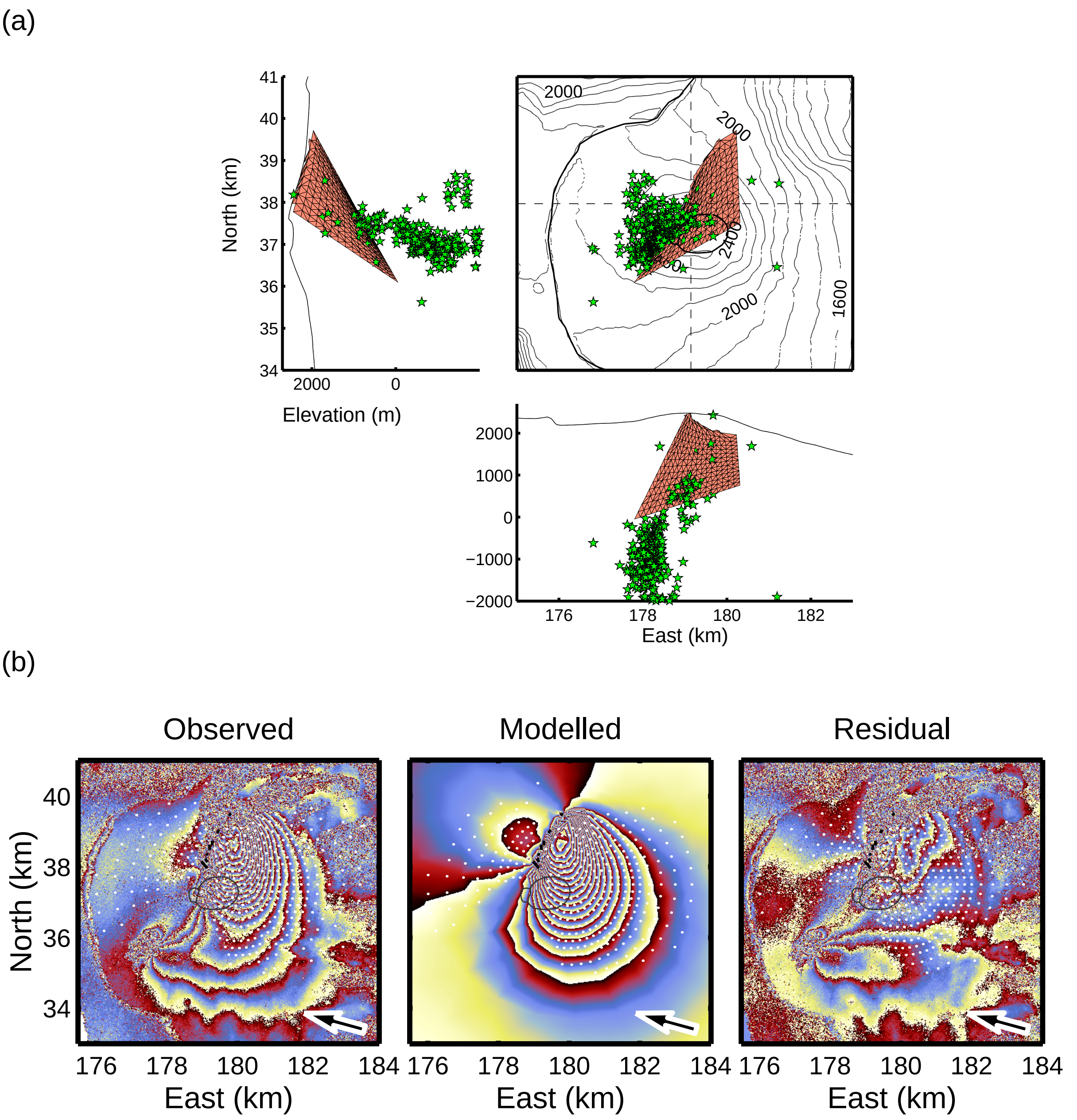

Figure 3.16: ***[March 1998, Model B]*** *(a) Geometry of the maximum-probability single dike model that reaches the northern eruption fissures (#980303 on Table 3.2), plotted with the relocated hypocenters of the preeruption microearthquakes [Battaglia, 2001]. Interestingly, the southern endpoint of the bottom side lies 2200 m beneath the Hudson crater. (b) Observed, modelled and residual interferograms corresponding to the model shown in (a). The dike was assumed to reach the ground at black lines. White dots denote subsampled data points.*

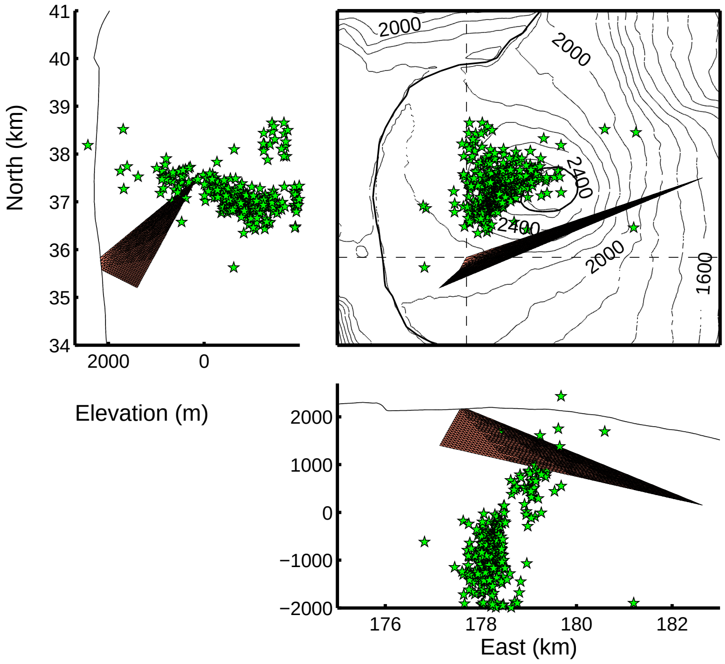

Figure 3.17: ***[March 1998, Model B]*** *Geometry of the maximum-probability dike model of seven parameters that reaches the southern eruptive fissure obtained from inverting the residual data shown in Figure 3.16b. Green stars are the relocated hypocenters of the preeruption microearthquakes [Battaglia, 2001]. The used data points are shown in green dots in Figure 3.18b. This geometry is not consistent with seismicity and tilt change data.*

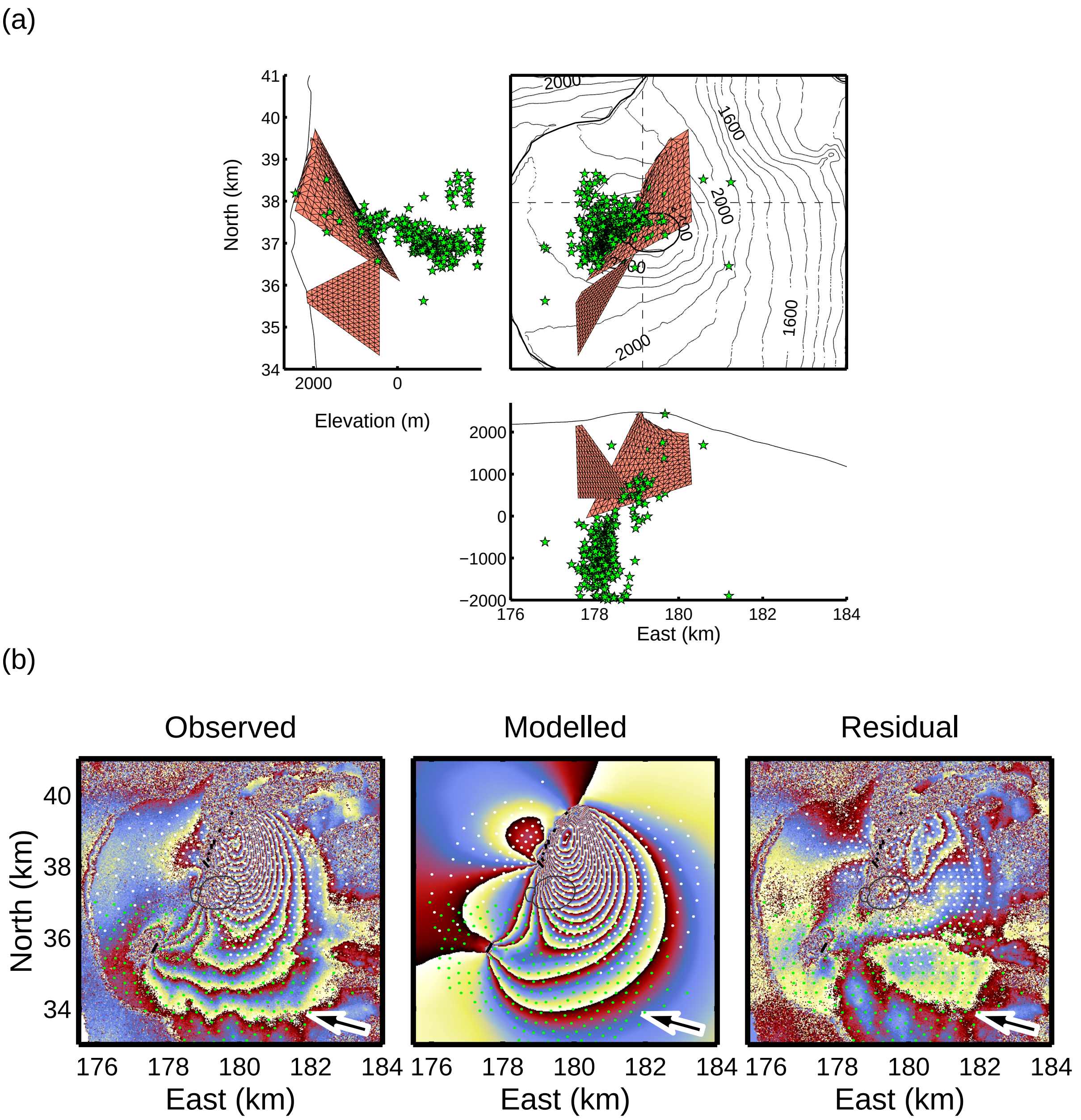

*Figure 3.18: **[March 1998, Model B]** (a) Geometry of the maximum-probability model (#980304 on Table 3.2) for the southern dike whose twist angle and vertical angle of the bottom side are fixed to zero, plotted with the northern dike of Figure 3.16a. The dikes have a common dip angle of about 70 degrees. The northern end of the southern dike bottom, located close to the hypocenters of the preeruption microearthquakes, is consistent with a common magma path for the two dikes. Green stars are the relocated hypocenters of the preeruption microearthquakes [Battaglia, 2001]. Note that the hypocenters do not include those which occurred after the northern eruption onset. (b) Observed, modelled and residual interferograms corresponding to the model shown in (a). White dots are the subsampled data points used in the first inversion for the northern dike, and green dots are those used for the second inversion for the southern dike.*

Model C: Deep pressure source + northern dike + southern dike

Next, a pressure source not reaching the ground is assumed to account for the large-wavelength displacements. Then, the residual data are inverted by assuming that individual dikes correspond to the northern and southern eruptions.

To explain the large-wavelength displacements, a rectangular pressurized source is first tested; the nine model parameters are: position (three parameters), height, length, strike, dip, inclination of the top and bottom sides, and overpressure (see Section 2.2 for a complete description). Inverting the subsampled data (inversion #980305 on Table 3.2) predicts a subhorizontal sill-type source that moderately dips ($\sim 30°$) toward the southeast (Figure 3.19a). This model well explains (93%) the large-wavelength displacements (Figure 3.19b).

An oblate ellipsoidal source is next assumed for inverting the same data set. The 11 model parameters are: center coordinate (three parameters), axis lengths (three parameters), horizontal and vertical angles of the longest axis, rotation angle around the longest axis, and overpressure (Section 2.2). The predicted model (#980306 on Table 3.2, Figure 3.20a) is consistent with the rectangular model; they have comparable width, length, dip and strike angles and location. This ellipsoidal model also well explains (93%) the large-wavelength displacements (Figure 3.20b).

In both models, the volume change is in the order of that erupted during one succesive eruption (Table 3.2). Because of its thickness, the oblate ellipsoidal model reaches about 1300 m a.s.l.whereas the average elevation of the rectangular model is about 500 m a.s.l. The difference between the estimated overpressures, 3.5 and 0.6 MPa for the rectangular and ellipsoidal sources respectively, is mainly due to this depth difference.

As shown, the rectangular and oblate ellipsoidal models both explain the long-wavelength displacements. The ellipsoidal source, however, is probably inappropriate because such a large reservoir at a shallow level with a roof aspect ratio (thickness/width) of less than 0.5 should not be stable when underpressurized [*Roche et al.*, 2001]. In addition, if it existed, we would expect some evidence from geophysical, petrological and geochemical data. The rectangular sill model is thus preferred to the oblate ellipsoidal model.

The residual displacements for both the rectangular sill (Figure 3.19b) and the ellipsoidal source (Figure 3.20b) show fringes in the area connecting the northern and southern eruption sites. Although these fringes are consistent with a subsidence, there is no reasonable explanation for such a process, and they are likely to be an artifact. The rectangular source creates less fringes in this area and thus it is prefered to the ellipsoidal model also in this respect.

The short-wavelength residual displacements obtained from the rectangular model (Figure 3.19b) are further inverted by assuming that separate dikes reach the northern and southern eruptive fissures (#980307 and #980308 on Table 3.2). The shallow dip for the northern dike ($\sim 35°$) is questionable as it is different from the results from other eruptions on the northern flank [*Froger et al.*, 2004, Section 2.3.4]. Figure 3.21a shows the geometries of the maximum probability models corresponding to the northern and southern dikes and the sill. It is beyond the resolution of InSAR data to predict the connections between the three intrusions. The modelled ground displacements with the three sources are superimposed and compared with the observed interferogram (Figure 3.21b); the data fit is fairly well except the area connecting the northern and southern eruption sites and that east of the northern eruptive fissures.

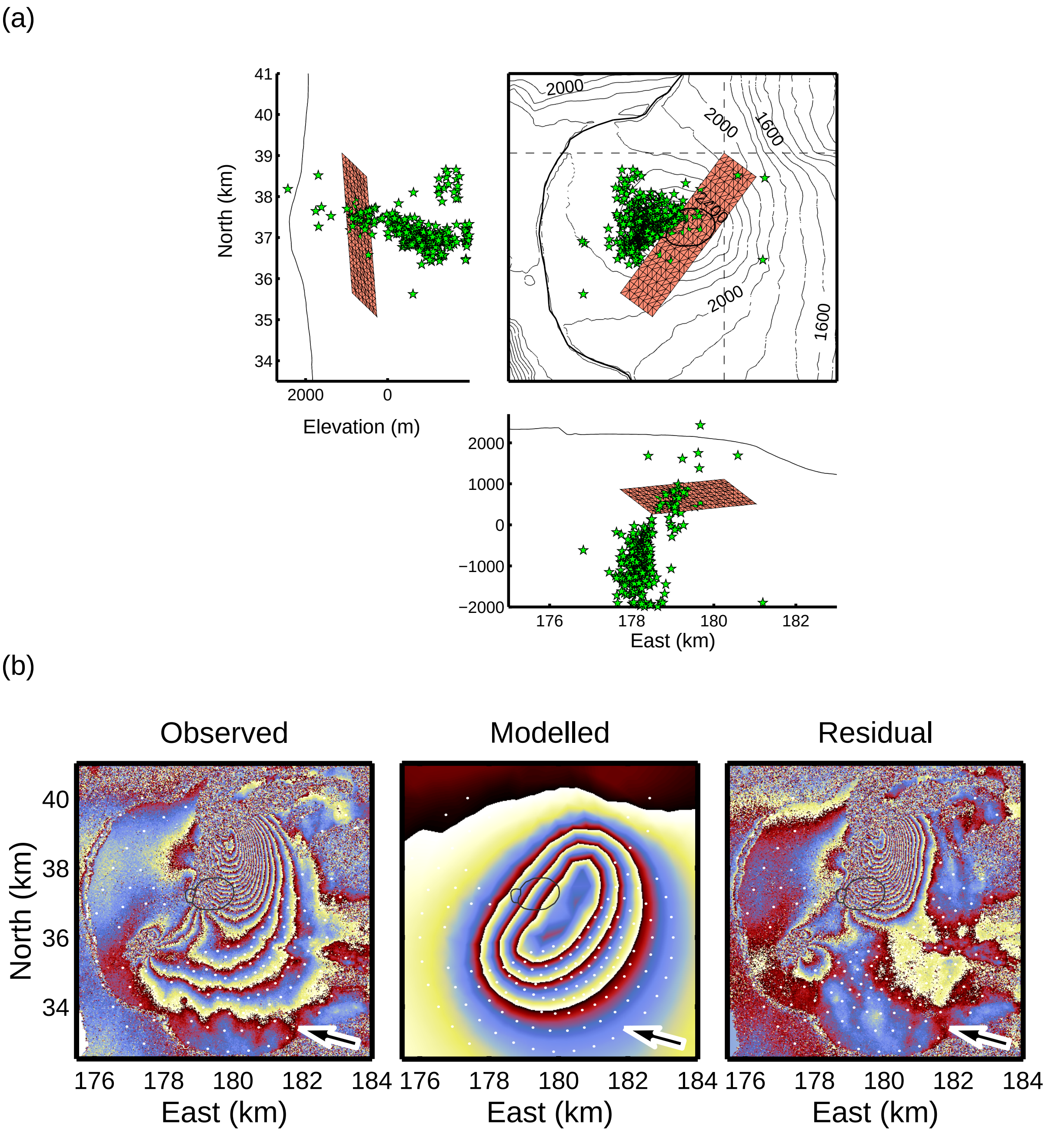

Figure 3.19: ***[March 1998, Model C]*** *(a) Geometry of the maximum-probability rectangle pressure source obtained from inverting large-wavelength displacements (#980305 on Table 3.2), plotted with the relocated seismicity [Battaglia, 2001]. (b) Observed, modelled and residual interferograms, corresponding to the model shown in (a). White dots indicate subsampled data points.*

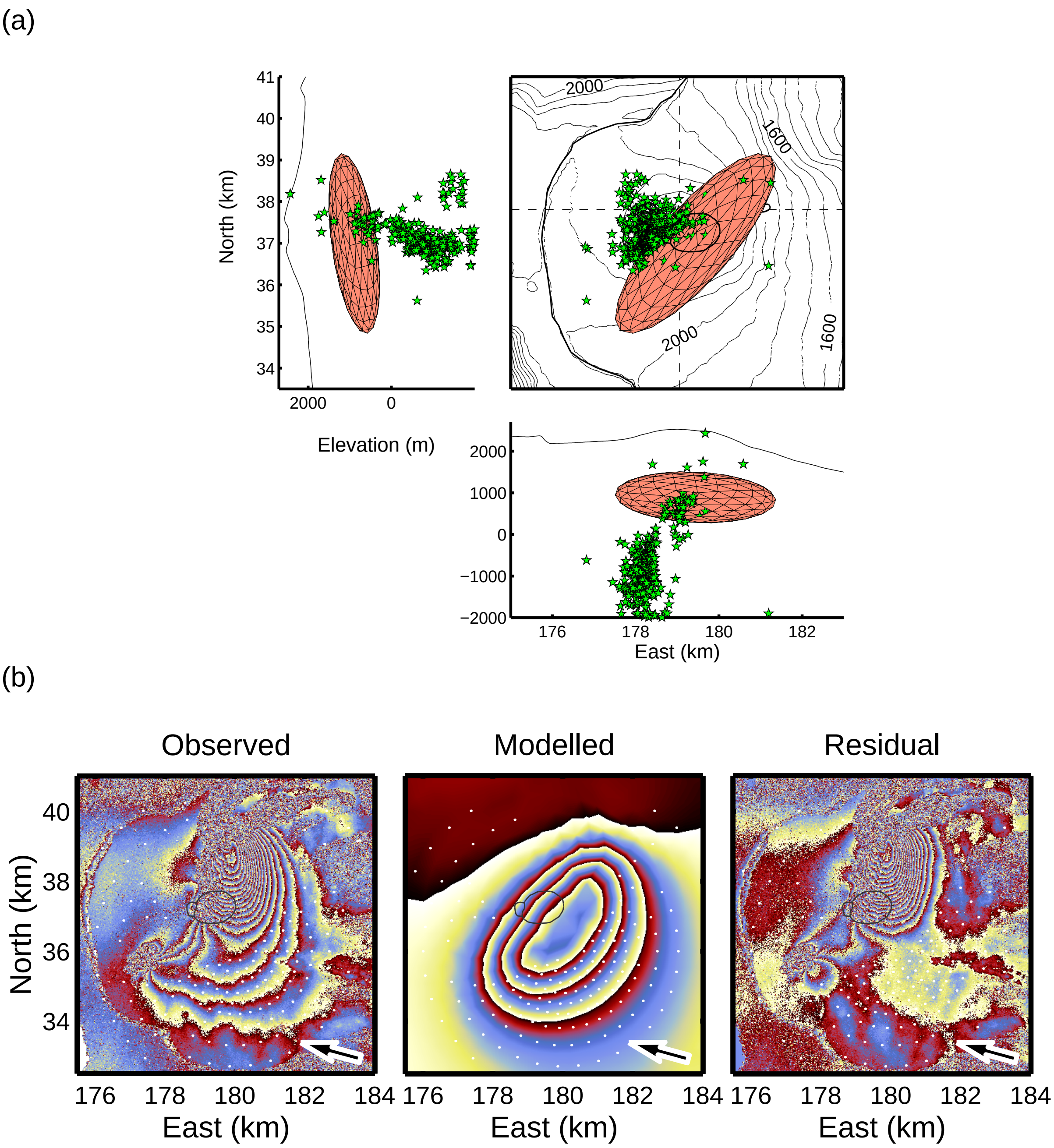

Figure 3.20: ***[March 1998, Model C]*** *(a) Geometry of the maximum-probability ellipsoidal pressure source obtained from inverting large-wavelength displacements (#980306 on Table 3.2), plotted with the relocated seismicity [Battaglia, 2001]. (b) Observed, modelled and residual interferograms, corresponding to the model shown in (a). White dots indicate subsampled data points.*

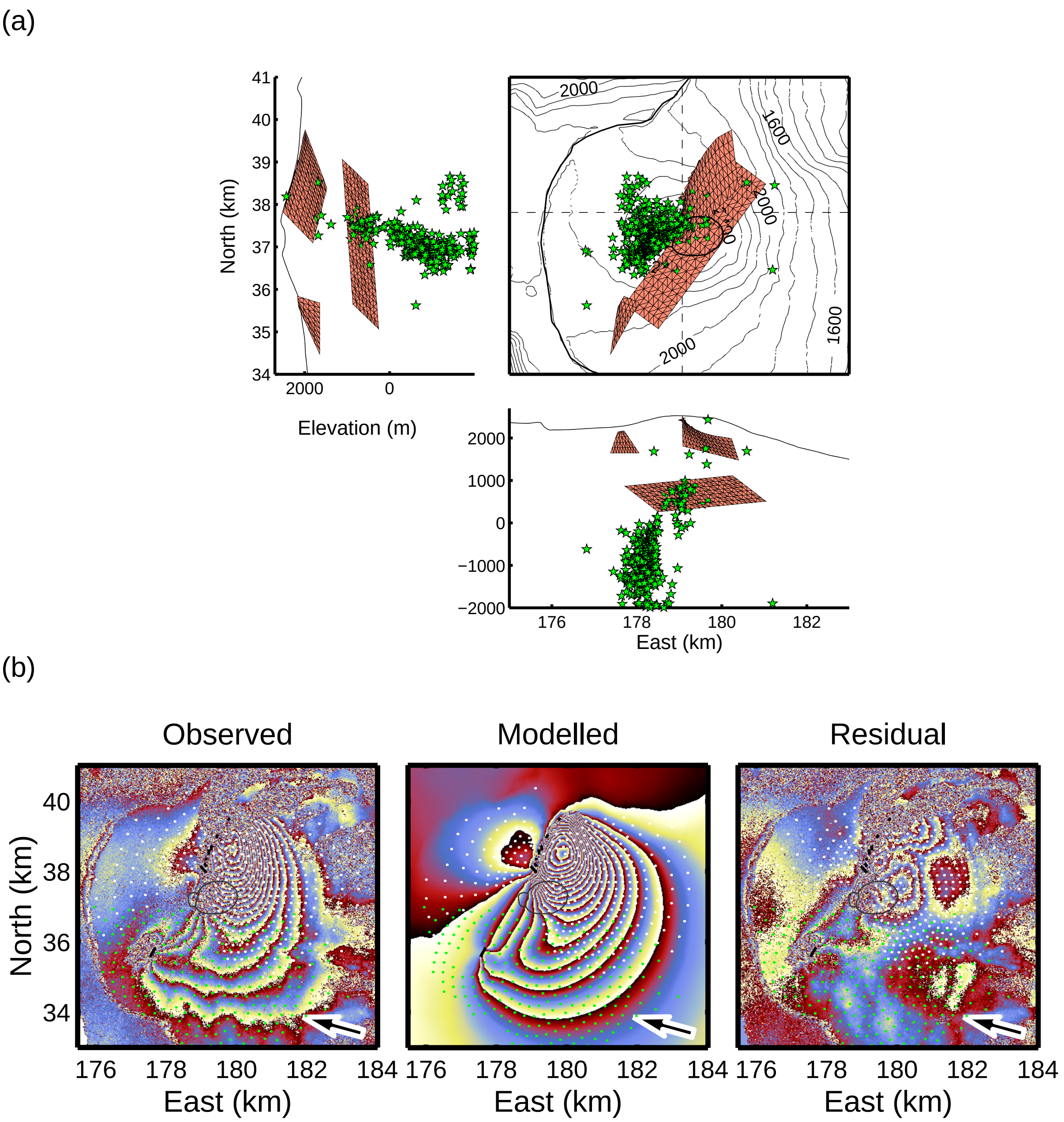

Figure 3.21: ***[March 1998, Model C]*** *(a) Geometry of the deep sill of Figure 3.19a and two shallow dikes (#980305, #980307, #980308 on Table 3.2) plotted with the relocated seismicity [Battaglia, 2001]. (b) The modelled interferogram created from superposing the displacements created by the three sources shown in (a) is compared with the observed data. White and green dots are the inverted subsampled data for the northern and southern dikes, respectively. See Figure 3.19b for the inverted data for the sill.*

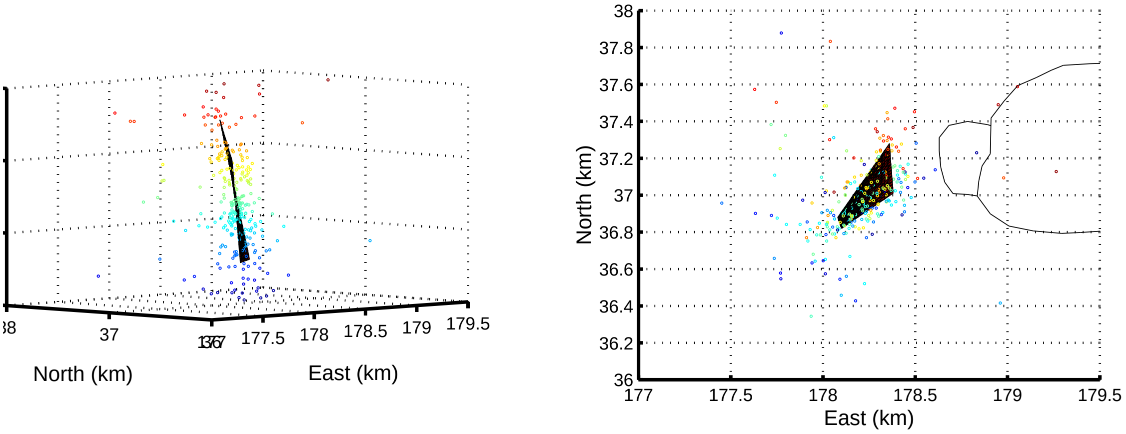

Figure 3.22: ***[March 1998, Model D]*** *Geometry of the deep dike model surrounded by seismicity at the elevation of 0–1500 m below sea level. Color indicates the depth of the hypocenters.*

Model D: Deep dike surrounded by preeruption earthquake locations

Finally, another possibility of the origin of the wide fringes is tested. A region of very high seismicity is observed at elevations of 0–1500 m below sea level. *Battaglia et al.* [2005] discusses that the lateral elongation of this region has the same orientation as the alignment connecting craters Hudson, Kapor and Krafft. Here, we assume that the microearthquakes were generated around the propagating dike, and we fix the geometry to the region of high seismicity. Figure 3.22 shows the geometry of the tested quadrangle dike, plotted with the seismicity. The predicted fringes continue outside the Enclos Fouqué caldera (Figure 3.23), unlike the observed fringes limited inside the caldera. In addition, an extremely high overpressure of 150 MPa was required to produce two fringes. Therefore, the wide fringes could not have been caused by a dike at the elevation 0–1500 m below sea level.

Preferred Model

The single Y-shaped dike model (Model A) did not well explain the interferogram east of the southern eruption site and therefore this model is not preferred. To quantitatively compare the data fit of Models B and C, the percentages of explained data (Equation 3.5) are calculated from InSAR data points (without subsampling) in the area covering the vicinity of the northern and southern eruption sites excluding lava flows. In these calculations, the modelled displacements are interpolated. The percentages for the two models do not indicate a significant difference: 84% for Model B and 83% for Model C. The two dikes model (Model B, Figure 3.18) and the three sources model (Model C, Figure 3.21) equally well explain the observed displacements. Tilt data [*Battaglia and Bachèlery*, 2003] do not seem consistent with a sill intrusion, though this should be verified with a quantitative analysis. The two dikes model (Model B, Figure 3.18) is proposed as the preferred model for the March 1998 event. The preferred model is originated at sea level; this is significantly deeper than the result of *Sigmundsson et al.* [1999] who estimated the depth of the dike bottom to be 760 m using Okada's model. The dip angle of Model B, 70° is also significantly different from 45° of the model of *Sigmundsson et al.* [1999], although it should be noted that the dip angle of this study is the averaged value.

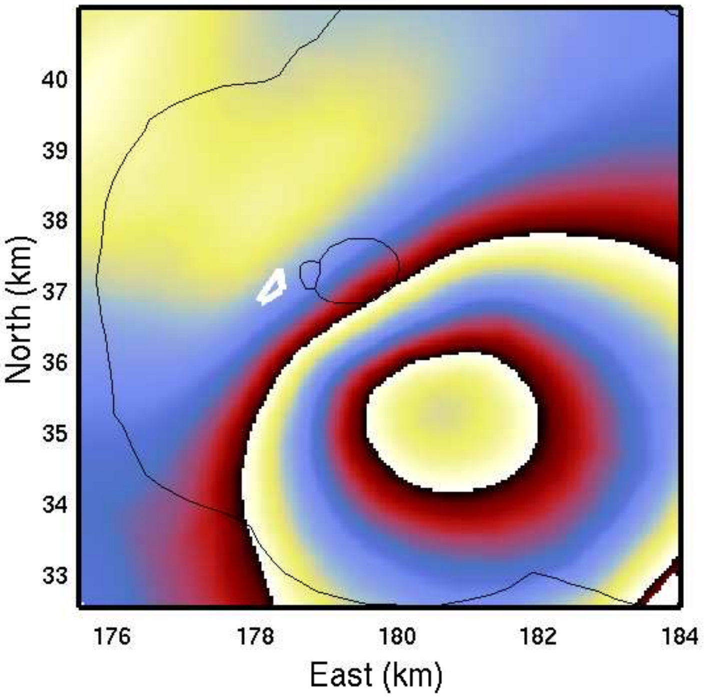

Figure 3.23: ***[March 1998, Model D]*** *Interferogram modelled with the dike at the elevation of 0–1500 m below sea level as indicated by the seismicity (Figure 3.22). The assumed dike geometry is indicated by white line. The overpressure of 150 MPa was assumed. Note that the fringes open outside the caldera contrary to observation (Figure 3.1).*

3.4 July 1999 Eruption

3.4.1 Overview

On 19 July 1999, a seismic swarm above sea level and ground deformations (tilt and extensometric data) were detected almost simultaneously about 50 minutes before the eruption onset. The eruption started at two fissures, one located at the eastern rim of Dolomieu crater and the other on the eastern flank next to it, almost simultaneously (Figure 3.13). Several other fissures opened a few hours later, forming a set of en echelon eruptive fissures in an N110 direction within and east of Dolomieu crater. About 36 hours after the eruption onset, the activity almost ceased except for some gas emissions. However, a new eruptive fissure opened two or three days later, about 1 km southeast of the en echelon eruptive fissures. The activity on this new fissure continued until 31 July.

3.4.2 Sources of interferometric signals in data

The interferogram for the July 1999 eruption (Figure 3.2) has a low signal to noise ratio due to several reasons: (1) The altitude of ambiguity is relatively small (40.1 m), which enhances noise that result from errors in the DEM and from atmospheric disturbance [*Massonnet and Feigl*, 1998]. (2) Displacements associated with the March 1998 eruption are included. The day of the first image acquisition is 1 April 1998 when the March 1998 eruption was still continuing; thermal contraction of magma of the March 1998 intrusion is observed (see Section 3.3.2). (3) The strike of the eruptive fissures is subparallel to the line-of-sight direction. This makes the interferogram insensitive to the largest displacements, which are expected to be perpendicular to the dike surface.

Figure 3.24 shows the interpretation of the signals. Some fringes corresponding to about 10 cm of displacements toward the satellite are observed east of the eruptive fissures. If we look into details, two lobes are observed east of the fissures; this seems to suggest a dike intrusion reaching the summit eruptive fissures and another one beneath the area connecting the summit fissures and the southeastern fissure. The area between the two sets of fissures is displaced away from the satellite, probably indicating a subsidence above a dike. Unfortunately, the northern lava flow covers a large part of this area and thus the detailed displacements cannot be known.

3.4.3 Analysis and results

Due to the bad quality of data, the interferogram could not be unwrapped with the unwrapping software SNAPHU. Fringes are thus counted by hand and converted to displacements in the line-of-sight direction, resulting in 79 data points (white dots on Figure 3.25b) .

Two models are considered:

(Model A) Single dike,

(Model B) Simultaneous inversion: summit and southeastern dikes.

Model A: single dike

First, a single dike extending from the main summit eruptive fissures to the secondary (southeastern) one is assumed to account for the observed displacements. The dike bottom

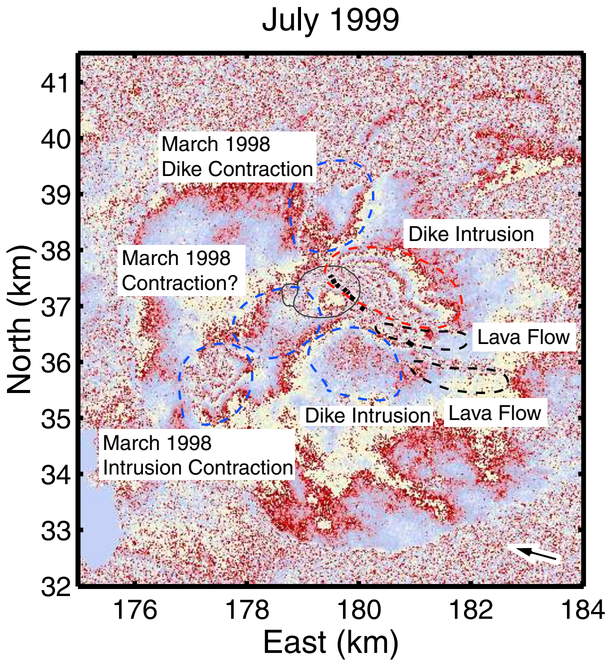

Figure 3.24: Interpretation of signals of the July 1999 interferogram (Figure 3.2). Red dashed curve: displacements toward the satellite. Blue dashed curve: displacements away from the satellite. Black dashed curve: decorrelated area due to lava flows.

is assumed to have the same curvature as its top because preliminary inversions indicated a better fit for such models than those with a straight bottom. Except for that, the same model parameters as in the JGR parer are assumed (Figure 2.2). This single dike model is not expected to explain the two lobes but may explain general data characteristics. Since no displacement associated with the southeastern eruptive fissure is observed, it is assumed that the dike segment connecting the main part of the dike and the fissure caused negligible ground displacements, and thus the segment associated with the southeastern fissure is not modelled.

An inversion (#990701 on Table 3.2) predicts a dike whose deeper quadrangle-like part is short, with a height of about 100 m. It lies almost at a constant depth of 350 m below the ground (Figure 3.25a). The northwestern part connected to the main eruptive fissures in and next to Dolomieu crater dips toward northeast, while the southeastern part slightly dips in the inverse direction. The model explains the general data characteristics, though the data fit around the southwestern half of the model (i.e., the part connecting the main and secondary eruptive fissures) is not good (Figure 3.25b). The confidence intervals are relatively large; for example, about 6 MPa for the overpressure and 260 m for the bottom elevation (Table 3.2). This results from the small number of data points associated with only one satellite direction. The relatively large estimated overpressure compared to other eruptions (9.1 MPa) may be due to the deep superficial segmented part; when segmented, a dike would require a larger overpressure to create the same amount of ground displacements.

Model B: Simultaneous inversion: summit and southeastern dikes

Next, two dikes are considered; the first one corresponds to the main eruption site in and at the rim of the Dolomieu creater, the second one to the connection between the main and

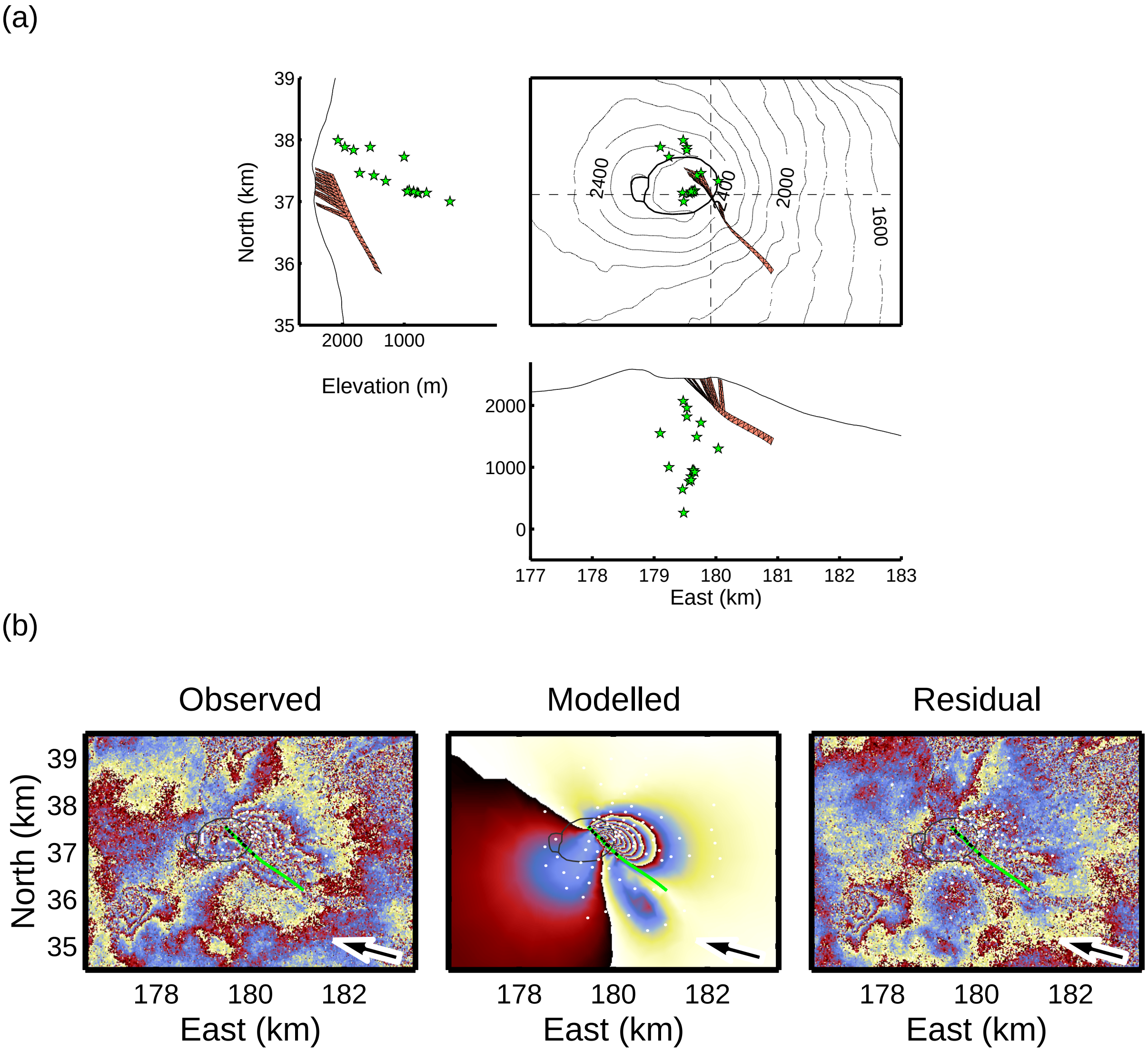

*Figure 3.25: **[July 1999, Model A]** (a) Geometry of the maximum probability model for a single dike, assumed to explain the whole displacements caused during the July 1999 eruption (inversion #990701; Table 3.2). The green stars denote the relocated hypocenters of the microearthquakes [Battaglia, 2001]. (b) Observed, modelled and residual interferograms for the dike model shown in (a). Assumed eruptive fissures and top of the deeper part are drawn in thick black lines and green curve, respectively.*

secondary (southeastern) eruption sites (inversion #990702 on Table 3.2). Due to the proximity of the sources, a simultaneous inversion is performed. The eruption from the southeastern fissure started 3 days after the end of the eruption from the main fissures, suggesting that the dike connecting to the main fissures might have already been solidified when the second one started. Therefore, the simultaneous inversion is made in such a way that the modelled displacements corresponding to the two dikes are summed and compared with the observed data (Section 3.2.1 and Figure 3.12b). The first dike is modelled by seven parameters instead of eight taken for inversion #990701, by fixing D_top to 200 m as determined from preliminary inversion results. The second dike is modelled with four parameters. It is practically a rectangle (note that the top side is a curve parallel to the topography) with parameters P0, Dip, Botelv, D_top. Because of the relatively large number of model parameters (eleven), the inversion tuning parameter (number of models evaluated in each iteration) $n = 10$ is assumed so that the inversion converges in an acceptable interval of time (Section 3.2.1). It should be noted that this increases the risk for the solution to be caught in a local minimum of the misfit function, and it leads to less precise determination of the confidence intervals.

Figure 3.26a shows the geometries of the maximum probability model for the two dikes. The main dike is an inverted triangle dipping toward northeast, which is consistent with the single dike model (Figure 3.25a). The appraisal indicates that the nearly horizontal bottom side (Botang $\sim 0°$) is also acceptable (inversion #990702 on Table 3.2). This large uncertainty can be explained by the presence of the second dike close to the southeastern end. The second southeastern dike moderately dips toward northeast. The top of the second dike was estimated at 254 m below the ground with a large confidence interval of 500 m. The bottom of the second dike lies at 600 m below the ground, which coincides with that of the first dike model. The two-lobed observed displacements are better explained by the two dikes (Figure 3.26b). The two dikes probably share a common feeding path and thus are expected to be located closer to each other, but more detailed geometries of the two dikes cannot be determined due to the limited resolution of the interferogram.

Preferred Model

The consistencies between the estimated geometries of Model A (Figure 3.25a) and B (Figure 3.26a) indicate the reliability of both results. The percentage of explained data on Table 3.2 for Model A (#990701) and Model B (#990702) can be directly compared because the same data set was inverted. The percentages indicate a better fit for Model B (96%) than for Model A (93%). For this reason, the two dike model (Model B) is proposed as the preferred model for the July 1999 event.

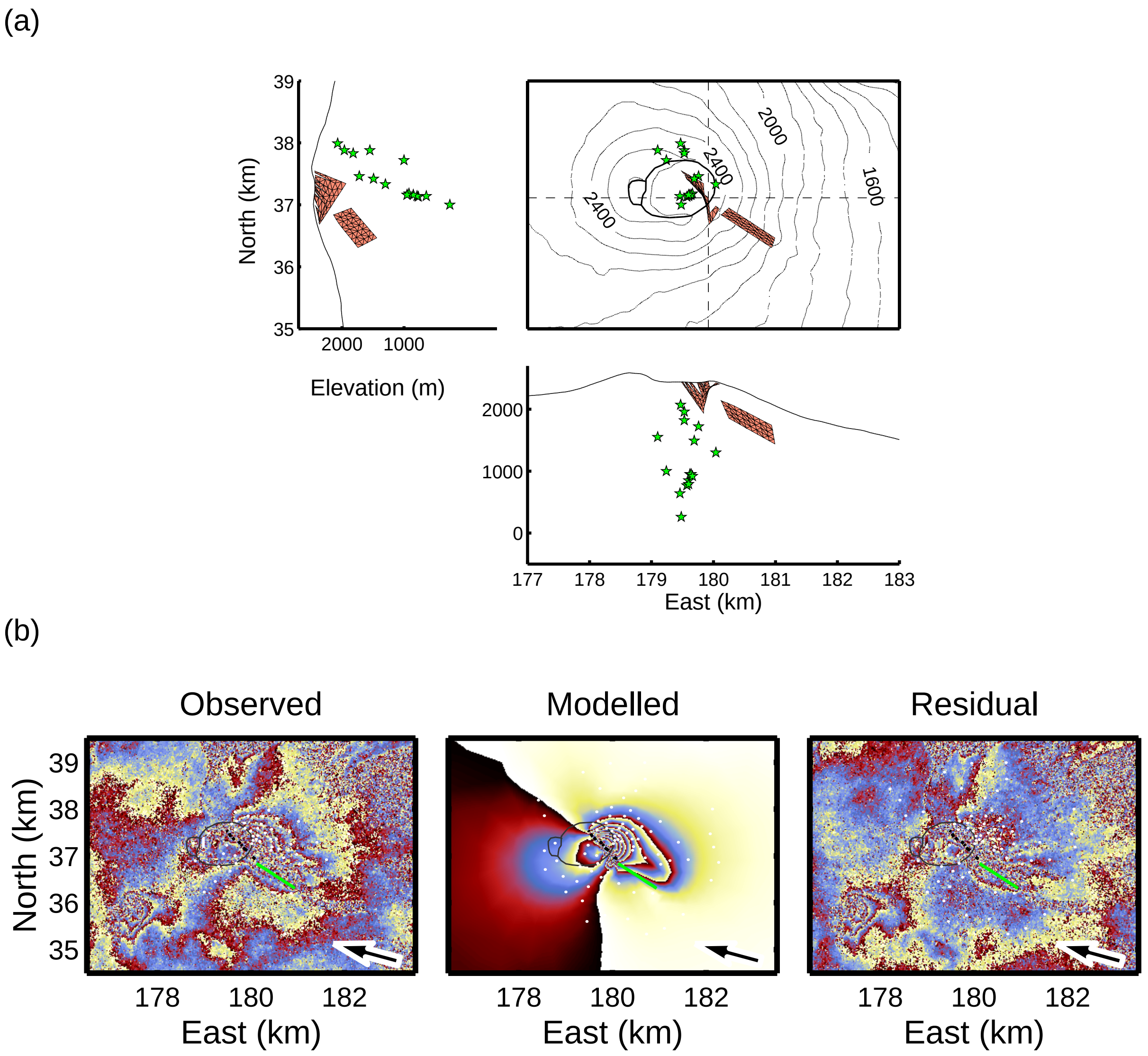

Figure 3.26: ***[July 1999, Model B]*** *(a) Geometry of the maximum probability models obtained from a simultaneous inversion for two dikes that explains the coeruptive displacements for the July 1999 eruption (inversion #990702; Table 3.2). The green stars are the relocated hypocenters of the microearthquakes [Battaglia, 2001]. (b) Observed, modelled and residual interferograms for the two dike models in (a). The black lines indicate the eruptive fissures which are connected to the main dike under Dolomieu crater, and the green line indicates the top of the second dike. White dots represent subsampled data points used in the inversion.*

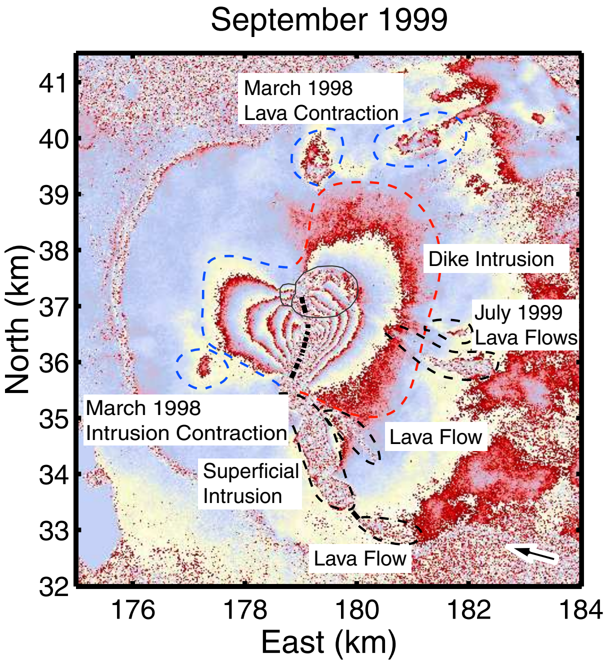

Figure 3.27: Interpretation of signals of the September 1999 descending interferogram (Figure 3.3). Red dashed curve: displacements toward the satellite. Blue dashed curve: displacements away from the satellite. Black dashed curve: decorrelated area due to lava flows.

3.5 September 1999 Eruption

3.5.1 Overview

On 28 September, about two months later, a seismic swarm was detected below the summit crater, above sea level. It started 81 minutes before the eruption onset and had 188 events. 30 minutes after the onset of the seismic swarm, i.e., 50 minutes before the eruption onset, ground deformations were recorded by tiltmeters and extensometers. Then the eruption started from a fissure in the western part of Dolomieu crater. The following eruptive fissures opened first to the north-west, then to the south of the initial point, forming a curved fissure trajectory (Figure 3.13). Less than 8 hours after the eruption onset, activity localized on the upper south flank. On 8 October, steam release was observed close to the Enclos Fouqué's southern border. Three days later, a new lava flow was found to have erupted from the location of the steam release. This vent was active until 21 October. The eruption close to the summit ended on 23 October.

3.5.2 Sources of interferometric signals in data

The descending interferogram shows clear fringes associated with the dike intrusion, indicating similar atmospheric conditions for the two days of image acquisition (Figure 3.27). The main eruption caused a symmetric heart-shape displacements with 17 cm of displacements toward the satellite east of the fissures and 12 cm of displacements away from the satellite west of the fissures.

A superficial intrusion along the southern rift zone, connecting the main and southern eruption sites, is indicated by an incoherent zone and displacements less than one fringe around it.

New dry fissures in this zone were observed in the field (T. Staudacher, personal communication, 2003), which further support the presence of such an intrusion. The zone where interferometric coherency is lost probably experienced intense surface fracturing associated with the intrusion. The east-west dimension of this zone is about 200 m, suggesting the formation of a small laccolith, i.e., a shallow intrusion between two subhorizontal layers with a domed roof [*Johnson and Pollard*, 1973; *Pollard and Johnson*, 1973]. Indeed, *Pollard and Johnson* [1973] showed from analogue experiments and theoretical derivations that laccoliths can fracture the ground surface over the top of the intrusion. The depth of the intrusion is estimated by an inversion later in this section.

3.5.3 Analysis and results

The main dike that created the heart-shaped displacement pattern and the superficial intrusion along the southern rift zone is modelled. The secondary eruption close to the southern border of the Enclos Fouqué caldera is not associated with any ground displacements.

For the main dike intrusion, inversions with superficial segments corresponding to those reported by the observatory (Figure 3.13) resulted in the vertical length of the segmented part (D_top) close to zero. As the precise eruptive fissure locations are difficult to identify because of lava flows, it is possible that the eruptive fissure was not segmented. For this reason, the different fissure segments are neglected and the dike top is assumed to be entirely connected to the ground. Preliminary inversions also found that data are better explained if the bottom side has the same curvature as the top side instead of being a straight line, as was the case for the single dike model of July 1999 (Figure 3.25). Thus, the same curvature as the dike top side is assumed for the dike bottom side.

The maximum probability model (Figure 3.28a; #990901 on Table 3.2) explains 93% of the observed data (Figure 3.28b). The model has a mean depth of around 250 m below the ground and a subvertical dip. The residuals on the eastern side in the Dolomieu crater area may indicate a deeper source.

The presence of a deeper source is tested by extending a part of the dike at depth at its northern end (Figure 3.29a). The extended part is subvertical, with its horizontal position at the border between Bory and Dolomieu craters. The bottom is set to 1700 m above sea level: the same bottom elevation as the February 2000 dike (Section 2.3.4). Assuming the same overpressure as the main part, this dike model better explains the heart-shape displacement pattern (Figure 3.29b). The percentage of explained data for this model was calculated to be 94%, using the same data set as the maximum probability model corresponding to a single dike (Figure 3.28a, 93% of data explained). This model is also consistent with the seismicity which is immediately below the bottom of the extended part. This result may indicate the existence of a subvertical feeding path under the summit, which was perhaps shared by the February 2000 eruption.

Displacements of 2.8 cm maximum (one fringe) associated with the shallow laccolithic intrusion connecting the main and southern secondary eruption sites are next modelled. The principal aim here is to estimate the depth of the laccolith. Here, the source is modelled by a half oblate ellipsoid, convex upward (Section 2.2). The bottom plane of the half ellipsoid is fixed to be parallel to the topography. Inversion of the data surrounding the incoherent area only explained the displacements east of the incoherent area with a geometry close to a dike (Figure 3.30, #990902 on Table 3.2). This is probably due to the simplified geometry considered. The horizontal extension of the model is probably far from reality. However, the vertical extension

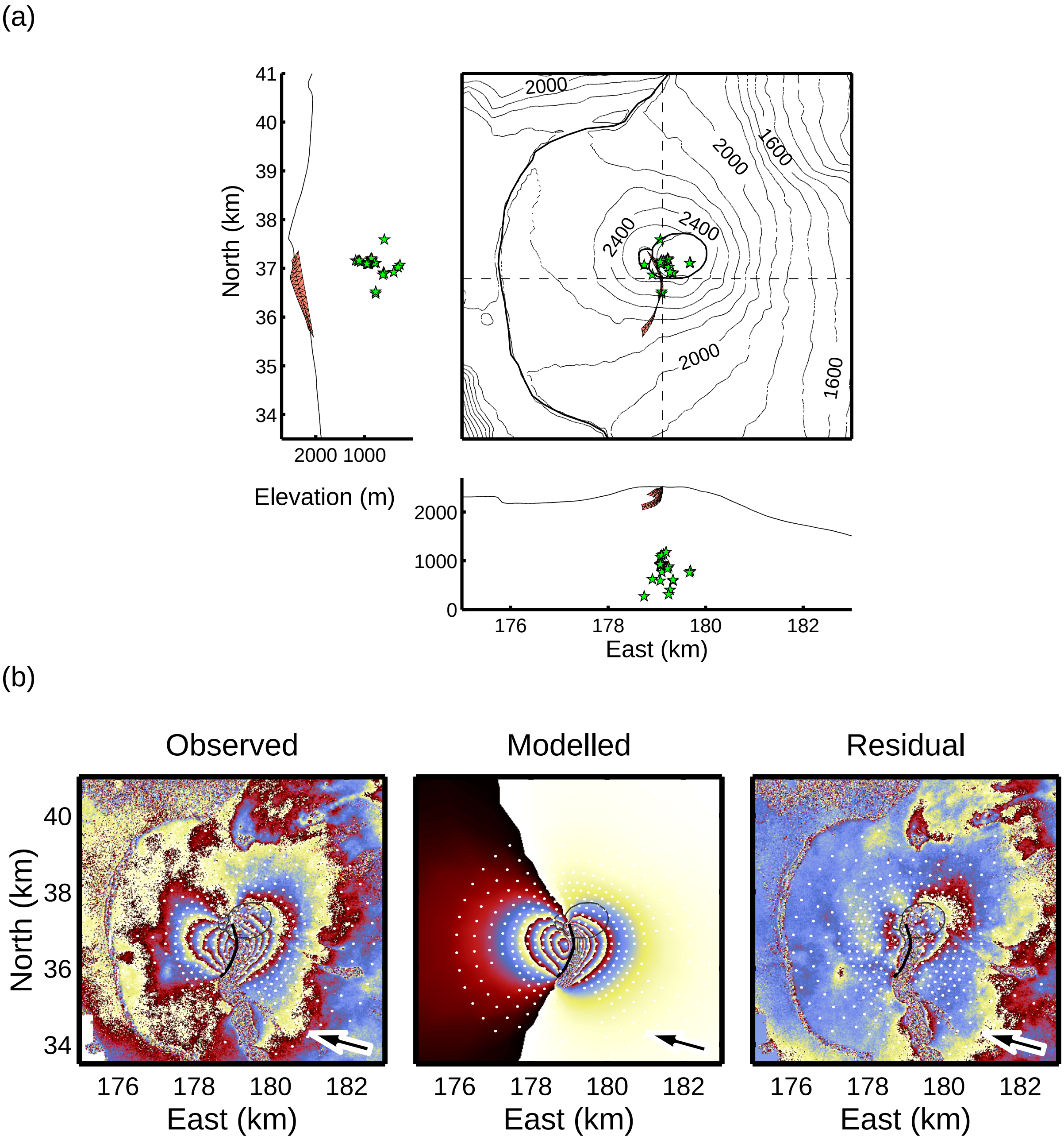

Figure 3.28: ***[September 1999]*** *(a) Geometry of the maximum-probability dike model (#990901 on Table 3.2) associated with the main eruption site in the summit and southern flank zone, plotted with the relocated seismicity [Battaglia, 2001]. Appraisal indicates deepest part lying 230–270 m beneath the ground. (b) Observed, modelled and residual interferograms for the dike model in (a). The residual in the Dolomieu crater area may indicate a deeper source connecting to the dike. The black line indicate the eruptive fissures which is connected to the dike. White dots represent subsampled data points used in the inversion.*

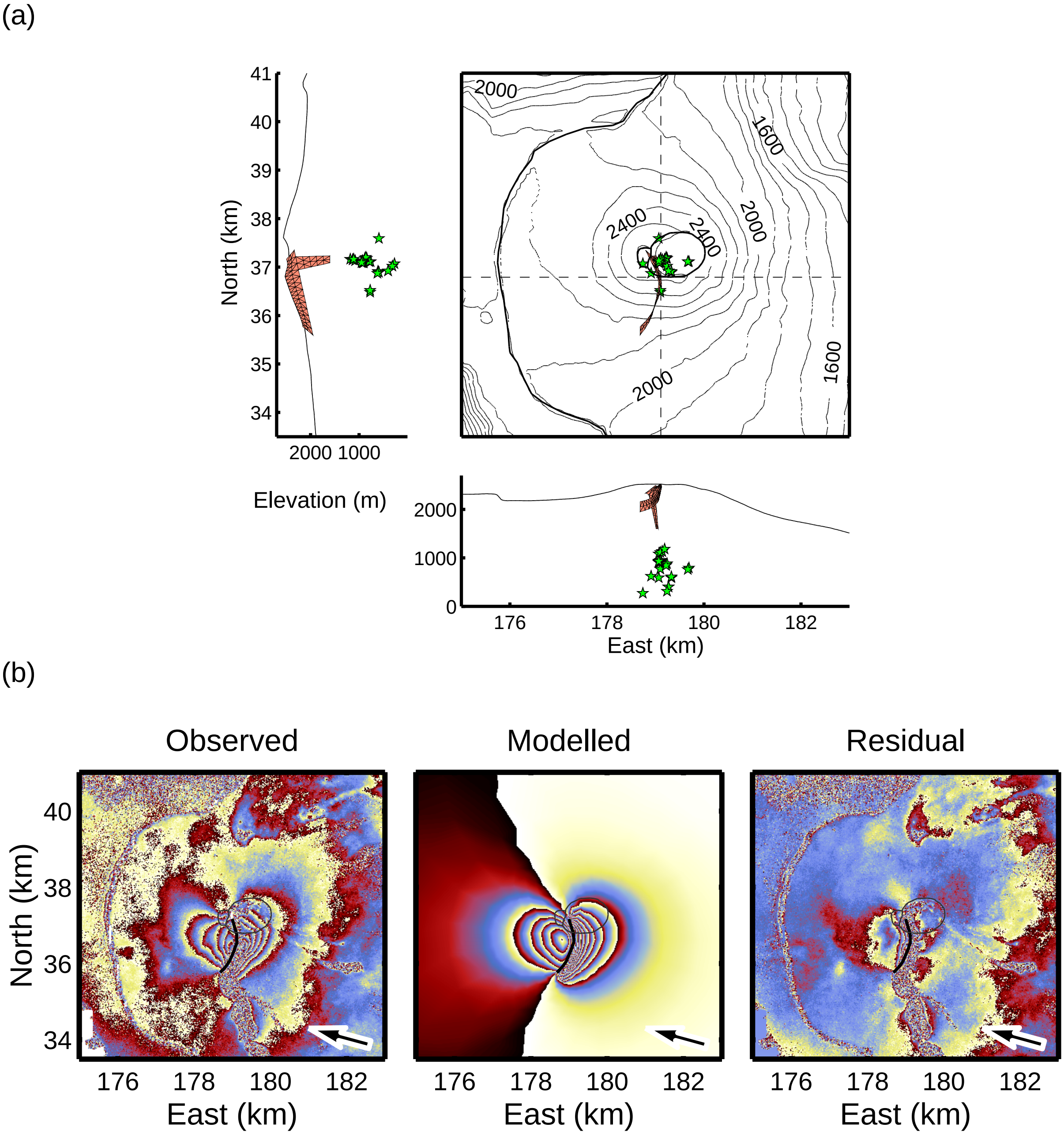

*Figure 3.29: **[September 1999]** (a) Geometry of the dike of the maximum-probability dike (Figure 3.28a) connected to a narrower magma path rooted 1700 m above sea level. (b) Observed, modelled and residual interferograms for the dike model in (a). The heart-shaped displacement pattern is well reproduced.*

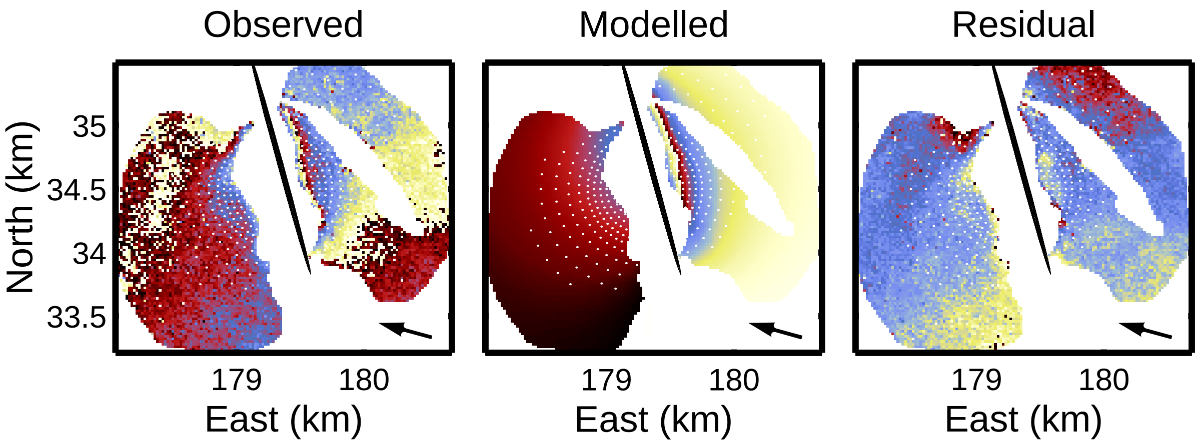

*Figure 3.30: **[September 1999]** Observed, modelled and residual interferograms, corresponding to a half oblate ellipsoidal pressure source whose bottom plane lies parallel to the topography. White dots and black mesh indicate subsampled data points and the pressure source estimated from an inversion, respectively.*

(depth) can give an inference on the intrusion depth. The top and bottom of the laccolith were estimated at about 45 m and 120 m below the ground, respectively.

Preferred Model

For the dike intrusion corresponding to the primary eruption site, a subvertical dike whose depth lies around 250 m (Figure 3.28a) and the subvertical dike connected to a dike-like feeding path (Figure 3.29a) equally well explained the observed interferogram (explained data 93% and 94%, respectively). The latter is proposed as the preferred model, however, because the symmetric fringes are better reproduced. For the shallow laccolithic intrusion connecting the primary and secondary eruption sites, no model was reliable enough to be proposed; however, the intrusion depth was roughly estimated at 45–120 m below the ground.

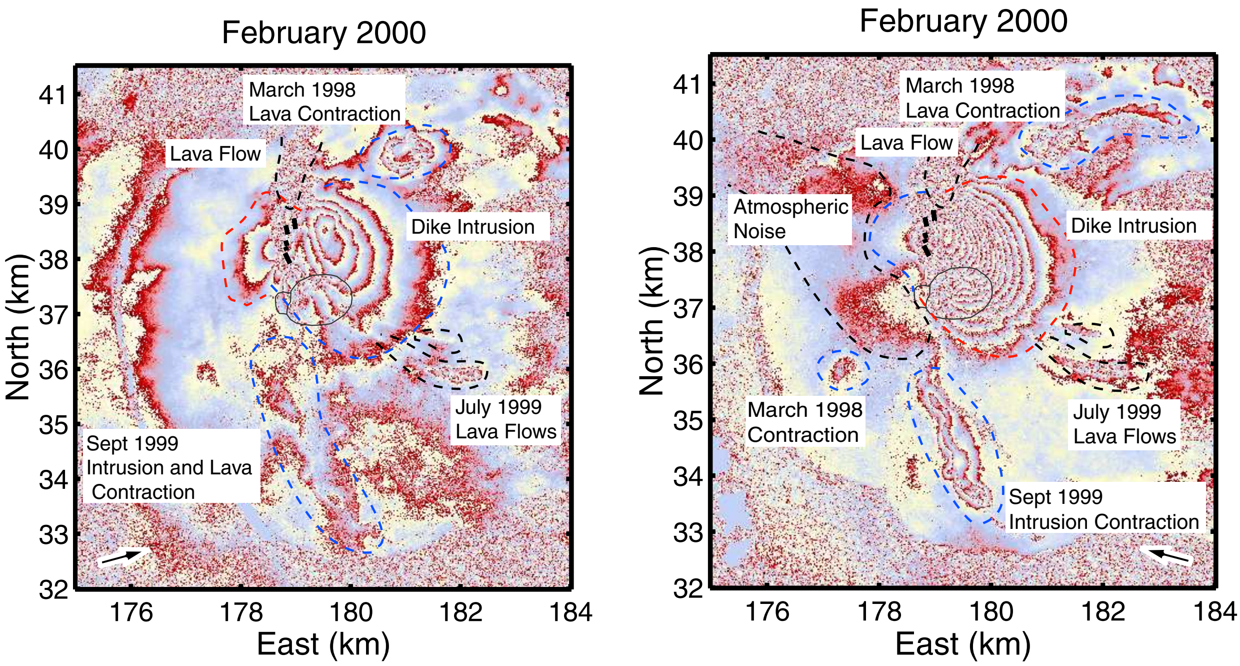

Figure 3.31: Interpretation of signals of the February 2000 interferograms. (left) For an ascending interferogram (Figure 3.4b). (right) For a descending interferogram (Figure 3.4c). Red dashed curve: displacements toward the satellite. Blue dashed curve: displacements away from the satellite. Black dashed curve: decorrelated area due to lava flows and atmospheric noise.

3.6 February 2000 Eruption

Figure 3.31 gives interpretation of the signals of an ascending (Figure 3.4b) and a descending (Figure 3.4c) interferograms for the February 2000 eruption. Refer to Section 2.3.4 for the analysis. The inversion result is included in Table 3.2 (inversion #000201).

3.7 June 2000 Eruption

3.7.1 Overview

Unlike the preceding eruptions, long-term anomalies in seismicity and deformation were observed for about two weeks before the eruption started on 23 June: (1) 12 deep earthquakes were recorded at around 6 km below sea level between 9-14 June, (2) a summit extensometer recorded a change from the beginning of the month, and (3) a tiltmeter recorded a tilt change since 12 June. One day before the eruption, a small seismic swarm with 36 events occurred. On 23 June, another seismic swarm occurred with much stronger earthquakes (magnitude up to 2.5) coincident with tilt changes. The seismicity and tilt changes indicated an intrusion that migrated toward the summit and then to the southeastern flank. Two sets of eruptive fissures opened on the southeastern flank of the volcano. The activity quickly localized to the lower one and lasted until 30 July.

3.7.2 Sources of interferometric signals in data

As stated, two ascending and one descending interferograms are available for inversions (Figures 3.5a, b and Figure 3.11). To the north of the eruptive fissures, the ascending interferograms show about 10 cm of displacements away from the satellite in the summit area and 17 cm of displacements toward the satellite on the southeastern flank (Figure 3.32). The area south to the fissures moved about 8 cm away from the satellite. The second image of the interferogram from an ascending orbit F2N (Figure 3.5a) was captured on 30 June 2000, only 7 days after the eruption onset. The similarity in the displaced area indicated in the two ascending interferograms shows that the dike had finished its formation 7 days after the eruption onset.

The satellite captured an image from the descending orbit F4F at 1458 UT on 23 June just an hour after the tremor emergence. The interferogram showing the displacements accumulated until this moment was created by taking the residual of two interferograms of F4F orbit; the first one includes the displacements caused by the February dike and by the June dike before 23 June (31 Jan. 2000 – 23 June 2000), and the second one only includes those created by the February dike (14 Dec. 1999 – 19 March 2000) (Figure 3.33). This interferogram is of better quality than those calculated with an image captured between Februrary and June 2000 eruptions, in which case the values of altitude of ambiguity were smaller than 12.5 m. No lava flow can be recognized in the figure, indicating that no or little amount of lava had been emitted in the first hour after the tremor emergence. On the other hand, it is interesting to note that the dike formation had almost completed to its final shape (compare with Figure 3.5b) before or just after the eruption onset. Indeed, the displaced area in Figure 3.5b is slightly more extended to the east than in Figure 3.33, indicating that the dike only slightly grew farther to the east after the eruption onset. The maximum displacement reaches 75% of that shown in 3.5b, suggesting that around this amount of the dike volume had been emplaced prior to the eruption onset. In this study, the interferogram shown in Figure 3.33 is not modelled.

From the descending direction, displacements toward the satellite reach 42 cm north of the eruptive fissures, and those away from the satellite amount to only 4 cm south of the eruptive fissures (Figure 3.32). In the inversions, the interferogram whose altitude-correlated fringes are removed (Figure 3.11) is used. Small displacements are indicated in the summit area north of Dolomieu crater, but these displacements are too small to be distinguished from an atmospheric disturbance.

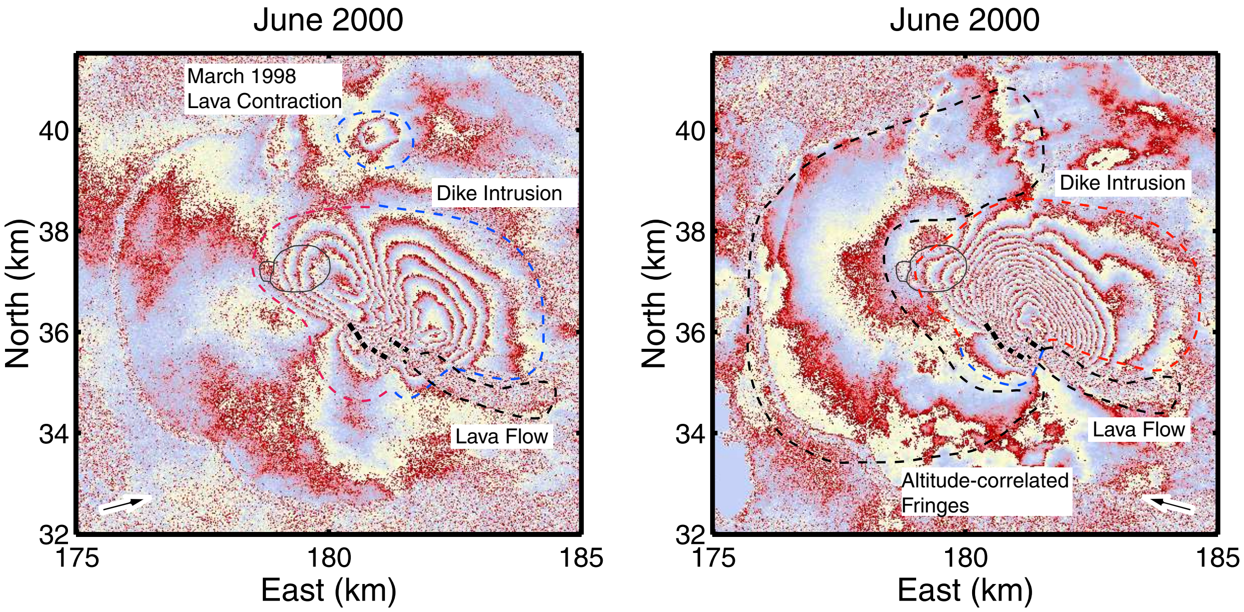

Figure 3.32: Interpretation of signals of the June 2000 interferograms. (left) For an ascending interferogram (Figure 3.5a). (right) For a descending interferogram (Figure 3.5c). Red dashed curve: displacements toward the satellite. Blue dashed curve: displacements away from the satellite. Black dashed curve: atmospheric noise and decorrelated area due to lava flows.

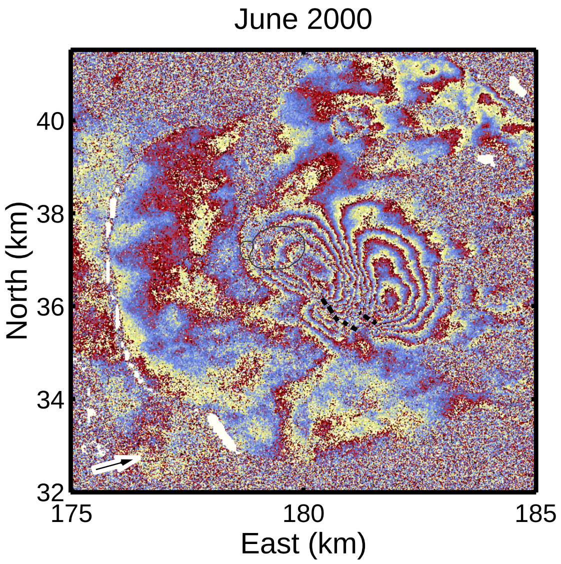

Figure 3.33: Descending interferogram created by taking residuals of those of 31 Jan. 2000 – 23 June 2000 and 14 Dec. 1999 – 19 March 2000 (both in F4F orbit). This interferogram shows the displacements until one hour after the tremor onset. Black lines indicate eruptive fissures [after Villeneuve, 2000]. Note that the extension of the eastern fissures is shorter than the fissure assumed in inversion (black lines in Figure 3.5).

3.7.3 Analysis and results

The interferograms from the three directions (Figures 3.5a, b and Figure 3.11) were successfully unwrapped using the recursive algorithm (Section 2.4.3). For simplicity, the two sets of eruptive fissures are approximated by two continuous fissures. The one at the lower altitude was slightly extended downslope from the position given in *Villeneuve* [2000] so that it is consistent with the interferometric data. The two ascending data (Figures 3.5a and 3.5b) and the corrected descending data (Figure 3.11) are subsampled and simultaneously inverted. The displacements are inverted assuming the following three models:

(Model A)	Single dike without along-dip curvature,
(Model B)	Single dike with along-dip curvature,
(Model C)	Two dike model.

Model A: single dike with along-dip curvature

First, a single dike with a straight bottom side is assumed. The assumed parameters are: P0, Dip, Shear, Botelv, Botlen, Twist, Botang (Figure 2.2) and D_top (Figure 2.4a), making a total of eight. The obtained maximum probability model (inversion #000601 in Table 3.2; Figure 3.34) is close to a trapezoid, as the model found for the February 2000 eruption, with its bottom side lies parallel to the topography 1300 m beneath the ground. The maximum probability model is far from explaining the data (Figure 3.35). From a standpoint that this is due to the approximation of a straight bottom side, a curved bottom side is then assumed (inversion #000602; see Figure 2.5 for the definition of the bottom side curvature). The maximum probability model, however, has a geometry very similar to the one corresponding to #000601 with the bottom side hardly curved (Table 3.2).

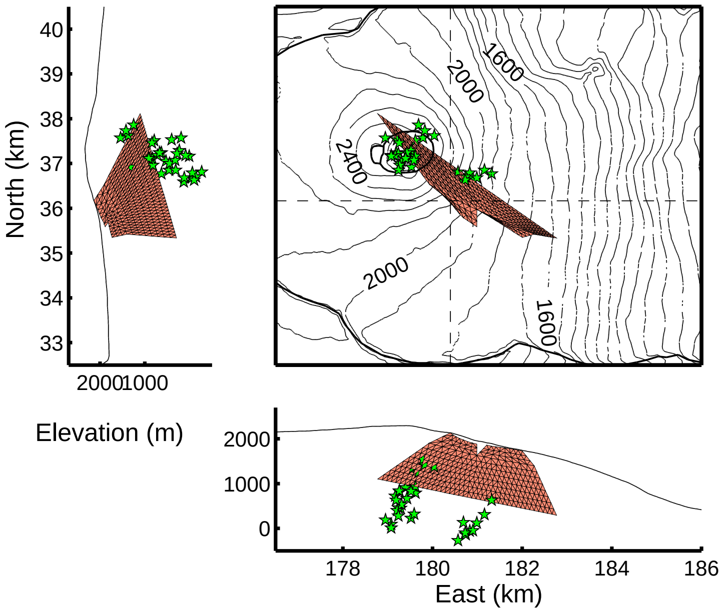

Figure 3.34: ***[June 2000, Model A]*** *Geometry of the maximum probability dike having a straight bottom side (#000601 on Table 3.2).*

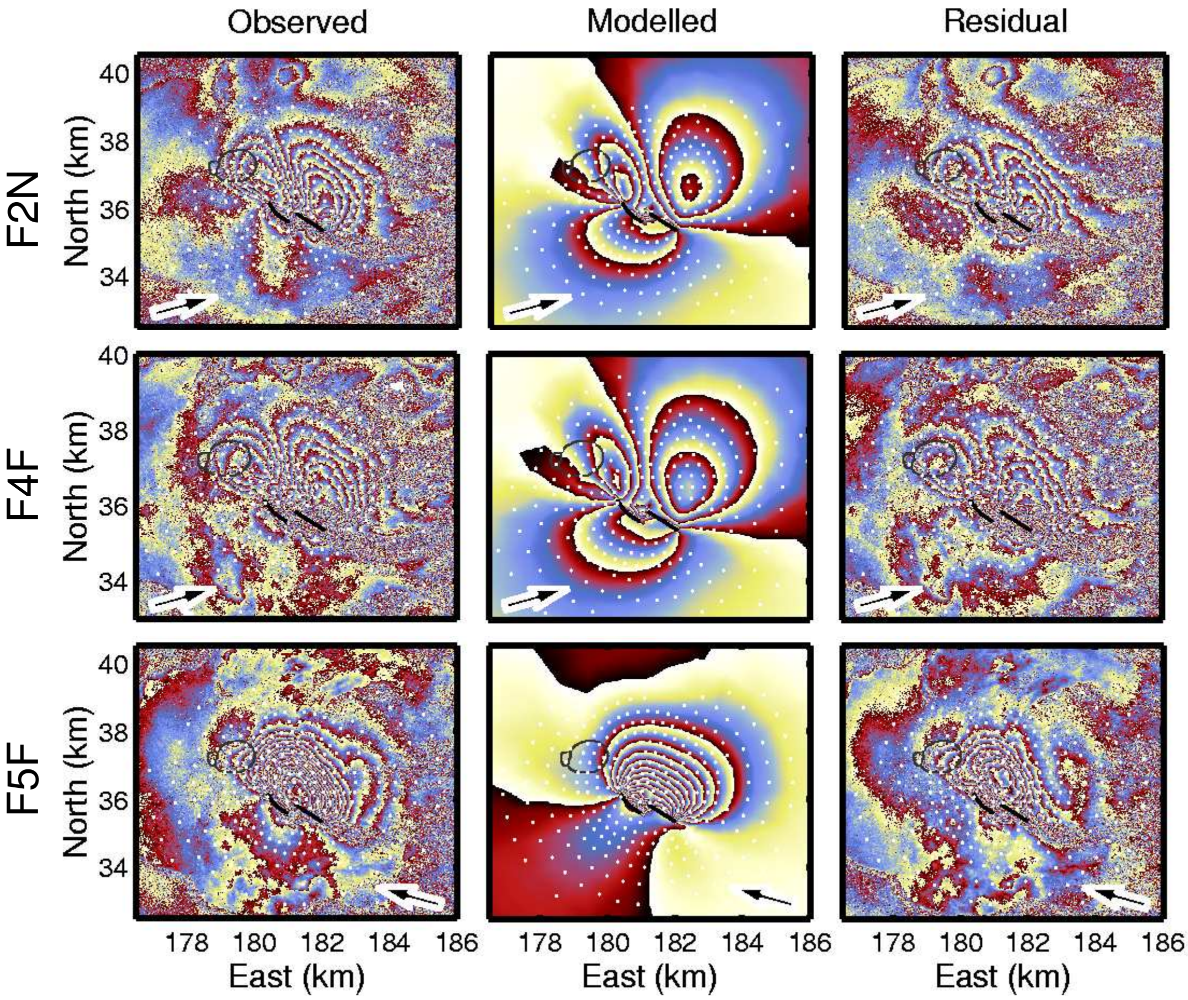

Figure 3.35: ***[June 2000, Model A]*** *Observed, modelled and residual interferograms corresponding to the dike model in Figure 3.34. This model is far from explaining the observed data. White dots and black lines indicate subsampled data points and the assumed eruptive fissures (top of the dikes), respectively.*

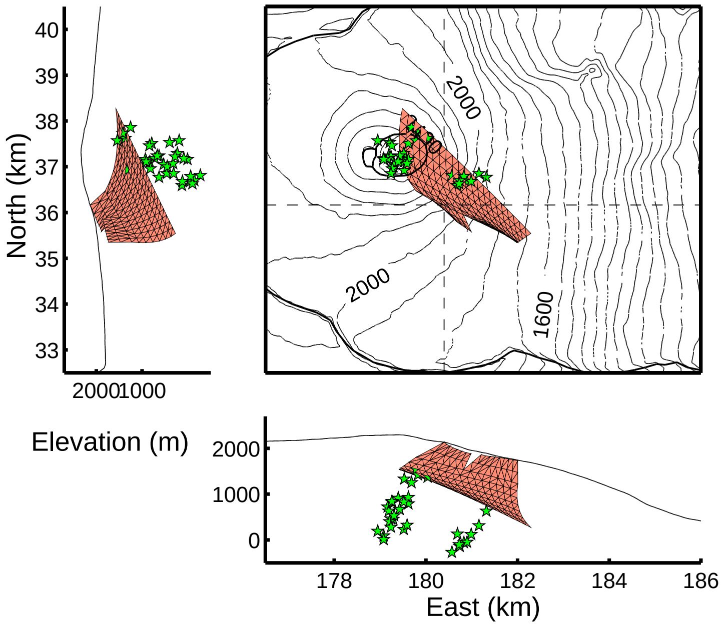

Figure 3.36: ***[June 2000, Model B]*** *Geometry of the maximum probability dike having a curvature of the bottom side and along-dip curvature as model parameters (inversion #000603 on Table 3.2). The bottom side lies subparallel to the topography at about 1300 m beneath the ground.*

Model B: single dike with along-dip curvature

Next, along-dip curvature of the dike (see Figure 2.5) is additionally introduced to explain the data, making a total of nine model parameters (#000603 on Table 3.2). This model explains the data to a certain extent (81%), with about 4 fringes of residual displacements for each direction (Figure 3.37). The geometry of the maximum probability model is significantly curved in the along-dip direction (Figure 3.36). While such curved dikes are not often found in the field, some were identified in the exposure of the Cilaos dike complex, Piton des Neiges [*Maillot*, 1999]. This result may also indicate two different intrusions, one horizontal (sill) and the other vertical (dike), starting from more or less the same point.

Model C: Two dikes

Finally, it is assumed that, on the ascending interferograms, the displacements toward the satellite to the east and away from the satellite to the west (Figure 3.5a) were caused by different pressure sources in the east and west. In order to determine the source of the western displacements, an inversion was performed without the data in the eastern area (#000604 on Table 3.2). This naturally creates large residuals in the eastern area unused in the inversion; but the displacements toward the satellite especially in the descending direction are well explained.

The result of the preceding inversion (#000604) is consistent with the idea that there were two independent intrusions corresponding to the two sets of eruptive fissures. This idea is tested by a simultaneous inversion, because the two sources are close to each other and their interaction cannot be neglected. Here, a forward modelling is done in such a way that a single boundary element computation takes into account the two sources (Section 3.2.1 and Figure 3.12c). Preliminary inversions with some fixed parameters did not lead to a better fit and to

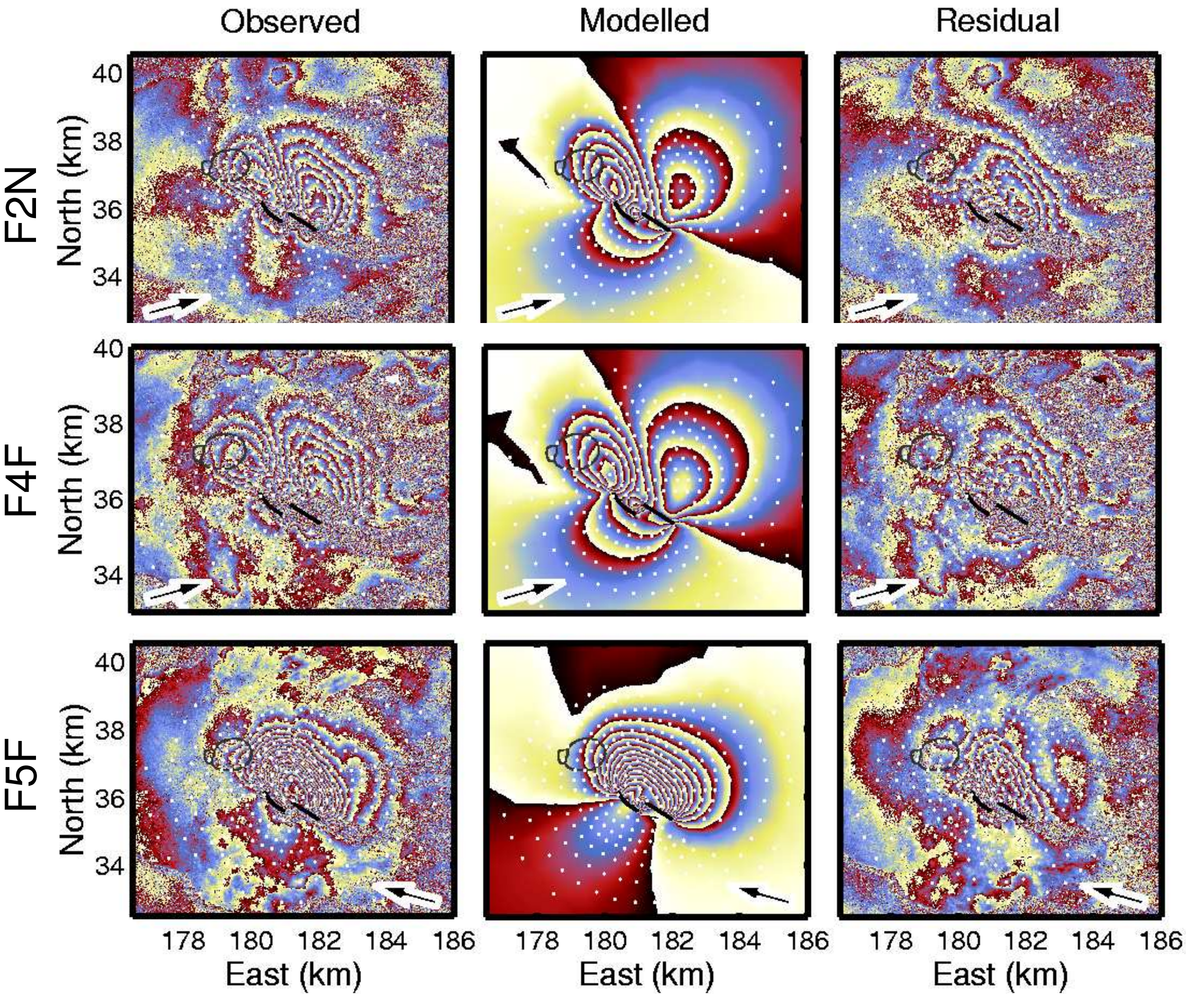

Figure 3.37: ***[June 2000, Model B]*** *Observed, modelled and residual interferograms for the dike model in Figure 3.36. This model explains 81% of the observed data. Three to four residual fringes for each satellite direction suggest that the intrusion was more complex than we assumed. White dots and black lines indicate subsampled data points and the assumed eruptive fissures (top of the dikes), respectively.*

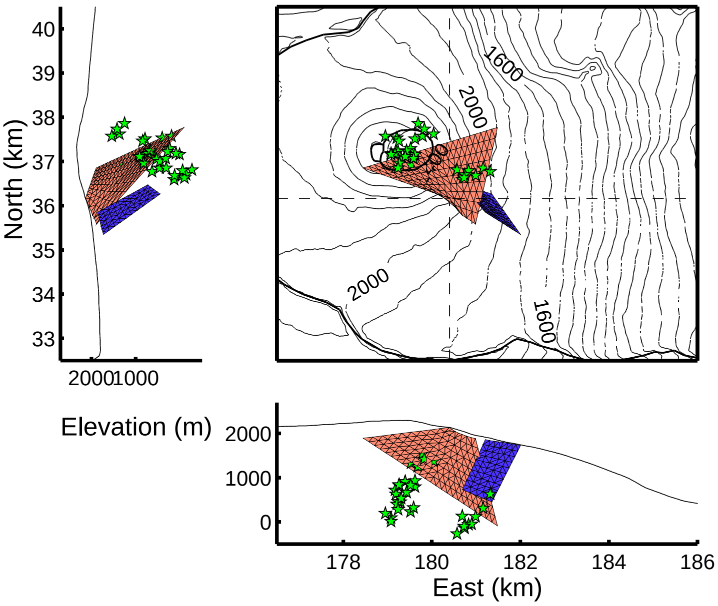

Figure 3.38: ***[June 2000, Model C]*** *Maximum probability model for the two dikes obtained from a simultaneous inversion (#000605 on Table 3.2).*

a realistic model than the single dike models (Model A and B). Thus, an inversion with 14 parameters, i.e., the same seven parameters taken in the JGR paper for each dike, is attempted. A reduced number of models $n = 5$ at each iteration is used for a quick convergence of the solution. The western dike indicated by the maximum probability model (shown in red in Figure 3.38; inversion #000605 on Table 3.2) extends beneath the summit, dips toward the north (Dip 63°), and is originated from sea level on the eastern end of the bottom side. The eastern dike (shown in blue in Figure 3.38) is closer to a rectangle, and also dips toward the north (Dip 74°). The overpressure of the eastern dike is three-fold larger than that of the western one, and the volume of the eastern dike amounts to half that of the western one. The two clusters of hypocenters of the preeruption microearthquakes may reflect a magma feeding path for the two dikes. However, the strike direction of the bottom side of the western dike is different from that of the top side by about 70° (parameter Twist), which makes the geometry to be mechanically unexplainable. Figure 3.39 compares the modelled displacements with the observed data. The model explains 80% of the observed data, which is similar to that of Model B (81%). Note that, due to an exploitative manner of the inversion, it is possible that the solution is caught in a local minimum.

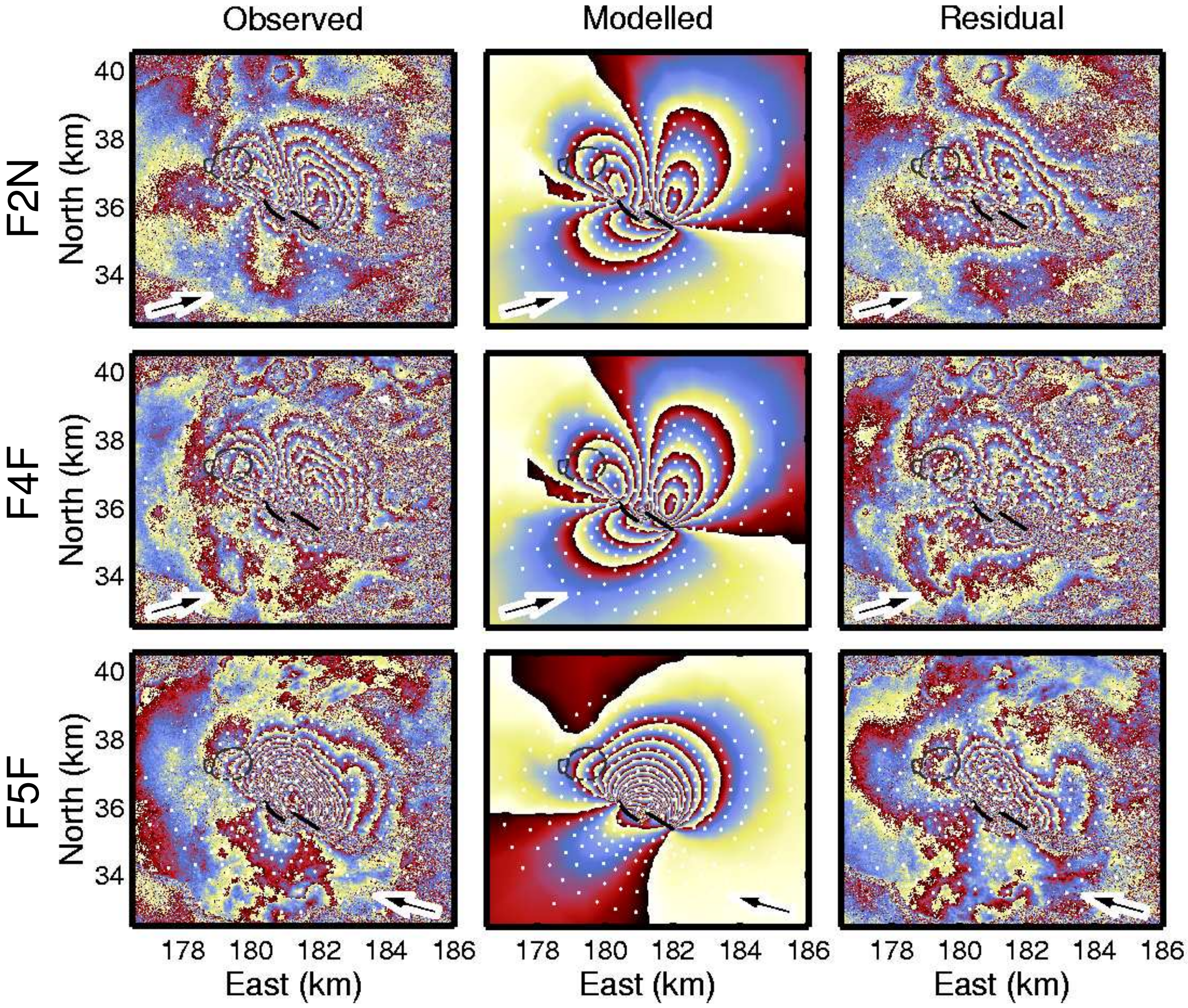

Figure 3.39: ***[June 2000, Model C]*** *Observed, modelled and residual interferograms for the dike model in Figure 3.38. This model explains 80% of the observed data. White dots and black lines indicate subsampled data points and the assumed eruptive fissures (top of the dikes), respectively.*

Preferred Model

The vertically-curved dike (Model B) best explains the observed displacements and thus this model is proposed as the preferred model. However, even this model did not fully explain the observation. What would we need to better explain the data? Three possibilities can be considered: (1) the overpressure is non-uniformly distributed, (2) the dike has a more complex geometry than that assumed, and (3) the inversions did not converge toward the global minimum. The third possibility is less likely because the same kind of inversions successfully find realistic models that well explain data for the four other eruptions.

Regardless of the significant misfits, all the inversion results indicate that the deepest part of the intrusion is shallower than about 1500 m, that the dike dips (dikes dip) toward the northeast, and that the eastern end of the bottom side is located beneath the summit Dolomieu crater.

3.8 Summary

The analyses in this chapter indicate detailed geometry and overpressure of the intrusions associated with the 1998–2000 eruptions at Piton de la Fournaise. Figure 3.40 shows the preferred models determined after the analysis for each eruption. The wide fringes associated with the March 1998 eruption were found to originate either from a deep dike (around sea level) connecting to the northern eruptive fissures, or from a sill intrusion at a depth of around 500 m above sea level. The March 1998, July 1999, February and June 2000 dikes were found to have eastward or northeastward dip angles, whereas the September 1999 dike at the summit and southern flank was found to be subvertical. For the June 2000 eruption, a vertically curved intrusion best explained the data, though a more complex geometry is needed to fully explain the data. For the July 1999 and September 1999 eruptions, one intrusion associated with the main eruption site and another one connecting the main and secondary eruption sites were observed on the interferograms and were modelled. Inversions indicated that the secondary intrusion associated with the July 1999 eruption is a dike originating at 350 m beneath the ground, and the secondary intrusion associated with the September 1999 eruption is probably a shallow laccolith at a depth range of 45–120 m.

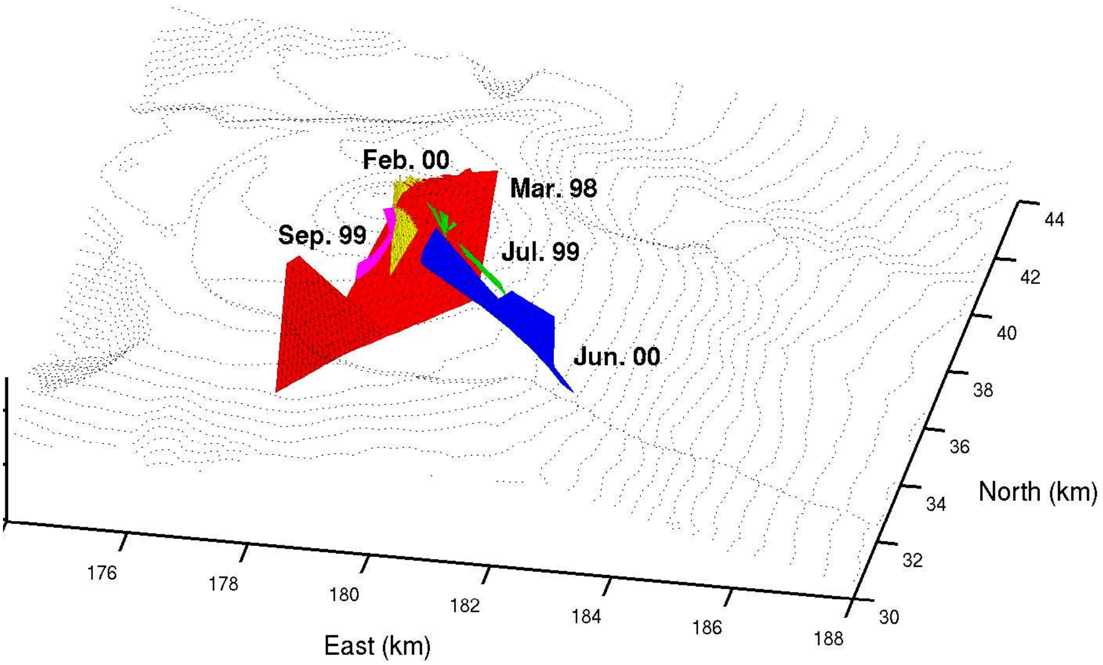

Figure 3.40: Perspective view for the preferred models determined after the analysis of each of the five eruptions of March 1998–June 2000, plotted with topographic contour lines of 100 m interval.

Chapter 4

Storage, Transfer, Emplacement of Magma and Volcano Growth

This chapter discusses the volcano-tectonic system of Piton de la Fournaise based on the dike emplacement geometries and overpressures estimated in Chapter 3 for the five eruptions between March 1998 and June 2000. The first section discusses the magma storage system. The lower limits of the depth of the magma source for the five eruptions are first calculated. Then, a shallower storage system above sea level is discussed with considerations of buoyancy and cooling rate of magma. The second section concerns the magma transfer and emplacement mechanisms. The geometry and size of the conduit are first investigated, then lateral dike propagation and possibly-associated pit-crater collapses, and relations between dike emplacements and seismicity are discussed. In the third section, effects of dike intrusions on the evolution of the volcano are discussed. This last section includes stress change analyses to quantitatively discuss (1) the influence of the stress field associated with dike intrusions on the following intrusions, and (2) the possible triggerings of seaward landslides by dike intrusions.

4.1 Magma Storage System

4.1.1 Depth of the source magma reservoir

Section 2.3.5 considered the factors affecting the volume balance of the magma leaving the source and the intruded and extruded magma, and concluded that the magma balance should roughly hold. However, the compressibility of exsolved gas in magma in the source also affects the volume balance [*Johnson et al.*, 2000]. From gravity and leveling measurements, *Johnson* [1992] showed that, during the 1983–1986 Pu‘u‘Ō‘ō eruption on Kilauea volcano, the volume change of the magma chamber was only 20–25% of the volume of magma transferred out of the chamber. The amount of exsolved gas, however, seems to be significantly different for each event; during the deflation events in November 1975, August 1981, and January 1983, the proportion was 50–70% [*Johnson et al.*, 2000].

Taking into account the compressibility of the magma in the source, the minimum possible depths of the magma source are reestimated based on the observation that deflation sources are not indicated in the interferograms (Figure 4.1; see Section 2.3.5 for other factors that might affect the magma budget). Consideration on the mechanical evolution of basaltic magma reservoirs suggests a spherical or a laterally elongated reservoir geometry [*Parfitt et al.*, 1993]. Therefore, the source is assumed to be a sphere or a sill-type horizontally lying square sheet.

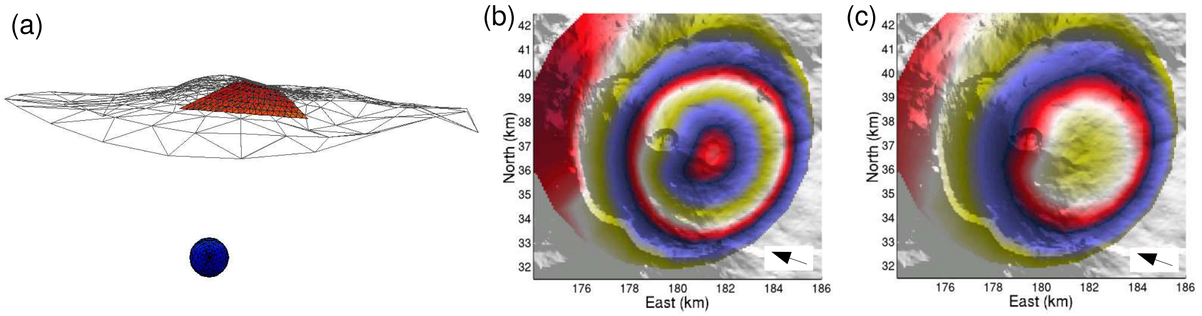

Depth 2 km b.s.l.

3 km b.s.l.

Figure 4.1: Example showing the method for estimating the minimum depth of the magma source. (a) Spherical magma reservoir of 1 km in diameter beneath the summit is assumed to deflate corresponding to the amount of intruded/extruded magma volume of the February 2000 eruption. (b) Modelled ground displacements when the center of the reservoir is at 2 km below sea level. (c) Same for the reservoir at 3 km below sea level. If the number of fringes are less than two (for the March 1998 eruption) or one (for the other four eruptions), it is considered that the fringes corresponding to the deflation source are indistinguishable.

The center of the sphere and sill-type sheet is set to be located beneath the summit. The diameter of the sphere and the length of the sill-type sheet are assumed to be 1000 m. As the detectability threshold, it is assumed that if the number of fringes is less than two, for the March 1998 event, and one, for the other four events, the fringes corresponding to the deflation source are indistinguishable. Ratio of intruded and extruded magma volumes (V_{out}) to source volume change (ΔV_c) 0.2, 0.5 and 1 are assumed corresponding to progressively smaller compressibility of the source.

The results are summarized in Table 4.1 for the spherical source, and in Table 4.2 for the sill-type source. The sill-type source gives systematically larger estimates than those for the spherical one. As expected, the more compressible the magma in the source is, the shallower the source can be. This shows that few things can be said about the minimum possible source depth without a proper knowledge of the exsolved gas content.

For comparison, Figure 4.2 shows the hypocenters of the preeruption microearthquakes. Since the preeruption microearthquakes are probably induced by magma intrusions, it is reasonable to consider that the source is located below the lower limit of the hypocenters. Accordingly, the minimum possible depth of the source indicated by the seismicity data is 5 km below sea level for the March 1998 eruption and sea level for the other four eruptions (here the deep microearthquakes associated with the June 2000 event at 5–7 km below sea level is not considered because it is not obvious if they correspond to an intrusion). As the source depth estimated from displacements cannot be shallower than that indicated by seismicity, our results indicate that, if the source is spherical, ΔV_c must be larger than 0.2 V_{out}. If we assume that magma cannot travel at depth without causing microearthquakes, then a spherical source location would be consistent with an exsolved gas content such that $\Delta V_c = 0.5\,V_{out}$, and a sill-like source would be consistent with $\Delta V_c = 0.2\,V_{out}$.

It should be noted that the above consideration does not exclude the possibility of the presence of shallower magma reservoirs as in the model of *Lénat and Bachèlery* [1990] (Figure 1.5). As discussed in Section 2.3.5, if magma in shallower reservoirs is pushed by magma of

Table 4.1: *Minimum possible depth of spherical magma source to be undetectable. The minimum possible depth is defined at the roof of the sphere 500 m above the center.*

	Lava Vol. (Mm^3)	Dike Vol. (Mm^3)	V_{out} (Mm^3)	Elev. (km) $\Delta V_c = V_{out}$	Elev. (km) $\Delta V_c = 0.5V_{out}$	Elev. (km) $\Delta V_c = 0.2V_{out}$
March 1998	45	5	50	-7.49	-5.24	-2.89
July 1999	1.8	0.2	2.0	-1.10	-0.24	0.97
Sept. 1999	1.5	0.2	1.7	-0.80	0.24	1.15
Feb. 2000	7.0	1.7	7.7	-3.91	-2.31	-0.59
June 2000	10	1.7	11.7	-5.01	-3.24	-1.34

Table 4.2: *Minimum possible depth of sill-type magma source to be undetectable*

	Lava Vol. (Mm^3)	Dike Vol. (Mm^3)	V_{out} (Mm^3)	Elev. (km) $\Delta V_c = V_{out}$	Elev. (km) $\Delta V_c = 0.5V_{out}$	Elev. (km) $\Delta V_c = 0.2V_{out}$
March 1998	45	5	50	-11.1	-10.0	-5.07
July 1999	1.8	0.2	2.0	-2.70	-2.17	0.11
Sept. 1999	1.5	0.2	1.7	-2.33	-1.84	0.24
Feb. 2000	7.0	1.7	7.7	-6.44	-5.72	-2.07
June 2000	10	1.7	11.7	-7.90	-7.09	-3.02

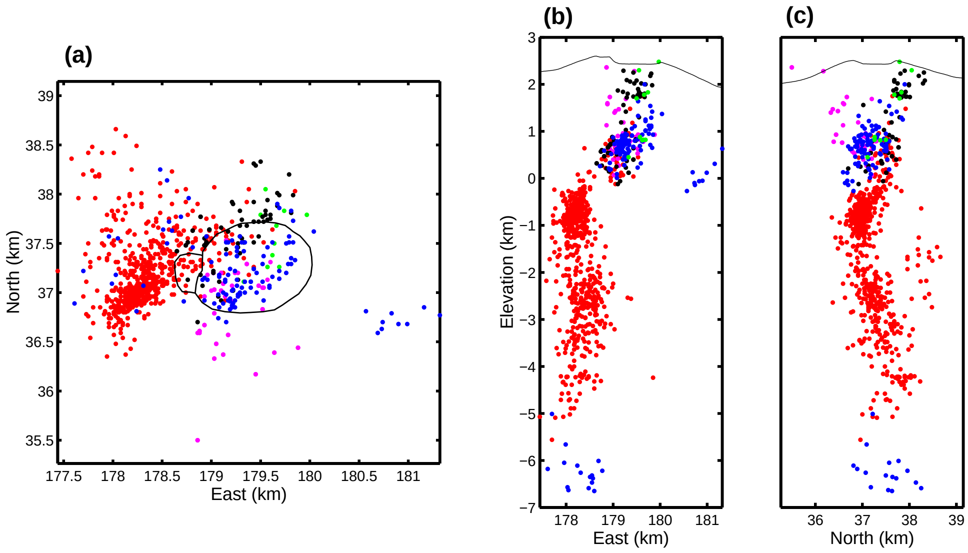

Figure 4.2: Hypocenters of the preeruption microearthquakes [Data courtesy of the observatory of Piton de la Fournaise]. Red = March 1998, Green = July 1999, Magenda = September 1999, Black = February 2000, Blue = June 2000. (a) Map view. (b) West-east cross-section. (c) South-north cross-section.

the same pressure and density from depth, no displacements are created. In this situation, the shallower reservoirs only serve as buffers.

4.1.2 Shallow magma storage at a level of neutral buoyancy

It is reasonable to assume that hypocenters of the preeruption microearthquakes are located around magma feeder paths. Comparisons of the seismicity and the geometries of the dike models determined in Chapter 3 suggest lateral propagation of dikes at a shallow level, because the horizontal dimensions of the seismic swarms are narrower than the widths of the modelled dikes (except for the March 1998 case which is not obvious). Lateral propagation of dikes occur when magma is neutrally buoyant [*Dieterich*, 1988; *Lister and Kerr*, 1991; *Pinel and Jaupart*, 2004; *Rubin and Pollard*, 1987]; more specifically, when the negative buoyancy force exerted on the magma above a certain level (level of neutral buoyancy) balances the positive buoyancy force exerted on the magma below this level. As mentioned in Section 1.4.1, buoyancy of magma is governed by the contrast of the densities of magma and host rock and also by the variation in the gradient of the tectonic stress normal to the dike surface (Equation 1.4). Considering that most of the dikes analyzed in Chapter 3 were estimated to be rooted at 1000 m or shallower beneath the ground, the level of neutral buoyancy for the magma in dikes is likely to be located at shallower than 1000 m in the central cone of Piton de la Fournaise. Since magma reservoirs are expected to be developed at depths where magma is neutrally buoyant, this suggests the existence of magma reservoirs at this shallow level.

Indeed, there are pieces of evidence for shallow (depth of 1000 m or less) reservoirs. The first one is the presence of pit-crater collapses [*Delorme et al.*, 1989; *Hirn et al.*, 1991; *Longpré et al.*, 2004]. A typical volume of the reservoirs should be several Mm^3, considering the size of the collapses (for the March 1986 collapse, diameter 150 m and depth 80 m [*Delorme et al.*, 1989]; for the November 2002 collapse, diameter 250 m and depth 25 m [*Longpré et al.*, 2004]). This is comparable to the volume of lava emitted in a typical eruption. The second piece of evidence is the short duration of preeruption seismic swarms of some eruptions. Two of the eruptions that occurred during a highly eruptive period between 1985 and 1987 (including about 20 eruptive and intrusive events [*Lénat et al.*, 1989a]) had preeruptive seismic swarms of less than 20 minutes (Figure 4.3; *Bachèlery* [1999]). By modelling tilt data, *Battaglia and Bachèlery* [2003] estimated the dike propagation velocity in the last one hour before the onset of the March 1998 eruption to be 0.45 m/s on average. If we assume that magma traveled from sea level to the ground (range of a typical preeruption seismic swarm) in an hour (a typical duration of preeruption seismic swarm), we obtain a vertical intrusion velocity of ~ 0.7 m/s [*Battaglia et al.*, 2005]. Then, we obtain a range of possible depth of the superficial reservoir 540–840 m, by assuming that magma propagated to the ground vertically in 20 minutes with these velocities. Such reservoirs could be created during a single event (eruption or intrusive event) or several events, and may not exist permanently.

4.1.3 Thermal viability of dikes and sills

Lénat and Bachèlery [1990] proposed a shallow magma storage model that consists of a plexus of dikes and sills (Figure 1.5). Following *Turcotte and Schubert* [2002], this subsection calculates the time required for a dike or sill to solidify based on heat conduction equations, and discuss under which conditions the Lénat and Bachèlery's model is plausible.

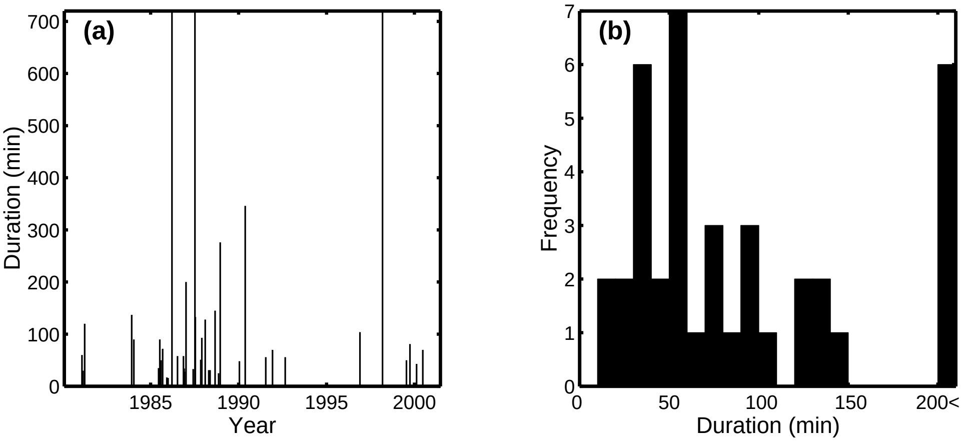

Figure 4.3: (a) Duration of preeruption seismic swarm for the eruptive and intrusive events between 1980 and 1998. The duration is defined by the time starting from the abrupt seismicity rate change till the eruption onset (for eruptions) or the end of the swarm (for intrusive events). The swarms of the March 1986, June 1987 and March 1998 eruptions lasted more than 30 hours. (b) Histogram for the duration of preeruption seismic swarm for the events shown in (a). Two events had less than 20 minutes of duration. 49% of the events had a seismic swarm of less than 60 minutes. Data from Bachèlery [1999].

Here, a one-dimensional dike or sill (i.e., infinite length and finite thickness) is considered. Note that the finite length of dikes or sills shortens the solidification time, meaning that the calculations hereby presented give overestimation of the solidification time. For simplicity, it is assumed that the physical properties of the country rock and solidifying magma are the same. At time $t = 0$, a dike or sill of temperature T_m starts to solidify at the contact of country rock of temperature T_0. The time required for a dike or sill of thickness b to completely solidify is

$$t_s = \frac{b^2}{16\kappa\lambda^2}, \tag{4.1}$$

where κ is the thermal diffusivity. λ is solved from the following equation:

$$\frac{L\sqrt{\pi}}{c(T_m - T_0)} = \frac{e^{-\lambda^2}}{\lambda(1 + \mathrm{erf}\,\lambda)}, \tag{4.2}$$

where L is the latent heat (energy liberated upon the solidification of 1 kg of magma), c is the specific heat (energy required to raise the temperature of a unit mass of material by one degree). erf is called the *error function* and defined by

$$\mathrm{erf}(\eta) = \frac{2}{\sqrt{\pi}} \int_0^{\eta} e^{-\eta'^2} d\eta'. \tag{4.3}$$

Equation 4.2 is solved numerically using Newton's recursive method [e.g. *Press et al.*, 1992].

Mohamed-Abchir et al. [1998] found that hydrothermal minerals of a huge hydrovolcanic event at Piton de la Fournaise had been formed at 180–400°C. *Björnsson* [1985] estimated the temperature at 4–5 km depth in Icelandic rift zones to be 500–600°C. From these studies, country rock temperatures T_0 of 200–600°C are assumed. Figure 4.4 shows the results for typical values of $L = 320\,\mathrm{kJ\,kg^{-1}}$, $T_m = 1200°\mathrm{C}$ and $c = 1.2\,\mathrm{kJ\,kg^{-1}\,K^{-1}}$.

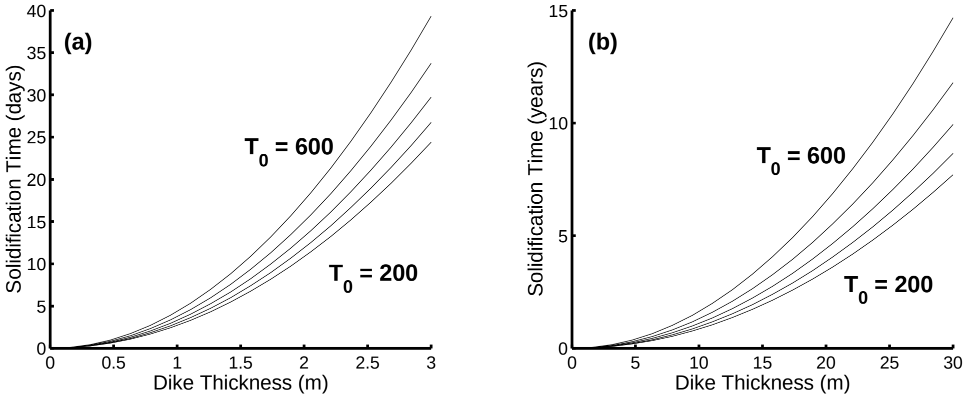

Figure 4.4: (a) Time required for a dike or sill to solidify, as a function of dike thickness. Results for country rock temperatures of 200, 300, 400, 500 and 600°C are presented. See text for other parameter values. (b) Same as (a), for larger dike thickness.

Most of the exposed intrusions at Piton de la Fournaise [*Grasso and Bachèlery*, 1995] and at Piton des Neiges [*Maillot*, 1999] have less than 1 m of thickness. As such dikes or sills should solidify within a few days (Figure 4.4a), it is unlikely that dikes and sills serve as magma storage units. Instead, thicker magma intrusions, laccoliths for instance, may remain molten for a long time (about one year for a thickness of 10 m, Figure 4.4b). Such thick intrusions could be created around the level of neutral buoyancy less than 1000 m beneath the summit (Section 4.1.2). There is no clear evidence or theoretical expectation, however, for the presence of reservoirs between sea level (2600 m beneath the summit) and about 1000 m beneath the summit.

4.1.4 Model of magma storage system

The considerations in this section are summarized in Figure 4.5. From seismicity data, the source that fed the March 1998 eruption should be located at 5 km below sea level or deeper. For the subsequent eruptions, the source can be located at shallower depths, but deeper than sea level (July and September 1999, and February 2000 eruptions) or deeper than 1.3 km below sea level (June 2000 eruption) (Section 4.1.1). At a shallow level less than about 1000 m beneath the summit, small reservoirs having a volume of a few Mm^3 may be located (Section 4.1.2). There is no clear evidence or theoretical expectation for the presence of storage units 0–1600 m above sea level (Section 4.1.3).

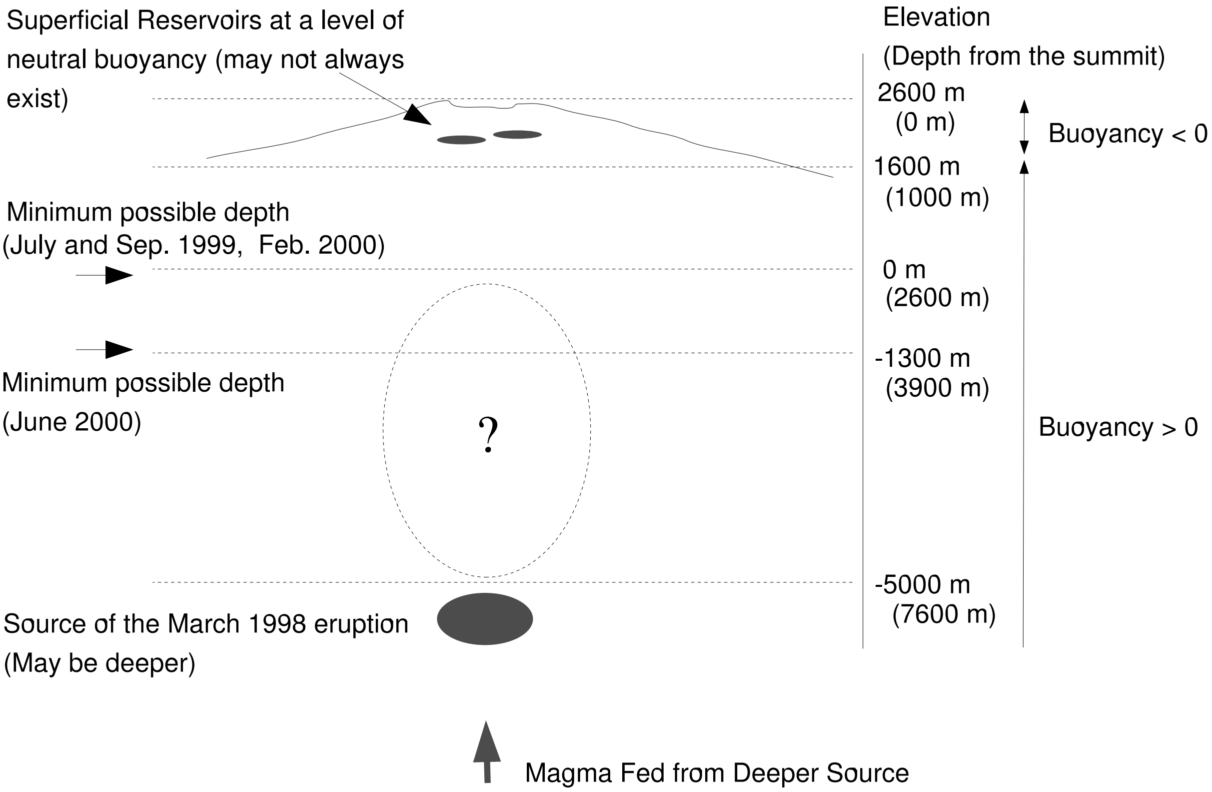

Figure 4.5: Magma storage system inferred from the estimation of the minimum possible depths of the magma sources, level of neutral buoyancy at a shallow level, and thermal conduction equations.

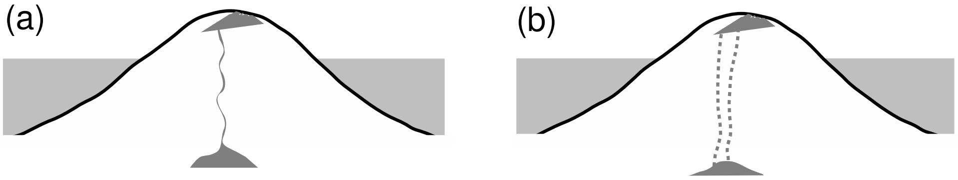

Figure 4.6: Two possible scenarios for explaining the lack of interferometric signals corresponding to the magma propagation between the source and dike. (a) The conduit is too narrow to cause detectable deformations, (b) the conduit closed once the eruption ceased.

4.2 Magma Tranfer and Emplacement

4.2.1 Conduit geometry at depth

Transfer of magma in fractures, or dikes, is the most efficient means of moving magma in the lithosphere [*Rubin*, 1995]. Indeed, *Delaney and Pollard* [1981] showed that less work is done around an elliptical conduit than a cylindrical conduit for the same volume of magma emplaced. In other words, an elliptical conduit can accomodate the same amount of magma as a cylindrical one at a lower pressure. In contrast, cylindrical conduits have advantages against elliptical conduits (dikes) for magma flow. To transport the same flux of magma, the cross-sectional area of a cylindrical conduit is 22.3 times smaller than that of an elliptical conduit having a semimajor axis to semiminor axis aspect ratio of 1000 [*Delaney and Pollard*, 1981]. Cylindrical conduits are, in addition, thermally more efficient and mechanically more stable once developped.

The separation of more than 1 km between the bottom of the dikes estimated in Chapter 3 and the magma sources (Section 4.1.1), as well as the vertically elongated seismicity patterns beneath the estimated dikes (Chapter 3), clearly indicate the presence of magma conduits between the sources and dikes. Evidence of such conduits are, however, not visible in the interferograms. As discussed in Section 2.3.5, this means either that magma migrated through a conduit too narrow to cause detectable displacements [*Amelung and Day*, 2002; *Cayol and Cornet*, 1998a; *Sigmundsson et al.*, 1999], or that the conduit between the magma source and the dike closed once the eruption ceased (Figure 4.6). The latter would be the case if magma was buoyant [e.g. *Dahm*, 2000] or it withdrew into the reservoir.

The geometry of the conduits can either be a fracture (dike) that opens for each eruption, or a cylindrical pipe filled with molten magma commonly used for several eruptions. For the latter, the radius of the pipe should be large enough ($>$3 m) to avoid solidification in the inter-eruption periods (typically several months, Figure 4.4b).

Tilt changes were detected almost simultaneously as the preeruption seismic swarms (except for the March 1998 event where tilt changes appeared when the migrating hypocenters of the swarm reached sea level). This indicates that the magma transfer through the conduit above sea level was detected by tilt data. In the following, it is shown that a cylindrical conduit cannot create the observed and detectable tilt changes, but that a dike-type conduit can.

Cylindrical conduit

The radial tilt change due to a vertical cylindrical source in an elastic half-space (Figure

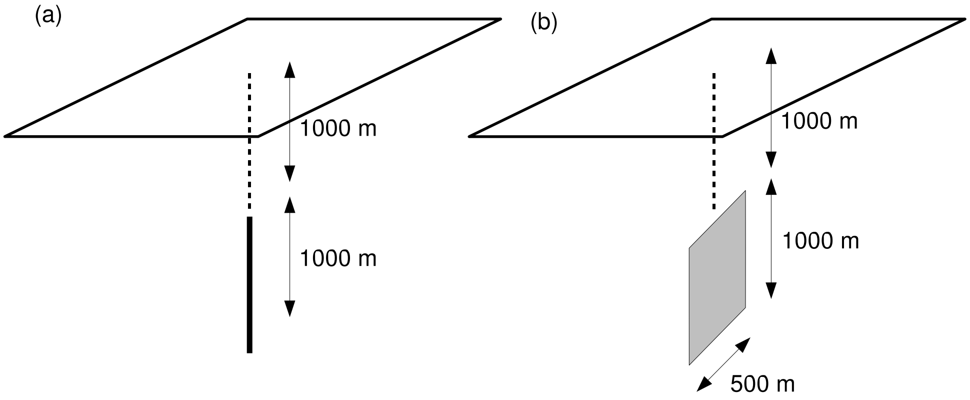

Figure 4.7: Geometries of the considered conduits. (a) Cylindrical conduit with radius 3 m, located between the depths of 1000 m and 2000 m. (b) Dike-type conduit of width 500 m, located between the depths of 1000 m and 2000 m.

4.7a) at the radial distance r on the ground $z = 0$ is given by [*Walsh and Decker*, 1971]

$$\gamma = fr\{(r^2 + c_1^2)^{-3/2} - (r^2 + c_2^2)^{-3/2}\}, \tag{4.4}$$

where c_1 and c_2 are the depths to the top $(z = c_1, r = 0)$ and bottom $(z = c_2, r = 0)$ of the cylindrical source. The intensity factor f can be approximated as [*Voight et al.*, 1999]

$$f = 2R^2 \frac{\Delta P}{E}(1 - \nu^2), \tag{4.5}$$

where R is the radius of the conduit and ΔP is the magma overpressure in the conduit, E is Young's modulus and ν is Poisson's ratio. We determine the maximum possible overpressure not causing failure. Tensile failure of a vertical cylinder does not occur as long as [*Jaeger and Cook*, 1979]

$$P < 2\rho_r gh + T_0, \tag{4.6}$$

where stresses in the rock mass are assumed lithostatic. P is the magma pressure, ρ_r is the host rock density, g ($\sim$ 10 m^2/s) is the gravity, h is the depth, and T_0 (several mega-pascals for typical rocks) is the tensile strength. From Equation 4.6, the maximum possible overpressure not causing failure at a depth of 1000 m would be $\Delta P = P - \rho_r gh = (2\rho_r gh + T_0) - \rho_r gh \sim 25\,MPa$. Taking other parameter values in Equations 4.4 and 4.5 as $c_1 = -1000\,m$, $c_2 = -2000\,m$, $R = 3\,m$, and $E = 5\,GPa$, $\nu = 0.25$ as assumed throughout in this thesis, we obtain a maximum tilt change of $\sim$ 0.026 microradians. This is way smaller than the observed (and detectable) values.

Dike-type conduit

We assume that the hypocenters of the preeruption microearthquakes reflect the spatial extension of the dike-type conduit, and consider a rectangular dike whose top and bottom sides are located at 1000 and 2000 m beneath the ground and whose horizontal width is 500 m (Figure 4.7b). We further assume an overpressure of 5 MPa, which is of the same order as that for the emplaced dikes estimated in Chapter 3. To directly compare the result with that of the cylindrical conduit, a half-space is assumed. A mixed BEM computation predicts that such a dike conduit would create a maximum tilt change amplitude of 19 microradians, which is, indeed, of the order of detected tilt changes.

As we have seen, magma is likely to be transported to the ground by dike propagation. This dike-type conduit tends to close when the overpressure at the reservoir decreases, because the magma between the reservoir and the level of neutral buoyancy (Section 4.1.2). This expectation is consistent with observed tilt signals (Figure 4.8). Typically at Piton de la Fournaise, anomalies in tilt signals start a few minutes after the onset of the preeruption seismic swarm, then, around the time of the eruption onset, the sense of the signals reverses. This reversal can be explained by the closure of the dike-type conduit.

When the overpressure at the reservoir becomes low enough that the whole width of the dike-type conduit can no longer be kept open, it is expected that the geometry of the conduit gradually changes to a cylinder, because, as mentioned, cylindrical conduits are more efficient for magma flows. This corresponds to localization of an eruption to a circular vent that typically occur a few hours to a few days after the eruption onset. From the above consideration, it is concluded that both the two scenarios given in Figure 4.6 were responsible for the lack of interferometric signals associated with magma conduits.

It is worth noting in addition that the preeruption microearthquakes for the March 1998 event showed an upward migration initiating at 5 km below sea level [*Battaglia et al.*, 2005], whereas those for the subsequent eruptions were restricted above sea level (except for a few for the June 2000 event at 6 km below sea level) (Figure 4.2). Since the tiltmeters did not detect any signal corresponding to the seismicity below sea level for the March 1998 event, this seismicity at depth may correspond to reopening or enlargement of a pre-existing cylindrical conduit, possibly partially molten, as proposed by *Battaglia et al.* [2005]. Once such a conduit is well developed, next magmas could ascend aseismically.

4.2.2 Size of the magma conduit

Some time after an eruption localizes to a circular vent, the lava output rate settles down and can be sustained for days to months (190 days for the Piton Kapor eruption of the March 1998 event [*Staudacher et al.*, 1998]), which allows us to consider the magma flow to be steady. Here a cylindrical pipe flow is considered, as a model of the magma flow from the source reservoir to the ground surface, in order to estimate the size of the conduit from observed output flow rates.

The pipe has a radius R and a height H, as illustrated in Figure 4.9. Assuming that magma is well degassed, which is the case some time after the localization of an eruption, it can be treated as an incompressible viscous fluid of viscosity η. Let us consider a cylinder with no elastic interaction with the surrounding medium (i.e., no buoyancy). For a steady-state laminar flow driven by the pressure gradient $dp/dz - \rho_m g$ along the pipe (z is reckoned positive downward from the ground and ρ_m is the magma density), the magma flow rate Q can be written as [e.g. *Jaupart*, 2000; *Turcotte and Schubert*, 2002]

$$Q = -\frac{\pi R^4}{8\eta}\left(\frac{dp}{dz} - \rho_m g\right). \tag{4.7}$$

We assume that the magma pressure at the top of the reservoir is equal to the lithostatic pressure $\rho_r g H$ plus an overpressure ΔP_c:

$$P_c = \rho_r g H + \Delta P_c. \tag{4.8}$$

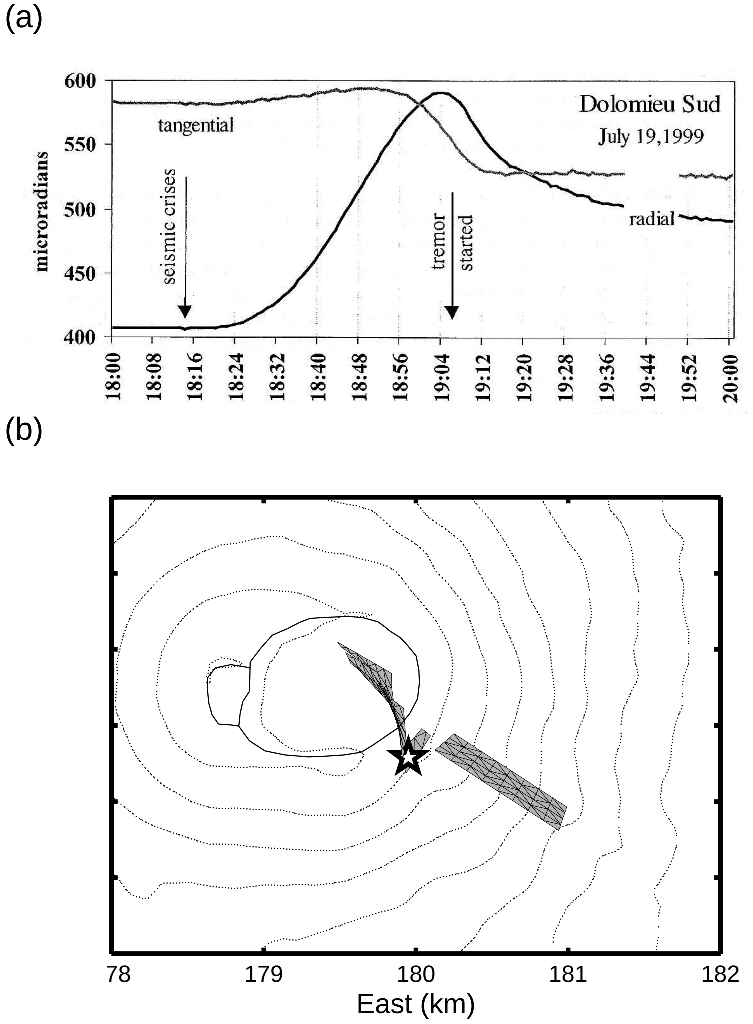

Figure 4.8: (a) Tilt signals observed at Dolomieu Sud station on the day of the July 1999 eruption onset. Radial and tangential components are with respect to the summit. Both components detected tilt changes a few minutes after the onset of the preeruption seismic swarm. Note that the signal reverses just before the tremor onset, which roughly corresponds to the eruption onset. [from Villeneuve [2000]] (b) Location of the tilt station is indicated by an open star. The preferred model of the dikes formed associated with the eruption (presented on Figure 3.26) is also shown.

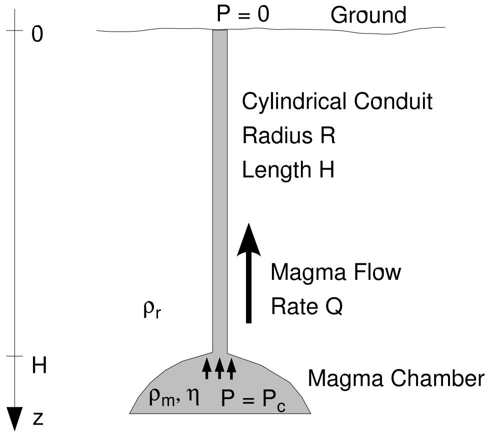

Figure 4.9: Model for a magma flow through a cylindrical conduit. The conduit cross-section has a radius of R and height of H. Magma flow is driven by the pressure gradient between the reservoir and the ground.

Then Equation 4.7 becomes [*Jaupart*, 2000]

$$\begin{aligned} Q &= -\frac{\pi R^4}{8\eta}\left(\frac{P_c}{H} - \rho_m g\right) \\ &= -\frac{\pi R^4}{8\eta}\left(\frac{\Delta P_c}{H} + (\rho_r - \rho_m) g\right), \end{aligned} \tag{4.9}$$

This equation indicates that the conduit radius R estimated by fixing the other parameters can be considered robust because it is in the fourth power.

The average temperature of the emitted lavas at Piton de la Fournaise is about 1160 °C. Magma at Piton de la Fournaise is in a transitional domain between alcalic and tholeiic, but closer to alcalic [*Upton and Wadsworth*, 1966]. Viscosities of an alcali basalt and a tholeiite of 1160 °C is roughly 100 Pa s and 1000 Pa s, respectively [e.g. *Murase and McBirney*, 1973]. From these values, the magma viscosity is assumed to be 300 Pa s. For the height of the conduit H, 7500 m is taken. This corresponds roughly to the lowest depth of the hypocenters of the preeruption seismic swarms for the March 1998 eruption. For the subsequent eruptions, it may be more appropriate to assume a smaller height (see Section 4.1.1), however, this height little affects the results. The host rock density is assumed to be 2600 kg/m^3, the average for the considered depths (taking values from an in-situ density profile of Kilauea; ground surface: 2200 kg/m^3, reservoir: 3000 kg/m^3 [*Ryan*, 1987]). Magma should be less dense than surrounding rock at the magma reservoir level as otherwise magma would not intrude upward. Here we assume 2400 and 2600 kg/m^3 for the average magma density. Note that, in reality, magma can become heavier than rock by degassing at superficial levels where the rock matrix is made of a superposition of uncompressed blocks and lava flows.

For the overpressure at the reservoir, we consider the values between two extremes: nearly zero (0.1 MPa) to the value causing shear rupture of a deep spherical reservoir $(\Delta P_c)_{max}$ (this gives a reasonable estimate at the onset of magma propagation). The tensile stress σ_t on the wall of a spherical cavity in an infinite medium having an internal pressure p_{in} and an external

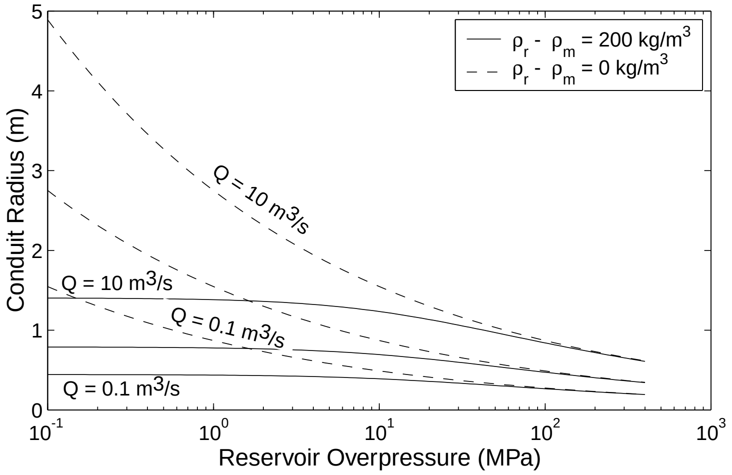

Figure 4.10: Relation between the magma overpressure in the reservoir and the radius of the cylindrical conduit. Magma flow rate Q of 0.1, 1, 10 m^3/s are assumed for the two cases of $\rho_r = \rho_m = 2600$ *(solid lines) and* $\rho_r = 2600$, $\rho_m = 2400$ *(broken lines).*

pressure p_{out} is (tensile positive) [*Timoshenko and Goodier*, 1970]

$$\sigma_t = -\frac{3}{2}p_{out} + \frac{1}{2}p_{in}. \tag{4.10}$$

Rupture occurs when σ_t exceeds the tensile strength T_0. For lithostatic pressure $p_{out} = \rho_r g h$ and $p_{in} = \rho_r g h + \Delta P_c$, we can calculate $(\Delta P_c)_{max}$ as

$$\begin{aligned} (\Delta P_c)_{max} &= 2(\rho_r g H + T_0) \\ &\sim 400\,\mathrm{MPa}, \end{aligned} \tag{4.11}$$

where T_0 of a few mega-pascals is neglected.

For the March 1998 eruption, *Villeneuve* [2000] estimated the lava output rate from the Piton Kapor vent (northern eruption site) to be 15–30 m^3/s three days after the eruption onset. From one week after the eruption onset until the end (which is 196 days after the eruption onset), the lava output rate sustained at a lower level (N. Villeneuve, personal communication, 2005). The mean lava output rate for the five eruptions between March 1998 and June 2000 is calculated by dividing the lava flow volume by the eruption period (see Table 2 in Chapter 2.3.4 for the values); it ranges from 0.7 to 4.3 m^3/s. At the last stage of an eruption, the magma flow rate can be a fraction of the average rate. From the above considerations, a range of magma flow rates of 0.1 to 10 m^3/s is assumed.

The radius R of the pipe is estimated by substituting the assumed values to Equation 4.9 (Figure 4.10). At an early stage, the magma flow rate is of the order of 10 m^3/s and magma is less dense than host rock due to exsolved gas contents, so we assume $\rho_m = 2400$ kg/m^3 and $\rho_r = 2600$ kg/m^3. Then, the radius of the conduit should be 0.7–1.4 m for the considered range of the overpressure in the reservoir. At a later stage, we have a small flow rate of the order of 0.1 m^3/s and the magma average density can be comparable to that of the host rock. When the magma and rock densities are the same, the radius of the conduit is governed by the overpressure in the reservoir ΔP_c and is 0.2–1.5 m.

As we have seen, the radius should be of the order of one meter. This is consistent with the result of *Pedersen and Sigmundsson* [2004b] who estimated the radius of a magma conduit to be less than one meter at Eyjafjallajökull volcano in Iceland. In reality, the surrounding rock may “push” the magma in the conduit, a process that generates buoyancy. When the horizontal stress is equal to the lithostatic pressure $\rho_r g z$ (hence neglecting the variation of horizontal tectonic stress) and $\rho_r > \rho_m$, the buoyancy works in such a way that the amplitude of the pressure gradient in Equation 4.7 is increased. Therefore, the radius may even be smaller than our estimated values.

The estimates would significantly differ if the flow was turbulent. The transition from laminar to turbulent flow occurs at the Reynolds number $Re \sim 2200$ [*Turcotte and Schubert*, 2002]. The Reynolds number is given by [e.g. *Turcotte and Schubert*, 2002]

$$Re \equiv \frac{2\rho_m |\bar{u}| R}{\eta}, \tag{4.12}$$

where $\bar{u}$ is the mean velocity

$$\bar{u} = -\frac{Q}{\pi R^2}. \tag{4.13}$$

The Reynolds number for the considered flow is found to be less than 53, which is significantly smaller than 2200. Thus, the assumption of laminar flow was appropriate.

4.2.3 Lateral propagation of dikes

As discussed in Section 4.1.2, comparisons of the widths of the vertically-elongated seismicity patterns and the wider widths of the laterally-elongated dikes estimated in Chapter 3 indicate lateral propagation of dikes at the shallowest 1000 m or so beneath the ground.

The first magma leaving the reservoir is gas-rich because exsolved gas has accumulated at the top of the reservoir [*Vergniolle and Jaupart*, 1990], making the magma much less dense than the surrounding rock. The dike propagation is probably guided by gas pockets at the tip of the dike [*Menand and Tait*, 2001], which is supported by the witness of a strong whistling noise at the onset of the September 1999 eruption [*Villeneuve*, 2000]. This buoyant dike propagates subvertically.

Lateral dike propagation is expected to start just after this first stage. As the eruption proceeds, the magma flow rate decreases in response to a decrease of the overpressure in the reservoir and to more degassed (i.e., more dense) magma, as in the case of a flow in a cylindrical conduit (Equation 4.9). The edifice weight creates a compressive stress field such that it prevents magma from ascending toward the summit [*Pinel and Jaupart*, 2000]. The tendency is that the smaller the magma flow rate, the more the magma is encouraged to propagate laterally [*Pinel and Jaupart*, 2004]. At the same time, degassed and hence densified magma also leads to creation of a level of neutral buoyancy (Figure 4.11). These two, the stress field due to the edifice weight and the degassed magma, create a level of neutral buoyancy that promotes lateral dike propagation.

Progressive opening of eruptive fissures, which typically completes in a few minutes [*Villeneuve*, 2000], corresponds to a transition from vertical to lateral dike propagation. For a typical eruption around the central cone, the center of activity shifts downslope and finally localizes at the lowest altitude. This is consistent with the above explanation as later-arriving magma is more encouraged to flow laterally.

More striking lateral magma propagation occurred with the eruption out of Enclos-Fouqué caldera associated with the March–September 1998 event and that close to the southern border of the caldera associated with the September 1999 event. As the interferogram of the September

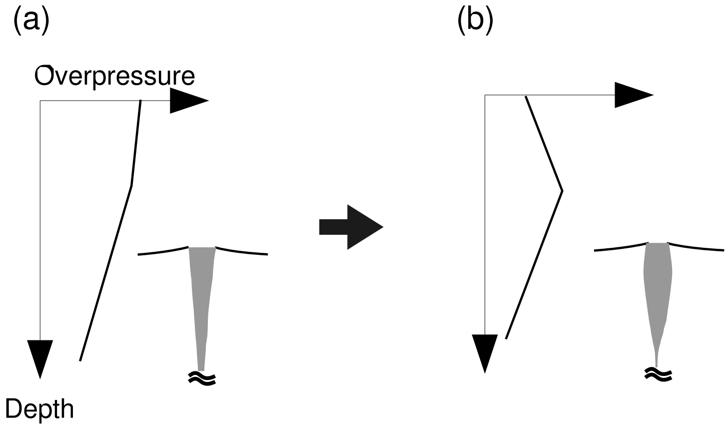

Figure 4.11: Schematic sketch showing the role of magma density change in the overpressure profile. See Figure 1.6 for the effect of buoyancy on the overpressure profile. (a) Just after the eruption onset. Magma is buoyant for the whole depth range. (b) A few minutes to a few hours after the eruption onset. Densification of magma can lead to create a level of neutral buoyancy, which is located at some depth around the depth of the maximum overpressure.

1999 eruption (Figure 3.3) indicates, these downrift magma propagations may occur concordant with the layers of lava flows parallel to the topography (i.e., in sills and laccoliths), in which case, the magma is not required to be at a level of neutral buoyancy. It should be noted, however, that magma could also propagate in dikes at its level of neutral buoyancy. Whichever the case is, magma is encouraged to erupt at the point where the topographic slope levels off, because the cross-sectional area of the magma flow is increased at that point in the presence of the pressure gradient change (Figure 4.12; *Fialko and Rubin* [1999]). This is possibly the reason why these secondary eruptions occurred close to the caldera border.

Such superficial lateral propagation of magma seems to be common, yet not frequent, at Piton de la Fournaise [*Bachèlery*, 1999]. Eruptions along the northern and southern rift zones outside the caldera occurred in 1977, 1986 and 1998 in the past 30 years (Figure 1.4). For the 1986 event, the eruption outside the southern border of the caldera occurred while the summit zone experienced persistent microearthquakes, and no gas was observed from the southernmost eruptive vent close to the seacoast [*Delorme et al.*, 1989]. For the March–September 1998 event, the lava emitted from the fissures outside the northern caldera border was also completely degassed [*Bachèlery*, 1999; *Villeneuve*, 2000]. These are consistent with the idea that, for eruptions along the rift zones far from the central cone, magma first rises to the summit zone (and erupt in some cases) and then laterally propagates along the rift zones [*Bachèlery*, 1999]. Magma heavier than surrounding rock can propagate downslope with the overpressure created by its own weight.

4.2.4 Pit-crater collapses

Section 4.1.2 discussed that magma reservoirs shallower than 1000 m beneath the summit are mechanically favoured. It is interesting to consider what might happen if a new magma reaches one of such reservoirs. When the new magma is enough overpressurized and enough buoyant, it passes through the reservoir and erupts. At a later stage when the magma is encouraged

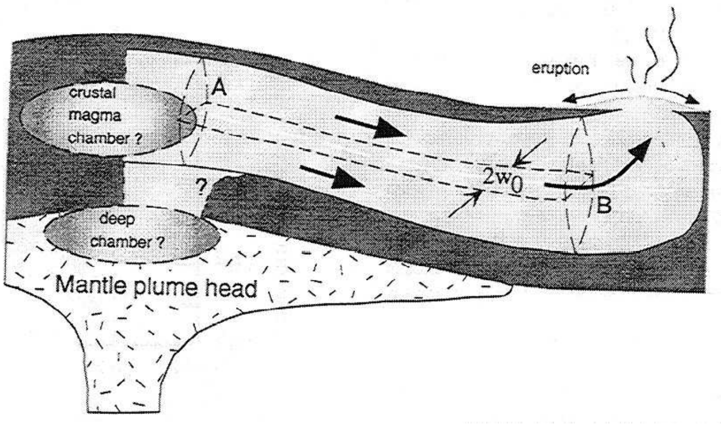

Figure 4.12: Magma propagating parallel to the topographic slope is expected to erupt at the point where the slope levels off, because the cross-sectional area of the magma flow is increased in the presence of the pressure gradient change. [from Fialko and Rubin [1999]]

to propagate laterally, magma pressure may induce a rupture on the reservoir side wall and create a lateral magma flow driven by magma supply from depth and also by its own weight. Then, if magma supply from depth stops, the reservoir is likely to be drained. As pointed out by *Bachèlery* [1999], such drainage associated with a superficial magma flow causes pit-crater formations, and in some cases, leads to phreatic and phreatomagmatic eruptions due to ascent of high temperature water in the hydrothermal system.

4.2.5 Model of magma transfer and emplacement

The above discussions are summarized to propose a model of magma transfer and emplacement associated with typical eruptions in the central cone of Piton de la Fournaise. First, overpressurized magma in the reservoir intrudes upward in a dike (Figure 4.13a). The overpressure keeps the dike open. The upward dike propagation is driven by the buoyancy of the gas pocket and gas-rich magma at the dike tip. The dike has a vertically-elongated shape because the upward propagation is dominantly driven by buoyancy. Just after the eruption onset, the dike shallower than $\sim$1000 m quickly grows laterally because of denser magma, mainly in the direction of the slope (Figure 4.13b). As a result, eruptive fissures progressively open downslope. As the overpressure in the reservoir is relaxed, the magma flow rate decreases and the dike-type conduit starts to close from its lower end, except at its center where a cylindrical conduit is being developed. Several hours to a few days after the eruption onset, the eruption localizes to a circular vent (Figure 4.13c). A cylindrical conduit having a radius of $\sim$1 m is developped and the eruption continues for days to weeks. Magma in the dike solidifies; the laterally-elongated upper part creates observable static displacements, whereas the conduit part is practically closed and becomes undetectable by InSAR (Figure 4.14).

4.2.6 Relations with seismicity

It appears, for the five eruptions analyzed in this study, that the dikes were emplaced (solidified) above the upper limit of the active region of the preeruption microearthquakes. Does this ap-

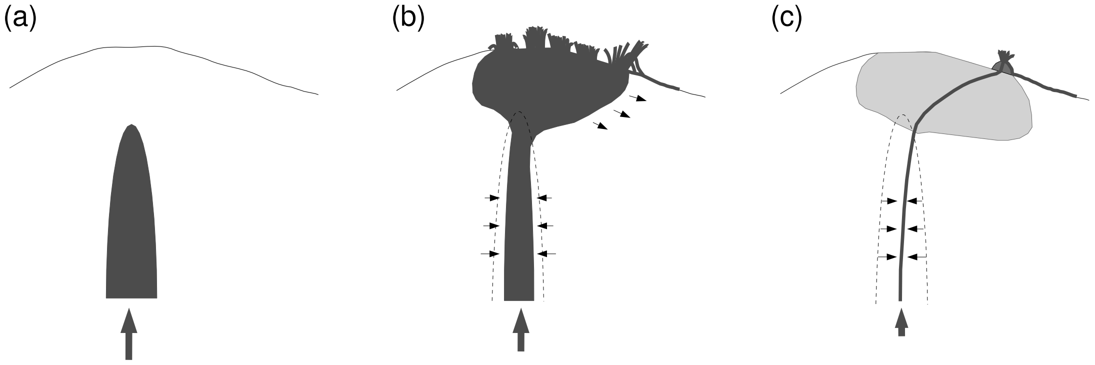

Figure 4.13: Mechanism of magma transfer and emplacement associated with typical eruptions in the central cone at Piton de la Fournaise. (a) Overpressurized magma in the reservoir intrudes upward in a dike. The upward dike propagation is driven by the buoyancy of the gas pocket at the tip and gas-rich magma. (b) After the eruption onset, the dike shallower than ∼1000 m quickly grows laterally, mainly in the direction of the slope. The lateral propagation results from the magma at its neutral buoyancy. As the overpressure in the reservoir is relaxed, the magma flow rate decreases and the dike-type conduit starts to close. (c) Eruption localizes; a cylindrical conduit having a radius of ∼1 m is developped and the eruption continues for days to weeks. Magma solidifies with leaving practically a laterally-elongated dike shallower than about 1000 m.

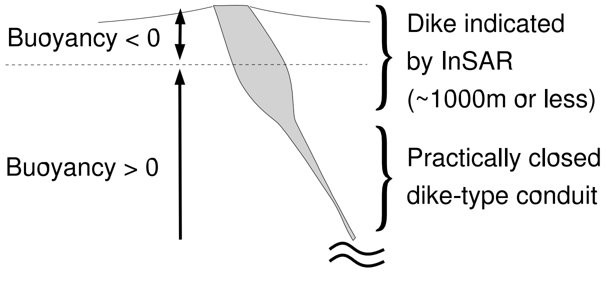

Figure 4.14: Cross-sectional sketch showing a thickness profile of a solidified dike. The dike-type conduit is practically closed and is not detectable by InSAR.

parent anticorrelation of seismicity and dike emplacement stem from a single physical process, or is it just a coincidence?

The upper limit of the hydrothermal system of Piton de la Fournaise is located a few hundred meters below the ground [*Lénat et al.*, 2000], which roughly corresponds to the bottom of the emplaced dikes except for that associated with the March 1998 eruption. As indicated by Coulomb's failure criteria [e.g. *Jaeger and Cook*, 1979], the higher the pore pressure, the easier shear failures (earthquake) occur. This may explain the more active seismicity at the hydrothermal levels. The next question is if magma is discouraged to stagnate around the hydrothermal area. The larger the difference in the densities of magma and the surrounding rock, the more magma is discouraged to stagnate at the corresponding level. As a hydrothermal system is independent of density difference, the hydrothermal system does not probably play an active role in the emplacement of dikes.

Another explanation for the lack of microearthquakes at depths shallower than 1000 m is that the differential stress is simply not enough for a fault to slip. Indeed, *Rubin and Gillard* [1998] showed that volcano-tectonic earthquakes are likely to be induced by dike intrusions on preexisting faults when the differential stresses are large enough. Again, since a large differential stress would not discourage a dike to be emplaced, such a stress field does not explain the dike emplacements.

The above considerations indicate that the relationship between the lack of microearthquakes and dike emplacements is complex, if any, and more detailed studies are needed to understand the apparent anticorrelation. As both seismic and deformation signals reflect stress state of the edifice, such studies may provide new insights on the mechanical system of the volcano.

4.3 Evolution of the Volcano

4.3.1 Contribution of dike intrusions to volcano growth

Basaltic shield volcanoes principally grow by dike intrusions and lava flow emplacements. Here, the contribution of dike intrusions to the volcano growth is discussed.

Assuming the preferred dike models estimated in Chapter 3 (Figure 3.40) allows calculations of the three-dimensional displacement field and slope changes during the March 1998 – June 2000 period (Figure 4.15). The maximum displacements in the eastern, northern and upward components are estimated to be 50 cm, 36 cm and 83 cm during the period (Figure 4.15a-c), corresponding to 22, 16 and 36 cm/year. The eastern and upward displacement rates are significantly larger than those estimated from trilateration and GPS data between 1981 and 1995 of 13 and 7 cm/year [*Briole et al.*, 1998]. Since shallow dipping dikes enhance vertical to horizontal displacement ratio [*Pollard et al.*, 1983], the relatively large upward to eastward displacement ratio in 1998–2000 may indicate more shallow-dipping dike intrusions than in the longer period of 1981–1995.

Slope changes, defined by the change in the maximum gradient of the topography, indicate that the northern to southeastern flank steepend about 2×10^{-2} degrees (350 microradians) by the dike intrusions (Figure 4.15d). Since relatively few number of eruptions occur along the northeastern axis [*Bachèlery*, 1981; *Michel and Zlotnicki*, 1998], such steepening may continue. Instability caused by such small slope changes, however, may be negligeable compared to that caused by internal stress buildup due to dikes.

The total volume of all the preferred dike models is 4.9 Mm^3. This is about 8% of the total lava flow volume of about 60–70 Mm^3 (Table 2 in Section 2.3.4). It should be noted, therefore, that the effect of lava flow emplacements is required for a more detailed long-term forecast of the growth of the edifice as was done by *Annen et al.* [2001].

4.3.2 Predicting Eruption Locations

It is a challenge to quantitatively predict the position and direction of dike intrusions and resulting eruptive fissures because they can be governed by complex factors such as heterogeneous and anisotropic stress field and mechanical properties of rock. In general, nevertheless, dike emplacements show some regularities on volcanic systems, which manifests the influence of global stress field and mechanical properties of the edifice. Such regularities include radial (and sometimes also circumferential) dikings with respect to the summit (e.g., Galapagos volcanoes, *Chadwick and Dieterich* [1995]), and persistent dikings along well developped volcanic rift zones (Hawaiian and Icelandic volcanoes, e.g., *Walker* [1999]). At Piton de la Fournaise, the eruptive fissures are preferentially formed in four directions with respect to the summit [*Michel and Zlotnicki*, 1998]: 5°N-35°N (northern rift zone, corresponding to the March 1998 northern eruption and February 2000 eruption), 95°N-120°N (southeast; the July 1999 and June 2000 eruptions), 155°N-185°N (southern rift zone, the September 1999 eruption), and 255°N (southwest; the March 1998 southern eruption). (Note that *Bachèlery* [1981] and *Bachèlery et al.* [1983] found a 80°N axis instead of 95°N-120°N axis from the directions of old eruptive fissures, and an alignment of scoria cones at 105°N.)

As mentioned before (Section 3.1.1), the locations of the eruptions analyzed in this study seem to follow a spatial periodicity. This section attempts to quantitatively explain this periodicity by examining the normal stress changes induced by an intrusion on potential dike surfaces.

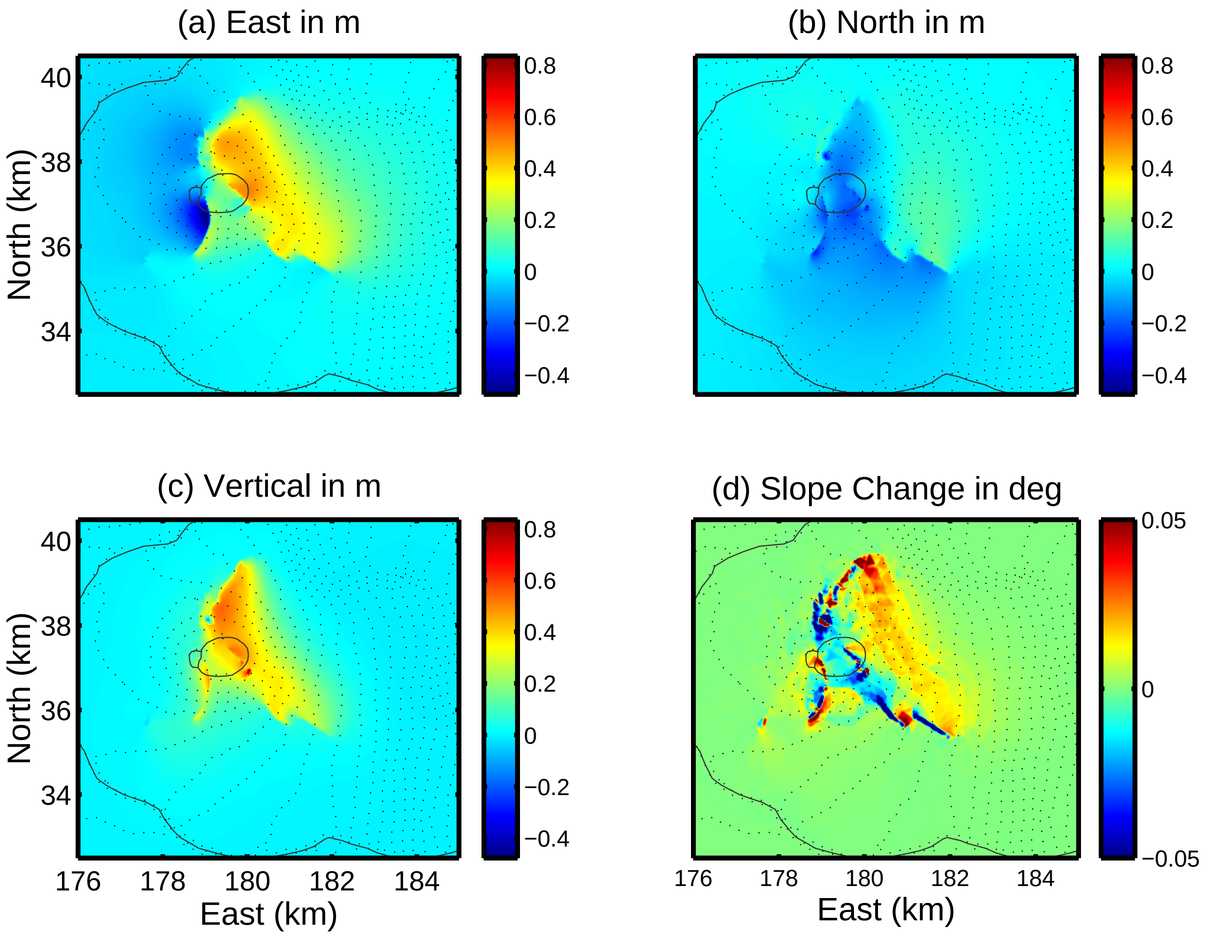

Figure 4.15: Modelled displacements, (a): east, (b): north, (c): upward components, and (d) slope changes (change in the maximum gradient of the topography) due to the preferred dike models for the five eruptions (Figure 3.40). Solid curves are the borders of Bory and Dolomieu craters and Enclos-Fouqué caldera. Dotted curves are the elevation contours of 100 m interval. Unit of the colorbars for the displacements are in meters for (a)–(c), and in degrees for (d).

Six radial potential dike surfaces are considered: to the north, northeast, southeast, south, southwest and northwest with respect to the summit. The geometry of these surfaces are defined after the preferred dike models for the 1998–2000 eruptions determined in Chapter 3 (Figure 3.40) i.e., the northern surface after the February 2000 dike, the southeastern surface after the June 2000 dike, the southern surface after the September 1999 dike, and the southeastern surface after the March 1998 southern dike. At the northeast and northwest axes where there were no intrusions, vertical surfaces are assumed. Table 4.3 lists the geometrical parameters of the potential dike surfaces considered. The bottom of the potential dike surfaces is set at 1000 m above sea level, which is lower than the bottom of most of the estimated dikes. The top is set 200 m below the ground parallel to the topography for a technical reason. The normal stress change $\delta\sigma_n$ due to the preferred dike models for the 1998–2000 events are calculated on the potential dike surfaces at other axes using the mixed BEM.

A necessary condition for a dike to intrude on a given surface within the edifice is that the magma overpressure ΔP overcomes the tensile strength T_0:

$$\Delta P = P_m - \sigma_n > T_0, \tag{4.14}$$

where P_m is the magma pressure and σ_n is the normal stress. Next, we consider that the normal stress changed from the initial state σ_n to $\sigma_n' = \sigma_n + \delta\sigma_n$. Then, the change in the overpressure is

$$\begin{aligned} \delta(\Delta P) &= \{P_m - (\sigma_n + \delta\sigma_n)\} - \{P_m - \sigma_n)\} \\ &= -\delta\sigma_n. \end{aligned} \tag{4.15}$$

A positive $\delta(\Delta P)$ leads to more chance that Equation 4.14 is met; namely, a negative (positive) change in the normal stress encourages (discourages) an intrusion on the considered surface.

It should be noted that a dike does not necessarily intrude where $\delta\sigma_n$ is minimum, because of the follwing reasons. (1) The condition 4.14 depends on the pre-intrusion stress σ_n. This is the reason why it is only possible to say that a dike intrusion is encouraged or discouraged. (2) Dike propagation depends not only on the initial stress field of the edifice but also on the stress field created by the dike itself; that is, the stress field is perturbed by the propagating dike. (3) Magma may intrude through a different path and simply not reach the considered surfaces. For these reasons, two assumptions are made in order to relate $\delta\sigma_n$ to the direction of dike intrusions. First, all the six potential dike surfaces are assumed to have the same σ_n at the initial stage, which is the case for an isotropic stress field. Next, it is assumed that magma ascends below the summit to the elevation of the considered potential surfaces, so that the surfaces have an equal chance to be intruded (for the same $\delta\sigma_n$) from the tip closer to the summit. Under these assumptions, the potential surface having the minimum $\delta\sigma_n$ at the tip closer to the summit has the maximum probability to be intruded, at the time of next magma ascension.

Results

First, normal stress changes due to each of the March 1998–June 2000 dike intrusions are shown, in order to understand the effects of each intrusion. The March 1998 intrusions (Figure 4.16a) encourage intrusions on the upper area of the southern and southeastern surface, with a preference (larger change of normal stress) on the southern one. The reason why the following intrusion (July 1999 on the southeastern flank) was not on the southern flank may be due to an unfavorable magma pathway for a southern eruption. The July 1999 intrusion (Figure 4.16b) decreases normal stresses on relatively small areas of the southeastern and northeastern

Table 4.3: Geometrical parameters of the potential dike surfaces

	Strike (°N)	Dip (°)	Shear (°)	Botelv (m)	Botlen	Twist (°)	D_top (m)	Eruptions
North	10	65	10	1000	1.3	0	200	Mar. 98, Feb. 00
Northeast	70	90	0	1000	1	0	200	
Southeast	130	70	0	1000	1	10	200	Jul. 99, Jun. 00
South	190	90	0	1000	1	0	200	Sep. 99
Southwest	230	70	0	1000	1	0	200	Mar. 98
Northwest	290	90	5	1000	0.8	0	200	

surfaces, and not significantly on other surfaces. The September 1999 intrusion (Figure 4.16c) encourages a northern intrusion by giving the maximum decrease at the tip of the northern surface. The February 2000 intrusion (Figure 4.16d) encourages the southern and southeastern intrusions. The June 2000 intrusion (Figure 4.16e) encourages northern and southern intrusions.

Next, cumulative normal stress changes up to the February 2000 intrusion are shown; that is, for example, the normal stress changes by the March 1998 and July 1999 intrusions are summed to estimate the favoured intrusion location. This is more appropriate for discussing the likelihood of the subsequent intrusions because, in reality, the stresses are accumulated. The normal stress changes due to the March 1998 and July 1999 intrusions (Figure 4.17a) favors a southern intrusion, which is consistent with the occurrence of the September 1999 eruption. The cumulative stress change for the March 1998, July and September 1999 intrusions gives the maximum decrease at the southern tip of the northern surface (Figure 4.17b), which is again consistent with the following eruption in February 2000, although northwestern and northeastern intrusions are also encouraged. Then, the February 2000 dike adds a negative normal stress change on the southeastern surface (Figure 4.17c), where the following eruption occurred.

From the calculations, we can conclude that the location of a dike emplacement is influenced by the stress changes due to previous dikes. That few numbers of eruptions occur at the northwestern and northeastern axes is probably related to the more frequent eruption occurrences along the northern rift zone, because intrusions on the northern flank do not encourage northwestern and northeastern intrusions as they do to other axes (Figures 4.16a and 4.16d). The eruptive fissure directions in 50 years before the current eruptive cycle [*Michel and Zlotnicki*, 1998] indicate that the periodicity of the studied period, with eruptions occurring successively from the north to the south, is not a general tendency. This may be explained by the fact that small differences in the intrusion geometries and overpressure distributions might guide the following eruptions to be at completely different sites.

In a longer term, the stress change analysis procedure made in this section probably cannot fully explain the eruption location pattern, because it neglects other volcano-scale long-term stress evolution such as relaxation of stresses by slip on an ancient volcanic complex. One may be able to estimate a long-term process that alters the stress field by trying to introduce such stressing process in a way that it well explains the eruption location pattern.

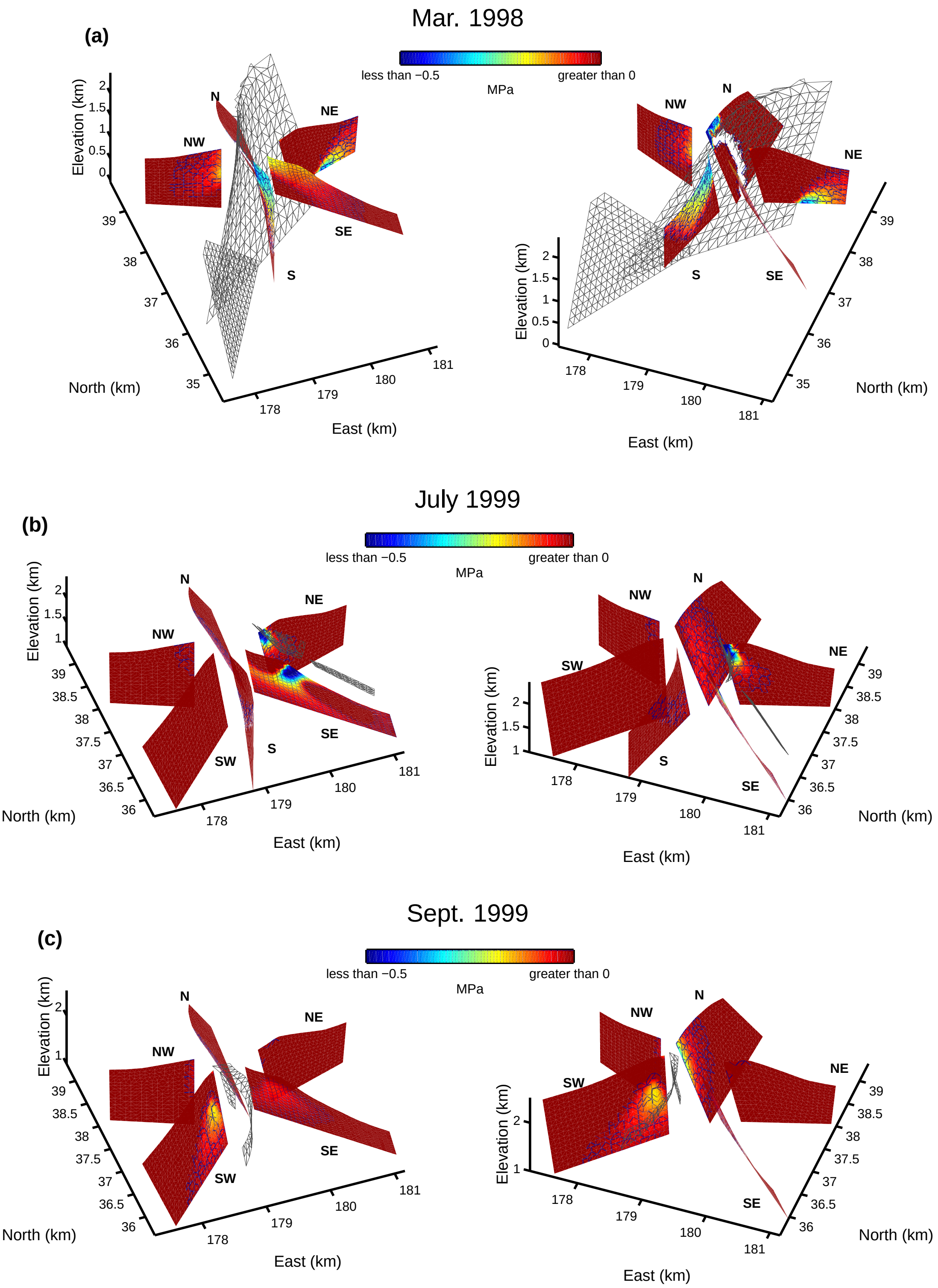

Figure 4.16: Perspective plots from two view angles showing the changes in normal stress on potential dike surfaces caused by the preferred dike models determined in Chapter 3. The source dike is shown in black mesh. The colorscale corresponds to the stress change in megapascals, with positive values clipped to dark red. Negative and positive normal stress changes indicate that dike intrusions are encouraged and discouraged, respectively. Stresses at the intersection of the source and potential dikes are not given because they are singular. (a) March 1998 dikes. (b) July 1999 dike. (c) September 1999 dike. (d) February 2000 dike. (e) June 2000 dike.

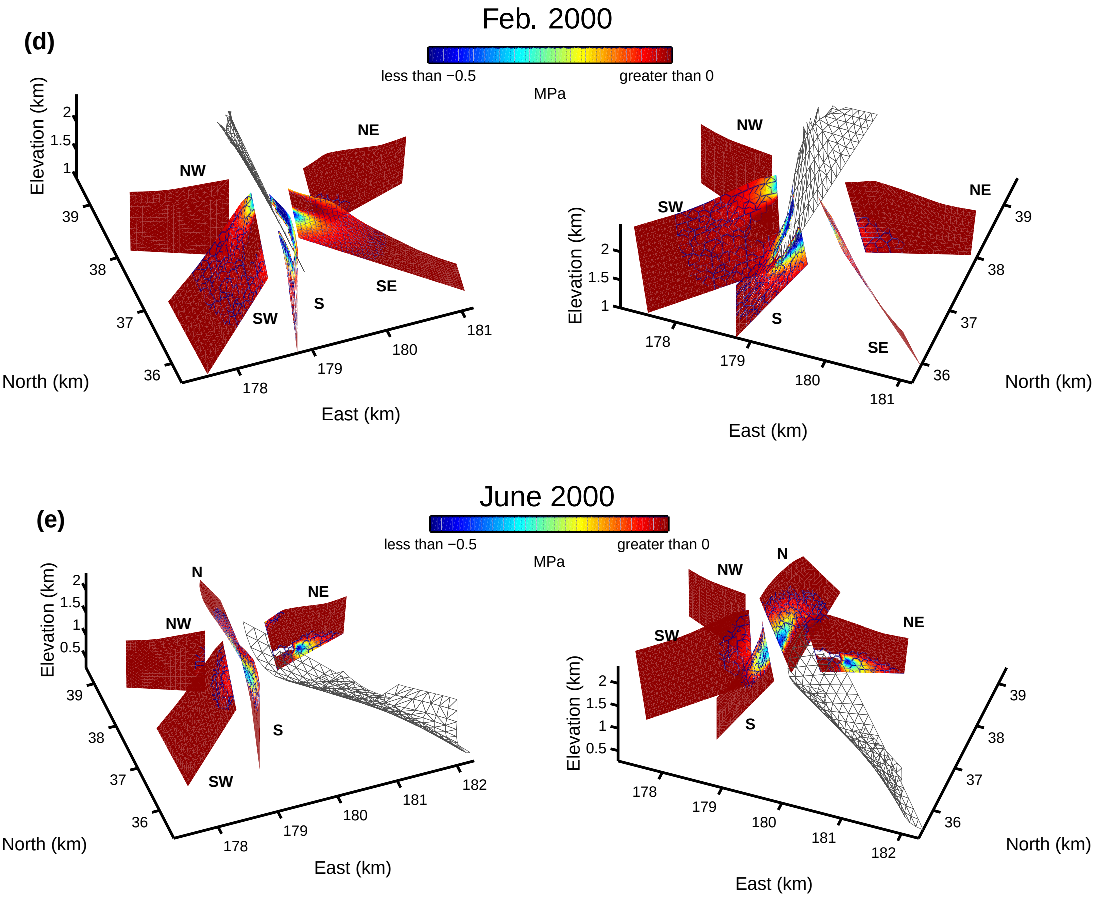

Figure 4.16: Continued.

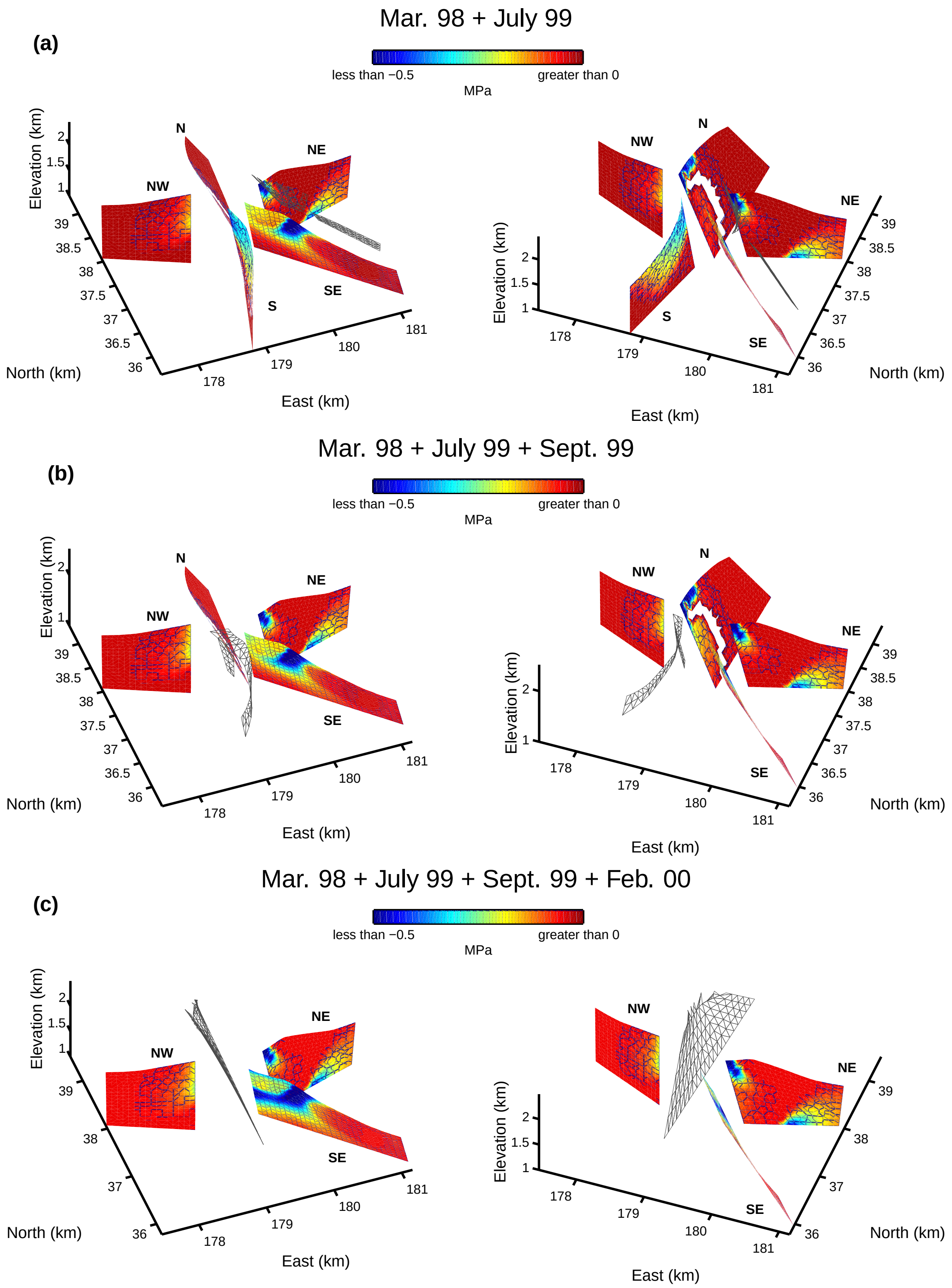

Figure 4.17: Perspective plot from two view angles for the cumulative normal stress changes on potential dike surfaces, corresponding to successive dike intrusions. The normal stresses on the potential surfaces at which a dike is already emplaced are not calculated because of the singularity. The colorscale corresponds to the stress change in megapascals, with positive values clipped to dark red. For visibility, only newly-added source dike mesh is drawn. (a) March 1998 and July 1999 dikes. (b) March 1998, July and September 1999 dikes. (c) March 1998, July and September 1999, and February 2000 dikes.

4.3.3 Triggering of Landslides by Dike Intrusions

As stated in Section 1.1.1, Piton de la Fournaise has experienced recurrent seaward landslides. While the driving force of the landslides is gravity, dike intrusions of the type analyzed in this study can trigger them [*Elsworth and Day*, 1999; *Iverson*, 1995]. To investigate the possibility of this triggering mechanism, Coulomb failure stress changes due to the preferred dike models (Figure 3.40) are calculated using the mixed BEM on potential fault planes at several depths and dip angles.

Using Coulomb's failure assumptions [e.g. *Jaeger and Cook*, 1979], we can define Coulomb failure stress change $\Delta\sigma_f$ as [e.g. *Harris*, 1998; *King et al.*, 1994; *Steacy et al.*, 2005]:

$$\Delta\sigma_f = \Delta\tau + \mu(\Delta\sigma_n + \Delta P_p), \tag{4.16}$$

where $\Delta\tau$ is the shear stress change on a fault (positive in the direction of fault slip), $\Delta\sigma_n$ is the normal stress change (positive in extension). ΔP_p is the pore pressure change in the fault zone (positive in compression), and μ is the friction coefficient (0 $< \mu <$ 1).

To use Equation 4.16 to study the triggering of fault slips, we have to make a few assumptions because of our lack of knowledge about the role of pore fluids. The assumptions are [*Harris*, 1998]: (1) The medium is homogeneous and isotropic, (2) The medium is undrained but fluids do not flow freely (this is equivalent to considering an undrained situation immediately after a static stress change), (3) Fault zone materials are ductile so that $\sigma_{xx} = \sigma_{yy} = \sigma_{zz}$. Under these assumptions, the pore pressure has a negative correlation with the normal stress change, i.e.,

$$\Delta P_p = -B\Delta\sigma_n, \tag{4.17}$$

where B is the Skempton parameter [for the detail see *Harris*, 1998], and Equation 4.16 becomes

$$\Delta\sigma_f = \Delta\tau + \mu'\Delta\sigma_n, \tag{4.18}$$

where $\mu' = \mu(1-B)$ is called the effective friction coefficient. Although Equation 4.18 is convenient and is commonly used in studies on earthquake triggering, we must bare in mind that we might miss some important clues in interpretating our data due to the simplifying assumptions mentioned above [*Harris*, 1998].

Slip is encouraged when $\Delta\sigma_f$ is positive, and vice versa. Note that it is not possible from the Coulomb failure stress change analysis to directly predict if a fault would slip or not, because we do not know how much Coulomb failure stress had already accumulated on the fault before the stress changes.

Effective frictional coefficient between 0 and 0.6 are reported from several applications [*Harris*, 1998]; here, endmember cases of μ' = 0 and 0.6 are presented. The direction of the fault slip is assumed to be eastward (seaward) because we are interested in the triggering of seaward fault slips. The eastward dip angles of the potential fault tested are: -10°, 0°, 10° and 20°. Coulomb failure stress changes for the four dip angles are calculated at five depths: -1000, 0, 500, 1000, 1500 m above sea level. The range of considered depths include potential slip planes due to a possible boundary between an old dense intrusive body (remnant of the Alizés volcano) and the younger Piton de la Fournaise between -1000 and 0 m below sea level [*Lénat et al.*, 2001; *Rançon et al.*, 1989], hyaloclastites at sea level [*Oehler et al.*, 2005], and hydrothermally-altered materials at elevations shallower than 1000 m above sea level [*Lénat et al.*, 2000].

Results

Figures 4.18 and 4.19 show the Coulomb failure stress changes due to the preferred dike models for the five eruptions, for $\mu' = 0$ and 0.6, respectively. These figures indicate on which part of the edifice and at which dip angle seaward shear failures are more encouraged by the type of intrusions that occurred between 1998 and 2000.

If μ' is uniform in the edifice, slip is more likely to occur at depths of 1000–1500 m above sea level beneath the northern and the eastern flank of the edifice where Coulomb failure stress changes are the largest. Dip angles of -10° to 10° are slightly preferred to 20°.

In a long term, dikes intruding in different axes may relax the Coulomb failure stress that accumulated during the five eruptions at some potential slip zones. However, the stress would probably accumulate beneath the northeast and eastern flank of the edifice, because of a greater number of intrusions at the northern and southeastern or eastern axes compared to the northeastern axis. The situation may be the same for the southeastern flank of the edifice, because similar seaward-dipping dikes as that of February 2000 eruption is indicated also on the southern flank for the September 2003 and May 2004 eruptions (P. Tinard, personal communication, 2005).

Figure 4.20 shows interferograms calculated from the ENVISAT images for the coeruptive displacements of the January 2004 eruption that occured on the northern flank of the central cone [*Tinard et al.*, 2004]. The descending interferogram (Figure 4.20b) shows about 33 fringes, indicating displacements toward the satellite up to 92 cm. The color orders of fringes from the both ascending and descending directions indicate that the eruption was probably accompanied by a combination of a sill intrusion and a slip along the sill plane (mode I + mode II). It is likely that this event has relaxed the accumulated Coulomb failure stress at a shallow plane. This event, however, did not trigger any large-scale landslide.

The positive Coulomb failure stress changes at deeper levels (1000 m below sea level and sea level), although the amplitudes are smaller, suggest that shallow dike intrusions may also trigger slip at these levels. Indeed, a soft layer with a smaller cohesion and friction coefficient compared to other layers may slip with a relatively smaller Coulomb failure stress change.

On the other hand, eastward fault slips west of the intrusion zone are discouraged (negative Coulomb failure stress change). This indicates that rift-zone intrusions only promote eastward slip (and possibly landslides) east of the intrusion zones.

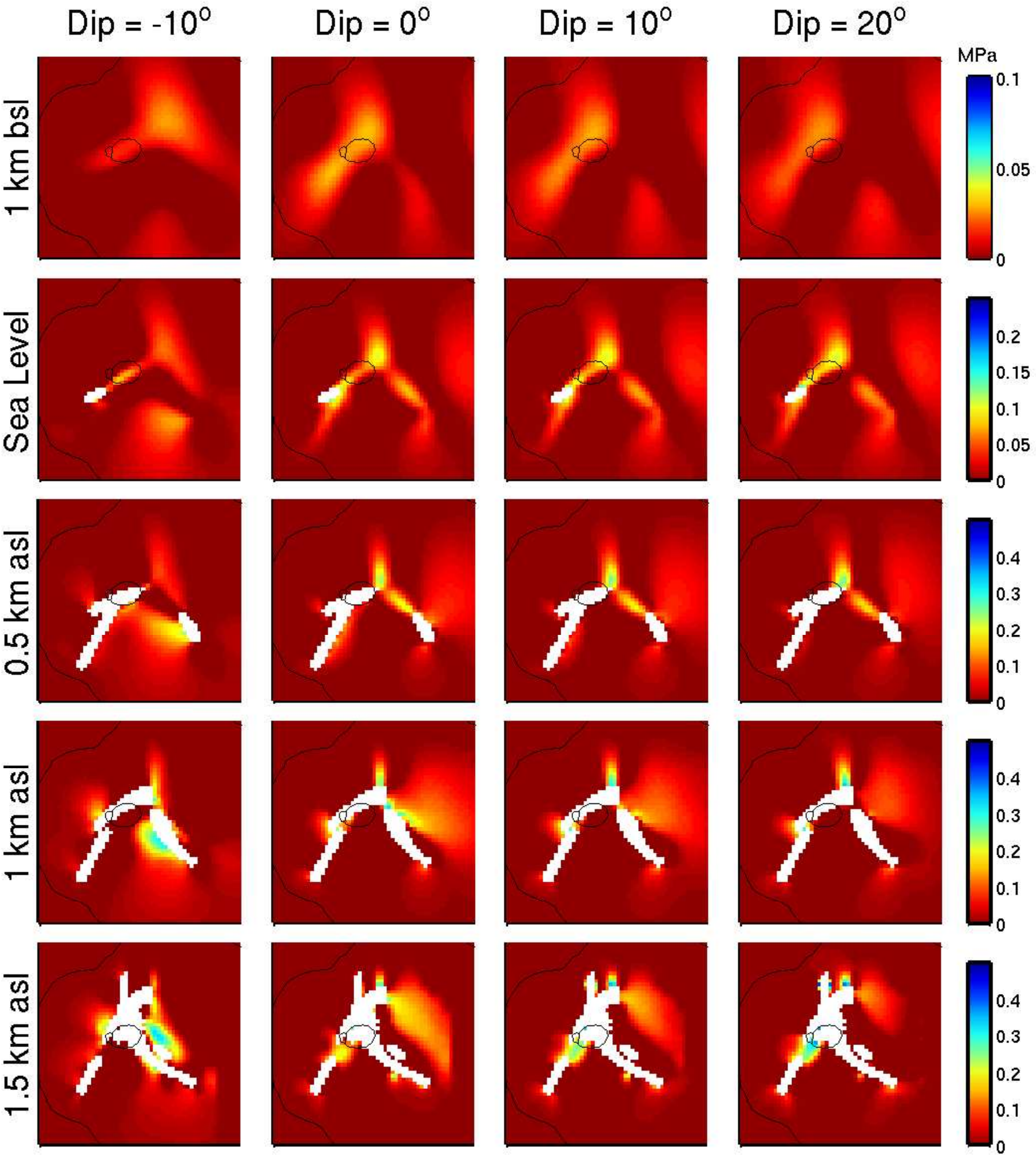

Figure 4.18: Coulomb failure stress changes (Equation 4.18) on potential fault planes caused by the preferred dike models for the five eruptions of March 1998–June 2000 (Figure 3.40). The effective friction coefficient $\mu' = 0$ *is assumed. The calculations are made at depths of -1, 0, 0.5, 1, 1.5 km above sea level. Potential faults are assumed to have an eastward slip with four eastward dip angles of -10°, 0°, 10° and 20° (reckoned positive when the eastern end is lower than the western end).*

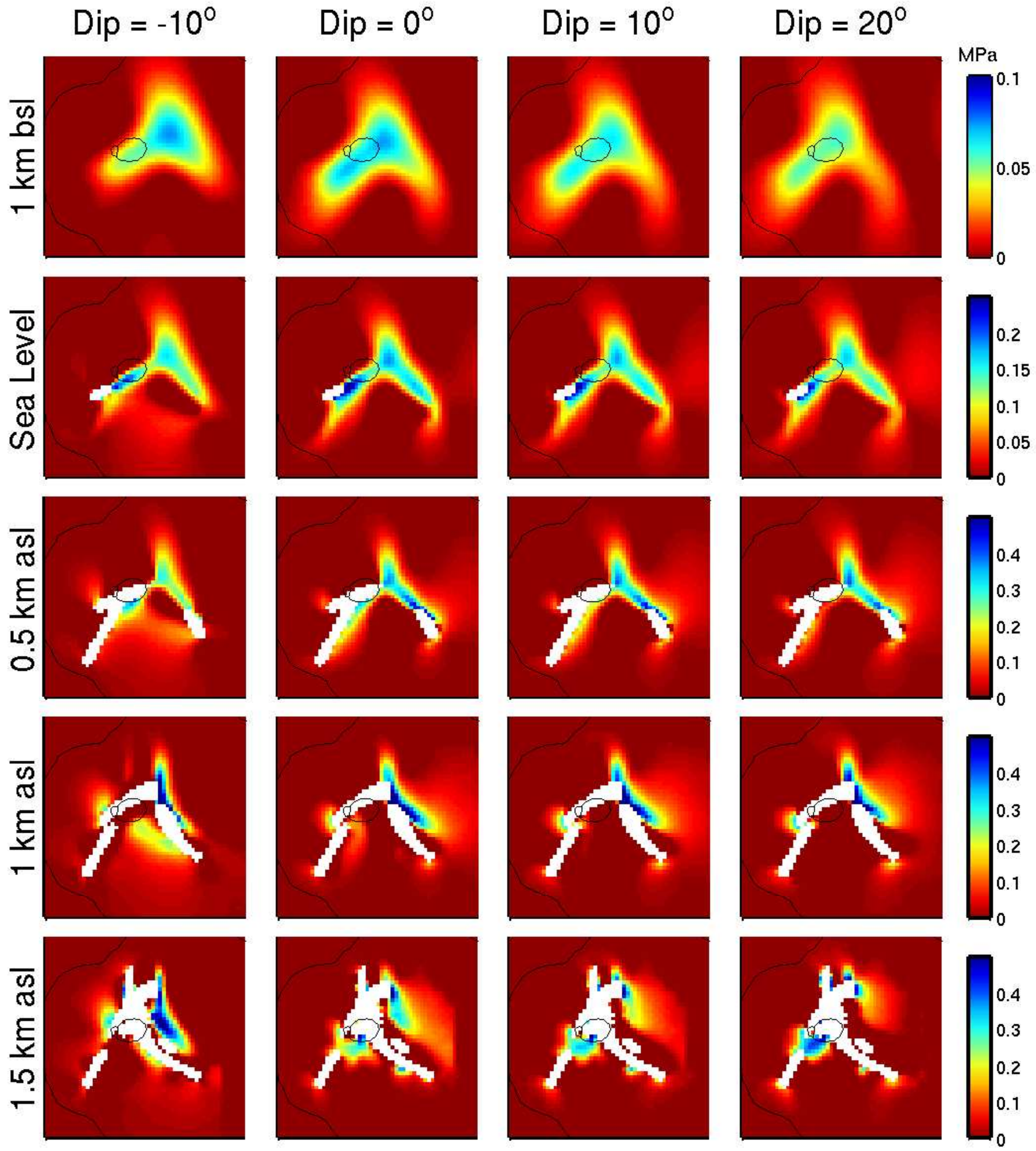

Figure 4.19: Same as Figure 4.18 except that potential faults are assumed to have an effective friction coefficient μ' of 0.6.

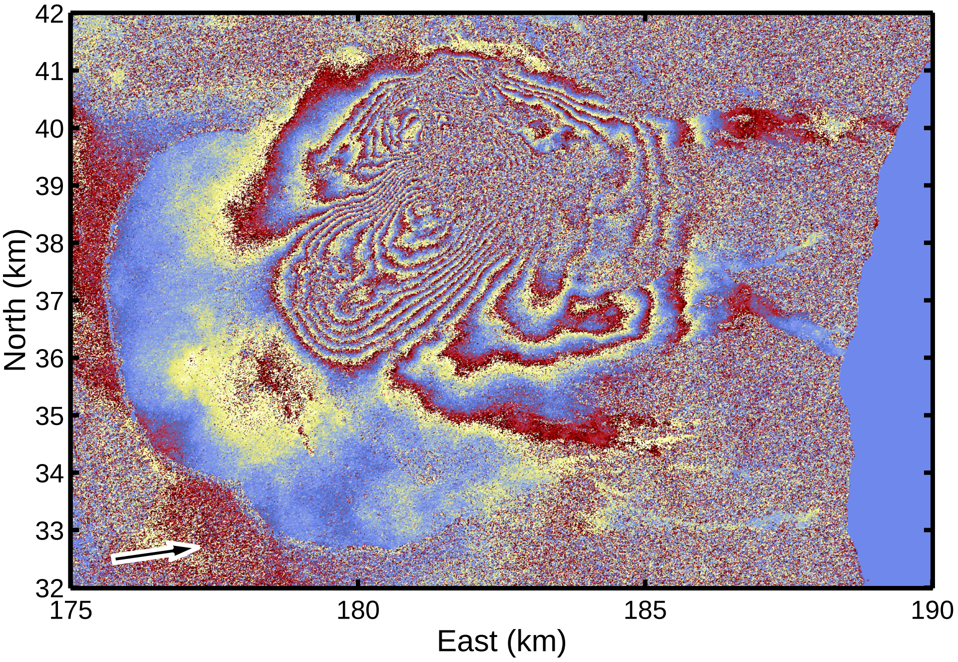
(a) January 2004 Ascending

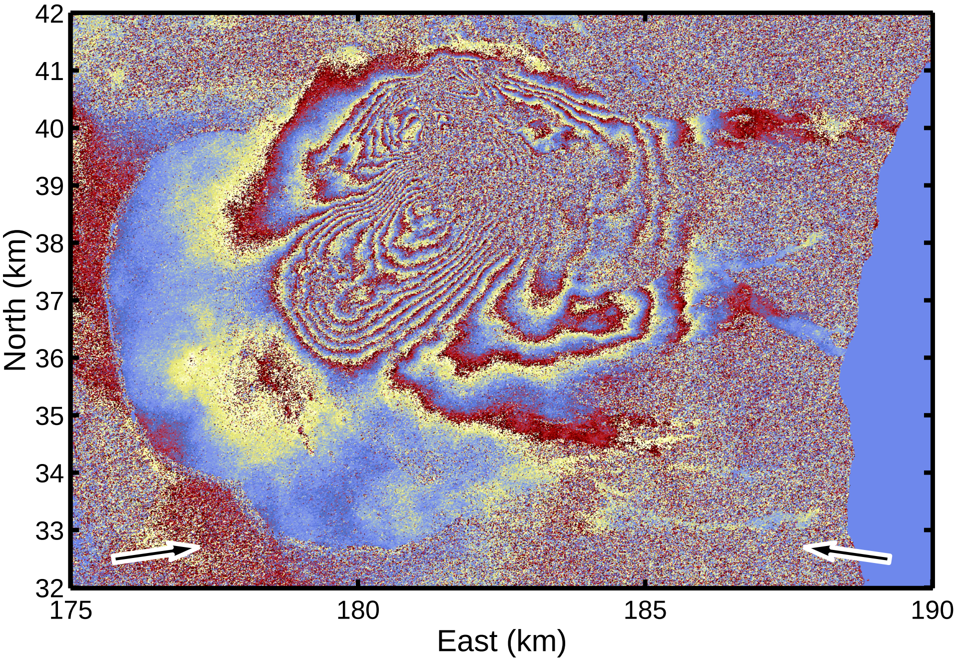
(b) January 2004 Descending

Figure 4.20: Interferograms showing the coeruptive displacements of the January 2004 eruption. (a) From ascending orbit. On the summit and the northeastern flank area, 11 fringes, which correspond to a maximum displacement of 30 cm toward the satellite, are recognized. This area of range decrease is located between the areas of range increase, indicating that the displacements do not result from a simple inflation. (b) From descending orbit. About 33 fringes are recognized, indicating a maximum displacement of 92 cm toward the satellite.

Chapter 5

Conclusions and Perspectives

SAR interferometry (InSAR) reveals complexity and variety of displacement patterns and hence of dike intrusion characteristics at Piton de la Fournaise volcano. To fully benefit from the high resolution and high precision of the InSAR data, a new method was developed that allows more complex and realistic modelling of the ground displacement data than simple analytical methods that were frequently used. The method, with application to interferograms of the five eruptions between March 1998 and June 2000, provided good constraints on the dike emplacements associated with the eruptions. Taking into account the modelled results with other sets of observation such as seismicity, tilt changes and lava output rates as well as theoretical expectations of magma movement, brought new insights on the magmatic processes that take place in the volcano. The careful modelling of the dike emplacements permitted to further predict the future development of the volcano.

Method of modelling interferometric data

We showed in Chapter 2 that a combination of InSAR data, a three-dimensional mixed boundary element method and a neighbourhood algorithm inversion gives detailed and reliable information on dike intrusions. Synthetic tests showed that a test model can be well retrieved by the inversion method within predicted uncertainties, and that all the tested subsampling methods are acceptable for our dike intrusion problem. For the InSAR data, the marginal probability density functions of model parameters indicate small uncertainties and trade-offs. Incorporating data noise correlation is found to be important; a misfit function that takes this into account leads to a significantly different maximum probability (best fit) model.

We further showed that models which neglect the topography, including a single rectangular dislocation model, poorly estimate the geometry at depth and overpressure (or opening). Overestimations in overpressure (or opening) and dike height amount to about 30%, and in volume to about 20%. This indicates the importance of taking realistic topography into account. A dike model coupled with a basal slip plane, as may exist under Enclos-Fouqué caldera, showed that the observed asymmetric displacements cannot be attributed to a slip on a basal plane, but are solely caused by the dip of the dike.

The residuals of the observed interferograms and model predictions indicate oversimplifications of the model. The homogeneity and isotropy assumptions on the edifice, and the uniform overpressure assumption could be the origin of the residuals. The effect of overpressure distribution can be studied by the mixed BEM, but relaxing the homogeneity and isotropy assumptions requires a different modelling method.

Geometries of the dike intrusions

In Chapter 3, application of the method revealed that the dike intrusions, associated with the eruptions between 1998 and 2000, were restricted above sea level (2600 m beneath the summit). The wide fringes associated with the March 1998 eruption were found to be caused either by a deep dike originating from sea level and reaching the northern eruptive fissures, or by a sill-type intrusion at a depth of around 500 m above sea level. The subsequent two eruptions in July and September 1999 were associated with shallow dikes whose bottom side lie less than a few hundred meters beneath the ground. For these eruptions, InSAR indicated superficial intrusions (depths shallower than 350 m (July) and 120 m (September)) connecting the main eruption site at the summit and a secondary one located downslope. The dikes associated with the last two eruptions analyzed in this thesis, in February and June 2000, are estimated to be rooted 1000 and 1500 meters beneath the ground. The one corresponding to the June 2000 eruption may be curved along the dipping direction.

Magma storage system

The minimum possible depths of the source magma reservoirs that fed the eruptions were estimated by taking into account the observation that the interferograms do not indicate any deflation source associated with the eruptions. It was found that such estimates may provide better constraints than those indicated by seismicity, if we have a good knowledge of the compressibility of the reservoirs.

The laterally elongated geometries of dikes determined by modelling indicate that a level of neutral buoyancy for the emplaced magma is located shallower than the bottom sides of the dikes which mostly lie around or less than 1000 m beneath the ground. This predicts the existence of shallow magma reservoirs around the level of neutral buoyancy beneath the summit.

Thermal conduction equations predict that magmatic intrusions having a thickness of less than one meter, which is found to be the case for the intrusions analyzed in this thesis, completely solidify in a few days. This excludes the idea that sheet like intrusions (dikes and sills) or cylindrical conduits having a radius of the order of one meter serve as magma storage or conduits for the subsequent eruptions.

Magma transfer during an eruption

The separation of more than 1 km between the estimated dikes and the magma sources calls for magma conduits between the sources and dikes. Considering that tiltmeters and extensometers detected upward magma propagation when the preeruption seismic swarm appeared above sea level, it was shown that the magma was transported in a dike and not in a cylindrical conduit. This dike-type conduit, however, transforms into a cylindrical conduit as eruption proceeds. The lava output rate constrained the radius of such a cylindrical conduit to be of the order of one meter.

The fact that the dike-type conduit practically closes (leaving a narrow cylindrical conduit), as indicated by the lack of signal in the interferometric data, is consistent with buoyant magma and with the location of this dike-type conduit beneath the level of neutral buoyancy. Shallower, magma stabilized and dikes were formed (did not close), as evidenced by interferograms, around the level of neutral buoyancy. Along this level, magma can flow downslope under the ground. This explains the localization of magma vents around the lowest fissures as well as secondary eruptions that often occur further downslope. If a new magma arrives at one of the shallow magma reservoirs, and if, at a late stage of an eruption, magma starts to flow downslope by gravity along the level of neutral buoyancy, then the reservoir may eventually be deplenished and a pit-crater collapse may occur.

The appropriateness of the proposed model of magma transfer can be evaluated by modelling the spatio-temporal evolution of dikes using continuous deformation data such as GPS and tilt. Better knowing about the contrast of magma and host rock densities can provide constraints on the stress field of the edifice, as buoyancy is controlled by the density contrast and variation of normal stress exerted on dikes. Understanding the relationships between propagating dikes and accompanied volcano-tectonic microearthquakes, especially the apparent anticorrelation such that microearthquakes do not frequently occur at the depths where dikes are emplaced, may further provide important findings on the stress state of the edifice.

Volcano growth

In Chapter 4, possible development of the volcano was also investigated by considering the effects of the five eruptions analyzed in this thesis. Displacements accumulated during the five eruptions clearly show east–upward growth of the volcanic edifice east of the rift zones. The slopes were estimated to have been steepened less than 2×10^{-2} degrees (350 microradians). Since the intruded volume for the five eruptions is only about 8% of the total lava flow volume, the effect of lava flow emplacements is required for a detailed long-term forecast of the growth of the edifice.

Asymmetric fringe patterns for the eruptions on the northern flank (March 1998 and February 2000) were best explained by dikes dipping seaward by about 65°. Similar asymmetric fringe patterns obtained on the southern rift zone for the September 2003 and May 2004 eruptions indicate a similar seaward dip angle. These indicate that the minimum principal stress along the rift zones is in east-west direction and inclined about 25° vertically. Such a stress condition may be associated with a weakness area created by gravitational instability, though further studies are needed to confirm the mechanism. This is fundamental to the formation of the rift zones of Piton de la Fournaise and hence is an important point to predict the future development of the volcano.

A dike intrusion changes the stress field of the edifice. If the normal stress on a potential dike plane is relaxed, intrusion on this plane is encouraged. It was found that, in the period of March 1998–June 2000, a dike intrusion encouraged the following intrusion(s), meaning that normal stress change analyses provide useful means to predict future eruption locations. A more mechanically appropriate way to predict the eruption locations would be to model the dike propagation in the three-dimensional stress field, because a dike propagation itself change the stress field of the edifice.

The analysis of Coulomb failure stress change indicated that the shallow dike emplacements most encourage slip of potential subhorizontal basal planes at depths of 1000–1500 m above sea level. At greater depths, the stress changes due to dike emplacements may be negligeable; however, a seaward landslide may be triggered by a propagating dike at depth.

Bibliography

Aki, K., and V. Ferrazzini, Seismic monitoring and modeling of an active volcano for prediction, *J. Geophys. Res.*, *105*, 16,617–16,640, 2000.

Amelung, F., and J. W. Bell, Interferometric synthetic aperture radar observations of the 1994 Double Spring Flat, Nevada, earthquake (M5.9): Main shock accompanied by triggered slip on a conjugate fault, *J. Geophys. Res.*, *108*(B9), 2433, doi:10.1029/2002JB001953, 2003.

Amelung, F., and S. Day, InSAR observations of the 1995 fogo, Cape Verde, eruption: Implications for the effects of collapse events upon island volcanoes, *Geophys. Res. Lett.*, *29*, doi:10.1029/2001GL013760, 2002.

Amelung, F., S. Jónsson, H. Zebker, and P. Segall, Widespread uplift and ’trapdoor’ faulting on Galàpagos volcanoes observed with radar interferometry, *Nature*, *407*, 993–996, 2000a.

Amelung, F., C. Oppenheimer, P. Segall, and H. Zebker, Ground deformation near Gada ’Ale Volcano, Afar, observed by radar interferometry, *Geophys. Res. Lett.*, *27*, 3093–3096, 2000b.

Anderson, E. M., The dynamics of sheet intrusion, *Proc. R. Soc. Edinburgh*, *58*, 242–251, 1938.

Annen, C., J.-F. Lénat, and A. Provost, The long-term growth of volcanic edifices: numerical modelling of the role of dyke intrusion and lava-flow emplacement, *J. Volcanol. Geotherm. Res.*, *105*, 263–289, 2001.

Aoki, Y., P. Segall, T. Kato, P. Cervelli, and S. Shimada, Imaging magma transport during the 1997 seismic swarm off the Izu Peninsula, Japan, *Science*, *286*, 927–930, 1999.

Avallone, A., P. Briole, C. Delacourt, A. Zollo, and F. Beauducel, Subsidence at Campi Flegrei (Italy) detected by SAR interferometry, *Geophys. Res. Lett.*, *26*, 2303–2306, 1999.

Bachèlery, P., Le Piton de la Fournaise (Ile de la Réunion): Etude volcanologique, structurale et pétrologique, *thèse de doctorat, Université Clermont-Ferrand II*, 1981.

Bachèlery, P., Quelques réflexions à propos de concepts récents sur la structure du Piton de la Fournaise, Réunion, *Comité National Français de Géodésie et de Géophysique, Rapport Quadriennal 1991–1994*, 107–112, 1995.

Bachèlery, P., Le fonctionnement des volcans boucliers: exemple des volcans de la Réunion et de la Grande Comore, *habilitation à diriger des recherches, Université de la Réunion*, 1999.

Bachèlery, P., and P. Mairine, Evolution volcano-structurale du Piton de la Fournaise depuis 0,53 M.a., in *Le voicanisme de la Réunion, Monographie*, edited by J.-F. Lénat, pp. 213–242, 1990.

Bachèlery, P., L. Chevallier, and J.-P. Gratier, Structural characteristics of historical eruptions of the Piton de la Fournaise (Reunion Island), *C. R. Acad. Sci. Paris*, *296*, 1345–1350, 1983.

Battaglia, J., Quantification sismique des phénomènes magmatiques sur le Piton de la Fournaise entre 1991 et 2000, *thèse de doctorat, Université Paris 7 Denis Diderot*, 2001.

Battaglia, J., and P. Bachèlery, Dynamic dyke propagation deduced from tilt variations preceding the March 9, 1998, eruption of the Piton de la Fournaise volcano, *J. Volcanol. Geotherm. Res.*, *120*, 289–310, 2003.

Battaglia, J., V. Ferrazzini, T. Staudacher, K. Aki, and J.-L. Cheminée, Pre-eruptive migration of earthquakes at the Piton de la Fournaise volcano (Réunion Island), *Geophys. J. Int.*, *161*, 549–558, 2005.

Beauducel, F., and F.-H. Cornet, Collection and three-dimensional modeling of GPS and tilt data at Merapi volcano, Java, *J. Geophys. Res.*, *104*, 725–736, 1999.

Beauducel, F., P. Briole, and J.-L. Froger, Volcano-wide fringes in ERS synthetic aperture radar interferograms of Etna (1992-1998): Deformation or tropospheric effect?, *J. Geophys. Res.*, *105*, 16,391–16,402, 2000a.

Beauducel, F., F.-H. Cornet, E. Suhanto, T. Duquesnoy, and M. Kasser, Constraints on magma flux from displacements data at Merapi volcano, Java, Indonesia, *J. Geophys. Res.*, *105*, 8193–8203, 2000b.

Bechor, N., and H. A. Zebker, Time series interferometry: toward weekly observations, *Eos Trans. AGU*, *85*(47), G51B–0090, fall Meet. Suppl., Abstract, 2004.

Björnsson, A., Dynamics of crustal rifting in NE Iceland, *J. Geophys. Res.*, *90*, 10,151–10,162, 1985.

Björnsson, A., K. Saemundsson, P. Einatsson, E. Tryggvason, and K. Grönvold, Current rifting episode in North Iceland, *Nature*, *266*, 318–323, 1977.

Boivin, P., and P. Bachèlery, The behaviour of the shallow plumbing system at La Fournaise volcano (Réunion Island). a petrological approach, *Geophysical Research Abstracts*, *5*, 11,455, paper presented at EGS-AGU-EUG Joint Assembly, Nice, France, 2003.

Bonafede, M., Hot fluid migration: an efficient source of ground deformation: application to the 1982–1985 crisis at Campi Flegrei, Italy, *J. Volcanol. Geotherm. Res.*, *48*, 187–198, 1990.

Bonafede, M., M. Dragoni, and F. Quareni, Displacement and stress fields produced by a centre of dilatation and by a pressure source in a viscoelastic half-space: application to the study of ground deformation and seismici activity at Campi Flegrei, Italy, *Geophys. J. R. Astron. Soc.*, *87*, 455–485, 1986.

Bos, A. G., S. Usai, and W. Spakman, A joint analysis of GPS motions and InSAR to infer the coseismic surface deformation of the izmit, Turkey earthquake, *Geophys. J. Int.*, *158*, 849–863, 2004.

Briole, P., D. Massonnet, and C. Delacourt, Post-eruptive deformation associated with the 1986-1987 and 1989 lava flows of Etna detected by radar interferometry, *Geophys. Res. Lett., 24*, 37–40, 1997.

Briole, P., P. Bachèlery, B. McGuire, J.-C. R. J. Moss, and P. Sabourault, Deformation of Piton de la Fournaise: Evolution of the monitoring techniques and knowledge acquired in the last five years, in *Volcanic Risk - The European Laboratory Volcanoes*, edited by C. et al., pp. 467–474, Office for Official Publications of the European Communities, European Communities, proceedings of the Second Workshop. Santorini, Greece, 2 to 4 May 1996, 1998.

Bureau, H., N. Metrich, F. Pineau, and M. P. Semet, Magma-conduit interaction at Piton de la Fournaise volcano (Reunion Island): a melt and fluid inclusion study, *J. Volcanol. Geotherm. Res., 84*, 39–60, 1998.

Bürgmann, R., P. A. Rosen, and E. J. Fielding, Synthetic aperture radar interferometry to measure Earth's surface topography and its deformation, *Annu. Rev. Earth Planet. Sci., 28*, 169–209, 2000.

Bürgmann, R., M. E. Ayhan, E. J. Fielding, T. J. Wright, S. McClusky, B. Aktug, C. Demir, O. Lenk, and A. Türkezer, Deformation during the 12 November 1999 Düzce, Turkey, earthquake, from GPS and InSAR data, *Bull. Seismol. Soc. Am., 92*, 161–171, 2002.

Burke, K. C., The African plate, *South African J. Geol., 99*, 341–409, 1996.

Carter, A., A morphological and structural analysis of the fractures on the summit of Piton de la Fournaise, Reunion Island, *DEA Memoire, Université Clermont-Ferrand II*, 2004.

Cayol, V., and F. H. Cornet, 3D mixed boundary elements for elastostatic deformation fields analysis, *Int. J. Rock Mech. Min. Sci. Geomech. Abstr., 34*, 275–287, 1997.

Cayol, V., and F.-H. Cornet, Three-dimensional modeling of the 1983-1984 eruption at Piton de la Fournaise Volcano, Reunion Island, *J. Geophys. Res., 103*, 18,025–18,037, 1998a.

Cayol, V., and F. H. Cornet, Effects of topography on the interpretation of the deformation field of prominent volcanoes - Application to Etna, *Geophys. Res. Lett., 25*, 1979–1982, 1998b.

Cayol, V., J. H. Dieterich, A. T. Okamura, and A. Miklius, High magma storage rates before the 1983 eruption of Kilauea, Hawaii, *Science, 288*, 2343–2346, 2000.

Cervelli, P., M. H. Murray, P. Segall, Y. Aoki, and T. Kato, Estimating source parameters from deformation data, with an application to the March 1997 earthquake swarm off the Izu Peninsula, Japan, *J. Geophys. Res., 106*, 11,217–11,237, 2001.

Cervelli, P., P. Segall, F. Amelung, H. Garbeil, C. Meertens, S. Owen, A. Miklius, and M. Lisowski, The 12 September 1999 Upper East Rift Zone dike intrusion at Kilauea Volcano, Hawaii, *J. Geophys. Res., 107*(B7), doi:10.1029/2001JB000602, 2002.

Chadwick, W. W., and J. H. Dieterich, Mechanical modeling of circumferential and radial dike intrusion on Galapagos volcanoes, *J. Volcanol. Geotherm. Res., 66*, 37–52, 1995.

Chen, C. W., and H. A. Zebker, Network approaches to two-dimensional phase unwrapping: intractability and two new algorithms, *J. Opt. Soc. Am., 17*, 401–414, 2000.

Chevallier, L., and P. Bachèlery, Evolution structurale du volcan actif du Piton de la Fournaise, Ile de la Réunion - Ocean Indien occidental, *Bull. Volcanol.*, *44*, 723–741, 1981.

Chevallier, L., and W. J. Verwoerd, A numerical model for the mechanical behavior of intraplate volcanoes, *J. Geophys. Res.*, *93*, 4182–4198, 1988.

Courtillot, V., J. Besse, D. Vandamme, R. Montigny, J.-J. Jaeger, and H. Cappetta, Deccan flood basalts at the Cretaceous-Tertiary boundary?, *Earth Planet. Sci. Lett.*, *80*, 361–374, 1986.

Dahm, T., On the shape and velocity of fluid-filled fractures in the earth, *Geophys. J. Int.*, *142*, 181–192, 2000.

De Natale, G., and F. Pingue, Ground deformation modeling in volcanic areas, in *Monitoring and Mitigation of Volcano Hazards*, edited by R. I. Tilling and R. Scarpa, pp. 365–388, Springer-Verlag, Berlin, Germany, 1996.

de Voogd, B., S. P. Palome, A. Hirn, P. Charvis, J. Gallart, D. Rousset, J. Danobeitia, and H. Perroud, Vertical movements and material transport during hotspot activity: Seismic reflection profiling offshore La Réunion, *J. Geophys. Res.*, *104*, 2855–2874, 1999.

Delaney, P. T., and A. E. Gartner, Physical processes of shallow mafic dike emplacement near the San Rafael Swell, Utah, *Geol. Soc. Am. Bull.*, *109*, 1177–1192, 1997.

Delaney, P. T., and D. D. Pollard, Deformation of host rocks and flow of magma during growth of minette dikes and breccia-bearing intrusions near Ship Rock, New Mexico, *U. S. Geol. Surv. Prof. Paper*, pp. 1202–1263, 1981.

Delaney, P. T., and D. D. Pollard, Solidification of basaltic magma during flow in a dike, *American J. Sci.*, *282*, 856–885, 1982.

Delaney, P. T., D. D. Pollard, J. I. Ziony, and E. H. McKee, Field relations between dikes and joints: Emplacement processes and paleostress analysis, *J. Geophys. Res.*, *91*, 4920–4938, 1986.

Delorme, H., et al., March 1986 eruptive episodes at Piton de la Fournaise Volcano (Reunion Island), *J. Volcanol. Geotherm. Res.*, *36*, 199–208, 1989.

Dieterich, J. H., Growth and persistence of Hawaiian volcanic rift zones, *J. Geophys. Res.*, *93*, 4258–4270, 1988.

Dieterich, J. H., and R. W. Decker, Finite element modeling of surface deformation associated with volcanism, *J. Geophys. Res.*, *80*, 4094–4102, 1975.

Duffield, W. A., L. Stieltjes, and J. Varet, Huge landslide blocks in the growth of Piton de la Fournaise, la Reunion, and Kilauea Volcano, Hawaii, *J. Volcanol. Geotherm. Res.*, *12*, 147–160, 1982.

Dvorak, J. J., and D. Dzurisin, Volcano geodesy: The search for magma reservoirs and the formation of eruptive vents, *Review of Geophysics*, *35*, 343–384, 1997.

Dvorak, J. J., A. Okamura, and J. H. Dieterich, Analysis of surface deformation data, Kilauea volcano, Hawaii, October 1966 to September 1970, *J. Geophys. Res.*, *88*, 9295–9304, 1983.

Elsworth, D., and S. J. Day, Flank collapse triggered by intrusion: the Canarian and Cape Verde Archipelagoes, *J. Volcanol. Geotherm. Res.*, *94*, 323–340, 1999.

Feigl, K. L., J. Gasperi, F. Sigmundsson, and A. Rigo, Crustal deformation near Hengill volcano, Iceland 1993-1998: Coupling between magmatic activity and faulting inferred from elastic modeling of satellite radar interferograms, *J. Geophys. Res.*, *105*, 25,655–25,670, 2000.

Feigl, K. L., et al., Estimating slip distribution for the İzmit mainshock from coseismic GPS, ERS-1, RADARSAT, and SPOT measurements, *Bull. Seismol. Soc. Am.*, *92*, 138–160, 2002.

Feretti, A., C. Prati, and F. Rocca, Permanent scatterers in SAR interferometry, *IEEE Trans. Geosci. Rem. Sens.*, *39*, 8–20, 2001.

Fialko, Y., Probing the mechanical properties of seismically active crust with space geodesy: Study of the coseismic deformation due to the 1992 M_w 7.3 Landers (southern California) earthquake, *J. Geophys. Res.*, *109*, B03307, doi:10.1029/2003JB002756, 2004.

Fialko, Y., and M. Simons, Deformation and seismicity in the Coso geothermal area, Inyo County, California: Observations and modeling using satellite radar interferometry, *J. Geophys. Res.*, *105*, 21,781–21,794, 2000.

Fialko, Y., and M. Simons, Evidence for on-going inflation of the Socorro magma body, New Mexico, from interferometric synthetic aperture radar imaging, *Geophys. Res. Lett.*, *28*, 3549–3552, 2001.

Fialko, Y., Y. Khazan, and M. Simons, Deformation due to a pressurized horizontal circular crack in an elastic half-space, with applications to volcano geodesy, *Geophys. J. Int.*, *146*, 111–190, 2001a.

Fialko, Y., M. Simons, and D. Agnew, The complete (3-D) surface displacement field in the epcentral area of the 1999 M_w 7.1 Hector Mine earthquake, California, from space geodetic observations, *Geophys. Res. Lett.*, *28*, 3063–3066, 2001b.

Fialko, Y., M. Simons, and Y. Khazan, Finite source modelling of magmatic unrest in Socorro, New Mexico, and Long Valley, California, *Geophys. J. Int.*, *146*, 191–200, 2001c.

Fialko, Y., D. Sandwell, D. Agnew, M. Simons, P. Shearer, and B. Minster, Deformation on nearby faults induced by the 1999 Hector Mine earthquake, *Science*, *297*, 1858–1862, 2002.

Fialko, Y., D. Sandwell, M. Simons, and P. Rosen, Three-dimensional deformation caused by the Bam, Iran, earthquake and the origin of shallow slip deficit, *Nature*, *435*, 295–299, 2005.

Fialko, Y. A., and A. M. Rubin, Thermodynamics of lateral dike propagation: Implications for crustal accretion at slow spreading mid-ocean ridges, *J. Geophys. Res.*, *103*, 2501–2514, 1998.

Fialko, Y. A., and A. M. Rubin, Thermal and mechanical aspects of magma emplacement in giant dike swarms, *J. Geophys. Res.*, *104*, 23,033–23,049, 1999.

Froger, J.-L., O. Merle, and P. Briole, Active spreading and regional extension at Mount Etna imaged by SAR interferometry, *Earth Planet. Sci. Lett.*, *187*, 245–258, 2001.

Froger, J.-L., Y. Fukushima, P. Briole, T. Staudacher, T. Souriot, and N. Villeneuve, The deformation field of the August 2003 eruption at Piton de la Fournaise, Reunion Island, mapped by ASAR interferometry, *Geophys. Res. Lett.*, *31*, L14601, doi:10.1029/2004GL020479, 2004.

Fujiwara, S., H. Yarai, S. Ozawa, M. Tobita, M. Murakami, H. Nakagawa, K. Nitta, P. A. Rosen, and C. L. Werner, Surface displacement of the March 26, 1997 Kagoshima-ken-hokuseibu earthquake in Japan from synthetic aperture radar interferometry, *Geophys. Res. Lett.*, *25*, 4541–4544, 1998.

Fukushima, Y., V. Cayol, and P. Durand, Finding realistic dike models from interferometric synthetic aperture radar data: The February 2000 eruption at Piton de la Fournaise, *J. Geophys. Res.*, *110*, B03206, doi:10.1029/2004JB003268, 2005.

Furuya, M., Localized deformation at Miyakejima volcano based on JERS-1 radar interferometry: 1992-1998, *Geophys. Res. Lett.*, *31*, L05605, doi:10.1029/2003GL019364, 2004.

Furuya, M., Quasi-static thermoelastic deformation in an elastic half-space: theory and application to InSAR observations at Izu-Oshima volcano, Japan, *Geophys. J. Int.*, *161*, 230–242, 2005.

Gabriel, A. K., R. M. Goldstein, and H. A. Zebker, Mapping small elevation changes over large areas: differential radar interferometry, *J. Geophys. Res.*, *94*, 9183–9191, 1989.

Gillot, P.-Y., and P. Nativel, Eruptive history of the Piton de la Fournaise volcano, Reunion Island, Indian Ocean, *J. Volcanol. Geotherm. Res.*, *36*, 53–65, 1989.

Grasso, J. R., and P. Bachèlery, Hierarchical organization as a diagnostic approach to volcano mechanics: Validation on Piton de la Fournaise, *Geophys. Res. Lett.*, *22*, 2897–2900, 1995.

Gudmundsson, A., Form and dimensions of dykes in eastern Iceland, *Tectonophysics*, *95*, 295–307, 1983.

Gudmundsson, A., Emplacement and arrest of sheets and dykes in central volcanoes, *J. Volcanol. Geotherm. Res.*, *116*, 279–298, 2002.

Hanssen, R. F., *Radar Interferometry – Data Interpretation and Error Analysis*, 308 pp., Kluwer Academic Publishers, Dordrecht, The Netherlands, 2001.

Harris, R. A., Introduction to special section: Stress triggers, stress shadows, and implications for seismic hazard, *J. Geophys. Res.*, *103*, 24,347–24,358, 1998.

Hirn, A., J.-C. Lepine, M. Sapin, and H. Delorme, Episodes of pit-crater collapse documented by seismology at Piton de la Fournaise, *J. Volcanol. Geotherm. Res.*, *47*, 89–104, 1991.

Hooper, A., H. Zebker, P. Segall, and B. Kampes, A new method for measuring deformation on volcanoes and other natural terrains using InSAR persistent scatterers, *Geophys. Res. Lett.*, *31*, L23611, doi:10.1029/2004GL021737, 2004.

Ingraffea, A. R., Theory of crack initiation and propagation in rock, in *Fracture mechanics of rock*, edited by B. K. Atkinson, pp. 71–110, 1987.

Iverson, R. M., Can magma-injection and groundwater forces cause massive landslides on Hawaiian volcanoes?, *J. Volcanol. Geotherm. Res.*, *66*, 295–308, 1995.

Jacobs, A., D. Sandwell, Y. Fialko, and L. Sichoix, The 1999 (M_w 7.1) Hector Mine, California, earthquake: Near-field postseismic deformation from ERS interferometry, *Bull. Seismol. Soc. Am.*, *92*, 1433–1442, 2002.

Jaeger, J. C., and N. G. W. Cook, *Fundamentals of rock mechanics*, Chapman and Hall, London, 3rd ed., 1979.

Jaupart, C., Magma ascent at shallow levels, in *Encyclopedia of Volcanoes*, edited by H. Sigurdsson, B. Houghton, S. R. McNutt, H. Rymer, and J. Stix, pp. 237–245, Academic Press, 2000.

Johnson, A. M., and D. D. Pollard, Mechanics of growth of some laccolithic intrusions in the Henry Mountains, Utah: I. Field observations, Gilbert's model, physical properties and flow of the magma, *Tectonophysics*, *18*, 261–309, 1973.

Johnson, D. J., Dynamics of magma storage in the summit reservoir of Kilauea volcano, Hawaii, *J. Geophys. Res.*, *97*, 1807–1820, 1992.

Johnson, D. J., F. Sigmundsson, and P. T. Delaney, Comment on "volume of magma accumulation or withdrawal estimated from surface uplift or subsidence, with application to the 1960 collapse of Kilauea volcano" by P. T. Delaney and D. F. McTigue, *Bull. Volcanol.*, *61*, 491–493, 2000.

Jónsson, S., H. Zebker, P. Cervelli, P. Segall, H. Garbeil, P. Mouginis-Mark, and S. Rowland, A shallow-dipping dike fed the 1995 flank eruption at Fernandina volcano, galápagos, observed by satellite radar interferometry, *Geophys. Res. Lett.*, *26*, 1077–1080, 1999.

Jónsson, S., H. Zebker, P. Segall, and F. Amelung, Fault slip distribution of the 1999 M_w 7.1 Hector Mine, California, earthquake, estimated from satellite radar and GPS measurements, *Bull. Seismol. Soc. Am.*, *92*, 1377–1389, 2002.

Jónsson, S., H. Zebker, and F. Amelung, On trapdoor faulting at Sierra Negra volcano, Galápagos, *J. Volcanol. Geotherm. Res.*, *144*, 59–71, 2005.

Khazan, Y. M., and Y. A. Fialko, Fracture criteria at the tip of fluid-driven cracks in the Earth, *Geophys. Res. Lett.*, *22*, 2541–2544, 1995.

King, G. C. P., R. S. Stein, and J. Lin, Static stress changes and the triggering of earthquakes, *Bull. Seismol. Soc. Am.*, *84*, 935–953, 1994.

Labazuy, P., Recurrent landslides events on the submarine flank of Piton de la Fournaise volcano (Reunion Island), in *Volcano Instability on the Earth and Other Planets*, edited by W. J. McGuire, A. P. Jones, and J. Neuberg, 110, pp. 295–306, Geological Society Special Publication, 1996.

Lanari, R., et al., The use of IFSAR and classical geodetic techniques for caldera unrest episodes: application to the Campi Flegrei uplift event of 2000, *J. Volcanol. Geotherm. Res.*, *133*, 247–260, 2004.

Lénat, J.-F., and P. Bachèlery, Structure et fonctionnement de la zone centrale du Piton de la Fournaise, in *Le voicanisme de la Réunion, Monographie,* edited by J.-F. Lénat, pp. 257–296, 1990.

Lénat, J.-F., P. Bachèlery, A. Bonneville, and A. Hirn, The beginning of the 1985-1987 eruptive cycle at Piton de la Fournaise (La Reunion): New insights in the magmatic and volcano-tectonic systems, *J. Volcanol. Geotherm. Res.*, *36*, 209–232, 1989a.

Lénat, J.-F., P. Vincent, and P. Bachèlery, The off-shore continuation of an active basaltic volcano: Piton de la Fournaise (Réunion Island, Indian Ocean); Structural and geomorphological, interpretation from seabeam mapping, *J. Volcanol. Geotherm. Res.*, *36*, 1–36, 1989b.

Lénat, J.-F., D. Fitterman, D. B. Jackson, and P. Labazuy, Geoelectrical structure of the central zone of Piton de la Fournaise volcano (Reunion), *Bull. Volcanol.*, *62*, 75–89, 2000.

Lénat, J.-F., B. G. Malengreau, and A. Galdéano, A new model for the evolution of the volcanic island of Réunion (Indian Ocean), *J. Geophys. Res.*, *106*, 8645–8663, 2001.

Lister, J. R., and R. C. Kerr, Fluid-mechanical models of crack propagation and their application to magma transport in dykes, *J. Geophys. Res.*, *96*, 10,049–10,077, 1991.

Lohman, R. B., M. Simons, and B. Savage, Location and mechanism of the Little Skull mountain earthquake as constrained by satellite radar interferometry and seismic waveform modeling, *J. Geophys. Res.*, *107*(B6), 2118, doi:10.1029/2001JB000627, 2002.

Longpré, M.-A., T. Staudacher, and J. Stix, The November 2002 eruption at Piton de la Fournaise volcano, La Réunion Island: ground deformation, seismicity, and pit crater collapse, paper presented at IAVCEI General Assembly, Puón, Chile, 2004.

Lu, Z., D. Mann, J. Freymueller, and D. Meyer, Synthetic aperture radar interferometry of Okmok volcano, Alaska: Radar observations, *J. Geophys. Res.*, *105*, 10,791–10,806, 2000a.

Lu, Z., C. Wicks Jr., D. Dzurisin, W. Thatcher, J. Freymueller, S. McNutt, and D. Mann, Aseismic inflation of Westdahl volcano, Alaska, revealed by satellite radar interferometry, *Geophys. Res. Lett.*, *27*, 1567–1570, 2000b.

Lu, Z., C. Wicks Jr., J. A. Power, and D. Dzurisin, Ground deformation associated with the March 1996 earthquake swarm at Akutan volcano, Alaska, revealed by satellite radar interferometry, *J. Geophys. Res.*, *105*, 21,483–21,495, 2000c.

Lu, Z., T. Masterlark, J. Power, D. Dzurisin, and C. Wicks, Subsidence at Kiska Volcano, Western Aleutians, detected by satellite radar interferometry, *Geophys. Res. Lett.*, *29*, 1855, doi:10.1029/2002GL014948, 2002.

Lu, Z., T. Masterlark, D. Dzurisin, R. Rykhus, and C. W. Jr, Magma supply dynamics at Westdahl volcano, Alaska, modeled from satellite radar interferometry, *J. Geophys. Res.*, *108*, 2354, doi:10.1029/2002JB002311, 2003.

Lundgren, P., and P. Rosen, Source model for the 2001 flank eruption of Mt. Etna volcano, *Geophys. Res. Lett.*, *30*, 1388, doi:10.1029/2002GL016774, 2003.

Lundgren, P., S. Usai, E. Sansosti, R. Lanari, M. Tesauro, G. Fornaro, and P. Berardino, Modeling surface deformation observed with synthetic aperture radar interferometry at Campi Flegrei caldera, *J. Geophys. Res.*, *106*, 19,355–19,366, 2001.

Lungarini, L., C. Troise, M. Meo, and G. D. Natale, Finite element modelling of topographic effects on elastic ground deformation at Mt. Etna, *J. Volcanol. Geotherm. Res.*, *144*, 257–271, 2005.

Lyons, S., and D. T. Sandwell, Fault creep along the southern San Andreas from InSAR, permanent scatterers, and stacking, *J. Geophys. Res.*, *108*(B1), 2047, doi:10.1029/2002JB001831, 2003.

Maaloe, S., The generation and shape of feeder dykes from mantle sources, *Contrib. Mineral. Petrol.*, *203*, 215–249, 1987.

Maillot, E., Les systèmes intrusifs des volcans boucliers oceaniques: Ile de la Réunion (Océan Indien), *thèse de doctorat, Université de la Réunion*, 1999.

Mann, D., J. Freymueller, and Z. Lu, Deformation associated with the 1997 eruption of Okmok volcano, Alaska, *J. Geophys. Res.*, *107*, doi:10.1029/2001JB000163, 2002.

Massonnet, D., Etude de principe d'une détection de mouvements tectoniques par radar, in *Int. Memo.*, vol. 326, Centre National d'Etudes Spatiales, Toulouse, France, 1985.

Massonnet, D., and K. L. Feigl, Radar interferometry and its application to changes in the earth's surface, *Rev. Geophys.*, *36*, 441–500, 1998.

Massonnet, D., and T. Rabaute, Radar interferometry: limits and potential, *IEEE Trans. Geosci. Rem. Sens.*, *31*, 455–464, 1993.

Massonnet, D., M. Rossi, C. Carmona, F. Adragna, G. Peltzer, K. Feigl, and T. Rabaute, The displacement field of the Landers earthquake mapped by radar interferometry, *Nature*, *364*, 138–142, 1993.

Massonnet, D., P. Briole, and A. Arnaud, Deflation of mount etna monitored by spacebourne radar interferometry, *Nature*, *375*, 567–570, 1995.

Masterlark, T., Finite element model predictions of static deformation from dislocation sources in a subduction zone: Sensitivities to homogeneous, isotropic, Poisson-solid, and half-space assumptions, *J. Geophys. Res.*, *108*, doi:10.1029/2002JB002296, 2003.

Masterlark, T., Magma intrusion estimated from InSAR data: Sensitivities to homogeneous, isotropic, Poisson-solid, and half-space assumptions, *Eos Trans. AGU*, *85*(47), G51A–0050, fall Meet. Suppl., Abstract, 2004.

Masterlark, T., and Z. Lu, Transient volcano deformation sources images with interferometric synthetic aperture radar: Application to Seguam Island, Alaska, *J. Geophys. Res.*, *109*, B01401, doi:10.1029/2003JB002568, 2004.

McTigue, D. F., Elastic stress and deformation near a finite spherical magma body: Resolution of the point source paradox, *J. Geophys. Res.*, *92*, 12,931–12,940, 1987.

McTigue, D. F., and Segall, Displacements and tilts from dip-slip faults and magma chambers beneath irregular surface topography, *J. Geophys. Res.*, *15*, 601–604, 1988.

Menand, T., and S. R. Tait, A phenomenological model for precursor volcanic eruptions, *Nature*, *411*, 678–680, 2001.

Mériaux, C., and C. Jaupart, Simple fluid dynamic models of volcanic rift zones, *Earth Planet. Sci. Lett.*, *136*, 223–240, 1995.

Mériaux, C., and C. Jaupart, Dike propagation through an elastic plate, *J. Geophys. Res.*, *103*, 18,295–18,314, 1998.

Merle, O., and J.-F. Lénat, Hybrid collapse mechanism at Piton de la Fournaise volcano, Reunion Island, Indian Ocean, *J. Geophys. Res.*, *108*(B3), doi:10.1029/2002JB002014, 2003.

Michel, R., J.-P. Avouac, and J. Taboury, Measuring ground displacements from SAR amplitude images : application to the Landers earthquake, *Geophys. Res. Lett.*, *26*, 875–878, 1999a.

Michel, R., J.-P. Avouac, and J. Taboury, Measuring near field coseismic displacements from SAR images : application to the Landers earthquake, *Geophys. Res. Lett.*, *26*, 3017–3020, 1999b.

Michel, S., and J. Zlotnicki, Self-potential and magnetic surveying of La Fournaise volcano (Reunion Island): Correlations with faulting, fluid circulation, and eruption, *J. Geophys. Res.*, *103*, 17,845–17,857, 1998.

Mogi, K., Relations between the eruptions of various volcanoes and the deformations of the ground surfaces around them, *Bull. Earthq. Res. Inst., Univ. Tokyo*, *36*, 99–134, 1958.

Mohamed-Abchir, A., M. P. Semet, G. Boudon, P. Ildefonse, P. Bachèlery, and R. Clocchiatti, Huge hydrothermal explosive activity on Piton de la Fournaise, Réunion Island: The Bellecombe Ash Member, 2700 BC, in *Volcanic Risk - The European Laboratory Volcanoes*, edited by C. et al., pp. 447–455, Office for Official Publications of the European Communities, European Communities, proceedings of the Second Workshop. Santorini, Greece, 2 to 4 May 1996, 1998.

Mossop, A., and P. Segall, Volume strain within The Geysers geothermal field, *J. Geophys. Res.*, *104*, 29,113–29,131, 1999.

Murase, T., and A. R. McBirney, Properties of some common igneous rocks and their melts at high temperatures, *Geol. Soc. Am. Bull.*, *84*, 3563–3592, 1973.

Nelder, J. A., and R. Mead, A simplex method for function minimization, *Computer Journal*, *7*, 308–313, 1965.

Nercessian, A., A. Hirn, J.-C. Lepine, and M. Sapin, Internal structure of Piton de la Fournaise volcano from seismic wave propagation and earthquake distribution, *J. Volcanol. Geotherm. Res.*, *70*, 123–143, 1996.

Nishimura, T., S. Fujiwara, M. Murakami, M. Tobita, H. Nakagawa, T. Sagiya, and T. Tada, The m6.1 earthquake triggered by volcanic inflation of iwate volcano, northern japan, observed by satellite radar interferometry, *Geophys. Res. Lett.*, *28*, 635–638, 2001.

Oehler, J.-F., P. Labazuy, and J.-F. Lénat, Recurrence of major flank landslides during the last 2-Ma-history of Reunion Island, *Bull. Volcanol.*, *66*, 585–598, 2004.

Oehler, J.-F., B. van Wyk de Vries, and P. Labazuy, Landslides and spreading of oceanic hotspot and arc shield volcanoes on Low Strength Layers (LSLs): an analogue modeling approach, *J. Volcanol. Geotherm. Res.*, *144*, 169–189, 2005.

Okada, Y., Surface deformation due to shear and tensile faults in a half-space, *Bull. Seismol. Soc. Am.*, *75*, 1135–1154, 1985.

Okada, Y., and E. Yamamoto, Dyke intrusion model for the 1989 seismovolcanic activity off Ito, central Japan, *J. Geophys. Res.*, *96*, 10,361–10,376, 1991.

Okamura, A. T., J. Dvorak, R. Y. Koyanagi, and W. R. Tanigawa, Surface deformation during dike propagation: The 1983 east rift eruption of Kilauea volcano, Hawaii, *U. S. Geol. Surv. Prof. Paper*, *1463*, 165–182, 1988.

Owen, S., P. Segall, J. Freymueller, A. Miklius, R. Delinger, T. Arnadottir, M. Sako, and R. Bürgmann, Rapid deformation of the south flank of of Kilauea volcano, Hawaii, *Science*, *267*, 1328–1332, 1995.

Owen, S., P. Segall, M. Lisowski, A. Miklius, M. Murray, M. Bevis, and J. Foster, January 30, 1997 eruptive event on Kilauea Volcano, Hawaii, as monitored by continuous GPS, *Geophys. Res. Lett.*, *27*, 2757–2760, 2000.

Pagli, C., R. Pedersen, F. Sigmundsson, and K. L. Feigl, Triggered fault slip distribution on June 17, 2000 on the Reykjanes Peninsula, SW-Iceland captured by radar interferometry, *Geophys. Res. Lett.*, *30*(6), 1273, doi:10.1029/2002GL015310, 2003.

Parfitt, E. A., L. Wilson, and J. W. Head III, Basaltic magma reservoirs: factors controlling their rupture characteristics and evolution, *J. Volcanol. Geotherm. Res.*, *55*, 1–14, 1993.

Paul, A., J. P. Gratier, and J. A. Boudon, A numerical model for simulating deformation of Mount St. Helens volcano, *J. Geophys. Res.*, *92*, 10,299–10,312, 1987.

Pedersen, R., and F. Sigmundsson, InSAR based sill model links spatially offset areas of deformation and seismicity for the 1994 unrest episode at Eyjafjallajökull volcano, *Geophys. Res. Lett.*, *31*, L14610, doi:10.1029/2004GL020368, 2004a.

Pedersen, R., and F. Sigmundsson, Temporal development of the 1999 intrusive episode in the Eyjafjallajkull volcano, Iceland, derived from InSAR images, submitted to Bull. Volcanol., 2004b.

Pedersen, R., F. Sigmundsson, K. Feigl, and T. Árnadóttir, Coseismic interferograms of two M_s = 6.6 earthquakes in the South Iceland Seismic Zone, June 2000, *Geophys. Res. Lett.*, *28*, 3341–3344, 2001.

Pedersen, R., S. Jónsson, T. Árnadóttir, F. Sigmundsson, and K. L. Feigl, Fault slip distribution of two June 2000 M_w 6.5 earthquakes in South Iceland estimated from joint inversion of InSAR and GPS measurements, *Earth Planet. Sci. Lett.*, *213*, 487–502, 2003.

Peltzer, G., P. Rosen, F. Rogez, and K. Hudnut, Poroelastic rebound along the Landers 1992 earthquake surface rupture, *J. Geophys. Res.*, *103*, 30,131–30,145, 1998.

Pinel, V., and C. Jaupart, The effect of edifice load on magma ascent beneath a volcano, *Phil. Trans. R. Soc. Lond.*, *358*, 1515–1532, 2000.

Pinel, V., and C. Jaupart, Magma storage and horizontal dyke injection beneath a volcanic edifice, *Earth Planet. Sci. Lett.*, *221*, 245–262, 2004.

Pollard, D. D., On the form and stability of open hydraulic fractures in the Earth's crust, *Geophys. Res. Lett.*, *3*, 513–516, 1976.

Pollard, D. D., Elementary fracture mechanics applied to the structural interpretation of dykes, in mafic dyke swarms, in *Mafic Dyke Swarms*, edited by H. C. Halls and W. F. Fahrig, pp. 5–24, Geological Association of Canada Special Paper 34, 1987.

Pollard, D. D., and A. M. Johnson, Mechanics of growths of some laccolithic intrusions in the Henry Mountains, Utah: II. Bending and failure of overburden layers and sill formation, *Tectonophysics*, *18*, 311–354, 1973.

Pollard, D. D., and O. H. Muller, The effect of gradients in regional stress and magma pressure on the form of sheet intrusions in cross section, *J. Geophys. Res.*, *81*, 975–984, 1976.

Pollard, D. D., P. T. Delaney, W. A. Duffield, E. T. Endo, and A. T. Okamura, Surface deformation in volcanic rift zones, *Tectonophysics*, *94*, 541–584, 1983.

Pollitz, F. F., G. Peltzer, and R. Bürgmann, Mobility of continental mantle: Evidence from postseismic geodetic observations following the 1992 Landers earthquake, *J. Geophys. Res.*, *105*, 8035–8054, 2000.

Press, W. H., B. P. Flannery, S. A. Teukolsky, and W. T. Vetterling, *Numerical Recipes in C*, Cambridge Univ. Press, New York, 1992.

Pritchard, M. E., and M. Simons, A satellite geodetic survey of large-scale deformation of volcanic centres in the central Andes, *Nature*, *418*, 167–171, 2002.

Pritchard, M. E., and M. Simons, An InSAR-based survey of volcanic deformation in the central Andes, *Geochem. Geophys. Geosyst.*, Q02002, doi:10.1029/2003GC000610, 2004a.

Pritchard, M. E., and M. Simons, An InSAR-based survey of volcanic deformation in the southern Andes, *Geophys. Res. Lett.*, *31*, L15610, doi:10.1029/2004GL020545, 2004b.

Rançon, J.-P., P. Lerebour, and T. Auge, The Grand-Brule exploration drilling: New data on the deep framework of the Piton de la Fournaise volcano. part 1: Lithostratigraphic units and volcanostructural implications, *J. Volcanol. Geotherm. Res.*, *36*, 113–127, 1989.

Ranvier, F., Modelisation numerique des mouvements de flanc de l'Etna (Sicile, Italie) mis en evidence par interferometrie radar, *thèse de doctorat, Université Blaise Pascal*, 2004.

Raucoules, D., C. Carnec, M. Cruchet, C. Delacourt, D. Feurer, and S. L. Mouélic, Identification of landslides in La Reunion Island with JERS-1 and RADARSAT-1 radar interferometry, *Proc. of FRINGE 2003 Workshop, Frascanti, Italy*, 2003.

Reches, Z., and J. Fink, The mechanism of intrusion of the Inyo Dike, Long Valley Caldera, California, *J. Geophys. Res.*, *93*, 4321–4334, 1988.

Roche, O., B. van Wyk de Vries, and T. H. Druitt, Sub-surface structures and collapse mechanisms of summit pit craters, *J. Volcanol. Geotherm. Res.*, *105*, 1–18, 2001.

Rubin, A. M., Dike-induced faulting and graben subsidence in volcanic rift zones, *J. Geophys. Res.*, *97*, 1839–1858, 1992.

Rubin, A. M., On the thermal viability of dikes leaving magma chambers, *Geophys. Res. Lett.*, *20*, 257–260, 1993a.

Rubin, A. M., Tensile fracture of rock at high confining pressure: Implications for dike propagation, *J. Geophys. Res.*, *98*, 15,919–15,935, 1993b.

Rubin, A. M., Dikes vs diapirs in viscoelastic rock, *Earth Planet. Sci. Lett.*, *119*, 641–659, 1993c.

Rubin, A. M., Propagation of magma-filled cracks, *Annu. Rev. Earth Planet. Sci.*, *23*, 287–336, 1995.

Rubin, A. M., and D. Gillard, Dike-induced earthquakes: Theoretical considerations, *J. Geophys. Res.*, *103*, 10,017–10,030, 1998.

Rubin, A. M., and D. D. Pollard, Origins of blade-like dikes in volcanic rift zones, *U. S. Geol. Surv. Prof. Paper*, *1350*, 1449–1470, 1987.

Ryan, M. P., Elasticity and contractancy of Hawaiian olivine tholeiite and its role in the stability and structural evolution of subcaldera magma reservoirs and rift systems, *U. S. Geol. Surv. Prof. Paper*, *1350*, 1395–1447, 1987.

Salvi, S., S. Atzoni, C. Tolomei, J. Allievi, A. Ferretti, F. Rocca, C. Prati, S. Stramondo, and N. Feuillet, Inflation rate of the Colli Albani volcanic complex retrieved by the permanent scatterers SAR interferometry technique, *Geophys. Res. Lett.*, *31*, L12606, doi: 10.1029/2004GL020253, 2004.

Sambridge, M., Geophysical inversion with a neighbourhood algorithm - i. searching a parameter space, *Geophys. J. Int.*, *138*, 479–494, 1999a.

Sambridge, M., Geophysical inversion with a neighbourhood algorithm - ii. appraising the ensemble, *Geophys. J. Int.*, *138*, 727–746, 1999b.

Sambridge, M., and K. Mosegaard, Monte Carlo methods in geophysical inverse problems, *Rev. Geophys.*, *40*, 10.1029/2000RG000,089, 2002.

Sato, H., and M. C. Fehler, *Seismic wave propagation and scattering in the heterogeneous Earth*, Springer-Verlag, New York, 1998.

Schmidt, D. A., and R. Bürgmann, Time-dependent land uplift and subsidence in the Santa Clara valley, California, from a large interferometric synthetic aperture radar data set, *J. Geophys. Res.*, *108*(B8), 22416, doi:10.1029/2002JB002267, 2003.

Secor, D. T., and D. D. Pollard, On the stability of open hydraulic fractures in the Earth's crust, *Geophys. Res. Lett., 2,* 510–513, 1975.

Segall, P., and R. Harris, Slip deficit on the San Andreas fault at Parkfield, California, as revealed by inversion of geodetic data, *Science, 233,* 1409–1413, 1986.

Semet, M. P., J.-L. Joron, and T. Staudacher, The 1998–2002 activity of Piton de la Fournaise, Réunion Island: lessons in magma supply and transfers, *Geophysical Research Abstracts, 5,* 10,736, paper presented at EGS-AGU-EUG Joint Assembly, Nice, France, 2003.

Sheth, H. C., From Deccan to Reunion: no trace of a mantle plume, in *Plates, Plumes, and Paradigms*, edited by G. R. Foulger, J. H. Natland, D. C. Presnall, and D. L. Anderson, chap. 29, Geol. Soc. Am. Spec. Pap. 388, in press, 2005.

Sigmarsson, O., M. Condomines, and P. Bachèlery, Magma residence time beneath the Piton de la Fournaise Volcano, Reunion Island, from U-series disequilibria, *Earth Planet. Sci. Lett., 234,* 223–234, 2005.

Sigmundsson, F., H. Vadon, and D. Massonnet, Readjustment of the Krafla spreading segment to crustal rifting measured by satellite radar interferometry, *Geophys. Res. Lett., 24,* 1843–1846, 1997.

Sigmundsson, F., P. Durand, and D. Massonnet, Opening of an eruptive fissure and seaward displacement at Piton de la Fournaise volcano measured by RADARSAT satellite radar interferometry, *Geophys. Res. Lett., 26,* 533–536, 1999.

Simons, M., Y. Fialko, and L. Rivera, Coseismic deformation from the 1999 M_w 7.1 Hector Mine, California, earthquake as inferred from InSAR and GPS observations, *Bull. Seismol. Soc. Am., 92,* 1390–1402, 2002.

Staudacher, T., and J.-L. Cheminée, Piton de la Fournaise, *Bull. Global Volcanism Network, 24(7),* 1999.

Staudacher, T., P. Bachèlery, M. P. Semet, and J.-L. Cheminée, Piton de la Fournaise, *Bull. Global Volcanism Network, 23(3),* 2–4, 1998.

Staudacher, T., N. Villeneuve, and J.-L. Cheminée, Piton de la Fournaise, *Bull. Global Volcanism Network, 24(9),* 14–16, 1999.

Staudacher, T., N. Villeneuve, J.-L. Cheminée, K. Aki, J. Battaglia, P. Catherine, V. Ferrazzini, and P. Kowalski, Piton de la Fournaise, *Bull. Global Volcanism Network, 25(7),* 14–16, 2000.

Steacy, S., J. Gomberg, and M. Cocco, Introduction to special section: Stress transfer, earthquake triggering, and time-dependent seismic hazard, *J. Geophys. Res., 110,* B05S01, doi: 10.1029/2005JB003692, 2005.

Stieltjes, L., and P. Moutou, A statistical and probabilistic study of the historic activity of Piton de la Fournaise, Reunion Island, Indian Ocean, *J. Volcanol. Geotherm. Res., 36,* 67–86, 1989.

Tait, S., C. Jaupart, and S. Vergniolle, Pressure, gas content and eruption periodicity of a shallow crystallising magma chamber, *Earth Planet. Sci. Lett., 92,* 107–123, 1989.

Talebian, M., et al., The 2003 Bam (Iran) earthquake: Rupture of a blind strike-slip fault, *Geophys. Res. Lett.*, *31*, L11611, doi:10.1029/2004GL020058, 2004.

Timoshenko, S. P., and J. N. Goodier, *Theory of Elasticity*, McGraw-Hill, Singapore, 3rd ed., 1970.

Tinard, P., J.-L. Froger, Y. Fukushima, V. Cayol, P. Briole, T. Staudacher, and T. Souriot, One and a half year of INSAR monitoring of volcanic activity at Piton de la Fournaise, Réunion Island, with ASAR-ENVISAT data, *Eos Trans. AGU*, *85*(47), G51A–0056, fall Meet. Suppl., Abstract, 2004.

Troise, C., G. de Natale, F. Pingue, and J. Dvorak, Variable opening of dike-fed eruptive fissures determined from geodetic data: the 1971 and 1983 rift-zone eruptions of Kilauea Volcano, Hawaii, *Geodynamics*, *27*, 75–88, 1999.

Turcotte, D. L., and G. Schubert, *Geodynamics*, Cambridge Univ. Press, Cambridge, U. K., 2nd ed., 2002.

Turcotte, D. L., S. H. Emerman, and D. A. Spence, Mechanics of dyke injection, in *Mafic Dyke Swarms*, edited by H. C. Halls and W. F. Fahrig, pp. 25–29, Geological Association of Canada Special Paper 34, 1987.

Ueda, H., E. Fujita, M. Ukawa, E. Yamamoto, M. Irwan, and F. Kimata, Magma intrusion and discharge process at the initial stage of the 2000 activity of Miyakejima, Central Japan, inferred from tilt and GPS data, *Geophys. J. Int.*, *161*, 891–916, 2005.

Upton, B. G. J., and W. J. Wadsworth, The basalts of Réunion Island, Indian Ocean, *Bull. Volcanol.*, *29*, 7–22, 1966.

Vadon, H., and F. Sigmundsson, Crustal deformation from 1992-1995 at the Mid-Atlantic Ridge, SW Iceland, mapped by satellite radar interferometry, *Science*, *275*, 193–197, 1997.

van Dalfsen, E. Z., R. Pedersen, F. Sigmundsson, and C. Pagli, Satellite radar interferometry 1993 – 1999 suggests deep accumulation of magma near the crust-mantle boundary at the Krafla volcanic system, Iceland, *Geophys. Res. Lett.*, *31*, L13611, doi: 10.1029/2004GL020059, 2004.

Vasco, D. W., L. R. Johnson, and N. E. Goldstein, Using surface displacement and strain observations to determine deformation at depth, with an application to Long Valley Caldera, California, *J. Geophys. Res.*, *93*, 3232–3242, 1988.

Vasco, D. W., C. Wicks, K. Karasaki, and O. Marques, Geodetic imaging: reservoir monitoring using satellite interferometry, *Geophys. J. Int.*, *149*, 555–571, 2002.

Vergniolle, S., and C. Jaupart, Dynamics of degassing at Kilauea volcano, Hawaii, *J. Geophys. Res.*, *95*, 2793–2809, 1990.

Villeneuve, N., Apports multi-sources à une meilleure compréhension de la mise en place des coulées de lave et des risques associés au Piton de la Fournaise, *thèse de doctorat, Université de la Réunion*, 2000.

Vlastélic, I., T. Staudacher, and M. Semet, Rapid change of lava composition from 1998 to 2002 at Piton de la Fournaise (Réunion) inferred from Pb isotopes and trace elements: Evidence for variable crustal contamination, *J. Petrol.*, *46*, 79–107, 2005.

Voight, B., et al., Magma flow instability and cyclic activity at Soufriere Hills volcano, Montserrat, British West Indies, *Science.*, *283*, 1138–1142, 1999.

Walker, G. P. L., Basaltic-volcano systems, in *Magmatic Processes and Plate Tectonics*, edited by H. M. Prichard, T. Alabaster, N. B. W. Harris, and C. R. Neary, pp. 3–38, Geological Society Special Publication, 1993.

Walker, G. P. L., Volcanic rift zones and their intrusion swarms, *J. Volcanol. Geotherm. Res.*, *94*, 21–34, 1999.

Walsh, J. B., and R. W. Decker, Surface deformation associated with volcanism, *J. Geophys. Res.*, *76*, 3291–3302, 1971.

Ward, S. N., and S. E. Barrientos, An inversion for slip distribution and fault shape from geodetic observations of the 1983, Borah Peak, Idaho Earthquake, *J. Geophys. Res.*, *91*, 4909–4919, 1986.

Weertman, J., Theory of water-filled crevasses in glaciers applied to vertical magma transport beneath oceanic ridges, *J. Geophys. Res.*, *76*, 1171–1183, 1971.

Wicks, C., W. Thatcher, and D. Dzurisin, Migration of fluids neneath Yellowstone Caldera inferred from satellite radar interferometry, *Science*, *282*, 458–462, 1998.

Wicks, C. W., W. Thatcher, F. C. Monastero, and M. A. Hasting, Steady-state deformation of the Coso Range, east-central California, inferred from satellite radar interferometry, *J. Geophys. Res.*, *106*, 13,769–13,780, 2001.

Williams, C. A., and G. Wadge, The effects of topography on magma chamber deformation models: Application to Mt. Etna and radar interferometry, *Geophys. Res. Lett.*, *25*, 1549–1552, 1998.

Williams, C. A., and G. Wadge, An accurate and efficient method for including the effects of topography in three-dimensional elastic models of ground deformation with applications to radar interferometry, *J. Geophys. Res.*, *105*, 8103–8120, 2000.

Wright, T., Z. Lu, and C. Wicks, Constraining the slip distribution and fault geometry of the Mw 7.9, 3 November 2002, Denali fault earthquake with interferometric synthetic aperture radar and global positioning system data, *Bull. Seismol. Soc. Am.*, *94*, S175–S189, 2004.

Wright, T. J., Z. Lu, and C. Wicks, Source model for the M_w 6.7, 23 October 2002, Nenana Mountain Earthquake (Alaska) from InSAR, *Geophys. Res. Lett.*, *30*(18), 1974, doi: 10.1029/2003GL018014, 2003.

Yang, X., P. M. Davis, and J. H. Dieterich, Deformation from inflation of a dipping finite prolate spheroid in an elastic half-space as a model for volcanic stressing, *J. Geophys. Res.*, *93*, 4249–4257, 1988.

Yoder, H. S., *Generation of Basaltic Magma*, Natl. Acad. Sci., Washington, D. C., 1976.

Yokoyama, I., Crustal deformation caused by the 1914 eruption of Sakurajima volcano, Japan and its secular changes, *J. Volcanol. Geotherm. Res.*, *30*, 283–302, 1986.

Yun, S., P. Segall, and H. Zebker, Constraints on magma chamber geometry at Sierra Negra Volcano, galápagos Islands, based on InSAR observations, *J. Volcanol. Geotherm. Res.*, in press, 2005.

Zebker, H., F. Amelung, and S. Jónsson, Remote sensing of volcano surface and internal processes using radar interferometry, in *AGU Geophysical Monograph 116*, *Remote Sensing of Active Volcanoes*, edited by P. Mouginis-Mark, J. Crisp, and J. Fink, pp. 179–205, 2000.

Ziv, A., A. M. Rubin, and A. Agnon, Stability of dike intrusion along preexisting fractures, *J. Geophys. Res.*, *105*, 5947–5961, 2000.

Appendix A

Procedure for Running Inversions Using NA_MBEM code

This appendix describes the procedure for running inversions (the search stage) on dike intrusions using the code developed, NA_MBEM, named after the Neighbourhood Algorithm (NA) and the mixed boundary element method (MBEM). The following is a copy of the instruction file REAME.html, providing the necessary steps users should follow. The instruction is given for cases where dikes reach the ground surface (type (a) of Figure 2.1). Supplementary notes are added in italics. The auxilary functions used during the preparation steps are indicated by uppercase characters in the instruction file.

The codes are written in Matlab, i.e., platform-independent. However, NA_MBEM invokes the mixed BEM program written by Valrie Cayol, which has been compiled only under Linux and Unix at the moment. Hence the use of NA_MBEM is restricted to Linux and Unix machines.

Last modified: 21 August 2005

How to make an inversion using the Neighbourhood Algorithm and Mixed Boundary Element Method

(version NA_MBEM1.3)

Yo Fukushima

This document explains the procedure to make an inversion with the neighbourhood algorithm (Sambridge, 1999a), combined with the three-dimensional mixed BEM (Cayol and Cornet, 1997). This document consists of Procedure, Release Notes, Papers and Condition of use. Refer to Fukushima et al. (2005) for a more general explanation of the inversion procedure.

Procedure

(1) Creating fracture files
(2) Creating a topography mesh file
(3) Creating a mask file
(4) Filtering the unwrapped data
(5) Noise analysis
(6) Creating a data file
(7) Configurations I: na.input
(8) Configurations II: cdi.input
(9) Reprogramming subroutine programs
(10) Compilation
(11) Ready to lauch? Check for the files
(12) Launch
(13) Checking the result
(14) Scaling the misfit or an alternative way (optional: for those who makes an appraisal)

(1) Creating fracture files

You need two fracture files; hereafter called fractfile_a and fractfile_b. fractfile_a defines the eruptive fissures on the ground surface, and fractfile_b defines an approximated curve of the eruptive fissures. ATTENTION: order of fractures influences dip, shear and bottom angle direction; when fractures are saved South -> North in the fracture files, then the dike dips eastward when dip < 90, shears northward when shear > 0, and its bottom line is inclined toward South when theta > 0, etc.

Here is an example for fractfile_a.

```
4 1
178.895 37.924
178.865 37.984
178.834 38.044
178.804 38.104
2 1
178.836 38.158
178.809 38.221
2 1
178.842 38.24
178.816 38.332
3 1
178.853 38.451
178.837 38.53
178.82 38.609
4 1
178.995 38.55
178.986 38.6123
178.978 38.6747
178.969 38.737
```

This is the format used in MAILL_INTERFACE (*this program, developed by Jean-Luc Froger, creates topography meshes*). In this example, five segments are defined. If the fractures are longer than the mesh interval you wish to use (see (8) Configurations II: cdi.input), then it is recommended to subdivide the fracture as is the case in the first and the fourth fractures in the example. MKFRACT_A makes this subdivision automatically, so you might want to use it.

Here is an example for fractfile_b. This is just a list of coordinates (x, y)

```
178.8707   37.8694
178.8511   38.0047
178.8358   38.1294
178.8277   38.2790
178.8248   38.4132
178.8544   38.5143
178.9719   38.6600
179.0716   38.7776
179.2015   38.9054
```

You should make this file so that it smoothly approximates the fracture segments registered in fractfile_a. The easiest way to do it is to use PLOTFRACT3 to plot the fractures, then use GINPUT matlab function. The number of points is not important because when it is used automatic interpolation is done.

If you want to model a dike that has a significantly longer length than the surface eruptive fissure extension, then you can extend the points in fractfile_b and specify the option

TOPGEOM = 'keep' in MESHDIKE (see help meshdike).

(2) Creating a topography mesh file

Use MAILL_INTERFACE. This program can create topography meshes with the positions of the fractures (to which the top of the dikes are connected) specified. Use fractfile_a as the input fracture file. Or, if you want to control the mesh density close to the fractures, you can use MKDUMMYC. This function creates circluar points and writes out the coordinates of the points in the MAILL_INTERFACE input fracture format. After you got the resulting dummy.dat file, you combine it with your fractfile_a by executing 'cat your_fractfile_a dummy.dat > your_fractfile_a_and_dummy.dat' (*under Linux command line*). Then use your_fractfile_a_and_dummy.dat as your input for MAILL_INTERFACE.

In my case for the Feb 2000 eruption at Piton de la Fournaise, I created a dummy fracture file with MKDUMMYC, with density (*average point interval in the inner part*) 0.3km, radius for the inner part = 2km, radius for the outer part (*the point interval progressively becomes larger for this outer part*) = 6.5km. Then in MAILL_INTERFACE, I used angle_limite (*all the triangular elements will have angles larger than this value*) = 30, circle_creux (*hollow circle; an option to specify just the outside border of a circular mesh*) with rayon (*radius*) = 7km and number of points (*points along the circle*) = 20. This mesh was confirmed to precisely calculate the displacements.

Remember to note down the numbers of box-only nodes and elements. You should also check the coordinates of the point 1 of the DEM used (*that is, the offsets in x and y coordinates in the DEM*). You will need to write down these data in cdi.input file.

(3) Creating a mask file

Mask files are used when making data files. It is for InSAR data, which includes several unwanted parts (e.g. lava flows).

To make a mask file, simply make a raw file (type UCHAR in matlab) whose size is the same as your interferogram, with value = 1 where you want to keep and with value = 0 where you want to screen out. The simplest way to create a mask file is to use Photoshop. You open an interferogram, create a layer and make it transparent so that you can see the interferogram, then you save only the created layer in raw format. The same thing can be done with Gimp. But because Gimp does not read raw format, you should first convert your interferogram to a bmp or tiff image, work on Gimp, save the mask file in bmp or tiff, then convert the bmp (tiff) file to raw format. The conversions bmp <-> raw can be done with RAW2BMP and BMP2RAW, and tiff <-> raw with RAW2TIFF and TIFF2RAW.

(4) Filtering the unwrapped data

You can low-pass filter the unwrapped data you want to use with a matlab function FILTUNWR. Typically I use cutoff = 80m which corresponds to about 4 pixels.

(5) Noise analysis

This step is necessary if you want to make the appraising (model uncertainty analysis) with NAB. But you have an alternative way: see (14) Scaling the misfit or an alternative way. You use CALCACF to calulate the autocorrelation function of the (noise) data. Autocorrelation function defines the statistical correlation and the amplitude of the (noise) data. CALCACF calculates the variance and the correlation distance by assuming two types of theoretical autocorrelation function: exponential type and Gaussian type. Empirically, exponential type better represents the data noise characteristics. You can use the same unwrapped data as you use in the inversion, but you should mask the area where you observe displacements associated with dike intrusions.

If you want to calculate an average of several autocorrelation functions determined from different data sets, you can use MERGEACF.

(6) Creating a data file

Most of the following explanation applies to interferometric data.

First: make a file to specify the coordinates (x, y).

It should look as follows.

```
179.581 38.551
179.581 38.662
179.581 38.773
179.581 38.884
179.692 37.675
179.692 37.775
179.692 37.886
179.692 37.997
179.692 38.108
179.692 38.219
179.692 38.330
...
```

Use MAKEDATAPTS to create such points. This function generates points in a specified area. There are several options: 'Uniform' will create uniformly-gridded points, 'Circular' creates circular points, 'Quadtree' will create a non-uniform points based on the quadtree algorithm (it puts more points where the amplitude of InSAR data is larger). For Quadtree option, you will be asked for an unwrapped data and the necessary information. All the options will ask you for a mask file. Output file will be in ascii format.

Second step: retrieve the data value for the points specified

Use MAKEDATAFILE. It will create a data file of which format looks like the following (but saved as a binary).

```
x1 y1 compx1 compy1 compz1 data1 datatype1
x2 y2 compx2 compy2 compz2 data2 datatype2
x3 y3 compx3 compy3 compz3 data3 datatype3
...
```

Here the first two columns specify the coordinate, the following three are for the projection vector (radarlook for the case of InSAR data), data* corresponds to data value, and datatype is d or t where d stands for displacement and t for tilt. For GPS data, the program will ask for an input file which looks like the above format. Then the program will merge with other data (if you wish to make a joint inversion) and outputs a binary data file. **ATTENTION**: for GPS data, specify the components as **[0 0 -1]** for vertical, **[-1 0 0]** for east, and **[0 -1 0]** for north component (as a result, three lines are required for data per one three-component GPS station).

MAKEDATAFILE also creates a covariance matrix file. The program will ask for the data variance and correlation distance. If you want to put different weights to different data set, you put different values. For example, when you simultaneously use InSAR data and GPS data, data variance = 2 for InSAR and = 1 for GPS data will put weights on GPS data twice as large as those on InSAR data. Note that the absolute values themselves are not at all important in the behavior of the sampling program, since the algorithm takes into account only the rank of the misfit. For the correlation distance, it is mathematically appropriate to use the value estimated by the step (5), but many people just assumes data independency for simplicity. The covariance matrix becomes a diagonal in the case of independent data.

(7) Configurations I: na.input

The file na.input specifies the inversion parameters and the parameter bounds. The file is self-explanatory; refer to the file for explanation.

(8) Configurations II: cdi.input

The file cdi.input specifies the files used in the inversion, and all the other necessary information. You have to specify the followings.

fractfile_a
fractfile_b
mesh interval
topography mesh file
offset of the topography file (x)
offset of the topography file (y)
number of box-only nodes
number of box-only elements
datafile
data covariance matrix file

(9) Modify the subfunctions

You should reprogram the subroutine programs on your own need, when you want to do something different, in addition to na.input and cdi.input. Normally, the main program na_mbem.m does not have to be edited. The main na.m file invokes the following programs (except the ones written in the end of na.m file).

objfun: returns the misfit value corresponding to a set of model parameters
user_ini: a script that runs before inversion
user_fin: a script that runs after inversion

(10) Compilation

(optional) If you want to run the inversion on a command line, compile it with Matlab compiler:

```
mcc -m -O all na_mbem
```

(11) Ready to launch? Check for the files

> Confirm if there are the files given below.
> na_mbem : the main program you just compiled.
> Mc3f : the 3D mixed BEM program (Linux executable; can be in another directory having a path on your machine)
> *the fracture file (a) you created in Step (1)*
> *the fracture file (b) you created in Step (1)*
> *the topography file you created in Step (2)*
> *datafile you created in Step (6)*
> *covariance matrix file you created in Step (6)*

The files in italic are specified in cdi.input. Make sure that you have the same names.

(12) Launch

Just type

```
na_mbem #ID
```

on a Linux or Matlab command line to launch. You specify the inversion ID (e.g., 'na_mbem 123'). When the inversion is finished, it will create a file named, for example, "123.nares". This file contains all the evaluated model parameters and misfit values. You can visualize this result using PLOTNARES function. The best-fit mesh files and the result file of modelling are also saved with the ID number (dike_best_123.res, etc.), if you use the user_fin.m file that I created.

In every iteration, the evaluated sets of model parameter values as well as the misfit are diplayed.

When inversion finishes, default user_fin.m program automatically rescales P0 (overpressure) to correct the effect of mesh roughness (*it was found that a coarse mesh overestimates the displacements but less affecting the relative displacements over calculation points; this step corrects this effect. See Fukushima et al. [2005]*).

(13) Checking the result

Use PLOTNARES to plot the result of the inversion. You will have plots of (1) Iteration vs Misfit, (2) Parameter vs Misfit, and (3) Parameter vs Parameter. To see the best-fit dike geometry or the best-fit modelled displacements, etc., use the programs in the MATLAB analysis library (just type 'matlib') (*this library is named MATLIB and includes all the functions that I (+ Valérie Cayol and Jean-Luc Froger) have developed*). To see what functions are available, type 'help matlib' in the analysis library directory.

(14) Scaling the misfit or an alternative way (optional: for those who appraise the ensemble)

This step is necessary if you want to appraise the ensemble and if proper data variance value was not used in the covariance matrix file. If proper correlation distance was not used, you cannot make a proper appraisal; you should make another NA inversion with proper correlation distance which can be defined from the residual data of the first inversion (see below).

Scaling is done by invoking SCALENARES.

```
scalenares (naresfile, ND+1, scale)
```

where ND is the number of dimensions (misfit is saved in the (ND+1)th (last) column in .nares file) and scale is the scaling factor; if in the inversion you used data variance = 1 and you obtained, say, variance = 0.0001 for the residual data, then set scale to 1/0.0001.

An alternative and probably more appropriate way to make appraisal is to perform two NA runs.
1) for the first one, use arbitrary variance (this does not effect the searching behavior at all) and a plausible correlation distance (for example, 500 m), 2) for the second one, when creating the new covariance matrix, use the estimated variance and correlation distance of the residual data corresponding to the best fit model obtained from the first run. Then the result .nares file for the second inversion can be directly used in NAB, the appraising program without any correction.

Please inform me if you find some errors in this manual or programs. If you have questions (even if you thoroughly read this manual and papers), do not hesitate to mail me.

Release notes

(from NA_MBEM1.2 to NA_MBEM1.3: 21 Aug 2005)
- Updated meshdike.m. Serious bug fixed. In the case of d_top=0, the dike top nodes were mistakenly interpolated.

(from NA_MBEM1.1 to NA_MBEM1.2: 18 Aug 2005)
- Updated meshdike.m and meshfrac.m. Now segmentgeom = 'keep' option is implemented. Some bugs are also fixed.

(WHAT TO DO)
Previous Forward.m template files (Forward.m_for_rectangle etc.) are to be converted to the current objfun.m form.

(from NA9.3.4 to NA_MBEM1.1: 13 Jul 2005)
1. Overhaul of inversion code.
The inversion codes were overhauled, though the basic user interface has been kept as it was. The main modification is that I abandonned parallelized code. In fact, the parallelization was

useless on a platform with one CPU, and it did not really contribute on saving time even on multi-CPU machines and clusters. So I chose to clean the codes rather than to keep the functionality of parallelization. Hopefully, I will be able to implement parallelization in the future on an appropriate platform.

Here explains the main functions for inversion.
- na_mbem: main routine to launch an inversion.
- nasearch: the core program of the inversion. Basically this function works for all the inversion problems, but the version in this directory is slightly adjusted to the problem we are concerned.
- objfun.m: equivalent to former Forward.m. It returns a misfit value corresponding to a set of model parameters. As explained above, this function should be edited for each different application.

2. Meshdike
Meshing a dike used to be made using meshdike**.m. This function is also overhauled; meshdike.m is now written in a more sophisticated form (and put also in the library MATLIB). It calls meshfrac.m to create the main (quandrangle-like) mesh and every superficial segment mesh, then mergemesh.m to merge the meshes.

Meshdike has also improved in meshing the superficial segments; the element size and geometry is more homogeneous compared to the previous version, and you can specify how you want to connect to the main part.

(WHAT TO DO)
In meshdike.m, in the case topgeom = 'keep' is under construction.
Previous Forward.m template files (Forward.m_for_rectangle etc.) are to be converted to the current objfun.m form.

(from NA9.3.3 to NA9.3.4)
- Now a semispheroid source (that resembles a laccolith) is available to model. If you want to use this source, copy Forward.m_for_laccolith to Forward.m and appropriately tune it.
- meshdike10 bug fixed. There used to be a problem (1) when topgeom = 'keep' and a surface fracture was too short, (2) when botlen was too small (less than 0.2), (3) d_top = 0.
- scaleres.m (it calculates the percentage of data explained at the end) bug fixed; in certain cases it did not properly calculate the percentage.

(from NA9.3.2 to NA9.3.3)
- a set of programs for creating subsurface quadrangle mesh is added. The main function is makequadex3.m; this function invokes meshquadrangle.m, quadcorners.m, endpoints.m, ptrelline.m, axisrot.m, etc. When makequadex3 is used instead of meshdike, then you do not need fractfilea and fractfileb. However, cdi.input format has the same format for simplicity; so just give whatever values for the variables you do not use.
- a set of programs for creating subsurface ellipsoid mesh is added. The main function is triellipsoid.m. When this is used instead of meshdike, then you do not need fractfilea and fractfileb. However, cdi.input format has the same format for simplicity; so just give whatever values for the variables you do not use. NOTE: when the aspect ratio is too small, the boundary element computation does not converge (so the misfit corresponding to models having small aspect ratio would be 100%).
- Template Forward.m files are added. You find: Forward.m_for_dikereachingsurface,

Forward.m_for_quadrangle, and Forward.m_for_ellipsoid. Copy the one you wish to use to Forward.m.
- na.m bug fixed concerning MAXCALCTIME. (MAXCALCTIME is set so that iteration continues even if forward modeling fails for some reason.)

(from NA9.3.1 to NA9.3.2)
- meshdike10 bug fixed. Now it meshes properly in the case d_top = 0.

(from NA9.2.3 to NA9.3.1)
- meshdike10 replaced meshdike9. This version of meshdike lets you bend the dike vertically. Please see help of meshdike10 for detail.
- minor revisions of na.m. MAXCALCTIME defined; if a BEM calculation does not finish within this time, then misfit would be 100%.

(from NA9.2.2 to NA9.2.3)
- meshdike9 instead of meshdike8. The parameter 'botgeom' is removed. Instead, parameter 'botcurv' is added. This parameter specifies the curvature of the bottom side curve. The bottom is assumed parabolic, and botcurv is the angle between the line connecting the end points and that connecting an endpoint and the midpoint. Further, meshdike9 makes a clean delaunay thanks to a function CURVSPACE.
- loadcdiinput.m and other functions calling this function were modified, so as to reflect the above modification.
- user_fin.m was modified in such a way that it outputs the % data explained in Inversion_*.desc file.

(from NA9.2.1 to NA9.2.2)
- meshdike8 used instead of meshdike7. Now one parameter added to specify the geometry of the superficial and deeper parts connection. Retain the surface fissure length or let vary with bottom side length change.
- The above option is to be specified in cdi.input. As a result, loadcdiinput.m and other functions calling this function were modified.

(from NA9.2 to NA9.2.1)
- Now mesh interval of dike is to be specified in cdi.input. As a result, loadcdiinput.m, meshdike7_1.m, Forward.m, user_ini.m, and user_fin.m in the NA9.2.1 directory were updated.
- user_ini.m was modified. Now it writes current directory information in the inversion description file (Inversion_****.desc).

(from NA9.1 to NA9.2)
- meshdike7_1 is used instead of meshdike7. The way of taking the reference axis of the geometry change is modified. Now the reference axis is on the top of the dike (it used to be the filefractb projected onto the ground surface; this was problematic when the dike was not reaching the ground.).

(from NA9 to NA9.1)
- meshdike7 is used instead of meshdike5, meshdikesurf, meshdikecv, meshdikesurfcv. Now meshdike7 has all the functions of the four programs integrated. Also, a bug in the previous versions of meshdike was fixed, in the calculation of dip and shear. The resulting geometry of dike should not be different by using previous versions, but I expect a small difference in dip

and a considerable difference in shear.

(from NA8 to NA9)
- meshdike5 used instead of meshdike4. The difference is the definition of the middle point of the top side. Consequently, the definition of dip and shear would be different. The model values of the older version and those of the current version cannot be compared directly. The current version is closer to reality.
We can take several definitions because the top side is a curve and not a line.
- meshdikesurf and meshdikesurfcv now available. Theese meshing programs can completely connect to the ground surface (it can be buried, too). The former makes a straight bottom side, while the latter makes a curved bottom side (same curvature as the top side). To use them, just replace meshdike5 in Forward.m to one of these.
- The scaling factor for P0 is now automatically calculated and the overpressure values in the resulting result file (.nares) are automatically rescaled. At the moment, it is only valid for a constant overpressure. If you want to introduce two or more overpressure parameters (e.g., driving pressure and gradient), then user_fin.m should be modified appropriately.
- The variance and correlation distance of the residual for the best-fit model is now automatically calculated. It is displayed when the inversion is finished. This is useful if you want to appraise the ensemble. Further explanations are given close to the end of this note.

(from NA7 to NA8)
- The format of NA result file has changed in such a way that the file includes inversion information (ns1, ns2, nr, number of dimensions, model space bounds) as a header. Before version NA7, the result file had names na.res.$ID, where $ID is the ID number of the inversion. The new result file will have names $id.nares. This modification enabled NARES and other programs not to run without specifying na_input_$id.m, which used to contain the inversion information.

- Input m files, i.e., na_input.m and cdi_input.m are no longer used. Instead, you specify the necessary information in na.input and cdi.input. These files are read directly by the NA main program. This means that you do not have to recompile when na.input or cdi.input are updated.

- meshdike4 used instead of meshdike3. (Fixed the bugs; there used to be a problem in the connection between the superficial and main parts.)

Papers

Cayol, V., and F. H. Cornet (1997), 3D mixed boundary elements for elastostatic deformation fields analysis, Int. J. Rock Mech. Min. Sci. Geomech. Abstr., 34, 275-287, 1997.

Sambridge, M. (1999a), Geophysical inversion with a neighbourhood algorithm - I. Searching a parameter space, Geophys. J. Int., 138, 479-494.

Sambridge, M. (1999b), Geophysical inversion with a neighbourhood algorithm - II. Appraising the ensemble, Geophys. J. Int., 138, 727-746.

Fukushima, Y., V. Cayol, and P. Durand (2005), Finding realistic dike models from interferometric synthetic aperture radar data: The February 2000 eruption at Piton de la Fournaise, J. Geophys. Res., 110, B03206, doi: 10.1029/2004JB003268.

Condition of Use

- The codes can be modified on your conveniency, you must indicate that modification is made from this package.
- Due acknowledgment must be made of the use of this package in research reports or publications.
- Those who wish to use this package must contact me directly. In this way, I can see if my programs would fit his/her purpose and also might be able to offer the most stable version.
- Use of any part of this package will be taken as acceptance of these conditions.

I further would like to ask you to report bugs that seem important.

Résumé

Après cinq ans et demi de sommeil, le volcan du Piton de la Fournaise (île de la Réunion, Océan Indien) est entré dans un nouveau cycle d'activité en mars 1998. Des données d'interférométrie radar (InSAR) montrent que des déplacements complexes sont associés aux cinq premières éruptions du cycle survenues entre 1998 et 2000. Une méthode a été développée pour déterminer des géométries réalistes et les surpressions des intrusions de dykes à partir de données InSAR. Cette méthode est basée sur la combinaison d'une méthode d'éléments frontières 3D et d'une inversion de type Monte Carlo. Les caractéristiques du bruit des données sont prises en compte dans les inversions. Des tests synthétiques montrent qu'un modèle est retrouvé avec succès dans la limite d'intervalles de confiance étroits. Il a été montré que négliger la topographie induit une erreur de modélisation en profondeur et une surestimation des surpressions ou des ouvertures. L'application de la méthode à chaque éruption requiert des paramétrisations spécifiques des modèles. Dans certains cas, un dyke incurvé en surface doit être introduit, dans d'autres, l'inversion simultanée de deux dykes est nécessaire. La plupart des dykes déterminés ont un pendage vers la mer de 65 degrés. Le dyke associé à la première éruption du cycle (mars 1998) s'enracine au niveau de la mer (2600 m sous le sommet), tandis que les dykes suivants sont situés à moins de 1000 m sous la surface du sol. La forme latéralement allongée des dykes, les déformations pré-éruptives et les essaims sismiques peuvent être expliqués par un niveau de flottabilité neutre situé à moins de 1000 m sous la surface. Ceci est cohérent avec la présence de réservoirs magmatiques à ce niveau. La périodicité spatiale des intrusions de dykes, du flanc nord au flanc sud, est cohérente avec les modèles de transfert de contraintes. Finalement, des analyses en terme de contraintes de Coulomb montrent que les cinq éruptions modélisées ont principalement favorisé le glissement sur des plans potentiels subhorizontaux situés entre 1000 et 1500 m au dessus du niveau de la mer.

Magma transfer at Piton de la Fournaise volcano from 3D modelling of radar interferometric data for 1998-2000

Abstract

After five and a half years of quiescence, Piton de la Fournaise volcano (Réunion Island, Indian Ocean) entered into a new active period in March 1998. Synthetic aperture radar interferometry (InSAR) data show complex displacements associated with the first five eruptions that occurred between 1998 and 2000. A method was developed to find realistic geometries and overpressures of dike intrusions from the InSAR data. This method is based on a combination of a fully 3D boundary element method and a Monte Carlo inversion. The noise characteristics of the data are taken into account in the inversions. Synthetic tests show that a model is successfully retrieved within predicted narrow confidence intervals. Neglecting topography was shown to result in poor modelling at depth and in overestimation of overpressure or opening. Application of the method to each eruption requires specific parameterizations of the model(s); in some cases, a curved dike surface must be introduced, and in other cases, simultaneous inversions for two dikes are required. Most of the estimated dikes dip seaward with a typical angle of 65 degrees. The dike associated with the first eruption of the cycle (March 1998) is found to originate from sea level (2600 m below the summit), whereas those dikes associated with subsequent eruptions are estimated to be shallower than about 1000 m below the ground. Laterally elongated dikes, preeruption deformations and seismic swarms can be explained by a level of neutral buoyancy less than 1000 m beneath the ground. This is consistent with the presence of magma reservoirs at this level. For the studied period, the intruded volume amounts to 8% of the lava flow volume. The spatial periodicity of dike intrusions from the northern to the southern flank is consistent with stress transfer models. Finally, Coulomb stress analysis shows that the five eruptions modelled mostly encourage slip on potential subhorizontal planes located 1000–1500 m above sea level.

Discipline : Sciences de la Terre - Volcanologie

Mots-clés : Volcanologie, Modélisation numérique, Inversion, Interférométrie, Transfert de magma, Volcan du Piton de la Fournaise, Ile de la Réunion.

UMR 6524 Laboratoire Magmas et Volcans, Université Blaise Pascal Clermont II
5 rue Kessler, 63038 Clermont-Ferrand, France.